UNIVERSITY OF ALBERTA

INFLUENCE OF RATE EFFECTS ON THE RESIDUAL STRENGTH OF MOVING SLOPES

BY

© ATHAPATHTHU MUDIYANSELAGE PATHMA WEDAGE

A thesis submitted to the Faculty of Graduate Studies and Research in partial fulfillment of the requirements for the degree of Doctor of Philosophy.

DEPARTMENT OF CIVIL ENGINEERING

Edmonton, Alberta

Fall 1995

ISBN 0-612-06309-7

UNIVERSITY OF ALBERTA

RELEASE FORM

NAME OF AUTHOR: Athapaththu Mudiyanselage Pathma Wedage

TITLE OF THESIS: INFLUENCE OF RATE EFFECTS ON THE RESIDUAL STRENGTH OF MOVING SLOPES

DEGREE: Doctor of Philosophy

YEAR THIS DEGREE GRANTED: 1995

(Signed)..........................

Department of Civil Engineering,
University of Peradeniya,
Peradeniya,
Sri Lanka Telephone : 94 - 8 - 88029

Dated May 02 1995

UNIVERSITY OF ALBERTA

FACULTY OF GRADUATE STUDIES AND RESEARCH

The undersigned certify that they have read, and recommend to the Faculty of Graduate Studies and Research for acceptance, a thesis entitled INFLUENCE OF RATE EFFECTS ON THE RESIDUAL STRENGTH OF MOVING SLOPES submitted by A.M. Pathma Wedage in partial fulfillment of the requirements for the degree of Doctor of Philosophy

....
Dr. N.R. Morgenstern
Supervisor

....
Dr. D.H. Chan
Co-Supervisor

....
Dr. P.K. Robertson

....
Dr. T. Hrudey

....
Dr. K. Barron

....
Dr. J. Graham

Date May 02, 1995

To my husband Deepthi

ABSTRACT

The existing literature on the rate effects on residual strength is reviewed. Clearwater clay-shale, present in the foundation of Syncrude Tailings Dyke situated in northern Alberta, is tested under different rates, in both ring shear apparatus and the direct shear box. The clay-shale, which has a Plasticity Index of 107%, a Liquid Limit of 135%, natural water content of 23% and clay content of 49% shows an improved residual shear resistance at higher rates. It is found that the residual strength is increased by 3.4 - 3.5%, for a tenfold increase in the strain rate. The tested range of displacement rates is 0.185 mm/day to 7.0 mm/day. Judging from the existing literature on such rate effects, a broad correlation between the plasticity of clay and rate effects is obtained.

By extension of the plasticity theory, a constitutive relationship is developed to model the strain rate-dependence of residual strength. It can be easily incorporated into existing finite element plasticity codes. The model is coded in the program PISA™ (Chan and Morgenstern, 1992) and calibrated using an illustrative example.

A simulation of construction movements at Cell 23 of Syncrude Tailings Dyke has been done. Cell 23 of the tailings dyke has been identified as a problem area where more than 38 cm of horizontal movement has been observed at some locations over a period of 11 years. Clearwater clay-shale, present beneath portions of the dyke, is found previously sheared, due to glacial drag forces of the overlying till. The use of the rate-dependent model, for the shear zone, was found to provide a satisfactory basis for simulation of the movement pattern. The results of the deformation analysis provide the anticipated field velocities and show how they deteriorate with time to a reasonable accuracy.

Acknowledgments

The development of this thesis would not have been possible without the continuous love and support of my family, especially my husband Deepthi, whose courage, strength and understanding have helped me during the difficult periods in the past three years. I am deeply indebted to him for his sacrifices for my postgraduate education.

The smile of my four month old son, Pravin, has given me courage for me to complete this work. I am also thankful for the continuous support of my parents, my brothers and my sisters.

I am deeply grateful to Dr. N.R. Morgenstern for his continuous support, guidance and enthusiasm during the years of this research. His ideas, supervision and orientation were fundamental to the development of this work.

I thank Dr. D.H. Chan for his support and direction since the beginning of this work. His discussions and suggestions were invaluable to the accomplishment of this research.

The support offered by Syncrude Canada Ltd., by Mr. Steve Tan, who sent field data, is gratefully acknowledged. I also thank Omar and Leonard for helping me by translating a French report. Various supports given by Gerry and Steve in laboratory testing are appreciated.

Finally, I thank my friends for being with me in my difficult periods, in particular Priyanthi, Shahani, Manel, Chandrani and their families.

TABLE OF CONTENTS

LIST OF TABLES

LIST OF FIGURES

CHAPTER 1

INTRODUCTION

1.1 Purpose of the research

Many slopes, natural as well as man-made, show continuing movements with time at different rates. Natural slopes exhibit different types of behavior over long periods of time. For example, there may be periods in which the landslide is completely stationary, other periods of movement at constant velocity, and still other periods in which episodes of accelerating and decelerating movements occur. Large man-made structures, such as tailings dams, are often constructed adjacent to mining sites due to economic considerations. In some cases, geotechnically weak foundation soils are encountered which could create various problems during and after construction. One of the major problems associated with this type of construction is the excessive amount of movement of the slopes and the foundation soils, even though the Factor of Safety lies within acceptable limits.

The conventional approach to analyzing such large structures and natural slopes considers only limiting stability conditions, and no account is taken of the actual motions of the soil. When undertaking construction on moving ground, particularly when the movements are themselves induced by the construction operations, it is not only prudent, but often necessary, to define allowable velocity in order to control earthworks. An example of this is found in the mining operation using draglines at Syncrude Canada Ltd., situated in northern Alberta, Canada. If a critical velocity along a clay seam is exceeded, as measured by a borehole inclinometer, mining is stopped. The dragline is moved out of any potential danger and the mining scheme for that location is re-evaluated (List, 1992). For some natural landslides the movement signature itself may be the only effective means of assessing the risk to public safety. In both field situations, natural slopes and man-made slopes, the motions can be either slow-stable or accelerating. The slow-stable motions may be acceptable in many situations while accelerating motions may not. In both cases, limit analysis gives the same result. Therefore, the physical significance of a velocity concept in construction and monitoring in geotechnical practice is not clearly defined.

Often it is possible to identify causes of the motions such as fluctuations of water level due to drying and wetting, or changes in the stress field within slopes due to construction, erosion or other external factors. The time and rate-dependent response of materials involved in continuing movement is the least understood and yet it is an important part of understanding the behavior of the slope or the landslide.

There are basically three distinguishable time-dependent processes applicable to slope movements in general: primary consolidation, creep and strain rate effects on shear strength. Primary consolidation and creep are well studied processes which may be more significant in soft or normally consolidated soils than in overconsolidated soil.

When the total stress at a point in the soil is increased, excess pore pressure is generated; this subsequently dissipates with time, resulting in primary consolidation. Terzaghi's theory (1948) and Biot's theory (1965) of consolidation can be used to estimate consolidation movements.

The time-dependent response of a soil may assume a variety of forms owing to the complex behavior among soil structure, stress history, drainage conditions, and changes in temperature, pressure, and biochemical environment over time. Nonetheless, they follow a logical and often predictable pattern.

Time-dependent deformations result from both volumetric and shear stresses. Volume change results from both primary consolidation, which is described in a previous paragraph, and secondary compression, which is controlled by the viscous resistance of the soil structure. The latter is often referred to as volumetric creep. Time-dependent shear deformations are usually referred to as deviatoric creep or shear creep.

A characteristic relationship between strain rate and time exists for most soils, at least for simple stress states and drainage conditions. A general pattern of the logarithm of strain rate versus logarithm of time has been observed for undisturbed and remolded clay, wet clay or dry clay, normally consolidated and overconsolidated soil and sand (Singh and Mitchell, 1968). At any stress level, the logarithm of strain rate decreases linearly with the logarithm of time. At low stresses, the creep rates are small and of little practical importance. Creep is greater in normally consolidated soil than in overconsolidated soils. Although the magnitude of creep strains and strain rates may be small in sand or dry soil, the form of the behavior conforms with the same pattern (Mitchell, 1992).

Application of stress leads first to a period of transient creep, during which the strain rate decreases continuously with time, followed by creep which appears in some cases to be at nearly a constant rate for some period. If the shear stresses are high enough, an acceleration in creep rate occurs, leading to failure.

Various models with different assumptions regarding constitutive behavior of soils are available. Among them the double-yield-surface model for creep strain rates (Borja et al., 1990) is found capable of simulating creep movements in soft clays in certain field cases (Morsy et al., 1994). However, the application of this model is limited to normally or lightly overconsolidated clays.

The third cause for time dependent movements is the rate effects on the shear strength. The undrained shear strength as well as the residual strength of a clay increases with increase in rate of strain. Effect of strain rate on undrained strength has been studied by Kulhawy and Mayne (1990) for several clays. Their results indicate that the magnitude of the effect is about 10% for each order of magnitude increase in the strain rate. The phenomena studied in this thesis are the time-dependent movements caused by deformation rate-dependent residual strength of clays, which is a relatively narrow discipline compared to creep studies.

As the rate-dependence considered here is applied to the residual friction angle of a clay, the class of movements under consideration is concerned only with previously sheared soils. A good example for such a time-dependent movement is the foundation movement at the Syncrude tailings dyke. These movements have developed gradually over several years in response to the construction of the tailings dyke and related mining activities (Fair and Handford, 1986). It is noted that much of the foundation involves glacial till over the Clearwater Formation. The Clearwater Formation contains some weak, highly plastic units which create circumstances that are conducive to weakening by glacio-tectonic deformation. Localized movements have been observed within these plastic clay layers, which are found to be presheared and have an operational residual friction angle of about 6.5°. Years of monitoring reveals that the deformation rate varies with time during construction and for years after construction.

Features arising from glacio-tectonic deformation or glacial drag are widespread and have been recognized in Western Canada and the USA, and in both Eastern and Western Europe (Morgenstern, 1987). When the bedrock is weak, extensive shearing results with remnants containing slip surfaces at residual strength. This geological detail can exercise a dominant control on stability.

When sliding occurs along a shear surface, the ratio of the tangential to normal force depends on the rate at which each contact point is displaced. This happens as a result of different internal phenomena which might include the viscous flow of water and adsorbed films and the generation of suction in pore water. A general pattern of behavior has been reported for several clays, although in a different degree: the apparent residual frictional coefficient increases linearly with the logarithm of the shear strain rate.

When sliding occurs along a shear surface at a certain strain rate due to an externally applied load, the residual friction angle is mobilized corresponding to the particular strain rate, and the system of forces will be in equilibrium. At the next moment, there will be an unbalance of load due to the larger stresses carried by the zone at a higher strain rate than the zone at a lower strain rate. Therefore, a stress redistribution occurs resulting in a decrease of stresses in the zone with a higher strain rate. This redistribution cause further movements. In this way, after the application of initial stress, the movements will occur until the redistribution of stress is negligible and the sliding velocity becomes a minimum constant value.

The rate dependence of residual strength has been a topic of research for many years (Petley, 1966, Lupini et al., 1981, Skempton, 1985, Davis et al., 1993). Although a number of researchers have proposed relationships between residual strength and deformation rate or velocity (Van Genuchten, 1989, Bracegirdle et al., 1990, Davis et al., 1990, Nieuwenhuis, 1991, Davis et al., 1993), none appears to have continued their work towards the development of a stress-strain-time relationship for such a rate-dependent material.

The purpose of this research is to develop, from an extension of plastic theory, a constitutive model for a deformation rate-dependent material, to calibrate it with a series of ring shear and direct shear tests for sheared clay obtained from the Syncrude tailings dyke site, and to validate the model by applying it to real field cases.

1.2 Organization of the thesis and scope of each chapter

This thesis presents the outcome of a series of experimental investigations and a theoretical development of a model for the deformation rate-dependence of residual strength of clay and its relevance to account for slope movements.

Chapter two presents an empirical relationship for the rate of shear strain and residual friction angle for Clearwater clay-shale based on the results of ring shear and direct shear tests conducted on undisturbed samples, together with a comparison between them and other clays. Previous laboratory studies performed by Petley (1966), Lupini (1980), Skempton (1985), Lemos (1986) and previous empirical relationships obtained by Van Genuchten (1989), Bracegirdle (1990), Davis et al. (1990), Nieuwenhuis (1991) and Davis et al., (1993) are reviewed. A broad correlation is observed between plasticity and rate effects for the clays.

From an extension of classical plasticity theory, Chapter three develops constitutive relationships for a material with a deformation rate-dependent residual strength. The concept of a dynamic yield surface, defined as a function of stresses, strains and strain rates, is introduced here. The state of a point in the clay during plastic yielding is assumed to be described by the dynamic yield surface and the plastic strain increments are calculated from a non-associated flow rule. The resulting stress - strain relationship for a deformation rate-dependent material is found to be relatively simple for incorporating into existing finite element programs, and when the rate effects are zero, the relationship reduces to that of an elasto-plastic material. The developed rate-dependent stress - strain model is coded in PISA (Chan and Morgenstern, 1992) using the empirical relationship discussed in Chapter two. A numerical example is presented in order to demonstrate and verify the behavior of the model. The modified finite element program, PISA, is found to be capable of reproducing the laboratory results, if the model is used.

Chapter four presents an application of the model to an old landslide at Mam Tor, UK. For over 3200 years the Mam Tor landslide movements have been taking place at an average rate of 10m per century. However, movements would occur as a series of small displacements in winter months of heavy rainfall. Records of movement in the present century (in 1918, 1939, 1965, 1966 and 1977) indicate that slips leading to displacements typically about 0.3 m are still taking place, on average at 4-year intervals, in winter months of more than 200 mm rainfall. Previous studies carried out on this landslide by Skempton (1989) demonstrate that the movements occur as a result of rainfall and are controlled to some extent by the rate effects operating on the slip mass, which is sheared Edale Shale. Results of a deformation analysis for the year of 1977 are presented in this chapter, with known rainfall and pore pressure variations in the failed mass. The difficulties in calculating the excess pore pressure generation and dissipation were overcome in this analysis by using the field pore pressure measurements as input for the analysis. The use of a deformation rate-dependent model is found to give about a 10% reduction in overall movements. During the movement event, the residual friction angle of the shear zone is found to vary between 14-14.2° for an average of 0.1 m of movement per year.

Chapter five presents the results of deformation analyses carried out on a construction of a test embankment in an unstable slope in Salledes, France. Field movements up to six years after construction have been monitored and reported in Cartier and Pouget (1989). Sensitivity analyses for property variations of both shear zone and colluvium materials were conducted to select appropriate sets of parameters for the analyses. It is noted from the analyses that the movements are sensitive to the stiffness of the colluvium. The use of a hyperbolic elastic model for colluvium and a rate-dependent model for the shear zone was found capable of simulating the movement pattern due to construction of the trial embankment. The movements after construction show a direct correlation with the pore pressure variations beneath the embankment.

Chapter six discusses the application of the deformation rate dependent model to the analysis of movements at the Syncrude tailings dam site. Cell 23 of the tailings dam has been defined as a problem area where more than 38 cm of horizontal movements have been observed at some locations during a period of 11 years. Deformation analyses, based on knowledge of the field behavior for the first 8 years of construction, have been carried out in this study. Factors controlling the movements are identified and the significance of each factor is discussed. By using this history match approach, a set of material parameters is chosen for each material. Finally, observed behavior at two inclinometer locations were simulated for the rest of the construction years. The application of the deformation rate-dependent model to the shear zone was found to provide a satisfactory basis for simulation of the movement pattern for the field condition considered herein.

From this study, it is concluded that to model a pre-sheared clay in a deformation analysis, the rate-dependence of residual strength has to be taken into consideration. Such a behavior can be modeled simply by extending classical plasticity theory. When applied to an actual field problem, the overall behavior is complicated by other factors, such as the stiffness of overlying materials.

CHAPTER 2

RATE EFFECTS ON RESIDUAL STRENGTH

2.1 Introduction

The residual strength of cohesive soils is of importance in geotechnical engineering. The concept of residual strength has contributed enormously to the understanding of the behavior of soils subjected to large displacements under both drained and undrained conditions. It plays a major role in the behavior of old landslides, in the assessment of the engineering properties of soil deposits which contain pre-existing shear surfaces and in the assessment of the risk of progressive failure in stability problems in general.

For a given set of stress conditions and if deformed slowly to large strain under drained conditions, a soil will arrive ultimately at the same final water content and void ratio, regardless of its initial state. The strength of the soil, once this conditions has been reached, will be a minimum and is termed the residual strength. The friction angle corresponding to this strength is the residual friction angle ϕ_r'.

The approach to the residual state of an overconsolidated soil can be considered as taking place in two stages (Figure 2.1). First, after peak strength is passed, the strength decreases to the critical state value due to an increase in water content. Then, strength decreases to the residual value at large displacements due to reorientation of clay particles parallel to the direction of shearing. After the first stage, the strength of overconsolidated clay becomes similar to the strength of normally consolidated clay.

The effect of particle reorientation can be seen only in clays having platy clay minerals and having clay fraction exceeding about 25%.

The residual strength of the nonclay minerals is not much different than peak strength, and quartz, feldspar, and calcite all have the same value of $\phi'_r = 35°$ (Mitchell, 1992). Slip at contacting asperities is the dominant deformation mechanism for these nonclay minerals.

Basal plane slip is the dominant deformation mechanism at large strain in the clay minerals and other layer silicates. Compression textures with basal planes approximately perpendicular to the normal load are formed in the shear zone. Most of the deformation takes place in this zone, as well as in the zones of highly preferred particle orientation that enclose it. The behavior of layer silicates and solid lubricants, such as graphite and molybdenum disulphide (MoS_2), is similar (Mitchell, 1992).

Among the clay minerals, attapulgite shows a relatively high residual strength. This is because the lathlike particles occur as intermeshed aggregates, and the crystal structure gives a stair-step mode of cleavage. As a result, in shear, attapulgite behaves more like a massive mineral than a platy mineral (Chattopadhyay, 1972).

Various attempts have been made in the past to correlate residual strength with index properties. Lupini et al. (1981) reviewed some of the work. Residual strength is found to depend upon clay fraction, type of clay mineral, Plasticity Index, Liquid Limit, effective stress level and rate of shear.

In a preceding paragraph the similarity, in shear, between clay minerals and solid lubricants such as graphite has been mentioned. Graphite's lubricity is due to its lamellar type of crystal structure, which allows the planes of carbon atoms to slide easily over one another without disintegration. This behavior is ascribed to the strong bonding forces between the individual carbon atoms laying in the planes and to relatively weak van der Waal forces between planes. The frictional coefficient of graphite depends on the presence of condensable vapors such as water and oxygen. Only a very small amount of condensable vapor is necessary to decrease graphite's coefficient of friction. The role of condensable vapors has been explained as saturating the surfaces on graphite crystallites, especially the edge forces, thereby reducing the friction (Savage and Schaefer, 1956). The frictional coefficient of graphite increases with sliding velocity, which is due to the viscous effects of the saturating vapor (Clauss, 1972).

A similar behavior can be expected in clays due to the viscous flow of water and the adsorbed film. In addition to the viscous effects, at higher rates the increased area of real contact between sliding surfaces, within a particular time interval, and the generation of suction in the pore fluid can cause higher resistance to shear. It can be assumed that these three effects influence the rate effects on residual strength, although the actual contribution from each is not known. Nonetheless, it is widely accepted that the residual frictional coefficient, ratio of tangential to normal stress, along a shear zone in clay, increases with shear strain rate.

Examples of movements in old landslides exhibit different types of behavior over long periods of time. For example, there may be periods in which the landslide is completely stationary, or stable creep may exist with constant velocity, and still other periods in which episodes of accelerating and decelerating motions occur. When undertaking construction on moving ground, particularly when movements are themselves induced by construction operations, a criterion of allowable velocity is useful (List, 1992). However, such criteria are entirely based on experience and have no theoretical background. Conventional approaches in analyzing stability problems or landslides consider only limiting stability conditions and no account is taken of the actual motions of the soil. Therefore, in an attempt to analyze such cases where movement is involved, an understanding of rate effects (velocity) on residual strength is important. This chapter presents a summary of previous studies on rate effects and new results from a series of laboratory experiments conducted on a sheared clay shale (kca unit as denoted by the Syncrude Ltd.) from the Syncrude Tailings Dyke site, Fort McMurray. The geology of this site is discussed in section 2.3.2.

2.2 Previous research work

2.2.1 Laboratory studies

Petley (1966), in performing shear box tests on samples of London Clay and Edale Shale at shearing rates varying between 0.05 and 140 mm/day, showed that the residual strength of these materials increased by up to 1% to 2% per logarithm increase in rate of shearing (Figure 2.2).

In a series of tests on soils containing various sorts of discontinuities, Skempton & Petley (1967) showed that the strength along joints which do not show evidence of previous shear deformation closely approximated the shear strength of normally consolidated specimens of the same soil. In effect, the formation of the discontinuity had removed the cohesive element of its shear strength, the angle of shear resistance being relatively unaltered by either the overconsolidation or the formation of the discontinuity. Tests on sheared discontinuities, Skempton & Petley (1967) showed that these tend toward residual strength. Experiments by them on London Clay showed that the residual strength decreases very slightly with decreasing rates of shear; but for most practical purposes the effect can be neglected, even if the rate is reduced by two orders of magnitude. This result has been confirmed by Kenney (1967) for a wide range of clays. The above mentioned observations on low to medium plastic clays are somewhat contradictory of the test results discussed in the next paragraphs.

Bucher (1975), as reported by Lupini et al. (1981), used two strain-controlled ring shear devices of different design and reversal shear box tests to study the influence of stress history, stress level, shear rate and temperature on residual friction angle. He found that changing the shear displacement rate from $1.5*10^{-2}$ mm/min. to 15 mm/min. increased the residual strength of a clay with Plasticity Index of 27% by 24%.

La Gatta (1970) used a strain-controlled rotary shear apparatus testing either a disc or an annular specimen of varied height. He found that specimen preparation and stress history did not influence the residual strength. He also found that increasing shear displacement rate from $0.6*10^{-2}$ mm/min. to $60*10^{-2}$ mm/min., increased the residual strength of Cucaracha Shale (Liquid Limit of 63%, Plasticity Index of 20% and clay fraction of 48%) by 3.5%.

Lupini et al. (1981) tested a large number of natural soils in the ring shear apparatus. Their results showed that the residual shear behavior changes as the clay content of the cohesive soil increases. With some soils, the residual strength can be sensitive to the rate at which the soil is sheared. This effect has been explored by Lupini et al. (1981), who showed that increases in strain rate can cause increases in strength in the soil, with some brittleness becoming apparent when the strain rates are subsequently reduced. It would seem that the viscous drag forces on the particles as they are sheared tend to prevent their complete alignment. Lupini et al. (1981) termed this turbulent shear to distinguish it from the sliding shear at low strain rates. For the strain rate there is a threshold below which the effect is negligible.

Tests on clays over a range of speeds from about 100 times slower to 100 times faster than usual laboratory test rates (slow : 0.002 mm/min. - 0.01 m/min.) show that on average, the change in strength is less than 2.5% per log cycle (Figure 2.3) (Skempton, 1985).

For clays, the increase in strength is accentuated at rates exceeding 100 mm/min. when some qualitative change in behavior occurs (Figure 2.4). This is probably associated with a disturbance of the originally ordered structure producing what may be termed 'turbulent shear', in contrast with sliding shear, where particles are oriented parallel to the plane of displacement. It is also possible that pore pressures are generated and, as displacement continues, they dissipate, leading to an increase in strength. That some structural change has taken place in clays at rates of 400 mm/min. or more seems apparent from the fact that, on reimposing the slow rates, a peak is observed, the strength falling to residual only after considerable further displacement (Figure 2.5).

On the other hand, in a low clay fraction siltstone there is no qualitative change at rates even as high as 800 mm/min.; the strength only rises to a maximum and then falls directly towards the residual, and on restoring the slow rates the residual is almost immediately regained (Skempton, 1985). This effect points to pore pressure changes only.

Salt (1988) reported on extensive ring shear tests on clayey sandy silts from New-Zealand with Liquid Limit of 39% and Plasticity Index of 19%. He found a 2.2 to 3.6% shear strength increase for a tenfold increase in displacement rate. Van Genuchten (1989) tested a varved clay from the La Mure area in the French Alps and found a minimum increase of 5.75% ($\frac{T_1}{T_0}=1.0575$) for a jump of 25 in the velocities in direct shear tests whereas for the same clay, the ring shear tests of Nieuwenhuis (1991) showed an average increase of 4.0% ($\frac{T_1}{T_0}=1.04$) for a jump of 10 in the velocities.

Nieuwenhuis (1991) studied rate effects in the ring shear apparatus with speeds from 0.2 to 3.0 mm/hr. He ascribed the rate effects to both the development of negative excess pore pressure in the overconsolidated varved clays and to truly viscous behavior.

2.2.2 Constitutive models

Davis et al. (1993) studied a strength velocity relationship exhibiting both velocity weakening and velocity strengthening for different ranges of slip velocity. They discussed the effects of non-rigid motions of the sliding mass and results suggest overall stability will be unchanged from the simpler single rigid-block analysis commonly used.

They assumed the frictional strength of the sliding mass has some generalized velocity dependence and shear strength τ is given by

$$\tau = c' + \sigma' [\tan\phi + f(\upsilon)] \tag{2.1}$$

where f is some function of relative velocity. They used the following form of the function $f(\upsilon)$:

$$f(\upsilon) = -\mu(\frac{\upsilon}{\upsilon_R})\exp(-\frac{\upsilon}{\upsilon_R}) \tag{2.2}$$

where μ is a material constant and υ_R is a reference velocity. The negative sign on the right hand side of this equation results in velocity weakening for values υ smaller than υ_R and velocity strengthening for υ greater than υ_R. The function $f(\upsilon)$ has a minimum value when $\upsilon = \upsilon_R$.

This general weakening-strengthening behavior exhibited by equation 2.2 is typical for certain soils and rocks. (Davis et al. 1993). The minimum strength occurs when $\upsilon = \upsilon_R$. Similar weakening-strengthening behavior was suggested by Hvorslev (1960) with regard to clay, and has been observed by Lemos (1986), and Smith (1991).

Davis et al. (1990) used a non-linear model to fit experimental results. They assumed there exists a threshold relative velocity υ_R below which stable creep cannot occur. This relative velocity is the smallest non-zero creep velocity possible. They also assumed the Mohr -Coulomb strength criterion to be applicable (Figure 2.6).

For the static state,

$$\upsilon = 0 \text{ and } \frac{\tau}{\sigma'} < \tan\phi_r \tag{2.3}$$

On the other hand, if $\frac{\tau}{\sigma'}$ exceeds the static strength , $\tan\phi_r$, then creep will occur and the creep velocity must exceed the threshold value.

Then,

$$\upsilon \geq 0 \text{ and } \frac{\tau}{\sigma'} = \tan\phi_r + \beta\log\frac{v}{v_R} \tag{2.4}$$

here β plays the role of dimensionless viscosity.

The following relationships between ϕ'_{mob} (shear strength) and $\mathring{\delta}$ (rate of shearing) were obtained by Bracegirdle et al., (1990) using their results and the observations of Lupini (1980) and Lemos (1986) when performing tests on Kaolin in the ring shear apparatus.

$$\mathring{\delta} = \mathring{\delta}_o.\exp(c\Delta^R) \tag{2.5}$$

c and R are constants. $\mathring{\delta}_o$ is a low rate of shearing effectively corresponding to the static condition. (Bracegirdle et al, (1990) used $\mathring{\delta}_o = 0.01$ mm/day)

$$\Delta = \frac{\tan\phi'_{mob} - \tan\phi'_{rs}}{\tan\phi'_{rs}} \tag{2.6}$$

ϕ'_{rs} is the residual shear strength at the effective onset of movement. They compared their results with previous laboratory data (Figure 2.7).

The observations of Van Genuchten (1989) suggested a logarithmic relation between $\frac{\tau_1}{\tau_0}$ and $\frac{v_1}{v_0}$ instead of the linear Newtonian relation used earlier. Nieuwenhuis (1991) proposed the following relation combining his observations and Van Genuchten's observations.

$$\ln\frac{v_1}{v_0} = 57.575\ln\frac{\tau_1}{\tau_0} \tag{2.7}$$

This equation includes the contribution of all rate effects, negative excess pore pressures and true viscosity. v is the deformation rate in mm/hr.

Equation (2.2), proposed by Davis et al. (1993), considers both velocity weakening and strengthening behavior. When the velocity is v_R, $\tan\phi_r'$ will have a minimum value of $W_b \cos\beta\mu e^{-1}$, in which W_b is the effective weight of failure mass and β is the slope angle. The parameters in this equations are obtainable from ring shear tests. The strength velocity relationships presented by Davis et al. (1990), Bracegirdle (1992) and Nieuwenhuis (1991) consider v.....ity strengthening effects only, which is common for most clays. The relationship proposed by Bracegirdle (1992) is nonlinear in $\tan\phi_r'$ versus logarithmic displacement rate plot. The gradient almost reaches 90° when the rate is about 10 mm/day, which implies a 12% increase of strength over the strength at 0.1 mm/day . However, their equation gives a close approximation to the laboratory data when the velocity is less than 1 mm/day (Figure 2.7). The equations by Davis et al.(1990) and Nieuwenhuis (1991) are linear in a $\tan\phi_r'$ versus logarithmic displacement rate plot.

2.3 Laboratory testing program of residual strength

2.3.1 Introduction

The most commonly used apparatus to measure the drained residual strength of clays and clay shales is the direct shear box. The primary limitation of using direct shear is that the soil is sheared forward and then backward until a minimum shear resistance is measured. Each reversal of shear box results in a horizontal displacement that is usually about 5 mm. As a result, the specimen is not subjected to continuous shear deformation in one direction and therefore a full orientation of clay particles may not be obtained.

The main advantage of the ring shear apparatus is that it shears the specimen continuously in one direction for any magnitude of displacement. This allows clay particles to be oriented parallel to the direction of shear and the residual condition to be developed. The other advantages of the ring shear apparatus are the constant cross-sectional area during shear and minimal laboratory supervision during shear.

Two main factors make the ring shear apparatus appropriate for this study: its relative simplicity; and the fact that it tests a thin annular specimen of undisturbed clay with a short drainage path length, so that even at relatively fast rates the pore pressure may be dissipated. However, in this study of the Clearwater clay-shale (kca) at the Syncrude tailings dyke site, both the direct shear box and the ring shear apparatus were used to gain an understanding of the dependence of drained residual strength on the deformation rate. The deformation rates applied in these tests are of the same order as those observed in the field.

2.3.2 Review of geology of kca unit

The main objective of this laboratory testing program is to develop a relationship that describes the rate-dependence of residual strength of the kca unit at the Syncrude site, Fort McMurray.

Syncrude Canada Ltd. operates an oil sand mine about 40 km north of Fort McMurray in northern Alberta. Approximately 475 million cubic meters of sand, 400 million cubic meters of thick sludge and 50 million cubic meters of freewater require permanent storage within the Syncrude Tailings Pond. The downstream slope angles of the perimeter dyke are largely governed by the underlying geology and associated shearing resistance, as controlled by both strength parameters and pore pressure response.

In general, the foundation soils underlying the tailings disposal area consist of Pleistocene and Cretaceous units which overlie the McMurray Formation (km). The former Beaver Creek channel defines an approximate boundary between two distinct foundation geology conditions as illustrated in Figure 2.8. The portion of the dyke to the west of the creek is underlain by glacial till and Clearwater Formation (kc). The area to the east of the former creek channel is primarily underlain by Pleistocene fluvial sand and gravel (Pf) as well as glacial till (Pg). The Clearwater Formation has been eroded in the eastern area with the exception of localized remnants of its basal units (kca and kcw).

Figure 2.9 shows a borehole log at 15 m from the sampling location which is situated in Cell 18 of the Syncrude Tailings Dyke. A shear zone is found at a depth of about 3 m to 4 m. The clay samples were obtained in the form of blocks from the shear zone approximately about 3 m below ground surface. Preliminary classification tests had been performed on this clay and the results are summarized in Tables A2-1 & A2-2 . The soil can be classified as high plasticity, CH, according to the Unified Soil Classification system. The Liquid Limit, Plasticity Index and clay size fraction of the clay are 135, 107 and 49% respectively. The natural moisture content of the clay is 23%.

2.3.3 Testing procedure

To obtain a reliable relationship between deformation rate and residual strength it is necessary to perform a series of laboratory tests at various deformation rates. The minimum test rate should represent the field minimum rate and the maximum test rate should represent the field maximum rate. This implies a range of displacement rates from 0.027 mm/day (1 cm/year) to 1000 mm/day (100 cm/day) based on available literature. However, previous studies (Skempton, 1985) show that the variation of residual shear resistance when the displacement rate is less than about 0.1 mm/day is such that the rate effects can be neglected. Considering this factor, as well as the availability of laboratory equipment and the time consumption for very slow rates, in this study the minimum rate of deformation is chosen as 0.2 mm/day.

Six series of tests were carried out in a set of direct shear boxes with specimens 6.05 cm square in plan and 2.525 cm thick. Three of them were conducted with an effective normal stress of 100 kPa and the rest were loaded to 500 kPa. Consolidation stresses of 500 and 100 kPa were chosen to represent the average effective stress and minimum effective stress that could be encountered in the Syncrude Tailings Dyke field case. Under each normal stress, one intact specimen was tested and two specimens with shear surfaces were tested. Each specimen was subjected to three different deformation rates 0.7, 1.0 and 7.0 mm/day. Each specimen was first tested with 7.0 mm/day until the residual strength was reached. To minimize the disturbances due to reversal of shear direction after completing forward traverse, with a displacement of about 8 mm, the box was pushed back tc its original position while having the normal stress released, and then sheared again. The process was repeated until the strength of the clay had dropped to a steady residual value. Then single travels were performed at other rates. This technique is admittedly not perfect. After each reversal a small peak is often observed as shown in Figures A2-1 to A2-6 , and there is some danger of slurrying the clay on the slip surface. Ideally the displacements should be applied continuously in one direction.

A Bromhead ring shear apparatus was used for testing undisturbed clay specimens. The annular soil specimen (5 mm thick with inner and outer diameters of 70 mm and 100 mm respectively) is confined radially between concentric rings. It is compressed vertically between porous bronze loading platens by means of a lever loading system and dead weights. The details of the apparatus are reported in Bromhead (1979). Figure 2.10 shows the plan view and a side view of the ring shear apparatus.

The steps in preparing an undisturbed ring shear specimen are shown in Figure 2.11. Considerable difficulties in obtaining undisturbed ring shear specimens were experienced because of the high stiffness of the clay. The core-cutter method of preparation, which is found to be satisfactory for stiff fissured clays, was used. The following is a list of the steps taken in the core-cutter method of preparation.

A thin walled core cutter is pushed into a block of sample (Figure 2.11, stage (a)) and separated from it with a sharp edged blade (b). The stiffening ring is removed and the upper clay surface is planed with a straight-edge (c). The sample is inverted and located on the assembled molding rings (d). The sample assembly is aligned and a thin-walled inner core cutter is pushed firmly into the sample (e, f). The inner portion of the sample is removed (g). The annular sample together with the molding rings and the inner core cutter is placed on the confining ring (h, i). An annular spacer is placed on the sample and the sample is carefully pushed into the confining ring by hand (j). The top surface of the clay is planed with a straight-edge. The assembly containing the undisturbed specimen is screwed to the rotating table and the water bath is fitted. The upper loading platen is aligned and gently placed in position on the sample (k).

Two series of tests were carried out for intact clay samples under normal stresses 100 kPa and 500 kPa. A third series was carried out at 500 kPa on a shear surface, which is created by slowly rotating the top platen in the direction of shear. In each series, three deformation rates were applied: 7.0, 1.0 and 0.185 mm/day. Tests were continued until a stationary value of shear stress was reached. Figure 2.12 is a schematic presentation of each type of test.

From the initial rate of consolidation of the sample, a drained rate of shear was calculated for each test (direct shear test and ring shear test) to give at least 98% consolidation after 1 mm displacement. All samples were sheared at rates well below the computed drained displacement rate of 80 mm/day for the ring shear test and 8 mm/day for the direct shear test. The procedure described by Gibson & Henkel (1954) was used to calculate the drained displacement rate.

2.3.4 Laboratory versus field behavior

The relative thickness of active shear bands forming failure surfaces may cause differences between laboratory and field behavior. The 5 mm thick sample in the ring shear test (12.5 mm in direct shear) is constrained by the apparatus to fail along as thin a band as possible. Visual observations of sheared samples suggest that the active shear band developed during ring shear is found at the top of the sample. A significant difference between the field and laboratory samples is that in the field, multiple shear surfaces and/or thick shear bands may develop.

When presenting the laboratory results one should produce a characteristic curve for soil. However, assuming that the displacement rate across an active shear band is a direct function of shear strain rate and active shear band thickness, the displacement rate in the field will exceed that obtained in the ring shear apparatus by the ratio of the shear band thickness (field to laboratory). That is, if failure does occur in a shear band rather than along a failure surface, then it is strain rate rather than displacement that is fundamentally related to shear stress. For example, if under a given shear stress the active shear band could be increased ten times in thickness, the displacement rate would also increase tenfold. Therefore, in this study, the test results are presented in terms of shear strain rate rather than displacement rate.

2.3.5 Discussion of Results

Figures A2-1 to A2-9 present shear stress-horizontal displacement relationships from multiple rate direct shear and ring shear tests on the stiff clay samples obtained from the Syncrude tailings dike site.

In order to incorporate the resulting relationship between rate of shear and residual friction angle into finite element analysis and to present the results in dimensionless form, rate of deformation as observed from the tests has to be transferred to rate of shear strain. To convert the rate of deformation to the rate of shear strain ($\overset{\circ}{u}_x \Rightarrow \overset{\circ}{\varepsilon}_{xy}$) a uniform strain condition throughout the sample is assumed (Figure 2.13). However, this assumption could lead to an overestimation of strain rate, since the majority of shear occurs close to the top surface of the ring shear sample or at the middle in the direct shear test sample.

Table A2-3 summarizes the residual shear strength values and residual friction angles obtained from each test. Summarized results of the coefficient of friction vs. shear strain rate ($\overset{\circ}{\varepsilon}_{xy}$) are plotted in Figure 2.14. It can be seen from the Figure 2.14 that there is a scatter among the direct shear test data, whereas the ring shear test data fit to a smooth curve. A best fit curve is plotted for the direct shear test data considering the rate effects shown in the ring shear test results too. The coefficient of friction versus logarithm (base 10) of shear strain rate plot (Figure 2.15) shows linear approximations for the range of strain rates considered.

In general, results from the ring shear test give a lower bound to the friction angle under each normal stress value. Similar observations have been reported by Bishop et al. (1971), Bromhead (1979) and Stark et al. (1994). Higher values of residual friction angle measured from the direct shear box may be due to relatively short travel length in one direction without interruption and due to disturbance as a result of reversal. Non-linearity of the residual strength envelope is observed here, based on the differences in friction angle under each normal stress.

The interesting point to be made from the result is that a slope of approximately 0.0021 is observed from all the data of $\tan\phi$ vs. $\ln_e \overset{\circ}{\varepsilon}_{xy}$. This means when the shear strain rate is increased by 10 times, there is an increase of 3.4-3.5% in the residual strength for the range of strain rates from 0.02 /day to 0.7 /day. For the condition of pure shear as occurred in these tests the strain rate invariant ($\overset{\circ}{\varepsilon}^{p}$) can be expressed in terms of the shear strain rate ($\overset{\circ}{\varepsilon}_{xy}$) alone. If $\overset{\circ}{\varepsilon}^{p} = \sqrt{\frac{1}{2}\overset{\circ}{\varepsilon}{}^{p}_{ij}\overset{\circ}{\varepsilon}{}^{p}_{ij}}$ then, $\overset{\circ}{\varepsilon}^{p} = \overset{\circ}{\varepsilon}_{xy}$.

Thus, for the ring shear test

$$\tan\phi = 0.13 + 0.002145 \ln \overset{\circ}{\varepsilon}{}^{p} \tag{2.8}$$

where $0.02\ /\text{day} < \overset{\circ}{\varepsilon}{}^{p} < 0.7\ /\text{day}$

for the direct shear test,

$$\tan\phi = 0.147 + 0.002145 \ln \overset{\circ}{\varepsilon}{}^{p} \tag{2.9}$$

where $0.03\ /\text{day} < \overset{\circ}{\varepsilon}{}^{p} < 0.7\ /\text{day}$

Considering the static friction angle as ϕ_o and corresponding minimum rate as $\overset{\circ}{\varepsilon}{}^{p}_{o}$

Then,

$$\tan\phi - \tan\phi_o = 0.002145 \ln \frac{\overset{\circ}{\varepsilon}{}^{p}}{\overset{\circ}{\varepsilon}{}^{p}_{o}} \tag{2.10}$$

or,

$$\tan\phi = \tan\phi_o + 0.002145 \ln \frac{\overset{\circ}{\varepsilon}{}^{p}}{\overset{\circ}{\varepsilon}{}^{p}_{o}} \tag{2.11}$$

(i) If $\overset{\circ}{\varepsilon}{}^{p}_{o}$ is taken as 0.001/day, for ring shear test

$\tan\phi_o = 0.1152$ and $\phi_o = 6.6°$

which results in,

$$\tan\phi = \tan 6.6° \left(1 + 0.0186 \ln \frac{\overset{\circ}{\varepsilon}{}^{p}}{\overset{\circ}{\varepsilon}{}^{p}_{o}} \right) \tag{2.12}$$

(ii) If $\overset{\circ}{\varepsilon}{}^{p}_{o}$ is taken as 0.001/day, for direct shear test

$\tan\phi_o = 0.1322$ and $\phi_o = 7.5°$

which results in,

$$\tan\phi = \tan 7.5^\circ\left(1 + 0.0162\ln\frac{\dot{\varepsilon}^p}{\dot{\varepsilon}^p_o}\right) \tag{2.13}$$

There appears to be a rough correlation between the Liquid Limit and rate effects as well as between the Plasticity Index and rate effects (Figures 2.16 and 2.17). The test rates available for Cucaracha shale and silts of New Zealand are somewhat higher than those available for London Clay, Edale Shale and Clearwater Formation. These correlation are tentative and enough data points are not available to reach a final conclusion. Edale shale has the lowest LL and I_p shows a minimum percentage increase in strength per logarithmic increase in shear displacement rate. The Clearwater Formation shows higher rate effects which is in accordance with its higher LL and I_p. Salt's figures for the clayey sandy silts and La Gatta's figures for Cucaracha Shale show higher rate effects, which represent higher test rates than the slow tests discussed in this study. Plasticity data for the varved clay tested by Niewenhuis are not available; this limits the comparison with other clays. Nevertheless, rate effects show a nearly linear increase with the plasticity of the clay.

2.4 Conclusions

Figure 2.18 compares the strength ratio versus displacement rate as observed from the tests discussed in the previous section with those of other materials. The rate effects observed by Niewenhuis (1991) and Salt (1988) show similar trends as those for the tested Clearwater Formation. Previous tests performed by Petley (1966) indicate lower rate effects for London Clay and Edale Shale compared to the present tests on Clearwater Formation. The results of Kaolin as tested by Lupini (1980) and

Lemos (1986) indicate medium effects. A broad correlation is observed between plasticity and rate effects for the clays.

Table 2.1 Variation in residual strength of clays at slow rates of displacement (after Skempton, 1985)

Rate of displacement (mm/min.)		Strength ratio
field lowest	0.0001= 5 cm/year	0.97
lab	0.005 = 7 mm/day	1
field highest	0.35 = 50 cm/day	1.05

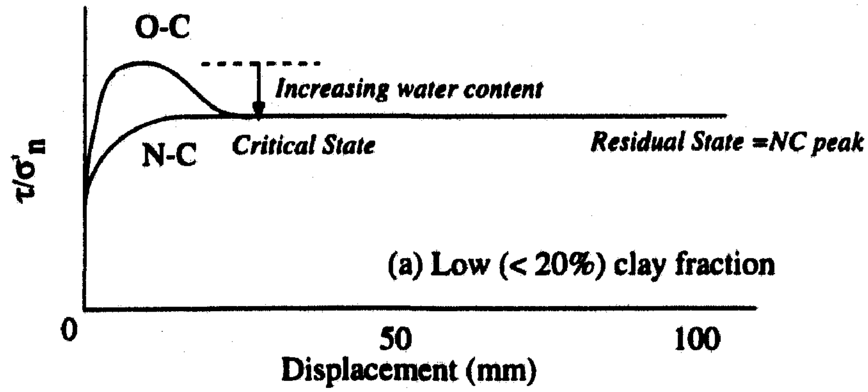

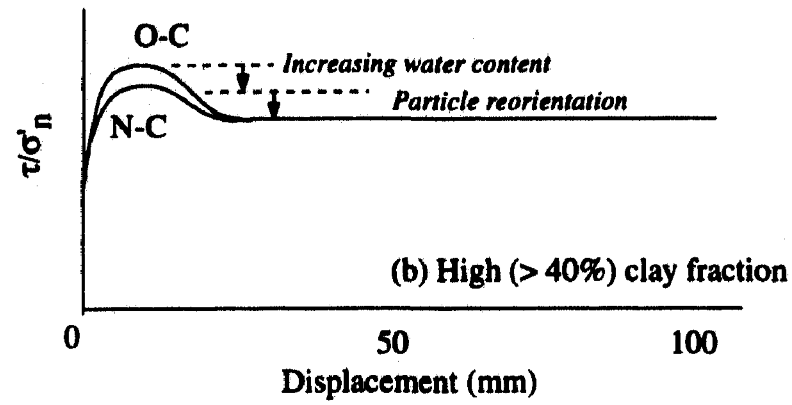

Figure 2.1 Stress-displacement curve at constant σ'_n

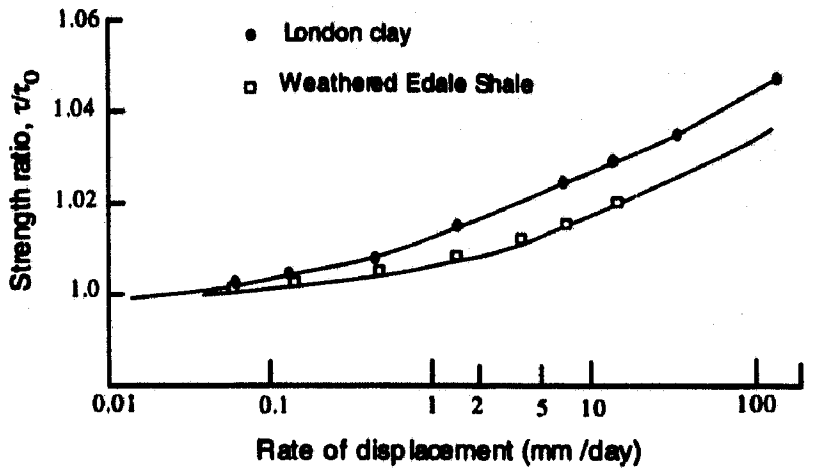

Figure 2.2 Relation between residual strength and of displacement (after Skempton et al., 1989)

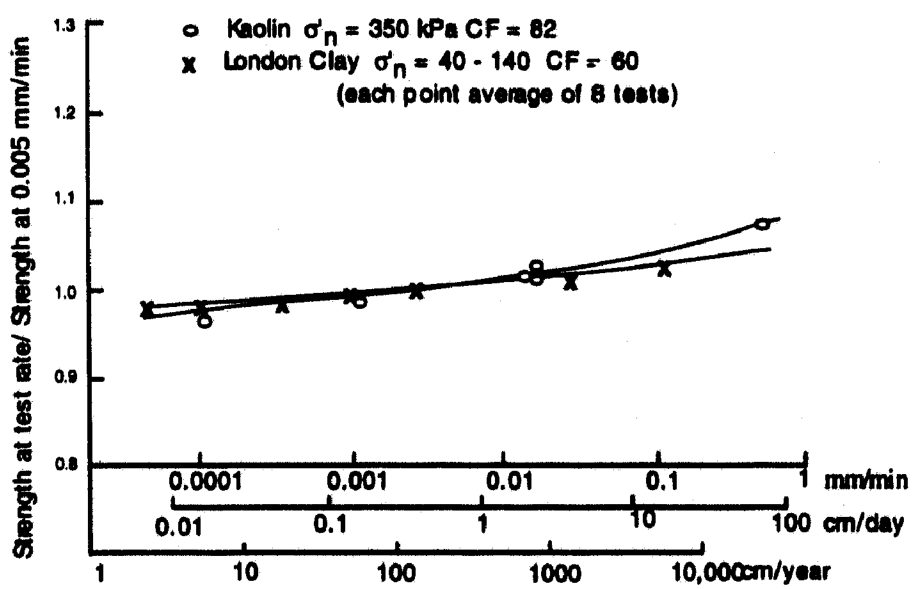

Figure 2.3 Variation in residual strength of clays at low rates of displacement (after Skempton and Petley, 1967)

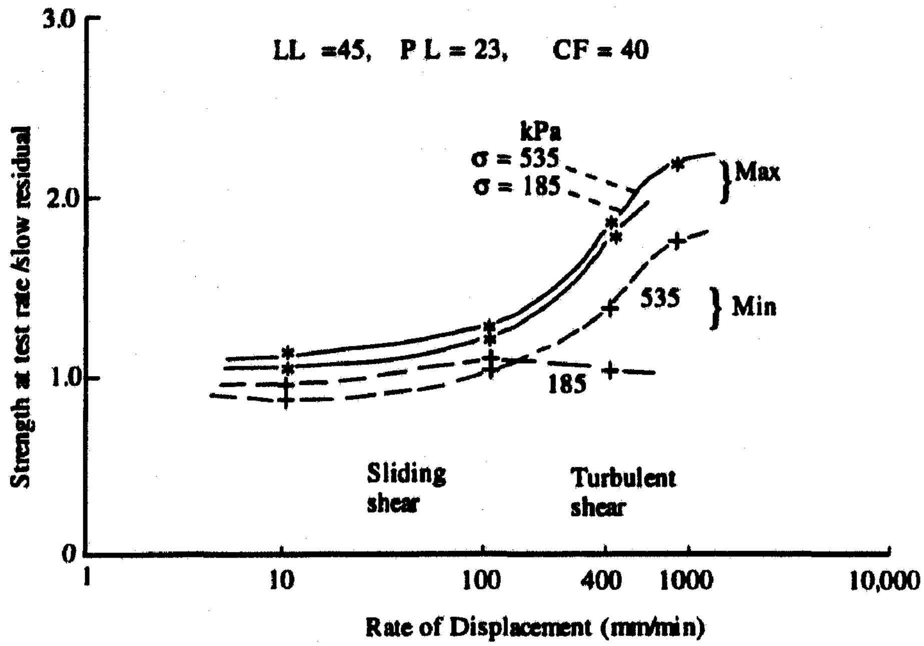

Figure 2.4 Kalabagh Dam ring shear tests, February 1984 (after Skempton,1985)

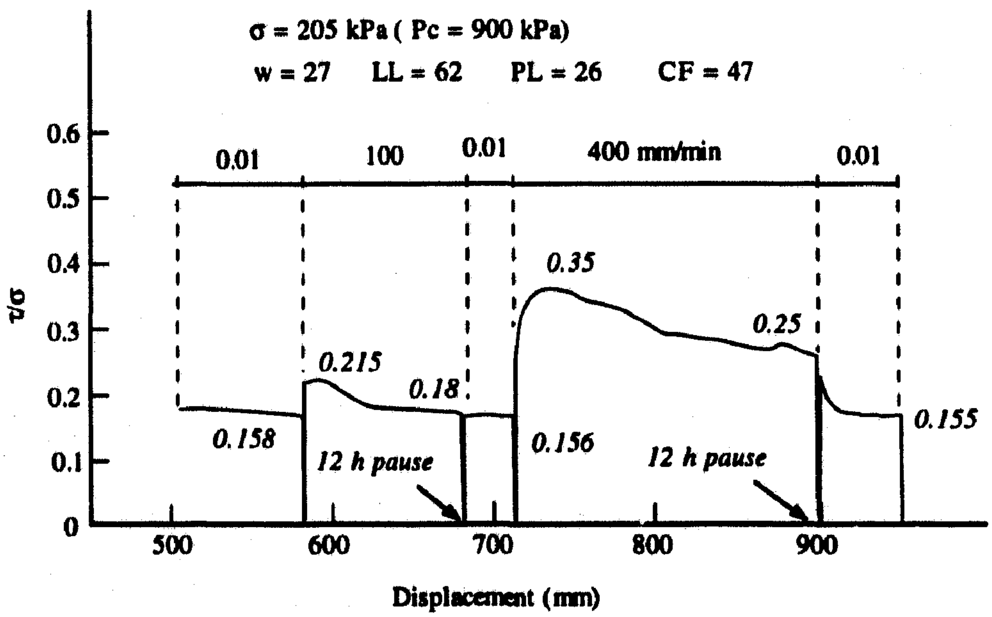

Figure 2.5 Kalabagh Dam ring shear test, August 1983 (after Skempton, 1985)

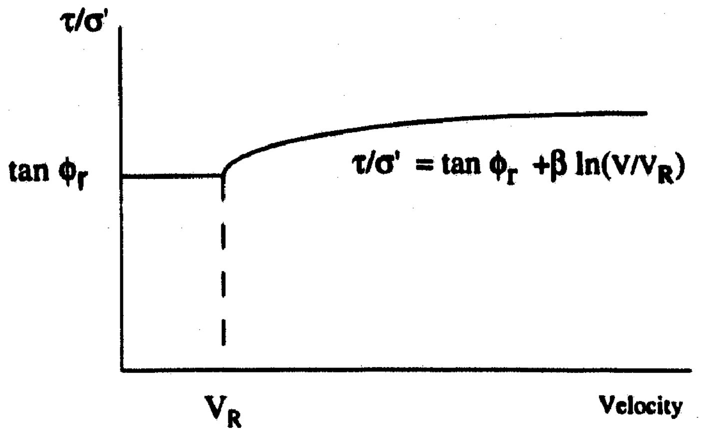

Figure 2.6 Residual strength vs. velocity (after Davis et al. (1990)

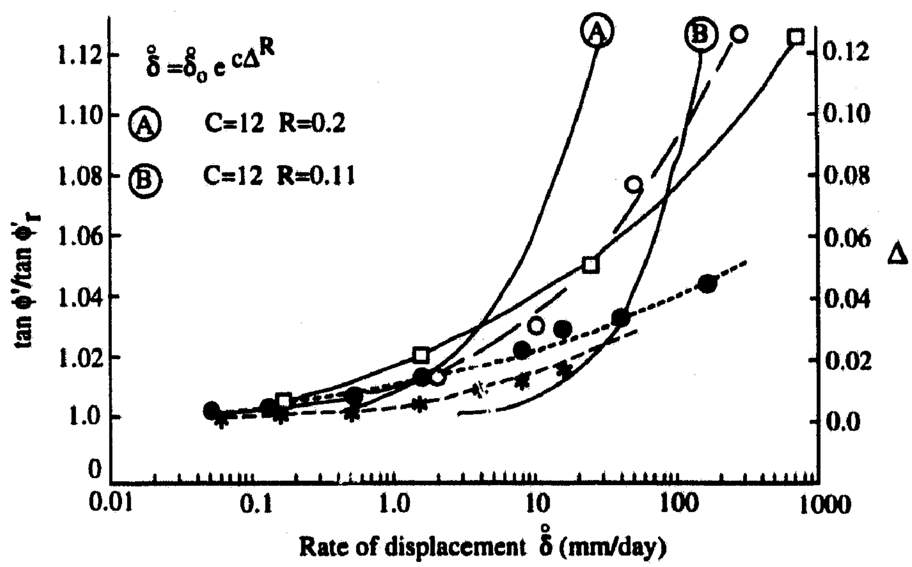

○ Kaolin, ring shear σ_n' =200 kN/m^2, Lemos (1986)
□ Kaolin, ring shear σ_n' =518 kN/m^2, Lupini (1980)
● London Clay, shear box } Petley (1966)
* Edale shale, shear box

Figure 2.7 Strength ratio vs. rate of displacement (after Bracegirdle et al. ,1990)

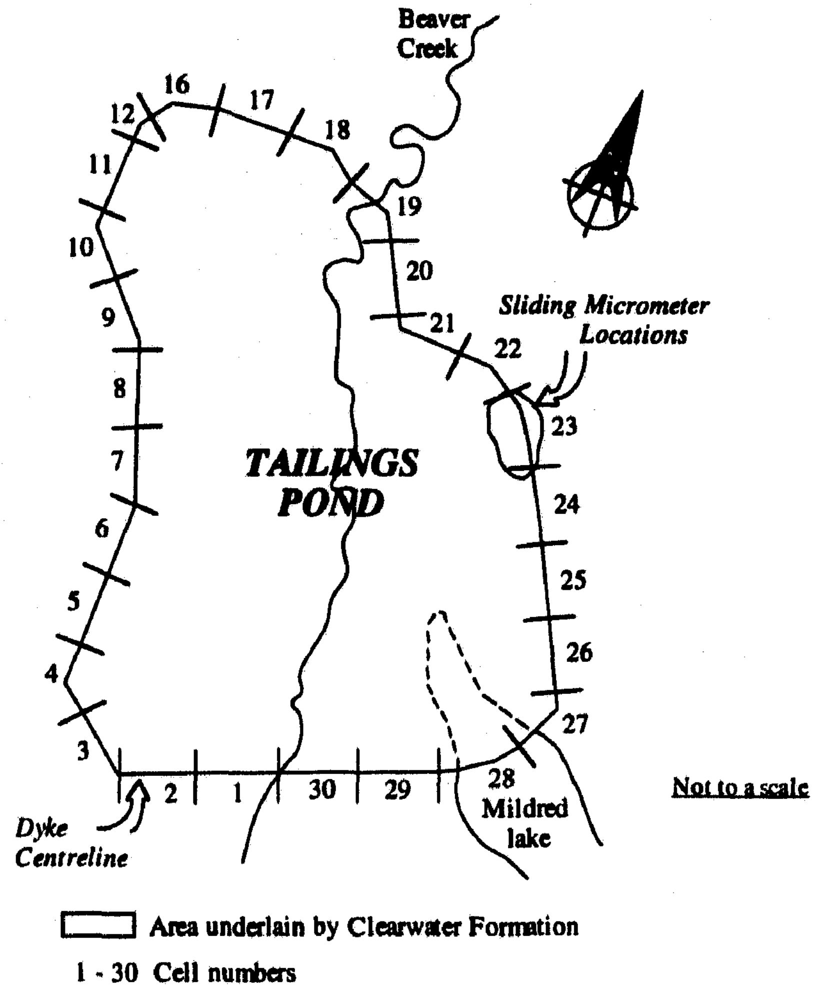

Figure 2.8 Layout of Syncrude Canada Ltd. Tailings Disposal Area

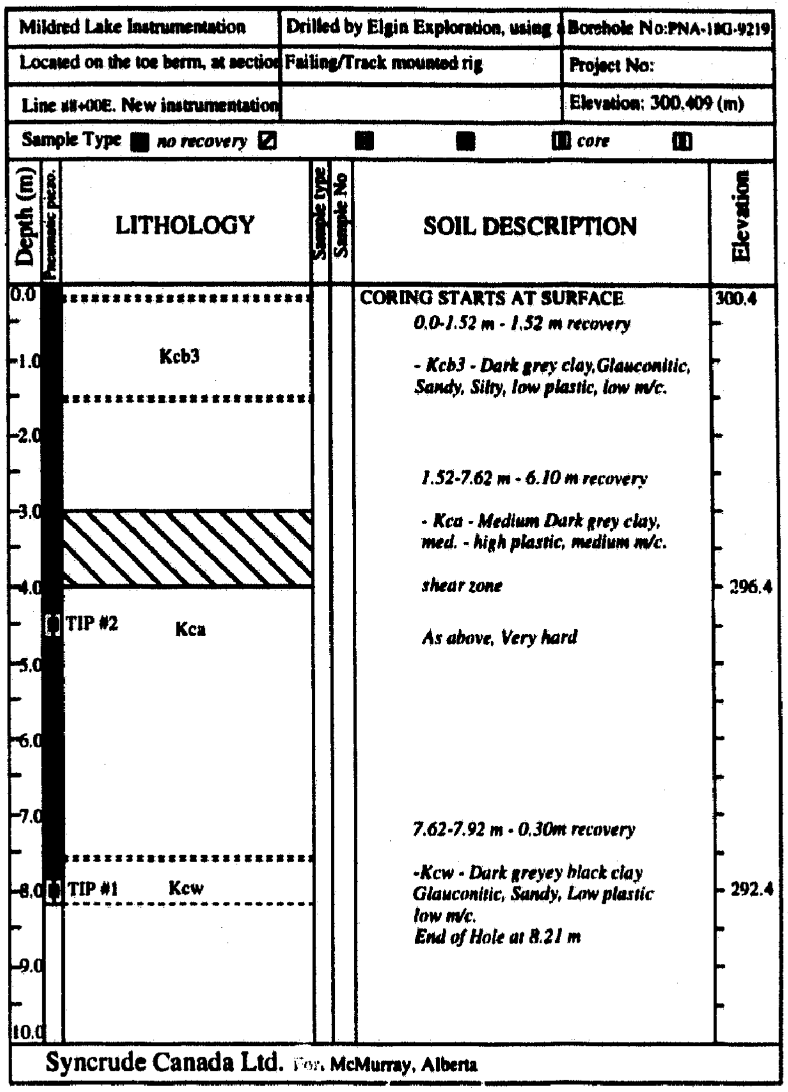

Figure 2.9 Borehole log at sampling location

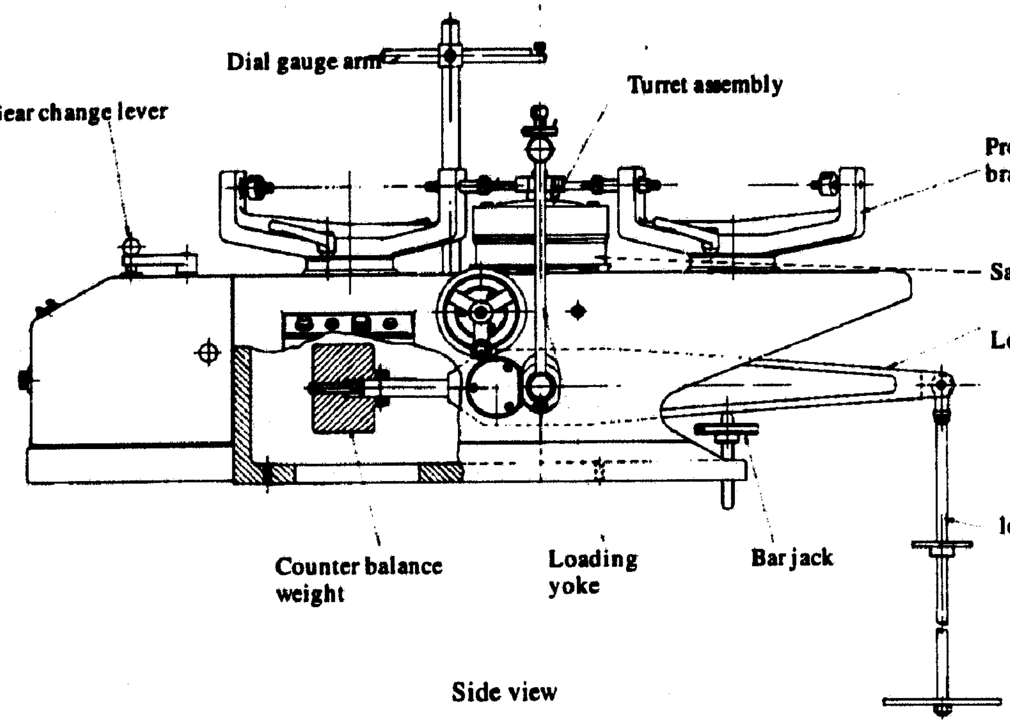

Side view

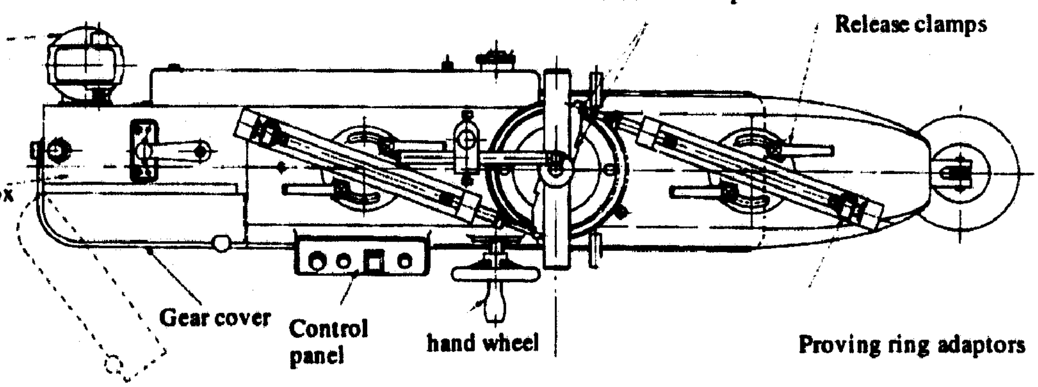

Plan

Figure 2.10 Ring shear aparatus setup (after Bromhead (1979)

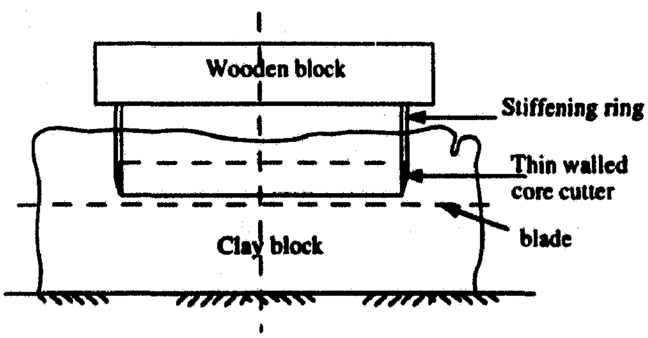

(a) Stiffened core cutter pushed into clay block sample
(b) Slice through block with blade

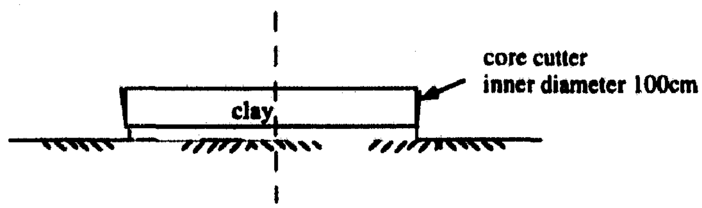

(c) Trim off upper surface of clay until flush with core cutter

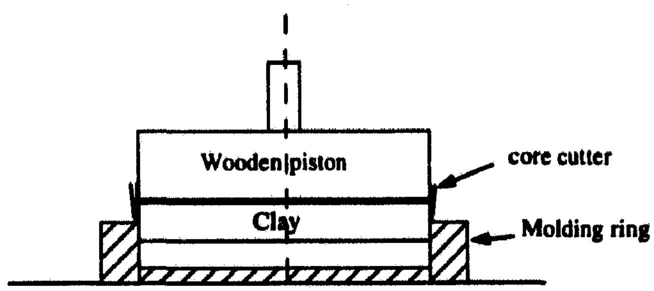

(d) Assemble core cutter on molding ring assembly
(e) Push clay into rings to rest against spacer
(f) Remove the core cutter

Figure 2.11 Preparation of ring shear sample (Contd. next page)

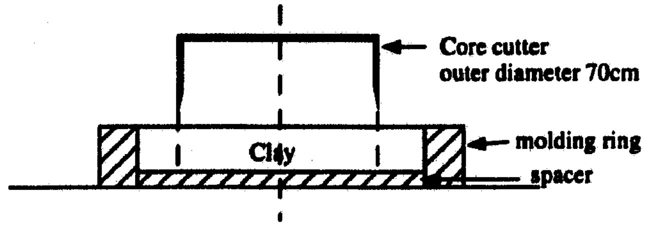

(g) Remove inner core with cutter

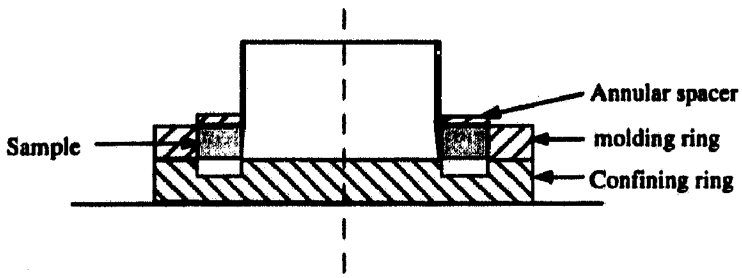

(h) Place outer confining ring on baseplate
(i) Place sample together with molding ring and core cutter on the confining ring
(j) Push the sample into the ring by gently pressing the spacer by hand

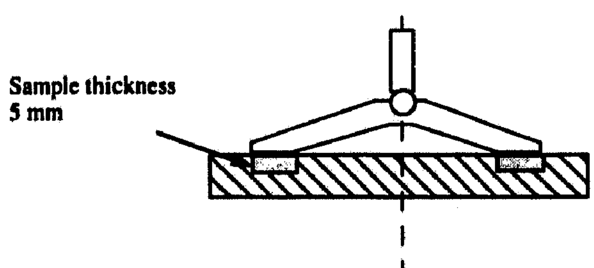

(k) Trim off the surface of sample
(l) Place and align the loading platen on the sample

Figure 2.11 (Contd.) Preparation of ring shear sample

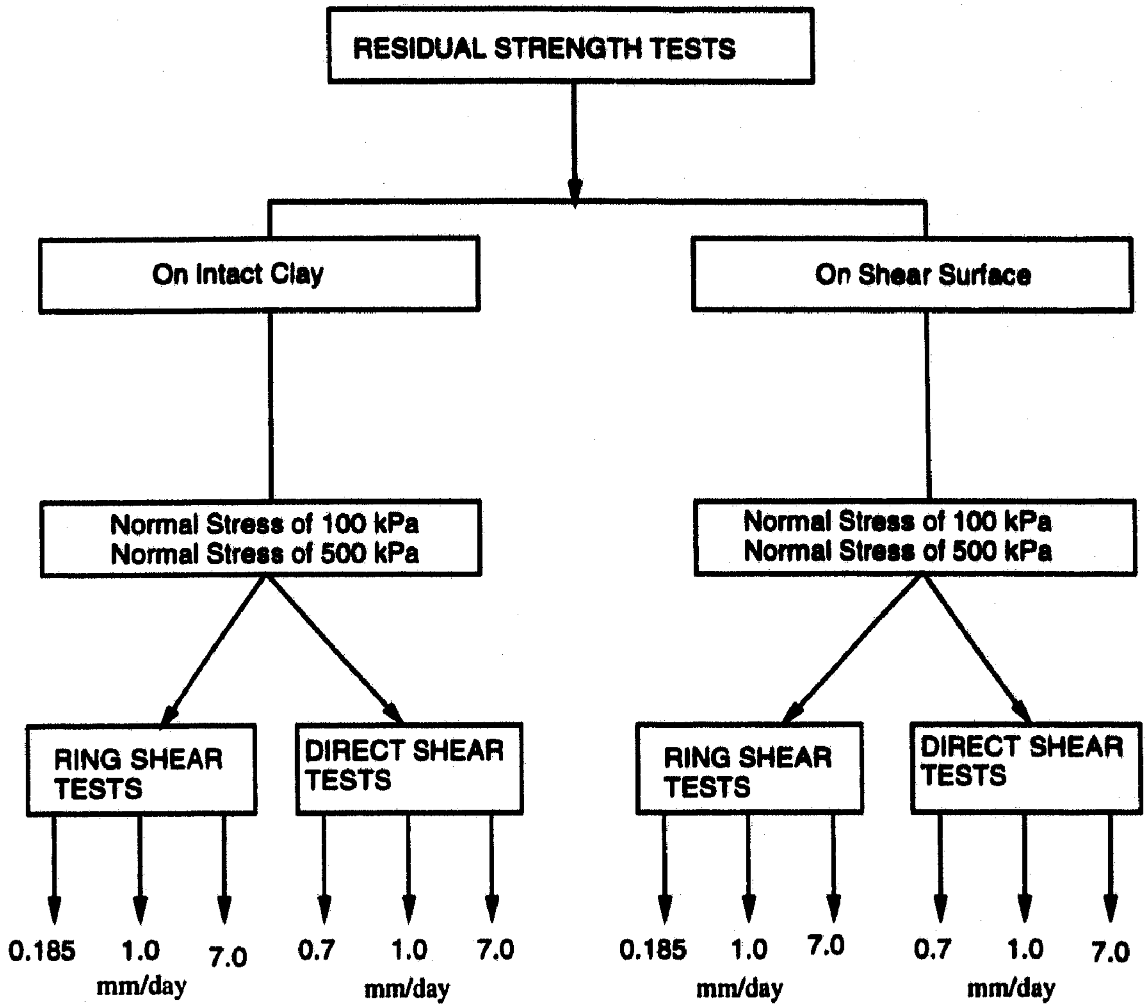

Figure 2.12 Laboratory residual strength testing program

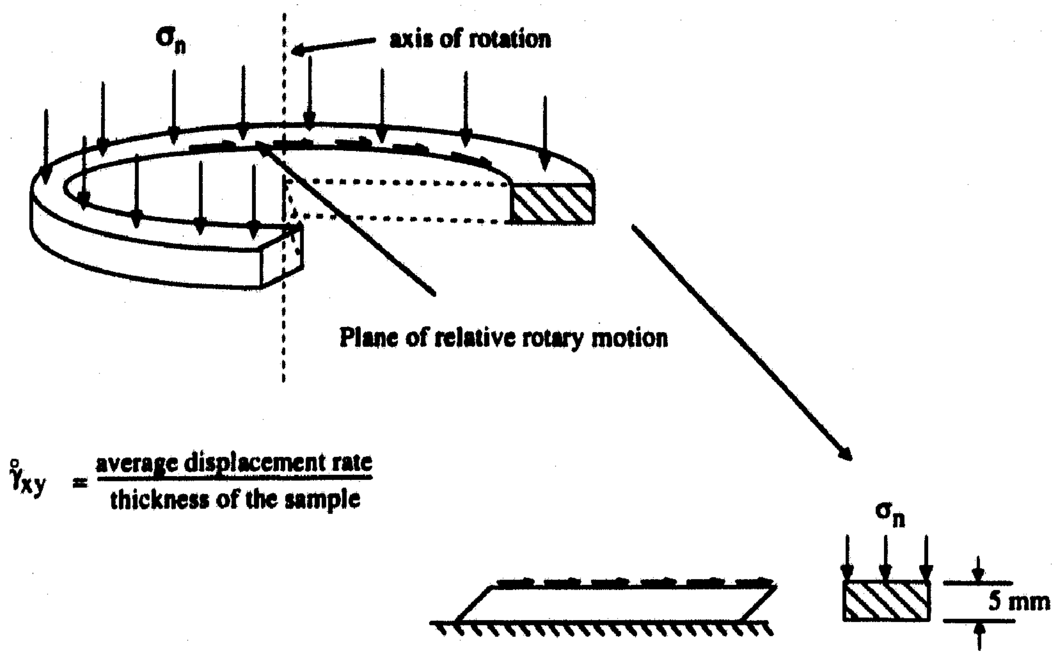

(a) Ring shear sample and assumption of uniform shear

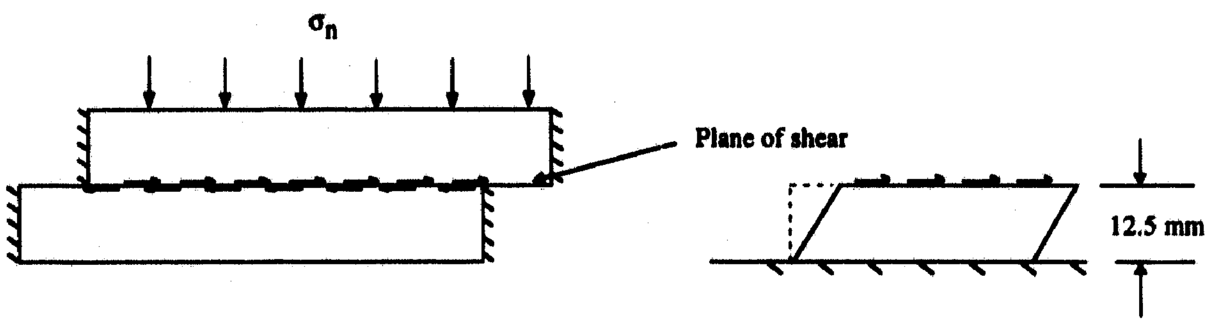

(b) Direct shear sample and assumption of uniform shear

Figure 2.13 Samples of Ring shear and Direct shear tests

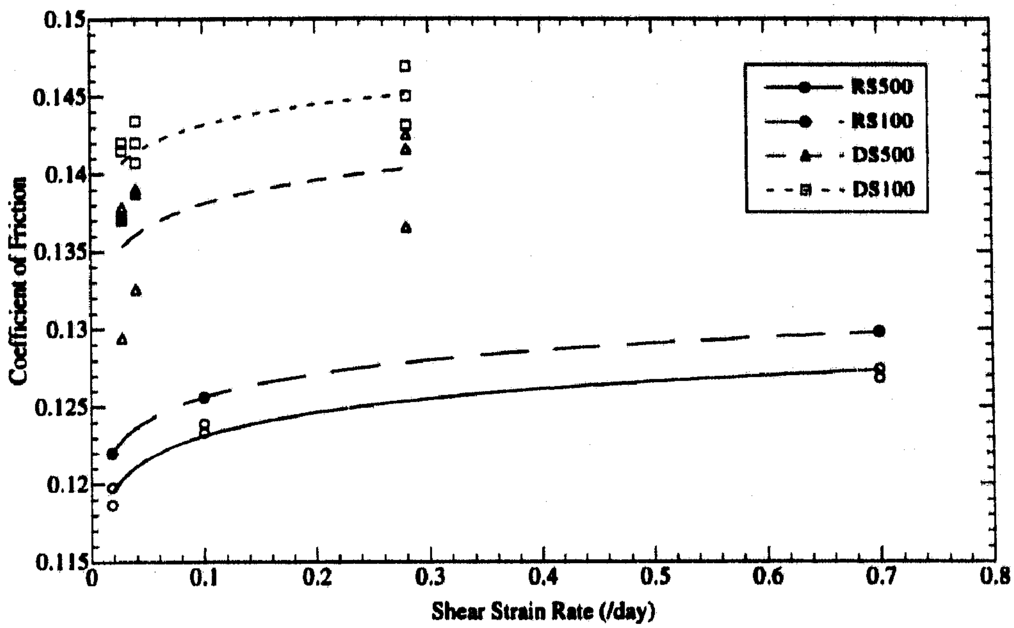

Figure 2.14 Coefficient of friction vs. rate of shear strain

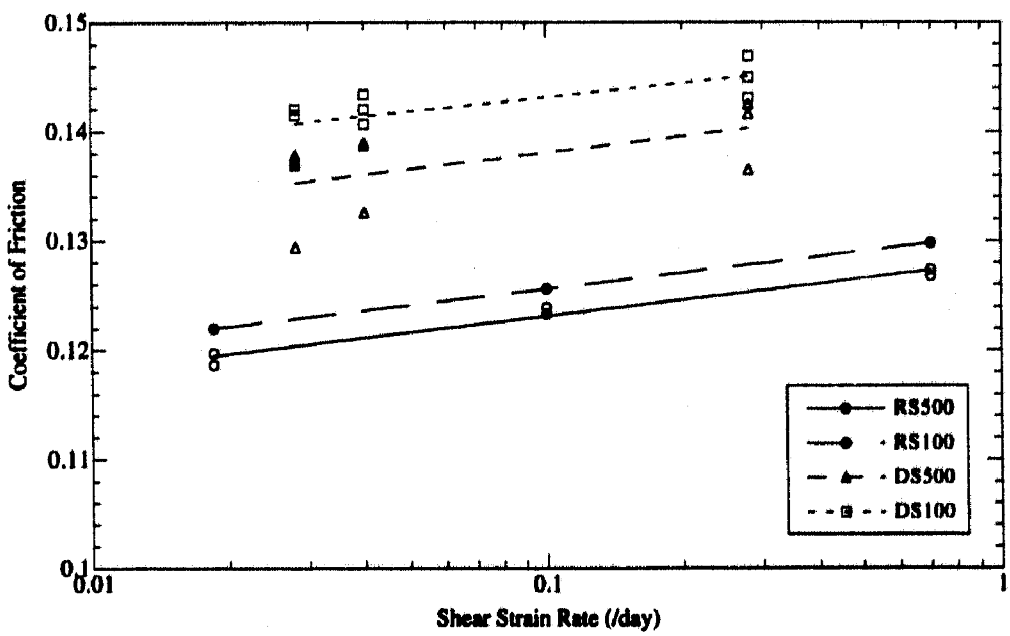

Figure 2.15 Coefficient of friction vs. rate of shear strain

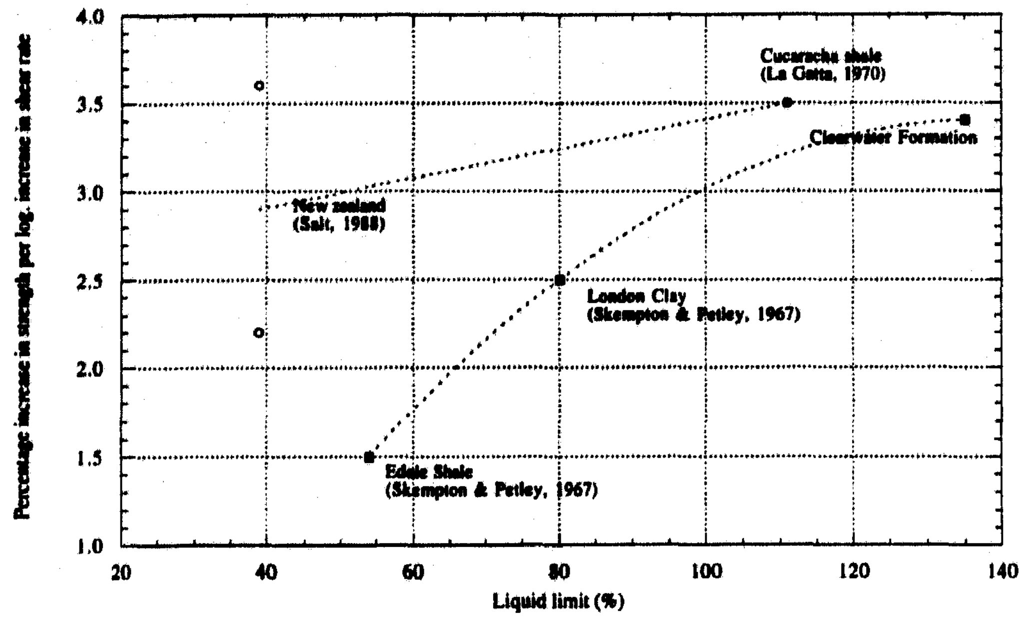

Figure 2.16 Correlation of rate effects to Liquid Limit

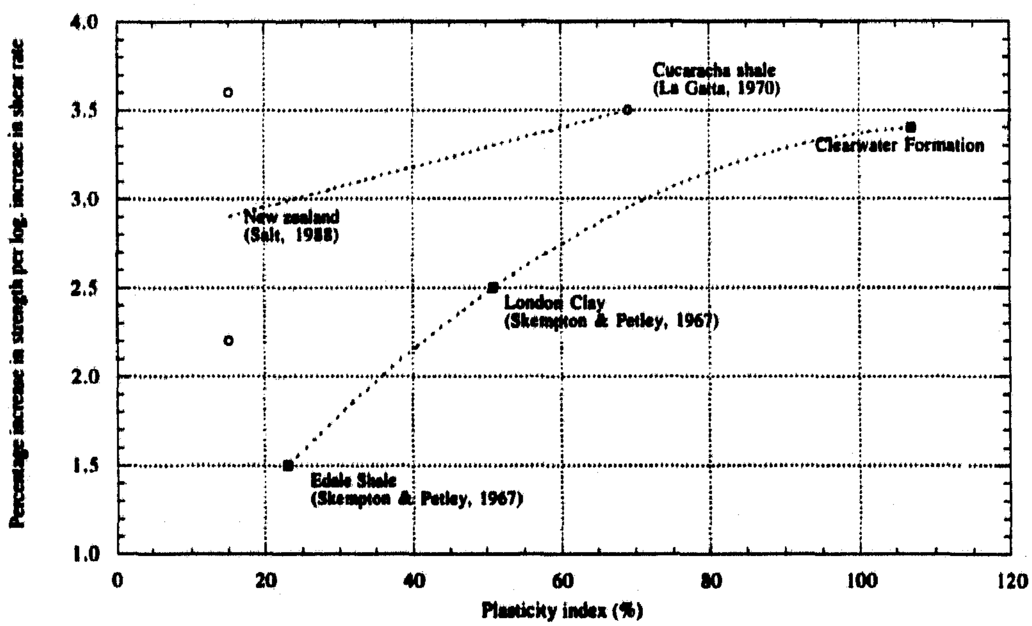

Figure 2.17 Correlation of rate effects to Plasticity Index

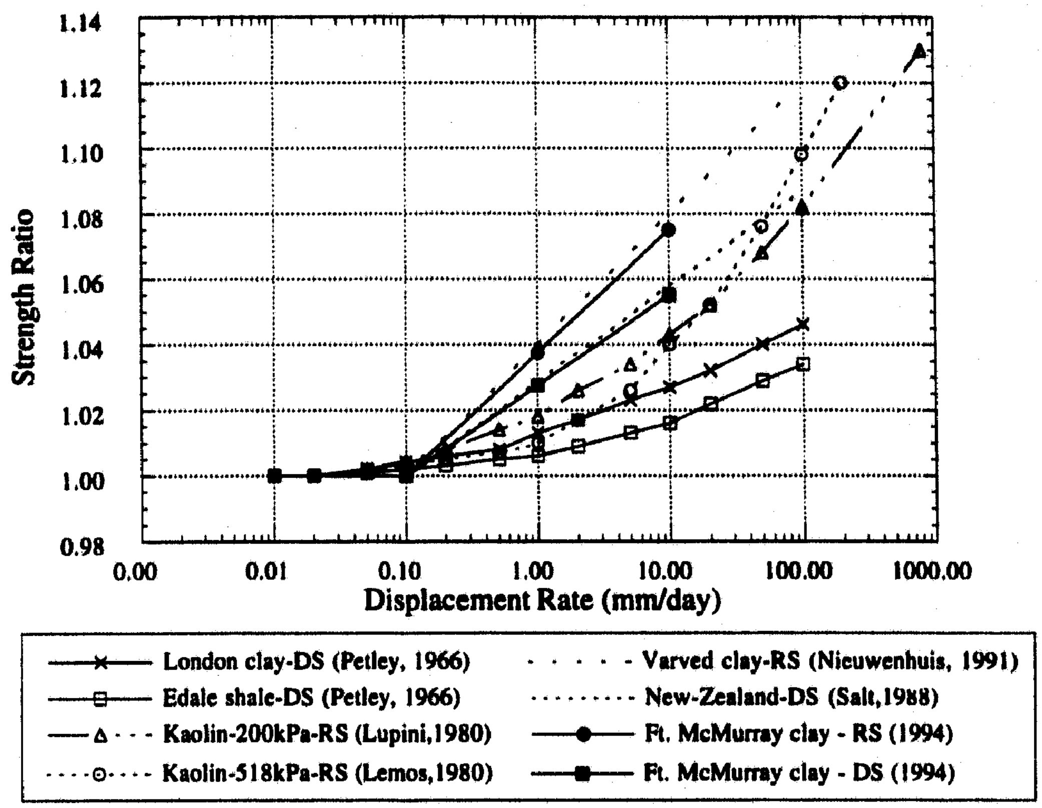

Figure 2.18 Comparision of test results with previous results

CHAPTER 3

FORMULATION OF RATE DEPENDENT CONSTITUTIVE MODEL

3.1 Introduction

Rate effects on inelastic deformations are commonly considered at the present time by either classical rate-independent theory or by the theory of viscoplasticity. In classical rate-independent theory, material properties are replaced by values measured from tests which replicate the strain rates of interest. This procedure gives reasonable answers for the problems where the bulk of the deformation occurs at a specific rate. But there can be no accuracy under widely varying conditions if the material parameters are strain rate sensitive. The approach of viscoplastic theory assumes that the inelastic deformation is a viscous flow driven by the excess of the applied stress over the static work-hardening value of the stress. Application of this method requires the assumption of the functional dependence of the plastic strain rate and the over-stress based on empirical data, and the use of a solution procedure different from that commonly used in plastic computer codes. The aim of this study is to perform a theoretical derivation of rate-dependent plasticity and to obtain a constitutive relationship which can be easily added to the existing plastic constitutive relationships.

3.2 General theory

The fundamental concept in classical plastic theory is the existence of a yield surface in stress space. This surface encloses the region of purely elastic behavior. When the state point reaches the yield surface, plastic strains are initiated. When a state point, corresponding to the stress and internal variables of the material is undergoing an increment of plastic flow, it remains on the yield surface. The surface must incrementally distort or translate in such a manner that the functional definition of the surface is still satisfied.

Experimental evidence shows, that for clays, the residual shear strength as observed in ring shear and direct shear tests is a function of the rate of deformation and, hence, rate of shear strain. Hence, the shear strength as described by the Mohr Coulomb failure criterion (which is considered to be adequate to represent the behavior of sheared clay) is a function of the rate of strain. Also the Mohr-Coulomb failure criterion is assumed to be a yield criterion. It should also be noted that the material considered here is previously sheared and therefore, it does not show a peak strength; it can only mobilize the residual strength.

The shear resistance-strain rate relation can be more precisely represented by a bilinear model in yield resistance-$\log_e$(strain rate) (Equation 2.12 and 2.13).

Then,

$$\tau = \sigma_n \tan\phi_o \qquad \text{when} \quad \mathring{\varepsilon}^p < \mathring{\varepsilon}^p_o \tag{3.1a}$$

$$\tau = \sigma_n \tan\phi_o \left(1 + b \ln \frac{\mathring{\varepsilon}^p}{\mathring{\varepsilon}^p_o}\right) \qquad \text{when} \quad \mathring{\varepsilon}^p \geq \mathring{\varepsilon}^p_o \tag{3.1b}$$

where,

b - strain rate hardening constant

$\mathring{\varepsilon}^p_o$ - reference plastic strain rate below which the rate effects are negligible

$\overset{\circ}{\varepsilon}^p = \sqrt{\frac{1}{2}\overset{\circ}{\varepsilon}^p_{ij}\overset{\circ}{\varepsilon}^p_{ij}}$ - effective plastic strain rate

ϕ_o - minimum effective friction angle

τ - shear stress

σ_n - normal stress

$\circ$ - denotes the material time derivative

Where, $\overset{\circ}{\varepsilon}^p_{ij} = \overset{\circ}{e}^p_{ij} - \frac{\overset{\circ}{e}^p_{kk}}{3}\delta_{ij}$ is the deviatoric plastic strain rate tensor, which is equivalent to the total plastic strain rate tensor, $\overset{\circ}{e}^p_{ij}$, since the material is assumed to behave according to the non-associated flow rule where no volumetric strains are considered.

Total strain rate, $\overset{\circ}{\varepsilon}$,

$$\overset{\circ}{\varepsilon} = \overset{\circ}{\varepsilon}^e + \overset{\circ}{\varepsilon}^p$$

The constitutive equations in plasticity are valid for any function f representing the static yield condition, provided the assumptions concerning perfectly plastic materials are satisfied, i.e., f does not depend on strains. However, considering the non-elastic part of the strain rate as defined by viscoplastic theories, Perzyna (1963) showed that the expressions representing the dynamic yield conditions for elastic, viscoplastic materials implicitly describe the dependence of the yield condition on strain rate. This function of stresses above the static yield criterion generates the non-elastic strain rate. Therefore, in this theory the radius of cylindrical yield surface, or the size of the yield surface in the stress space, depends on the strain rate.

For a rate-dependent theory, some form of rate variable must be included in the yield surface. The rate variable used in this formulation should be chosen to reflect as closely as possible the physical causes of time dependency in the soil response. For a small increment of applied stress there is an increment of elastic strain, which occurs instantaneously and an increment of plastic strain, which needs time to develop. Since the time dependence of plastic strain is a property of the material response to the applied stress, plastic strain rate may be considered as an internal variable.

Kocks (1975) states, "The physical explanation for the above observation lies in the fact that plastic strain is composed from the accumulation of a large number of dislocation motions within the metal crystal, each dislocation moving at a definite velocity. The total delay in the appearance of complete plastic strain is the time required for the accumulation of dislocation motion on all active slip planes."

In soils however, the plastic strains occur due to permanent slip between particles. Based on the above discussions on metals and the laboratory tests on soils, it is understood that the force required to overcome inter-particle friction is a function of time required or allowed for the plastic strains, i.e., plastic strain rates.

In the following section, a general rate-dependent plastic theory is formulated using the concepts of the flow rule of plasticity for the direction of the plastic strain increments, and the yield surface.

3.3 Derivation of rate-dependent constitutive model

The rate variable included here is the second strain rate invariant $\overset{\circ}{\varepsilon}{}^{p}$.

$$\overset{\circ}{\varepsilon}{}^{p} = \sqrt{\frac{1}{2}\overset{\circ}{\varepsilon}{}^{p}_{ij}\overset{\circ}{\varepsilon}{}^{p}_{ij}} \qquad (3.2)$$

$\overset{\circ}{\varepsilon}{}^{p}$ is the component of strain rate which governs the yield function, directly obtainable from the direct shear or ring shear tests.

When the plastic strain rates are sufficiently small (i.e. rate effects on the yield resistance is negligible), a point corresponding to the state of plastic deformation remains on the initial yield surface. Consequently, when the plastic strain rates increase, the yielding resistance and, hence, the dynamic yield function (hereafter referred to as the loading function) moves away (enlarges) from the initial yield surface (Figure 3.1). The change from the initial yield surface to the loading surface is entirely due to the rate hardening phenomenon. (note: this material is assumed to have no strain hardening or softening. Derivation of constitutive equations for a more general yielding behavior where strain hardening or softening is allowed is given in Appendix 3-1.)

If the loading function is represented by F , then, the condition defining continuous plastic deformation is $\overset{\circ}{F} = 0$. Therefore, for a rate sensitive material, the loading surface is a function of rate of strain based on the above explanation and as illustrated by Perzyna(1963) and Drysdale(1987). A simple extension to the plastic theory will be implemented in this study to achieve a close approximation of the behavior.

The static yield condition for an elastic, perfectly plastic material requires that:

$$f(\sigma_{ij}) = 0 \qquad (3.3)$$

The loading condition F of a rate dependent material is:

$$F(\sigma_{ij}, \overset{\circ}{\varepsilon}{}^{p}) = 0 \tag{3.4}$$

where $\overset{\circ}{\varepsilon}{}^{p}$ is the effective plastic strain rate as given by equation (3.2). F is obtained empirically and is such that when $\overset{\circ}{\varepsilon}{}^{p}$ less than $\overset{\circ}{\varepsilon}{}^{p}_{o}$, $F(\sigma_{ij}, \overset{\circ}{\varepsilon}{}^{p}) = f(\sigma_{ij})$.

Consider the Mohr-Coulomb criterion for the loading function for a two dimensional problem. F is given by:

$$F(\sigma_{ij}, \overset{\circ}{\varepsilon}{}^{p}) = \left[\left(\frac{\sigma_{xx} - \sigma_{yy}}{2}\right)^2 + \tau_{xy}^2\right]^{1/2} + \left(\frac{\sigma_{xx} + \sigma_{yy}}{2}\right)\frac{\tan\phi}{\sqrt{1 + \tan^2\phi}} = 0$$

(3.5a)

where $\tan\phi$ vs $\overset{\circ}{\varepsilon}{}^{p}$ is a bilinear relationship in a semi log plot

When, $\overset{\circ}{\varepsilon}{}^{p} < \overset{\circ}{\varepsilon}{}^{p}_{o}$,

$$\tan\phi = \tan\phi_o \tag{3.5b}$$

When, $\overset{\circ}{\varepsilon}{}^{p} \geq \overset{\circ}{\varepsilon}{}^{p}_{o}$,

$$\tan\phi = \tan\phi_o\left(1 + b\ln\frac{\overset{\circ}{\varepsilon}{}^{p}}{\overset{\circ}{\varepsilon}{}^{p}_{o}}\right) \tag{3.5c}$$

ϕ_o - static friction angle;

ϕ - mobilized friction angle;

$\overset{\circ}{\varepsilon}{}^{p}_{o}$ - reference (quasi static) strain rate;

b - strain rate hardening parameter;

or in terms of q and p in three dimensional stress space,

$$f(\sigma_{ij}) = q + p\tan\alpha_{\circ} = 0 \tag{3.6}$$

$$F(\sigma_{ij}, \overset{\circ}{\varepsilon}{}^{p}) = q + p\tan\alpha = 0 \tag{3.7}$$

where,

$$p = \sigma_{ii}/3; \tag{3.8a}$$

$$q = \frac{1}{\sqrt{2}}\sqrt{S_{ij}S_{ij}}; \tag{3.8b}$$

$$S_{ij} = \sigma_{ij} - \frac{\sigma_{kk}}{3}\delta_{ij}; \tag{3.8c}$$

and,

$$\tan\alpha = \sin\phi \tag{3.8d}$$

Condition defining plastic state, from equation (3.4),

$$\frac{\partial F}{\partial \sigma_{ij}}\overset{\circ}{\sigma}_{ij} + \frac{\partial F}{\partial \overset{\circ}{\varepsilon}{}^{p}}\overset{\circ\circ}{\varepsilon}{}^{p} = 0 \tag{3.9}$$

From Equations (3.5c), (3.7) and (3.8d), and differentiating Equation (3.7),

$$\frac{\partial F}{\partial \overset{\circ}{\varepsilon}{}^{p}} = \frac{pb\tan\phi_{\circ}}{\overset{\circ}{\varepsilon}{}^{p}}\left(1+\tan^{2}\phi\right)^{-\frac{3}{2}}$$

(According to the sign convention considered here $\frac{\partial F}{\partial \overset{\circ}{\varepsilon}{}^{p}}$ is always negative)

Rewriting equation (3.9);

$$\frac{\partial F}{\partial \sigma_{ij}}\overset{\circ}{\sigma}_{ij} - \left[-\frac{\partial F}{\partial \overset{\circ}{\varepsilon}{}^{p}}\right]\overset{\circ\circ}{\varepsilon}{}^{p} = 0 \tag{3.10}$$

Assuming increments of stresses are as the result of elastic deformation, then;

$$\overset{\circ}{\sigma}_{ij} = C^{e}_{ijkl}(\overset{\circ}{\varepsilon}_{kl} - \overset{\circ}{\varepsilon}^{p}_{kl}) \tag{3.11}$$

From the flow rule of plasticity,

$$\overset{\circ}{\varepsilon}^{p}_{kl} = \lambda \frac{\partial g}{\partial \sigma_{kl}} \tag{3.12}$$

Where the plastic potential function, g , is defined such that during plastic deformation there is no volume change and it passes through the same point in stress space as F . λ is a positive scalar quantity.

From (3.2) and (3.12)

$$\overset{\circ}{\varepsilon}^{p} = \sqrt{\frac{1}{2}\left(\lambda \frac{\partial g}{\partial \sigma_{ij}}\right)\left(\lambda \frac{\partial g}{\partial \sigma_{ij}}\right)} \tag{3.13}$$

Therefore,

$$\lambda = \overset{\circ}{\varepsilon}^{p} \Big/ \sqrt{\frac{1}{2}\left(\frac{\partial g}{\partial \sigma_{kl}}\right)\left(\frac{\partial g}{\partial \sigma_{kl}}\right)} \tag{3.14}$$

combining (3.12) and (3.14)

$$\overset{\circ}{\varepsilon}^{p}_{kl} = \frac{\overset{\circ}{\varepsilon}^{p}}{\sqrt{\frac{1}{2}\left(\frac{\partial g}{\partial \sigma_{mn}}\right)\left(\frac{\partial g}{\partial \sigma_{mn}}\right)}} \frac{\partial g}{\partial \sigma_{kl}} \tag{3.15}$$

From (3.10), (3.11) and (3.15),

$$\frac{\partial F}{\partial \sigma_{ij}} C^{e}_{ijkl} \left[\overset{\circ}{\varepsilon}_{kl} - \frac{\overset{\circ}{\varepsilon}^{p}}{\sqrt{\frac{1}{2}\left(\frac{\partial g}{\partial \sigma_{mn}}\right)\left(\frac{\partial g}{\partial \sigma_{mn}}\right)}} \frac{\partial g}{\partial \sigma_{kl}} \right] - \left[-\frac{\partial F}{\partial \overset{\circ}{\varepsilon}^{p}} \right] \overset{\circ\circ}{\varepsilon}^{p} = 0 \tag{3.16}$$

$$\left[-\frac{\partial F}{\partial \overset{\circ}{\varepsilon}^p}\right]\overset{\circ\circ}{\varepsilon}^p+\frac{\partial F}{\partial \sigma_{ij}}C^e_{ijkl}\frac{\partial g}{\partial \sigma_{kl}}\frac{\overset{\circ}{\varepsilon}^p}{\sqrt{\frac{1}{2}\left(\frac{\partial g}{\partial \sigma_{mn}}\right)\left(\frac{\partial g}{\partial \sigma_{mn}}\right)}}=\frac{\partial F}{\partial \sigma_{ij}}C^e_{ijkl}\overset{\circ}{\varepsilon}_{kl} \tag{3.17}$$

The above equation (3.17) is a first order nonlinear differential equation of $\overset{\circ}{\varepsilon}^p$ of the form;

$$\overset{\circ\circ}{\varepsilon}^p+\frac{\frac{\partial F}{\partial \sigma_{ij}}C^e_{ijkl}\frac{\partial g}{\partial \sigma_{kl}}}{\sqrt{\frac{1}{2}\left(\frac{\partial g}{\partial \sigma_{mn}}\right)\left(\frac{\partial g}{\partial \sigma_{mn}}\right)}\left[-\frac{\partial F}{\partial \overset{\circ}{\varepsilon}^p}\right]}\overset{\circ}{\varepsilon}^p=\frac{\frac{\partial F}{\partial \sigma_{ij}}C^e_{ijkl}\overset{\circ}{\varepsilon}_{kl}}{\left[-\frac{\partial F}{\partial \overset{\circ}{\varepsilon}^p}\right]} \tag{3.18}$$

Approximate solution for $\overset{\circ}{\varepsilon}^p$, and substitution if it in equation (3.15) gives: (The detailed solution is given in Appendix 3-2).

$$\overset{\circ}{\varepsilon}^p_{kl}=\left\{A-(A-\frac{\overset{\circ}{\varepsilon}^p_1}{C})e^{Bt}\right\}\frac{\partial g}{\partial \sigma_{kl}} \tag{3.19a}$$

where

$$A=\frac{\frac{\partial F}{\partial \sigma_{\alpha\beta}}C^e_{\alpha\beta mn}\overset{\circ}{\varepsilon}_{mn}}{\frac{\partial F}{\partial \sigma_{\alpha\beta}}C^e_{\alpha\beta mn}\frac{\partial g}{\partial \sigma_{mn}}} \tag{3.19b}$$

$$B=-\frac{\frac{\partial F}{\partial \sigma_{\alpha\beta}}C^e_{\alpha\beta mn}\frac{\partial g}{\partial \sigma_{mn}}}{\sqrt{\frac{1}{2}\left(\frac{\partial g}{\partial \sigma_{mn}}\right)\left(\frac{\partial g}{\partial \sigma_{mn}}\right)}\left[-\frac{\partial F}{\partial \overset{\circ}{\varepsilon}^p}\right]} \tag{3.19c}$$

$$C = \sqrt{\frac{1}{2}\left(\frac{\partial g}{\partial \sigma_{mn}}\right)\left(\frac{\partial g}{\partial \sigma_{mn}}\right)} \tag{3.19d}$$

and, $\overset{\circ}{\varepsilon}{}^{p}_{i}$ is the effective plastic strain rate at the end of i^{th} interval.

Substituting the above in equation (3.11):

$$\dot{\sigma}_{ij} = C^{e}_{ijkl}\left[\dot{\varepsilon}_{kl} - \left\{ \frac{\frac{\partial F}{\partial \sigma_{\alpha\beta}} C^{e}_{\alpha\beta mn}\dot{\varepsilon}_{mn}}{\frac{\partial F}{\partial \sigma_{\alpha\beta}} C^{e}_{\alpha\beta mn}\frac{\partial g}{\partial \sigma_{mn}}} - \left(\frac{\frac{\partial F}{\partial \sigma_{\alpha\beta}} C^{e}_{\alpha\beta mn}\dot{\varepsilon}_{mn}}{\frac{\partial F}{\partial \sigma_{\alpha\beta}} C^{e}_{\alpha\beta mn}\frac{\partial g}{\partial \sigma_{mn}}} - \frac{\dot{\varepsilon}^{p}_{i}}{\sqrt{\frac{1}{2}\left(\frac{\partial g}{\partial \sigma_{mn}}\right)\left(\frac{\partial g}{\partial \sigma_{mn}}\right)}} \right) e^{-\frac{\frac{\partial F}{\partial \sigma_{\alpha\beta}} C^{e}_{\alpha\beta mn}\frac{\partial g}{\partial \sigma_{mn}}}{\sqrt{\frac{1}{2}\left(\frac{\partial g}{\partial \sigma_{mn}}\right)\left(\frac{\partial g}{\partial \sigma_{mn}}\right)}\left[-\frac{\partial F}{\partial \dot{\varepsilon}^{p}}\right]}t} \right\} \frac{\partial g}{\partial \sigma_{kl}} \right] \tag{3.20}$$

Equation (3.20) is now a suitable incremental relation over a time step Δt which gives the change in stress in terms of the change in total strain and in terms of the parameters which can be calculated from the previous time step. The second term on the right hand side of equation (3.20) represents the rate effects.

Numerical stability during iterations is found not sensitive to the size of the time step, Δt. It can be selected based on the knowledge of changes in loading condition in an actual problem. If the external loading condition changes rapidly, a smaller Δt should be chosen. For example, in the analyses in Salledes test embankment (Chapter 5), where the construction was completed within few days, the selected Δt varied from 2 to 24 hours. In the deformation analyses of the Syncrude tailings dyke (Chapter 6) Δt of 30 days to 120 days were chosen.

Expressing equation (3.20) in incremental form over time interval Δt:

$$d\sigma_{ij} = C^{e}_{ijkl}\left[d\varepsilon_{kl} - \left\{ \frac{\dfrac{\partial F}{\partial \sigma_{\alpha\beta}} C^{e}_{\alpha\beta mn} d\varepsilon_{mn}}{\dfrac{\partial F}{\partial \sigma_{\alpha\beta}} C^{e}_{\alpha\beta mn} \dfrac{\partial g}{\partial \sigma_{mn}}} - \left(\frac{\dfrac{\partial F}{\partial \sigma_{\alpha\beta}} C^{e}_{\alpha\beta mn} d\varepsilon_{mn}}{\dfrac{\partial F}{\partial \sigma_{\alpha\beta}} C^{e}_{\alpha\beta mn} \dfrac{\partial g}{\partial \sigma_{mn}}} - \frac{\mathring{\varepsilon}^{p}_{\,}}{\sqrt{\dfrac{1}{2}\left(\dfrac{\partial g}{\partial \sigma_{mn}}\right)\left(\dfrac{\partial g}{\partial \sigma_{mn}}\right)}}\Delta t \right) e^{-\dfrac{\dfrac{\partial F}{\partial \sigma_{\alpha\beta}} C^{e}_{\alpha\beta mn} \dfrac{\partial g}{\partial \sigma_{mn}}}{\sqrt{\dfrac{1}{2}\left(\dfrac{\partial g}{\partial \sigma_{mn}}\right)\left(\dfrac{\partial g}{\partial \sigma_{mn}}\right)}\left[-\dfrac{\partial F}{\partial \mathring{\varepsilon}^{p}}\right]}\Delta t} \right\} \frac{\partial g}{\partial \sigma_{kl}} \right] \tag{3.21}$$

$$d\sigma_{ij} = \left(C^{e}_{ijmn} - \frac{C^{e}_{ijkl} \dfrac{\partial g}{\partial \sigma_{kl}} \dfrac{\partial F}{\partial \sigma_{\alpha\beta}} C^{e}_{\alpha\beta mn}}{\dfrac{\partial F}{\partial \sigma_{\alpha\beta}} C^{e}_{\alpha\beta mn} \dfrac{\partial g}{\partial \sigma_{mn}}} \left(1 - e^{-\dfrac{\dfrac{\partial F}{\partial \sigma_{\alpha\beta}} C^{e}_{\alpha\beta mn} \dfrac{\partial g}{\partial \sigma_{mn}}}{\sqrt{\dfrac{1}{2}\left(\dfrac{\partial g}{\partial \sigma_{mn}}\right)\left(\dfrac{\partial g}{\partial \sigma_{mn}}\right)}\left[-\dfrac{\partial F}{\partial \mathring{\varepsilon}^{p}}\right]}\Delta t} \right) \right) d\varepsilon_{mn}$$

$$- C^{e}_{ijkl} \frac{\partial g}{\partial \sigma_{kl}} \left(\frac{\mathring{\varepsilon}^{p}\Delta t}{\sqrt{\dfrac{1}{2}\left(\dfrac{\partial g}{\partial \sigma_{mn}}\right)\left(\dfrac{\partial g}{\partial \sigma_{mn}}\right)}} \right) e^{-\dfrac{\dfrac{\partial F}{\partial \sigma_{\alpha\beta}} C^{e}_{\alpha\beta mn} \dfrac{\partial g}{\partial \sigma_{mn}}}{\sqrt{\dfrac{1}{2}\left(\dfrac{\partial g}{\partial \sigma_{mn}}\right)\left(\dfrac{\partial g}{\partial \sigma_{mn}}\right)}\left[-\dfrac{\partial F}{\partial \mathring{\varepsilon}^{p}}\right]}\Delta t} \tag{3.22}$$

3.4 Behavior of a dynamic yield surface

The behavior of the dynamic yield surface in stress space is somewhat different from classical rate-independent theory. When the stress point (corresponding to the state of stress) reaches the initial static yield surface, that point reaches a plastic state.

Since $\overset{o}{\varepsilon}^{p}$ is zero (very small) on the static yield surface, at this instant no (very small) plastic strain occurs.

When the static yield surface is contacted and penetrated by a stress increment vector, the yield surface changes and expands according to Equation 3.4. If strain hardening is considered, concentric to the dynamic yield surface (loading surface), the static surface also translates in the same manner, with $\overset{o}{\varepsilon}^{p}$ zero. Since no strain hardening in the yield surface is considered in this model, the static yield surface remains unchanged. (Figure 3.1). When unloading occurs (by a decrease in strain rate), the loading surface will move inwards accordingly (from F_1 to F_2 as in Figure 3.1). If the state of a point lies on the loading surface F_1 (Figure 3.1), the strain rate is higher than if the point lies on the loading surface F_2.

Whenever the stresses and the loading surface are exterior to the static yield surface, plastic deformation occurs. With the stress point on the static surface, plastic deformations cease ($\overset{o}{\varepsilon}^{p}$ is zero or very small). Therefore, a point moving on the static surface is in a plastic state, but no (very small) plastic deformation is occurring.

3.5 Procedure for stress calculation for finite strain rate

The constitutive equations (Equation 3.22) derived in the previous section consists of two parts :

i.e. $$\underline{d\sigma} = \underline{C}^{EPR}\underline{d\varepsilon} + \underline{d\sigma}^{R} \qquad (3.23)$$

where,

$\underline{d\varepsilon}$ = strain increment vector

$\underline{d\sigma}$ = stress increment vector

$$\underline{C}^{EPR} = \left(C^e_{ijmn} - \frac{C^e_{ijkl} \frac{\partial g}{\partial \sigma_{kl}} \frac{\partial F}{\partial \sigma_{\alpha\beta}} C^e_{\alpha\beta mn}}{\frac{\partial F}{\partial \sigma_{\alpha\beta}} C^e_{\alpha\beta mn} \frac{\partial g}{\partial \sigma_{mn}}} \left(1 - e^{-\frac{\frac{\partial F}{\partial \sigma_{\alpha\beta}} C^e_{\alpha\beta mn} \frac{\partial g}{\partial \sigma_{mn}}}{\sqrt{\frac{1}{2}\left(\frac{\partial g}{\partial \sigma_{mn}}\right)\left(\frac{\partial g}{\partial \sigma_{mn}}\right)}\left[-\frac{\partial F}{\partial \overset{\circ}{\varepsilon}{}^p}\right]}\Delta t} \right) \right)$$

$$\underline{d\sigma}^R = -C^e_{ijkl} \frac{\partial g}{\partial \sigma_{kl}} \left(\frac{\overset{\circ}{\varepsilon}{}^p \Delta t}{\sqrt{\frac{1}{2}\left(\frac{\partial g}{\partial \sigma_{mn}}\right)\left(\frac{\partial g}{\partial \sigma_{mn}}\right)}} \right) e^{-\frac{\frac{\partial F}{\partial \sigma_{\alpha\beta}} C^e_{\alpha\beta mn} \frac{\partial g}{\partial \sigma_{mn}}}{\sqrt{\frac{1}{2}\left(\frac{\partial g}{\partial \sigma_{mn}}\right)\left(\frac{\partial g}{\partial \sigma_{mn}}\right)}\left[-\frac{\partial F}{\partial \overset{\circ}{\varepsilon}{}^p}\right]}\Delta t}$$

The first component of equation (3.23) relates stress change to strain change by the rate-dependent elasto-plastic constitutive matrix. The rate dependent elasto-plastic constitutive matrix, $\underline{C}^{EPR}$, reduces to the elasto-plastic constitutive matrix, $\underline{C}^{EP}$, when the rate effects are zero. In other words, based on the present derivation, stress states above the static yield function are possible provided that the plastic strain rate is not zero. In fact, this is the principal assumption of classical viscoplastic theory (Perzyna, 1963) that the rate of the plastic component of the strain tensor be a function of the excess stresses above the static yield condition. The functional dependence may be chosen to represent the results of tests on the behavior of the material under dynamic loading. From Equation (3.22), the magnitude of stress tensor above the static yield condition is given by;

$$d\sigma_{ij} = \left(\frac{C^{e}_{ijkl}\dfrac{\partial g}{\partial \sigma_{kl}}\dfrac{\partial F}{\partial \sigma_{\alpha\beta}}C^{e}_{\alpha\beta mn}}{\dfrac{\partial F}{\partial \sigma_{\alpha\beta}}C^{e}_{\alpha\beta mn}\dfrac{\partial g}{\partial \sigma_{mn}}} e^{\dfrac{\dfrac{\partial F}{\partial \sigma_{\alpha\beta}}C^{e}_{\alpha\beta mn}\dfrac{\partial g}{\partial \sigma_{mn}}}{\sqrt{\dfrac{1}{2}\left(\dfrac{\partial g}{\partial \sigma_{mn}}\right)\left(\dfrac{\partial g}{\partial \sigma_{mn}}\right)}\left[-\dfrac{\partial F}{\partial \overset{o}{\varepsilon}{}^{p}}\right]}\Delta t} \right) d\varepsilon_{mn} \quad (3.24)$$

Therefore, Equation (3.24) gives an equivalent stress tensor, relaxation of which would bring the state of a point from its current dynamic state to the previous dynamic state.

The second component ,$d\underline{\sigma}^{R}$, is the change in stress due to initial strain rate effects. It is a known quantity at the beginning of a time step, based on the previous time step.

3.5.1 Algorithm for Stress Increment Calculation.

The calculation of a stress increment due to a strain increment can be carried out in the following steps:

1 Calculate total strain increment vector $\Delta\underline{\varepsilon}$;

2 Calculate $\Delta\underline{\sigma}^{E} = \underline{C}^{E}\Delta\underline{\varepsilon}$;

3 Check if $F(\underline{\sigma} + \Delta\underline{\sigma}, \overset{o}{\varepsilon}{}^{p} = 0) = 0$

If $F(\underline{\sigma}+\Delta\underline{\sigma}, \overset{\circ}{\varepsilon}{}^{p}=0)<0$ no yielding

4 Calculate $\dot{\varepsilon}^{p}$;

$$\overset{\circ}{\varepsilon}{}^{p}=\sqrt{\frac{1}{2}\overset{\circ}{\varepsilon}{}^{p}_{ij}\overset{\circ}{\varepsilon}{}^{p}_{ij}} \quad \text{and} \quad \overset{\circ}{\varepsilon}{}^{p}_{ij}=\frac{\Delta\underline{\varepsilon}-\Delta\underline{\varepsilon}_{e}}{\Delta t}$$

5 If $F(\underline{\sigma}+\Delta\underline{\sigma}, \overset{\circ}{\varepsilon}{}^{p})>0$ determine yield ratio R

set $F(\underline{\sigma}+R\Delta\underline{\sigma}, \overset{\circ}{\varepsilon}{}^{p})=0$ and find R $0 \le R \le 1$

6 $\Delta\underline{\sigma}^{E}=\underline{C}^{E}R\Delta\underline{\varepsilon}$

7 $\Delta\underline{\sigma}^{p}=\underline{C}^{EPR}(1-R)\Delta\underline{\varepsilon}$, $\underline{C}^{EPR}$ was defined in Section 3.5

8 $\underline{\sigma}=\underline{\sigma}+\Delta\underline{\sigma}^{E}+\Delta\underline{\sigma}^{p}$

3.5.2 Incorporation of $\underline{d\sigma}^{R}$ to the Finite Element Solution

The incremental equilibrium equation is;

$$\int_{v}\underline{B}^{T}\Delta\underline{\sigma}\,dv=\Delta\underline{R}, \tag{3.25}$$

where,

$\underline{B}$ = Strain displacement matrix,

$\Delta\underline{R}$ = External load vector.

But, from Equation (3.23)

$$\Delta\underline{\sigma} = \Delta\underline{\sigma} + d\underline{\sigma}^R \tag{3.26}$$

Thus, $\int_v \underline{B}^T\left(\Delta\underline{\sigma} + d\underline{\sigma}^R\right)dv = \Delta\underline{R}$,

$$\int_v \underline{B}^T\Delta\underline{\sigma}\ dv + \int_v \underline{B}^T d\underline{\sigma}^R\ dv = \Delta\underline{R}, \tag{3.27}$$

But,

$$\begin{aligned}\Delta\underline{\sigma} &= \underline{C}^{EPR}\Delta\underline{\varepsilon}\\ &= \underline{C}^{EPR}\underline{B}\Delta\underline{\delta}\end{aligned} \tag{3.28}$$

where,

$\Delta\underline{\delta}$ = Incremental displacement vector

Therefore,

$$\int_v \underline{B}^T\left(\underline{C}^{EPR}\underline{B}\ \ dv\right)\Delta\underline{\delta} = \Delta\underline{R} - \int_v \underline{B}^T d\underline{\sigma}^R\ \ dv \tag{3.29}$$

$$\underline{K} = \int_v \underline{B}^T\left(\underline{C}^{EPR}\underline{B}\ \ dv\right) \tag{3.30}$$

where,

K = Element stiffness matrix

Therefore, the modified equilibrium equation becomes:

$$K\Delta\delta = \Delta R - \int_v B^T d\sigma^R\ \ dv \tag{3.31}$$

Therefore, in using the developed rate-dependent model, the right hand side of the equilibrium equation will have an additional term due to initial rate effects.

3.6 Numerical example

To illustrate the rate effects and to check the program for accuracy of modifications into program PISA (Chan and Morgenstern, 1992), a two-dimensional plane strain test was simulated for a soil specimen as shown in Figure 3.2. The specimen was approximated by two eight-noded quadrilateral elements, each having an area of 1 square meter. Due to symmetry only one quarter of the specimen had to be analyzed. The left and bottom boundaries were fixed in horizontal and vertical directions respectively. A confining pressure of 100 kPa was initially applied to the specimen.

A Young's Modulus, E, of 10,000 kPa, Poisson's ratio, υ, of 0.4 and a static friction angle, ϕ_0, of 8° were used as basic material properties. In addition, for the rate-dependent model, reference effective plastic strain rate, $\overset{\circ}{\varepsilon}{}^p_o$, was taken as 0.0001/day and the rate hardening parameter, b, was taken as 0.019 based on laboratory test results for the highly plastic Clearwater clay-shale (Equation 2.12).

Separate analyses were performed assuming the material to be deformation rate-dependent and deformation rate-independent. To check the accuracy of program computations, hand calculations were performed for a given strain increment. During the subsequent steps of the finite element analysis, prescribed vertical displacements were applied at the top boundary of the initially isotropically compressed specimen.

When vertical displacements are applied to the top boundary of the specimen, the vertical stress in the specimen increases until the stress state touches the failure envelope. Further displacements will not cause any change in vertical stress since the material is assumed to behave in an elastic, perfectly plastic manner (Figure 3.3).

Under these loading and boundary conditions, if the material were to be rate-independent, the specimen should yield at a vertical stress of 132.3 kPa. Separate analyses were performed at deformation rates of 0.5, 0.6, 0.7, 0.8, 0.9, 1.0 and 2.0 mm/day for a total of 20 mm vertical deformation. The vertical stresses with deformations are plotted in Figures 3.4 and 3.5. They show an increase in yield resistance with the deformation rate. There is an apperant change in the slope of the stress-strain plots prior to yielding, for the tests at higher displacements rates. This occurs as a result of considerably large strain increment in the first loading step. The vertical stress change as calculated from the finite element analysis is identical to the hand calculated stress change for a known deformation increment.

When the applied strain rate is higher than the reference strain rate, the p - q plot shows that the ultimate stress states always lie outside the static yield envelope (Figure 3.6 and Figure 3.7). In other words, depending on the applied strain rate, the material will reach a different yield surface (loading surface).

Furthermore, the effective friction angle, calculated using p - q values and using the rate-dependent theoretical relationship, are compared in Figure 3.8. They match perfectly, indicating that if the material is modeled using the discussed rate-dependent model, the modified *PISA* (Chan and Morgenstern, 1992) program is capable of following the given "residual friction angle - strain rate" relationship.

3.7 Summary

An extension of the plasticity theory is implemented here in order to accommodate deformation rate-dependent behavior of residual shear strength. The clay is assumed to behave elastically before yielding, then in a perfectly plastic manner, with no volume change during yielding. During plastic deformation, the shear resistance is found to be a function of plastic deformation rate and, hence, of strain rate.

The Mohr Coulomb failure criterion is taken as the rate-dependent yield criterion, in which the rate effects are included in the effective friction angle. During initial yielding and subsequent plastic deformations, the state of a point will satisfy the dynamic yield function (loading function). When the effective plastic strain rate decreases to the threshold strain rate, the loading function moves (collapses) to the static yield function. A non-associated flow rule is used to calculate the increment of plastic deformations. The computed stress strain relationship is found to be of two parts, namely, rate-independent and rate-dependent. The rate-independent component is the same as that from elasto-plastic theory.

The performance of the model is illustrated by a numerical example simulating a two-dimensional plane strain test. The results of the example indicate that if the material is modeled using the discussed rate-dependent model, the modified PISA program (Chan and Morgenstern, 1992) is capable of following the given "residual friction angle - strain rate" relationship. The model itself is capable of accurately estimating the deformation rate-dependence of residual strength.

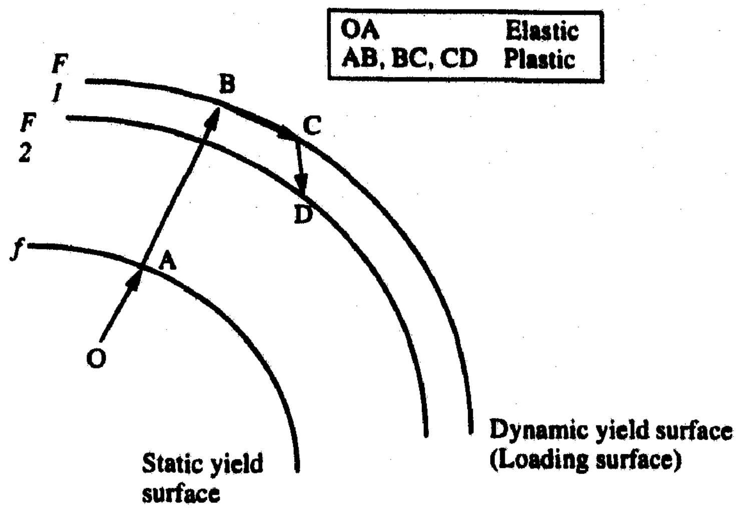

Figure 3.1 Behavior of static and dynamic yield surface

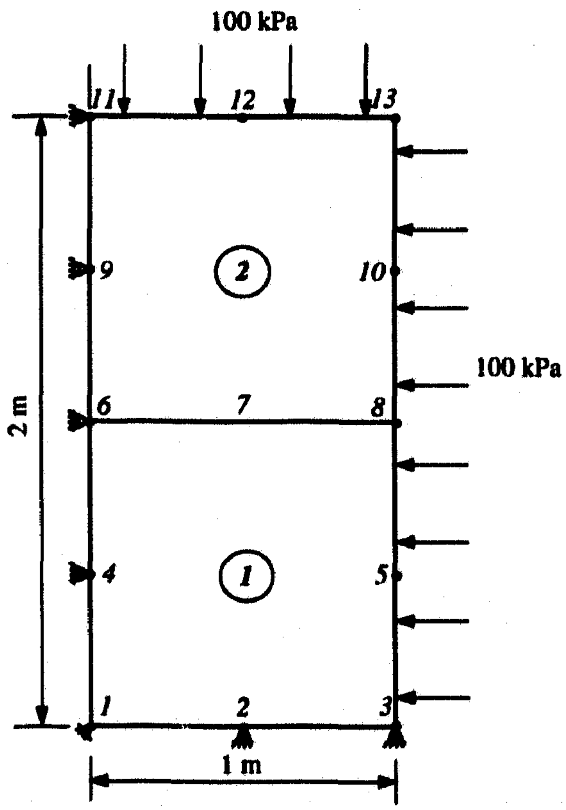

Figure 3.2 Finite element mesh showing boundary conditions

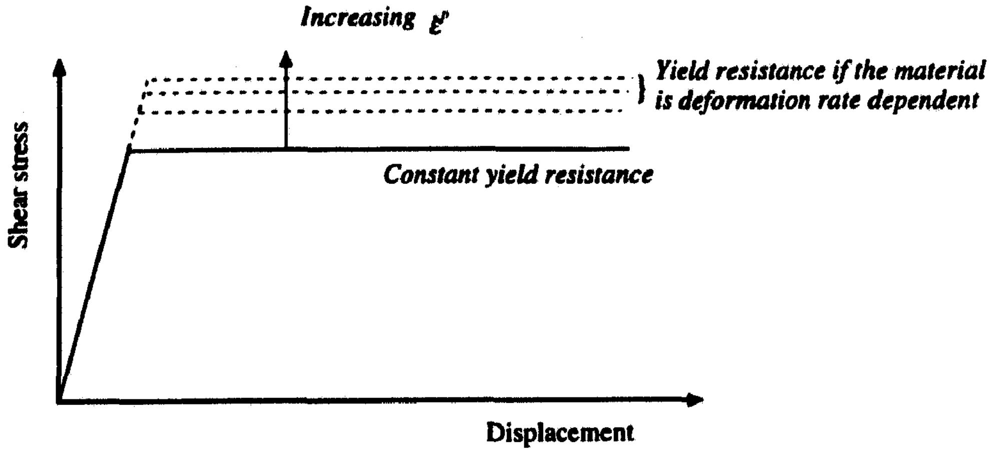

(a) Elastic perfectily plastic material

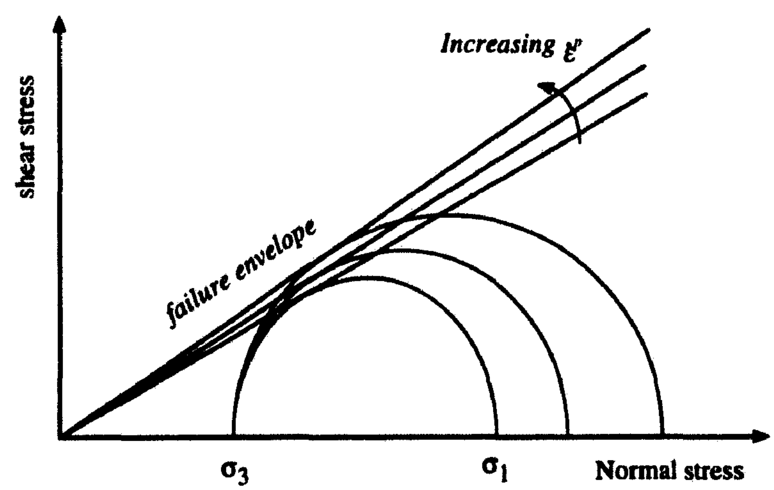

(b) Mohr circle representation of stresses

Figure 3.3 Yield criterion for a deformation rate dependent matreial

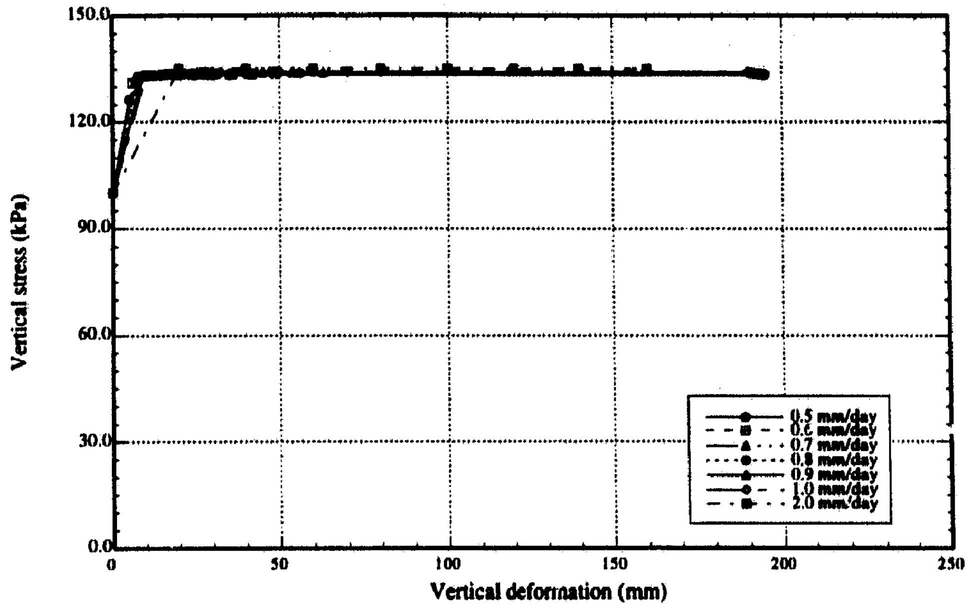

Figure 3.4 Variation of vertical stress with deformation

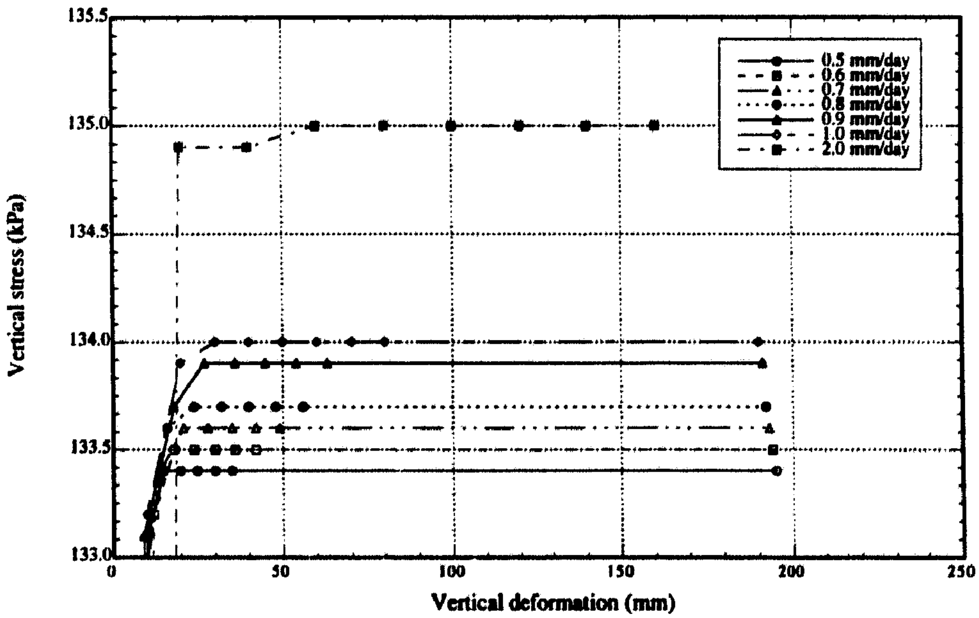

Figure 3.5 Close-up view of vertical stress vs. deformation

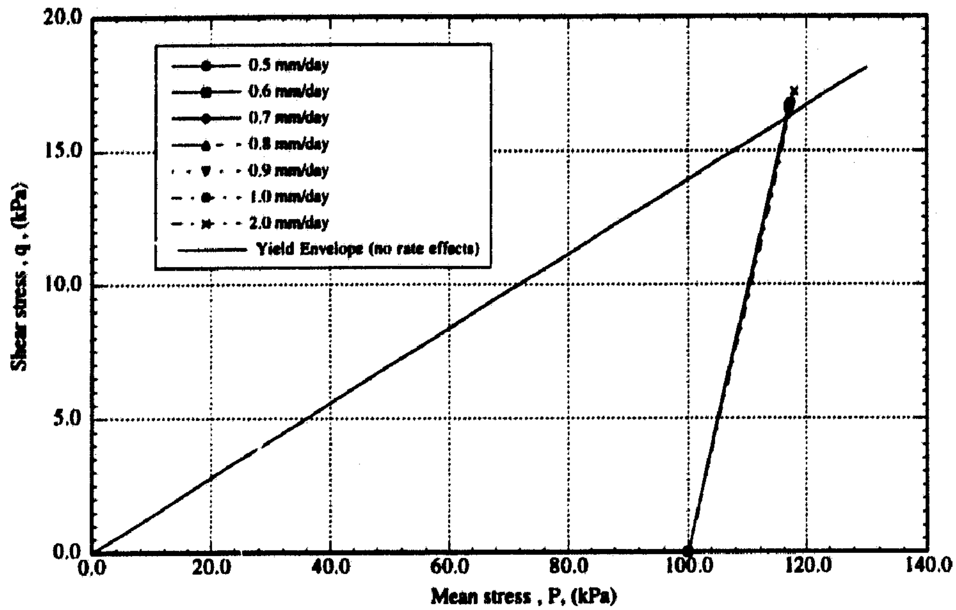

Figure 3.6 Stress Paths at different shearing rates

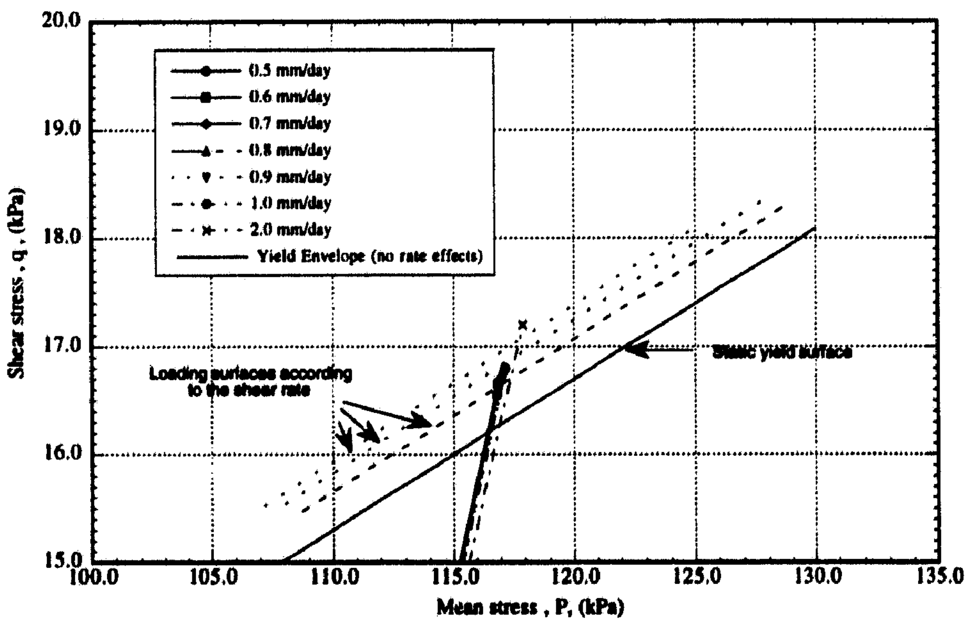

Figure 3.7 Close-up view of stress state at yielding

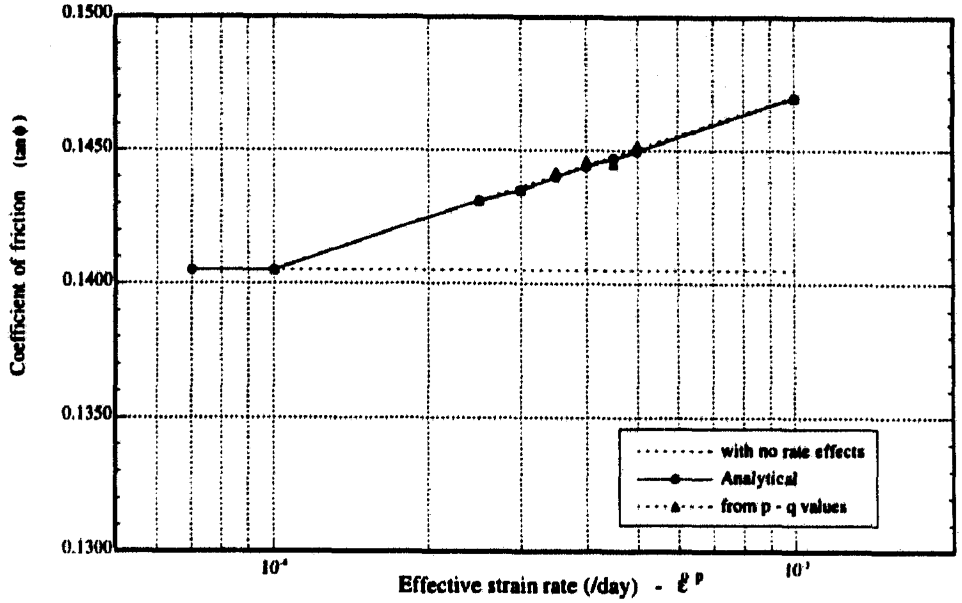

Figure 3.8 Coefficient of friction vs. strain rate

CHAPTER 4

THE MAM TOR LANDSLIDE

4.1 Introduction

The Mam Tor Landslide in Namurian mudstones in North Derbyshire is an example of a slump earth flow. It has been investigated by deep boreholes and piezometers. It has a length of 1000 m, a maximum width of 450 m and an average slope of 12° from the toe to the foot of the back scarp. The shear zone found at a depth of about 30 m, lies above hard mudstone of the Edale Shales. The upper slump sector moves on a curved slip surface within the 2 m thick shear zone.

Storm response movements, totaling less than 10 m in a century at Mam Tor produce a very small change in geometry under normal winter ground water conditions. However, records of movement show that slips leading to displacements typically of about 0.3 m are still taking place in winters with of more than 200 mm rainfall. The movements occur not as a continuous creep but rather as a series of small displacements in winter months when rainfall produces correspondingly high piezometric levels.

4.2 Geology and Dimensions of Landslide

A plan and a section of the Mam Tor landslide are given in Figure 4.1 and 4.2. Figure 4.1 shows geological boundaries as mapped by Stevenson (1972). Figure 4.2

shows about 100 m of Mam Tor Beds overlying Edale Shales. Carboniferous limestone outcrops a short distance south of the landslide.

The Edale Shales in their unweathered state are hard dark gray mudstones with occasional bands of siltstone and ironstone. The mudstones are weakened by fissures to a depth of the order of 10 m, resulting probably from stress release during valley formation, perhaps accentuated by permafrost action in the last glacial period. Observations in core samples, coupled with other data given by Stevenson and Gaunt (1971), demonstrate that the rock beneath the landslide has not been shifted from its natural position (Skempton et al., 1989).

The Mam Tor beds consist of gray micaceous Sandstone alternating with subsidiary Siltstone and Shale. The details of the geology and geological history can be found in Skempton et al. (1989).

The landslide has a length of 1000 m, a maximum width of 450 m and an average slope of 12° from the toe to the foot of the back scarp. From the crest of the scarp to the toe it has a total height of 280 m. The scarp face within the Mam Tor beds shows a slope of about 45° (Figure 4.2). Borehole data (locations are shown in Figure 4.1) provide the stratigraphy including the shear zone and the water level.

4.3 Soil Properties

Test data from Skempton et al. (1989) for samples taken from boreholes 1 and 2; and shear zone material in boreholes 1, 2 and 10 are given in Table 4.1 and Figure

4.3. The estimated value for residual strength parameter, ϕ'_r, based on index properties is 14°-15°.

For clays of medium to high plasticity the residual strength increases with rate of displacement. The relationship between rate of displacement and strength ratio for weathered Edale Shale is given in Figure 4.4. The shear strength parameters for slide debris, Mam Tor beds and Edale Shale are shown in Table 4.2.

4.4 Ground Water

Observations of the ground water level at about monthly intervals are reported in Skempton et al. (1989) for the winter months of 1977/1978. Casagrande-type piezometers (Casagrande, 1949) were used for measurement of water level at selected boreholes. A general pattern for seasonal fluctuations can be obtained from these data. Observations in borehole 1 and 7 with rainfall data are plotted in Figure 4.5. Borehole 7 shows a seasonal response of 0.7 m whereas at borehole 1 the response is 2 m.

A summary of data on the line of section in Figure 4.1 is given in Table 4.3. The first reading, at the end of October, 1977 is probably close to normal minimum level. The elevation of water in February, 1978 may be taken as that at the shear zone when ground water level is close to its seasonal maximum under normal conditions.

In the wet period, when the soil moisture deficit is effectively zero, the greater part of rainfall is able to seep down to the water table without being absorbed by the soil. Therefore, the rise in ground water level may be directly proportional to the rainfall. However, this response depends on several factors including permeability, slope angle, rainfall intensity and depth to water table.

Based on records of storm response at four other sites and the above factors, Skempton et al. (1989) deduced an approximation for storm response at Mam Tor as follows;

$\Delta h / R = 4.5$ for 100 mm in 10 days

$\Delta h / R = 5.0$ for 120 mm in 6 days

where, Δh is the rise in ground water level and R is the rainfall.

4.5 Landslide Movements

Radiocarbon dating of roots in the fossil soil beneath the earthflow demonstrate that for over 3200 years the Mam Tor landslide movements have been taking place at an average rate of 10m per century (Skempton et al., 1989). However movements would occur as a series of small displacements in winter months of heavy rainfall. Records of movement in the present century (in 1918, 1939, 1965, 1966 and 1977) indicate that slips leading to displacements typically about 0.3 m are still taking place. These movements occur on average at 4-year intervals, in the winter months of more than 200 mm rainfall.

Movements usually arise from reactivation of the middle and the bottom portion of the landslide, revealed by tension cracks in or above the 'upper' road, accompanied by subsidence and outward displacements. More rarely, as in December 1965, almost the entire landslide is reactivated. Movements of the lower road are consistently less than at the upper road, an observation consistent with the existence of compression ridges. Forward movements of the toe are therefore smaller than at the upper road, though on a large time scale the difference cannot be great, and clear proof of advance of the toe in recent times is provided by slide debris encroaching on Blacketlay barn (Skempton et al., 1989).

4.6 Deformation Analyses

In this study, deformation analyses in response to the changes in ground water level due to a winter rainstorm have been carried out, incorporating the deformation rate-dependent residual strength parameters for the shear zone. Basic material properties were obtained from Skempton et al. (1989) and are tabulated in Table 4.1 and 4.2.

The finite element program *PISA* (Program for Incremental Stress Analysis) developed at the University of Alberta (Chan and Morgenstern, 1992) has been used for the deformation analyses. The finite element mesh consisting of 340 elements (8 noded quadrilateral and 6 noded triangular elements)is given in Figure 4.6 for the cross section shown in Figure 4.2. Plane strain conditions are assumed with known pore pressure values throughout the duration. The interpolation technique proposed by De Alencar et al. (1992) was implemented here, in order to prescribe the pore pressure at each integration point in the finite element mesh for each time step.

All materials were considered to behave according to the elastic-plastic non-associated Mohr-Coulomb model, except for the shear zone where an additional rate dependence is incorporated into the residual friction angle. The elastic-plastic model as described in Chapter III is used here. Figure 4.4 was used to deduce a relationship between residual strength parameters and deformation rates for sheared Edale Shale which indicates that when the strain rate is increased by ten times there is an increase of 1.5% in the residual shear strength. This implies the rate hardening parameter, b, of 0.007. The reference plastic strain rate, $\dot{\varepsilon}^p_o$, is taken as 0.0001 /day.

Mam Tor beds at 100m to the left of the crest of the scarp are assumed to be unaffected by the landslide movements. Thus, the left boundary of the mesh is defined 100m from the crest. Similarly, 100m from the right side of the toe is defined as the other vertical boundary of the mesh. The bottom boundary of the mesh is defined at 130 m below the toe, where no movements are assumed to have occurred.

The water level data as seen from Figure 4.5 and Table 4.3 have been reported as representing a typical seasonal response at the Mam Tor landslide for an average winter with a normal rainstorm. Considering the water levels at the end of October and the end of March to represent the minimum and maximum water levels respectively, the variation of ground water level throughout the year (April to September) was extrapolated (Table 4.4). The calculated distribution of pore pressure at the end of September is shown in Figure 4.7

4.7 Results and Conclusions

The calculated deformation pattern after a year and the progress of movements at the road throughout the year, starting from October, are given in Figures 4.8 and 4.9. Figure 4.8 shows that for such a rainfall (average winter rainfall), the reactivation of movements are confined to a portion of the slip mass, with a small amount of movement at the toe area. Figure 4.9 shows the calculated accumulated movement at the road of 0.123 m, which indicates high rates of movement during winter months (Figure 4.10). As a result of the changes in deformation rate, the mobilized value of residual friction angle varies between 14° and 14.2°, which is in agreement with calculations performed by Skempton et al. (1989). In general, 0.123 m of movement per year results in about 12 m per century which is of the same order as the observations. Movements near the toe of the landslide are consistently less than at the upper road, an observation consistent with the existence of compression ridges. The calculated horizontal strain contours, as shown in Figure 4.11, indicate a zone with a horizontal compressive strain of 10% near the toe, which is in agreement with Skempton's observation.

Figure 4.12 shows maximum shear strain contours after a year (1977) of average rainfall. The shear strains are confined to the 1-2m thick shear zone. The yield zone is indicated by the shaded area in Figure 4.13.

If the clay in the shear zone were modeled with a rate-independent model, the movements at the road would be as shown by the dotted line in Figure 4.9. This implies that about 10% of the landslide movements due to ground water fluctuations are controlled by the rate effects on the residual strength. In addition, when the rate-independent model is used to model the shear zone, the magnitude of movement is about 0.123m in the first month. This is a considerable amount and therefore, it is difficult to say that the slide is stable. However, if the rate-dependent model is used, there is a damping effect; thus, the movements are controlled initially and continue over time at slower rates. As reported by Skempton et al. (1989), a reactivation of landslide occurs only when the rainfall is extremely heavy. Therefore, the calculated response from the rate-dependent model is much more realistic than that from the rate-independent model.

The overall similarity in observations and calculations of deformation pattern for the deformation analysis confirms the appropriateness of the selected model to represent the shear strength parameters at the shear zone. A selection of appropriate properties to model the shear zone is important in this type of problem where the movements are controlled by, and confined to, a previously formed zone.

Table 4.1 Index properties of slide debris and shear zone

Material	boreholes	water content (w)	Liquid limit (L_l)	Plastic Limit (L_p)	Plasticy Index (I_p)	Clay Fraction(F_c)
clay matrix	1, 2	22	43	25	18	-
clay matrix, micaceous	1, 2	23	42	30	12	-
mudstone	1	14	40	24	16	-
head	1, 2	21	49	24	25	-
slide debris		21	44	25	19	-
shear zone	1, 2, 10	22	53	28	25	35

Table 4.2 Shear strength parameters of four main components

Material	Youngs Modulus (kPa)	Poisson's Ratio	Cohesion c' (kPa)	Friction Angle ϕ' * (°)	Unit weight γ (kN / m^3)
Slide debris	45000	.40	-	18 - 19	18.5
Shear Zone	45000	.40	-	14 - 15	20
Mamtor beds	900000	.46	20	37	20
Edale Shale	900000	.46	50	26	20

* ϕ' corresponds to $\sigma_n' = 200$ kPa

Table 4.3 Piezometric levels (after Skemptonet al., 1989)

borehole	ground surface/ (m od)	distance from toe of landslide(m)	seasonal response (m)	piezometric level February 1978: depth below ground (m)	probable error (m)	elevation (m od)
8	359.8	700	0.7	8.4	±0.2	351.4[c]
9[a]	309.6	520	1.3	8.6	±0.5	301.0[c]
1	280.2	390	2.0	0.5	0	279.7[b]
10	273.3	320	9(?)	1.8	±2.5	271.8[c]
pond	-	230	-	-	+0.3	265.4[b]

a Adjacent to borehole 4

b Measured.

c Estimated, with probable error as noted.

Table 4.4 Piezometric level data for 1977/1978 rainfall data

X distance	Piezometric level (m)											
(m)	Nov-01	Dec-01	Jan-01	Feb-01	Mar-01	Apr-01	May-01	Jun-01	ul-01	Aug-01	Sep-01	Oct-01
50	400	400	400	400	400	400	400	400	400	400	400	400
260	378	378	378	378	378	378	378	378	378	378	378	378
370	367.23	367.23	367.23	367.23	367.23	367.23	367.23	367.23	367.23	367.23	367.23	367.23
450	350.7	350.933	351.167	351.4	351.322	351.244	351.167	351.089	351.011	350.933	350.856	350.778
630	299.7	300.133	300.567	301	300.856	300.711	300.567	300.278	300.278	300.133	299.989	299.844
760	277	277.667	278.333	279	278.778	278.556	278.334	278.111	277.889	277.667	277.445	277.223
830	262.5	265.5	268.5	271.5	270.5	269.5	268.5	267.5	266.5	265.5	264.5	263.5
920	262	262	262	262	262	262	262	262	262	262	262	262
1050	247.5	247.5	247.5	247.5	247.5	247.5	247.5	247.5	247.5	247.5	247.5	247.5
1150	230	230	230	230	230	230	230	230	230	230	230	230
1250	230	230	230	230	230	230	230	230	230	230	230	230

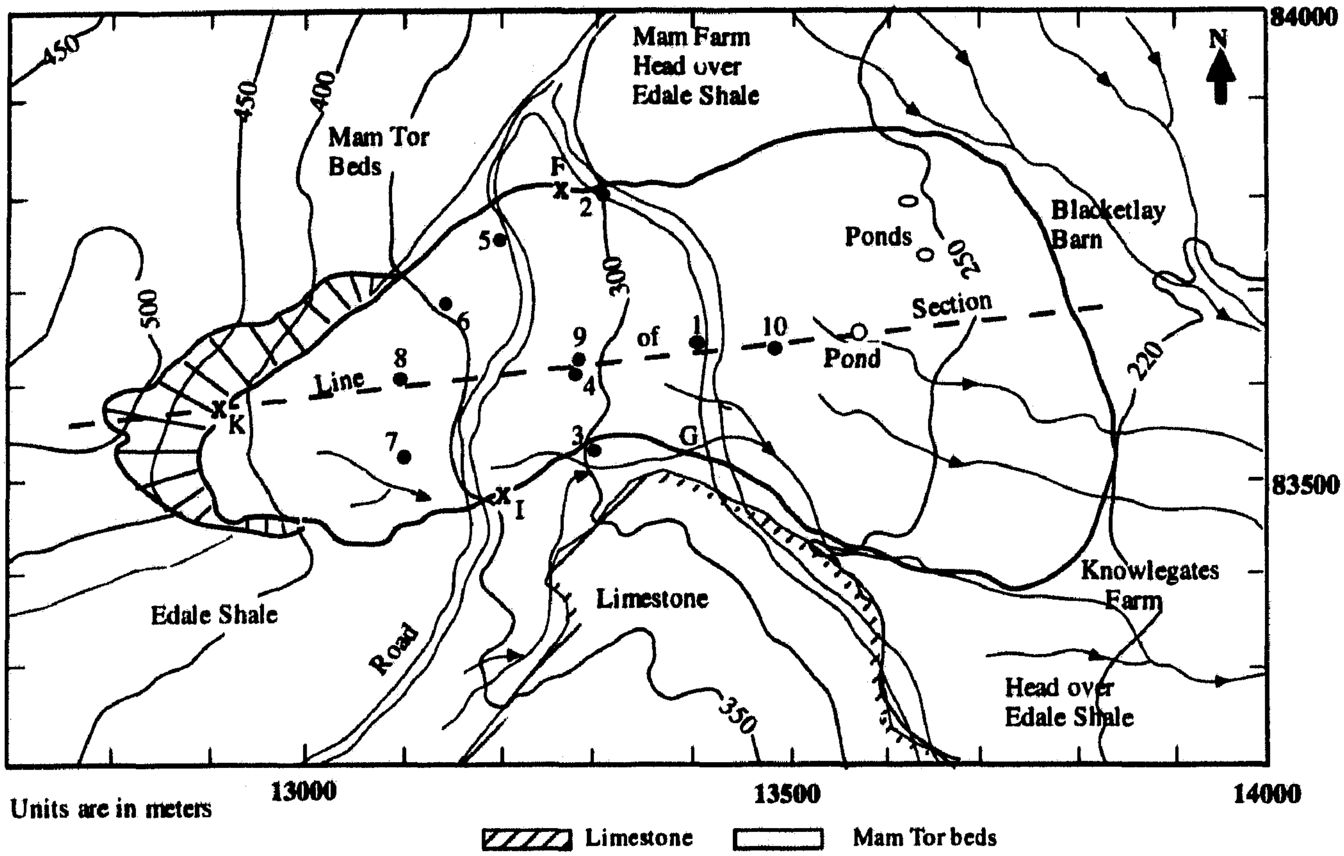

Figure 4.1 Plan of Mam Tor Landslide (after Stevenson, 1972)

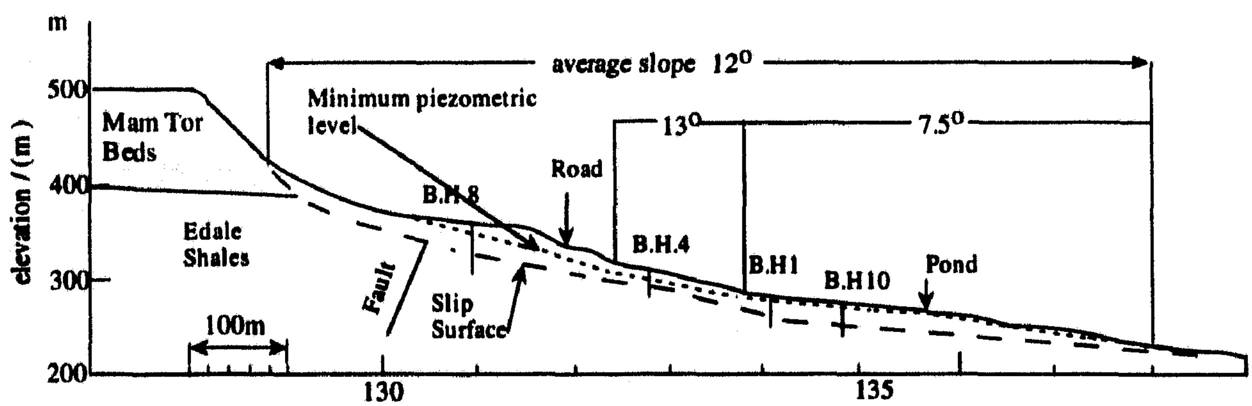

Figure 4.2 Longitudinal section (after Skempton et al., 1989)

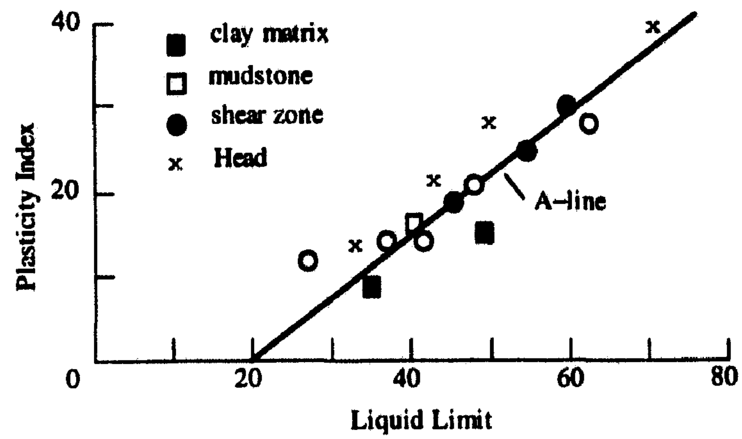

Figure 4.3 Plasticity chart for slide debris andshear zone (after Skempton et al., 1989)

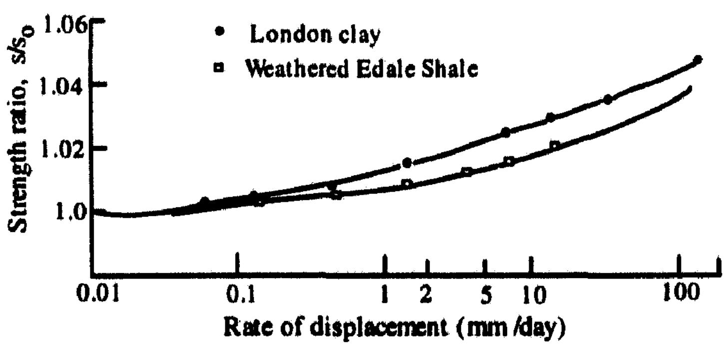

Figure 4.4 Relation between residual strength and of displacement (after Skempton et al., 1989)

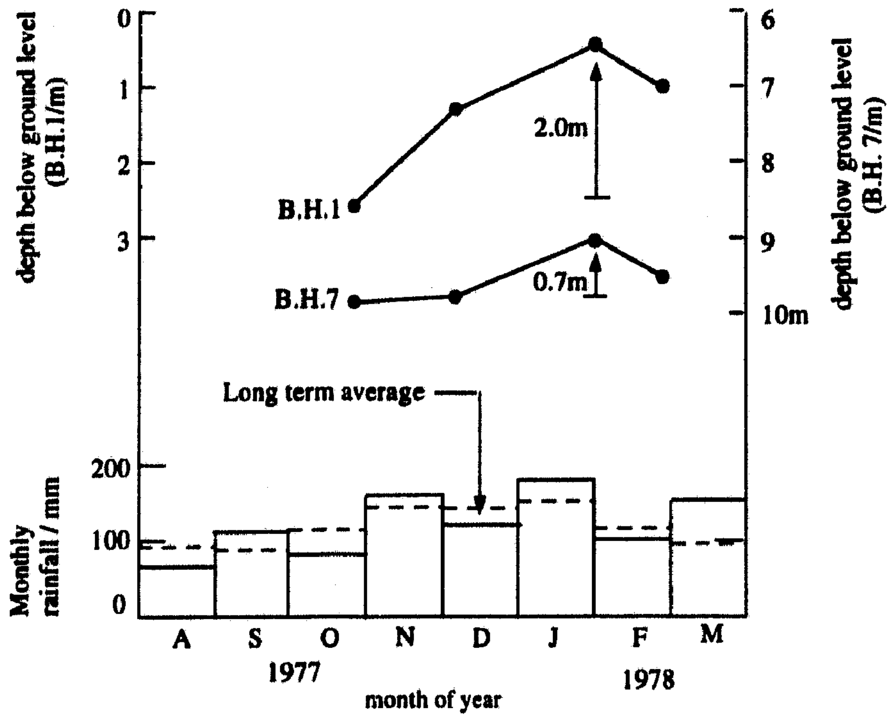

Figure 4.5 Piezometric levels, Mam Tor landslide

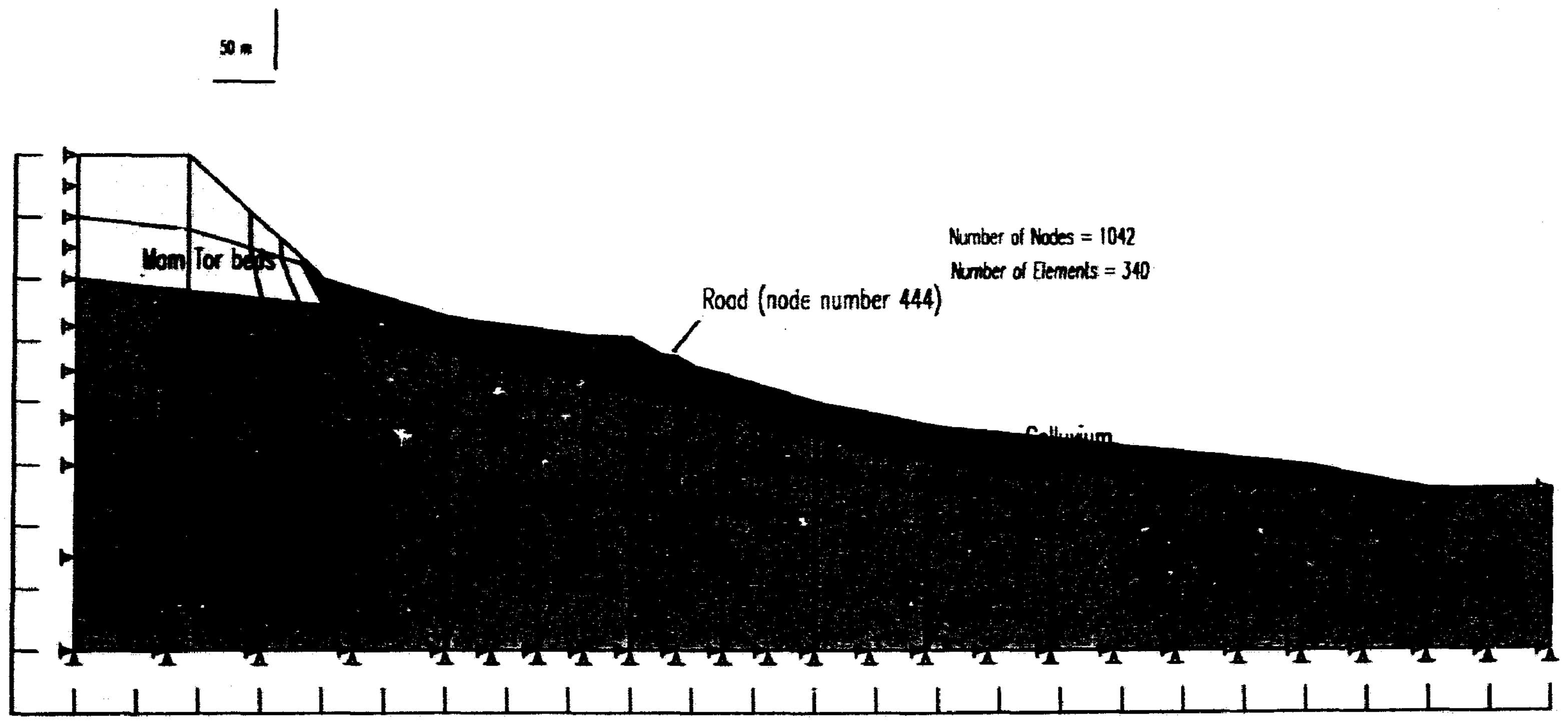

Figure 4.6 Finite element discritization of the Mam Tor Landslide

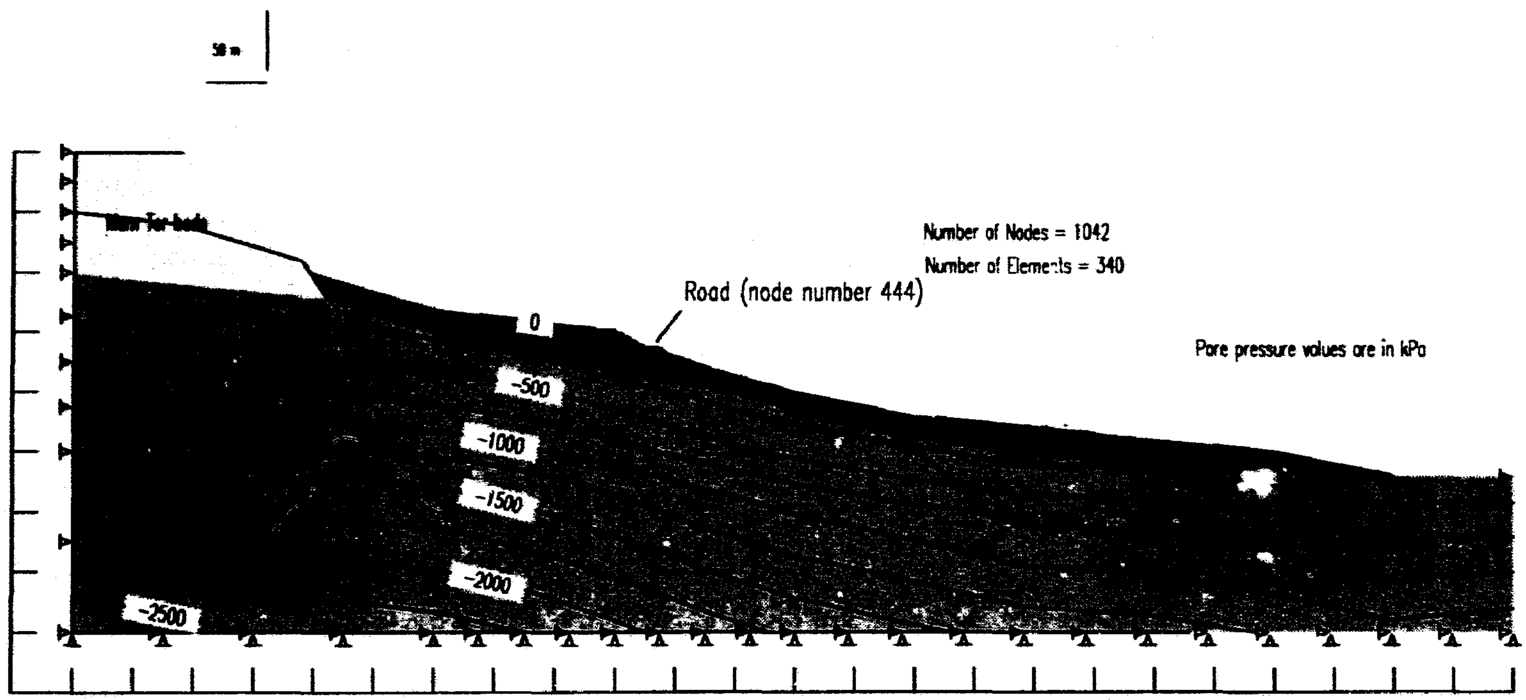

Figure 4.7 Pore water pressure contours

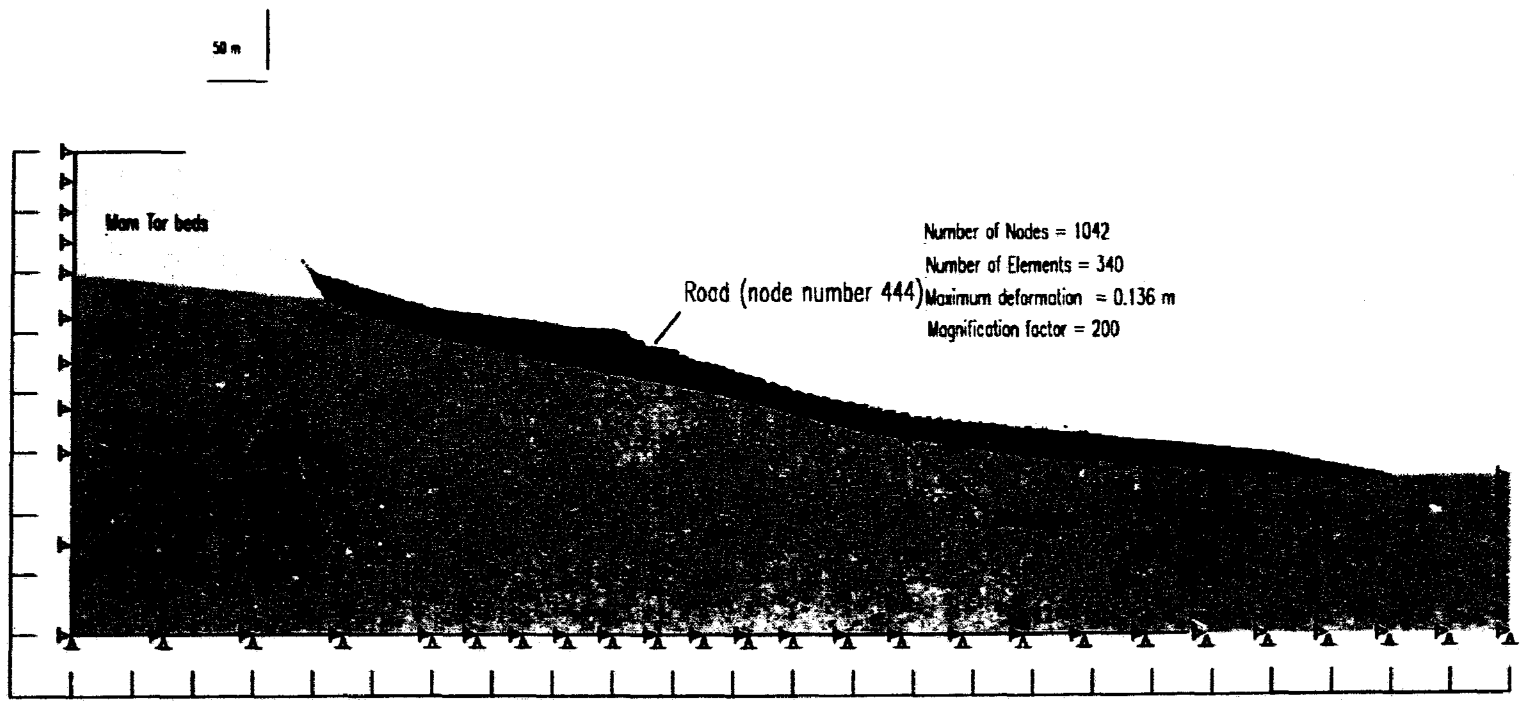

Figure 4.8 Displacement vectors after a year of average rainfall

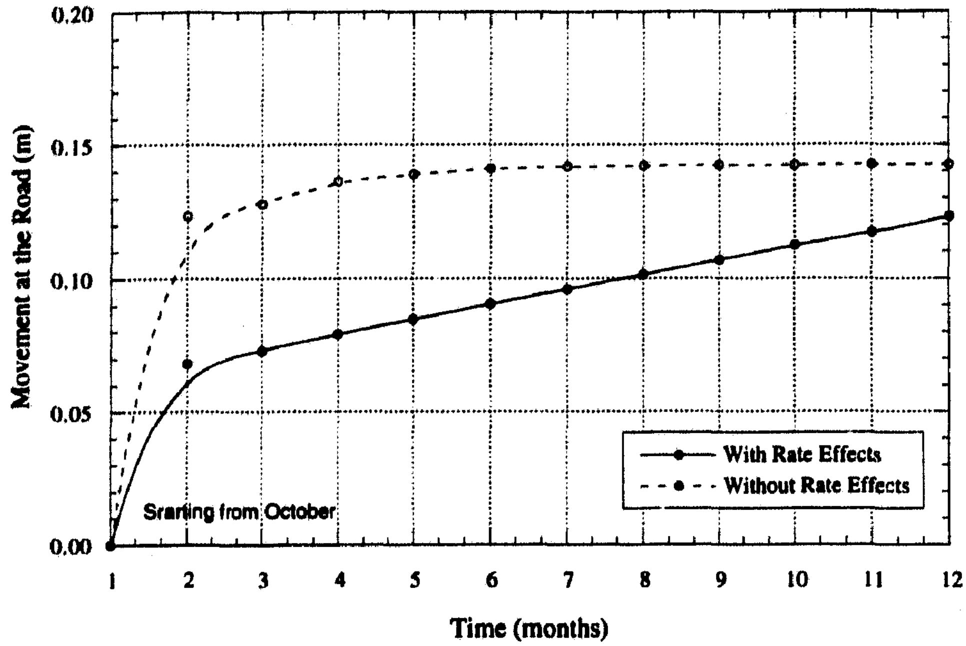

Figure 4.9 Movements at the road for an average yearly rainfall

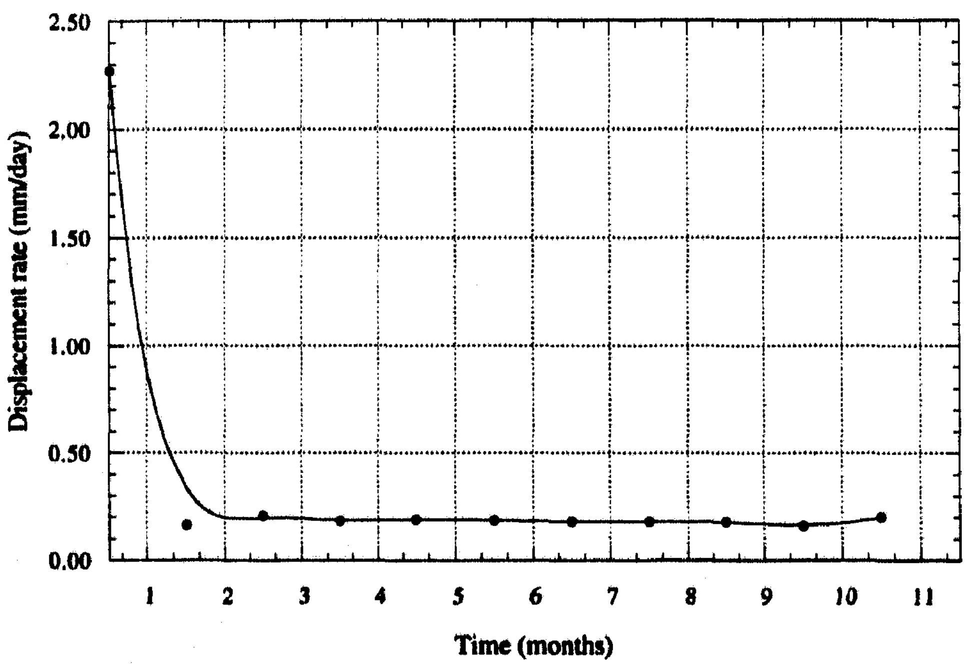

Figure 4.10 Displacement rate at the road for an average yearly rainfall

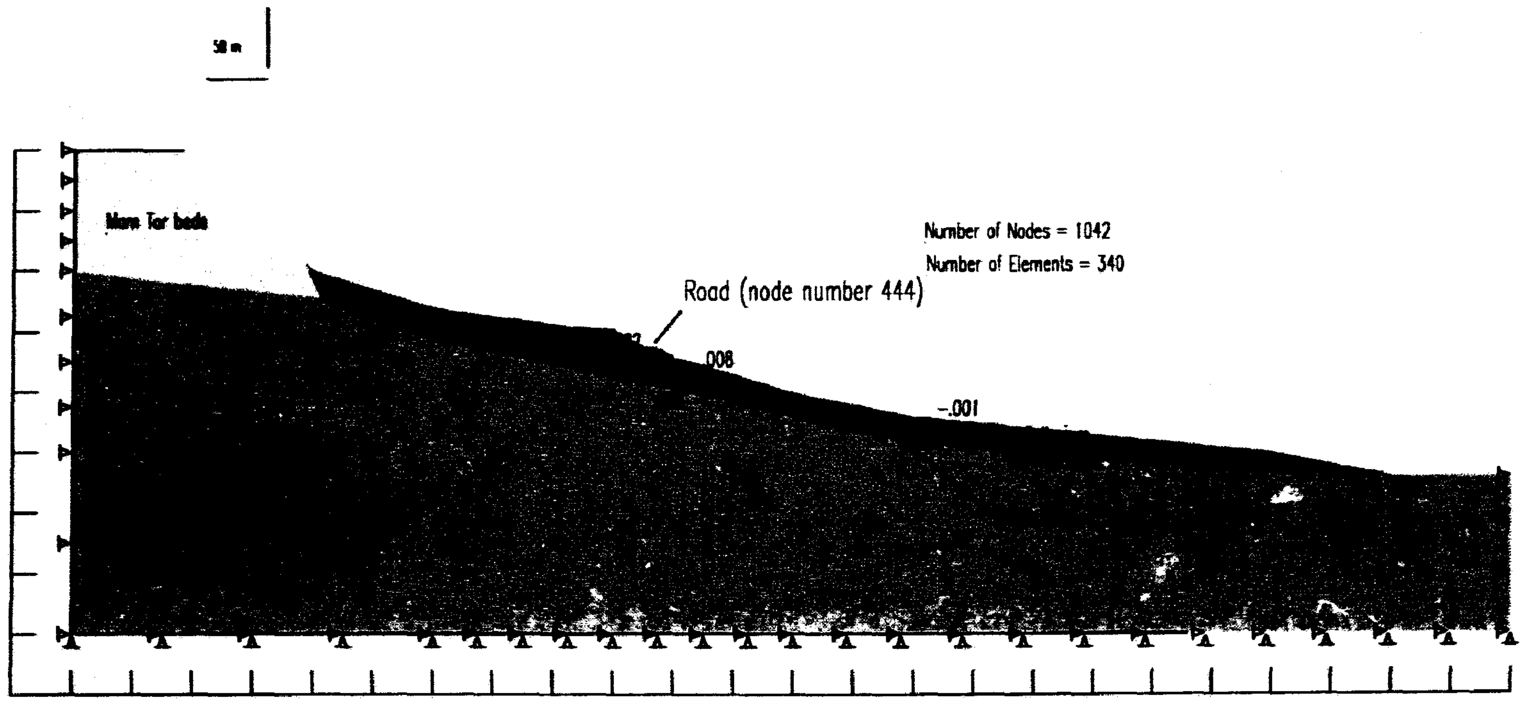

Figure 4.11 Horizontal strain contours

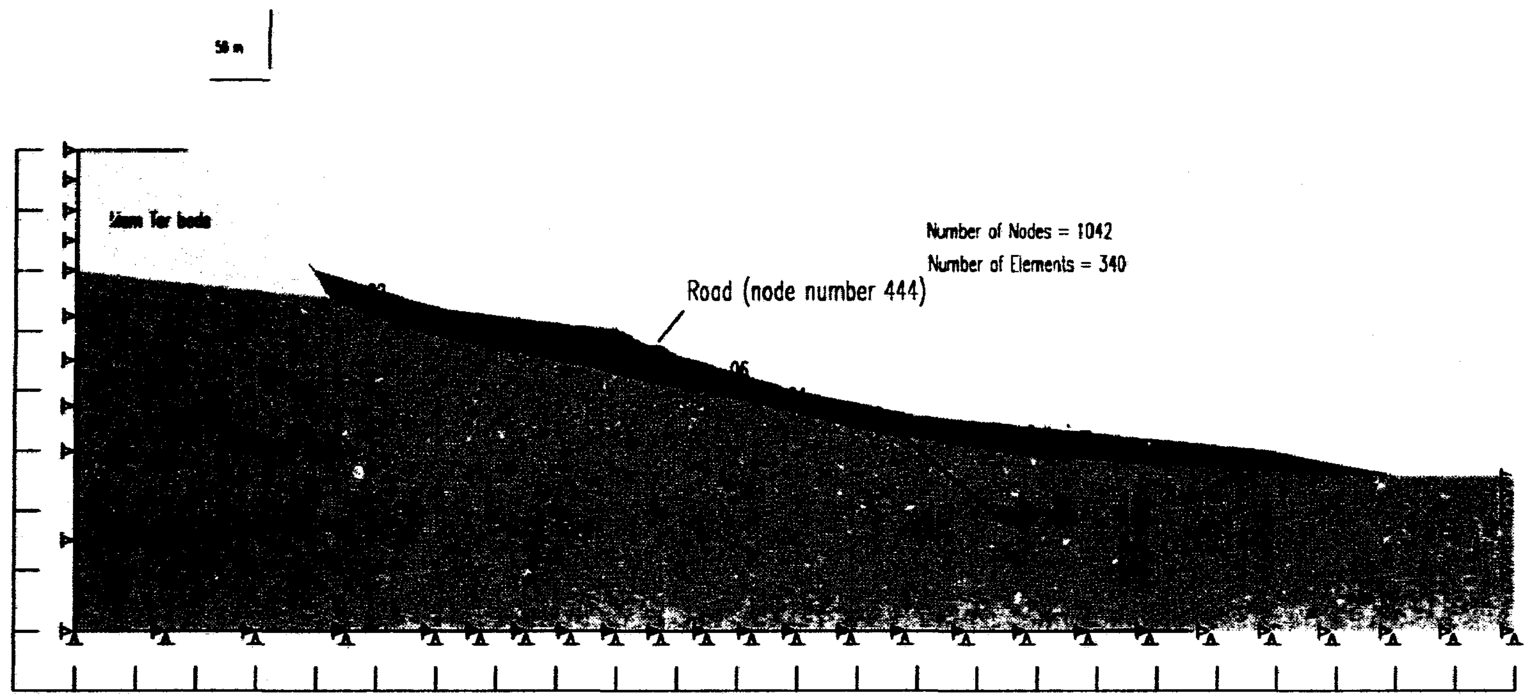

Figure 4.12 Maximum shear strain contours

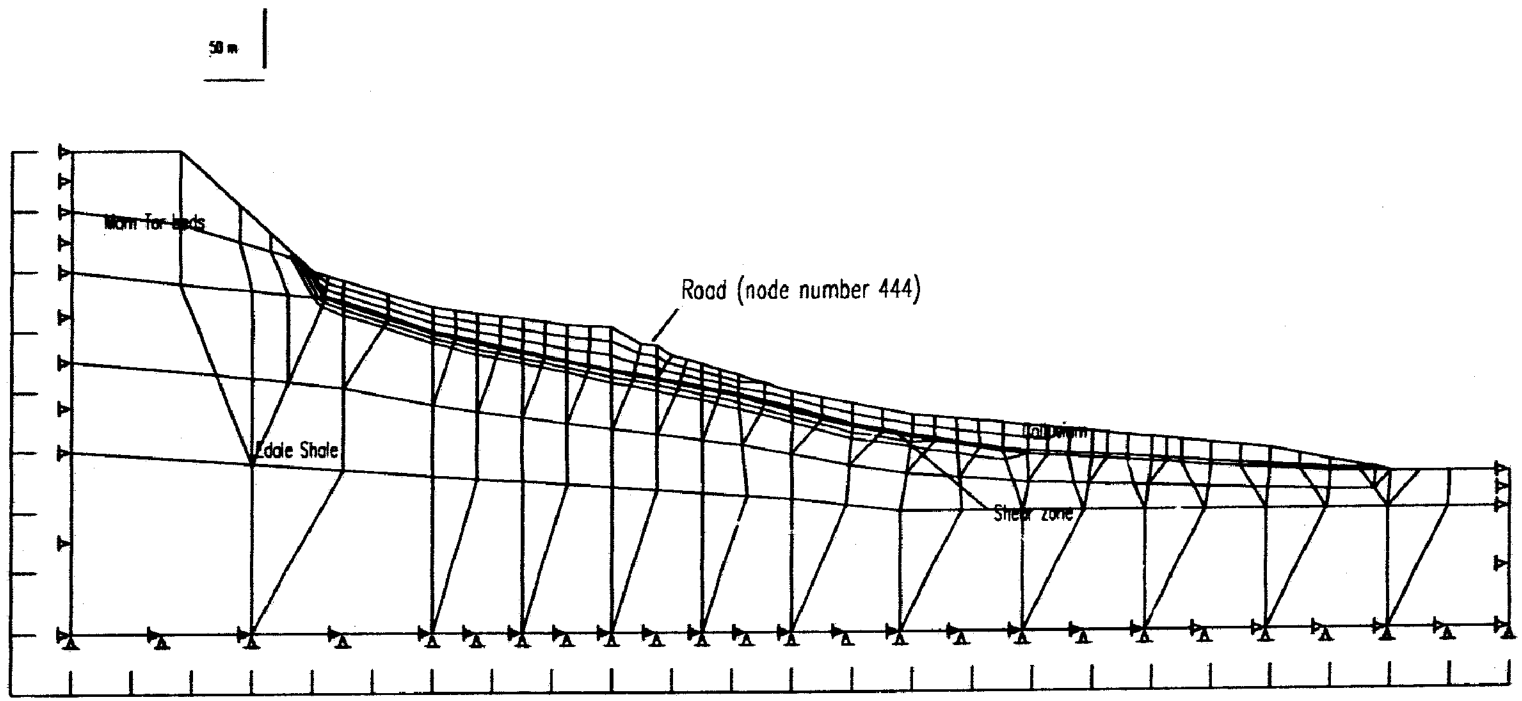

Figure 4.13 Yield zone

CHAPTER 5

SALLEDES TEST EMBANKMENTS ON UNSTABLE SLOPES

5.1 Introduction

The construction of highways and railways in France frequently poses problems from the behavior of embankments built on natural unstable slopes. Numerous difficulties have been encountered during construction of large highways, in spite of the anticipation of potential problems. There is general knowledge that localized pre-existing slip surfaces are susceptible to reactivation.

The analysis and estimation of the development of slow deformations of highway and railway embankments are largely dependent on an appreciation of safety and the consequences of these conditions. The warning levels with respect to the speed of the displacements and safety factors are to be defined. In order to attempt to provide answers to these problems and to furnish complete experimental evidence, the Central Laboratory of Bridges and Roadways has been involved in a series of large scale experiments since 1977 at Salledes, near Clermont-Ferrand.

A first embankment, named Embankment A, was constructed in March 1978 at a rate corresponding to an actual highway embankment construction rate until failure. The details on this experiment can be found in Blondeau et al. (1983). A second embankment, Embankment B, was constructed in phases between March and September 1980.

This chapter gives the results of deformation analyses carried out on the Salledes 'B' experimental embankment. The ultimate height of this embankment was 3.4 m. The results are compared with field measurements.

5.2 Review of Site Geology

The site is underlain by the Comte sedimentary group to the west and the Low Livradois crystalline group to the east. The subsoil conditions at the site basically comprise a sedimentary formation: both disturbed and undisturbed marl. It has been found that the formation of a volcanic dome at the top of the slope, altitude of 676 m, (Figure 5.1) shifted the upper marl layer and generated a network of fissures at its proximity. The volcanic dome is alkaline basalt and is surrounded by debris and colluvium. The structure of the site is affected by periglacial conditions during the Quaternary. Cycles of freeze and thaw produce an accumulation of large blocks which are submerged by the mud resulting from solifluction. Erosion, at different times, is made evident in the zones below the basalt, thus creating an asymmetric pattern from one slope to another (Cartier and Pouget, 1988).

5.3 Hydrological Conditions

The piezometric observations indicate that all piezometers react quickly and at the same time to changes in ground water conditions. Recharge occurs suddenly, in one to two weeks. When evapotranspiration is not sufficient, water infiltrates deeply into the soil until it reaches the water table and constitutes a sudden recharge of the entire slope at the same time. The observations of pore pressure measurements indicate the existence of a flow parallel to the slope up to a depth of 6 m. At deeper levels there exists a downward flow.

5.4 Description of Geotechnical Characteristics of Sub-soil

In general, the site consists of a layer of marl colluvium overlying disturbed, fissured marl (Figure 5.2). The underlying layer of compacted marl is found from a depth of about 7 m.

Marl colluvium is in the form of beige brown clay, very heterogeneous with englomerations of chalk and small basaltic elements and sandy layers. The thickness varies between 2 to 4 m. It is difficult to distinguish the level of contact with the disturbed marl below. The latter is, in general, very plastic with mottled colors: beige, light brown to green. Chalk particles and sandy formations are encountered as well. Marl, and calcareous marl are horizontally bedded and are encountered at 5 to 7 m deep. These formations are layers of alternating clay, green and very compacted, and bands of very stiff chalk (thickness $\approx$ 10 m) and they are generally highly altered at the top, up to one to two meters. A complete description of geotechnical properties of these soils is given in Cartier and Pouget (1988). Summarized properties which are relevant to the deformation analysis are shown in Table 5.1. The strength parameters for the colluvium were obtained from consolidated undrained triaxial compression tests under stress levels similar to the field stresses. The residual strength parameters for the shear zone were obtained from direct shear test results. The rate-dependent soil parameters were selected based on Figure 2.17, taking into consideration of the Plasticity Index and the relatively higher field displacement rates.

5.5 Instrumentation and Construction of Test Embankment B

Instrumentation as shown in Figure 5.3 has been installed to measure the changes in ground water conditions, total stresses and displacements. The construction of the embankment took place in two phases. In the first phase the embankment was constructed to a 3 m height in 5 days. The second phase began after 6 months when a further 0.4 m was added. The plan area of the embankment is 70 m in length and 13 m in width at its upper level. Fill material was alluvial gravel with a compacted unit weight of 22.5 kN/m^3. Layers of about 0.5 m were placed daily (Figure 5.4). Ground water pressure conditions prior to construction are plotted in Figures 5.5 and 5.6. Observation of piezometric readings indicate a flow parallel to the slope up to a depth of about 6 m. At deeper levels there exists a downward flow which is illustrated by the equipotentials in Figure 5.6. Pore pressure measurements during the first phase of construction (Figure 5.7) shows a maximum change of 4 kPa at depths of 12 m.

The pore pressure measurements, as well as evolution of movements for up to a period of six years, have been recorded by Cartier and Pouget (1988). The changes in pore pressure during this period are found to be directly related to the rainfall. At a depth of 6 m the amplitude of variation of pore pressure is significant, from 5.7 to 51.5 kPa.

5.6 Field Movements

The movements during and after construction of the embankment have been measured using inclinometers located up to about 60 m from the toe of the embankment. The horizontal movement at the toe during construction (as measured from slope inclinometer G1Q5) is plotted with height of the fill and time in Figures 5.8 and 5.9 respectively. They show a typical behavior of approaching failure if the construction is continued. The variation of pore pressure beneath the embankment during construction is rather limited to a maximum of 4 kPa, which is an indication of relatively high permeability sub-soil. The movements at the ground surface as measured from inclinometers G1Q5, G4R5, G6S6, F9N9 and G7T5 (locations are shown in Figure 5.3) are plotted in Figure 5.10 for five years after construction. These movements indicate a direct correlation with the pore pressure variations throughout the duration.

5.7 Deformation analysis

Finite element analyses have been carried out to understand the deformation mechanism beneath the test embankment B and hence in these slopes. The purposes of the analyses are to identify the factors which influence the deformation mechanism and to combine parameters, within the acceptable range of values for each material that would satisfactorily reproduce the field observations. The disturbed and sheared marl layer is modeled according to the rate-dependent non-associated Mohr Coulomb model (Chapter 3). The finite element mesh shown in Figure 5.11 was used for the analyses.

The first stage of loading aimed to simulate the initial gravity stress field, i.e. before the embankment construction. The exact magnitude of these stresses at every point is not known, but K_o is assumed to be around 0.85, although it is well known that K_o values reflect the local stress history and may vary from point to point. The initial stress field was applied by a 'switch on gravity' process. The stresses were generated due to the application of gravity forces, which are dependent on the unit weight of the material, and the horizontal stresses were calculated as a function of the Poisson's ratio (υ) of the material. The value of K_o is equal to $\upsilon/(1-\upsilon)$ for an isotropic, homogeneous, linear elastic material. Following the switch-on gravity stage, the construction sequence is carefully followed in these analyses and the measured pore pressure data are used as input to the analysis.

Effective stress analyses were performed using the pore pressure condition in the entire domain as an input for the analysis. The pore pressure at each integration point was interpolated from the measured piezometric data using the scheme proposed by De Alencar et al. (1992).

In the effective stress analysis, both colluvium and weathered marl (shear zone) were modeled according to the Mohr Coulomb model except for the first layer of loading. The use of elasto-plastic models for the first layer of loading resulted in higher initial movements, irrespective of the selected friction angles. In other words, the assumption of linear elastic behavior during the first layer of loading, where the strains are small, resulted in a good match to the field behavior.

A first series of analyses were performed by using fixed properties for the colluvium with a cohesion of 5 kPa and a friction angle of 15°. To see the influence of properties of the shear zone on the displacements, its parameters were varied within reasonable limits. The modulus and the static friction angle of the shear zone were varied as shown in Figure 5.12. The results show that a change in properties of the shear zone alone would not be sufficient to simulate the field movements. Among the various combinations of parameters analysis, T9 was found to give a similar shape for the field movement pattern and therefore parameters from T9, an initial modulus of 8,000 kPa and a static friction angle of 16°, were selected for further analyses. The material parameters used in the parametric study are tabulated in Table 5.2

The parametric variations of the shear zone alone were not capable of influencing the calculated movements as required. In the next series of analyses the initial modulus of the colluvium was varied between 10,000 kPa to 30,000 kPa while keeping the friction angle at 15°. Figure 5.13 shows that the increase in modulus of colluvium from 10,000 kPa to 30,000 kPa is able to move the movement pattern closer to the field values. Based on the results of T12, approximate values of soil properties for colluvium were chosen as ϕ_C=15°, E_C=30,000 kPa, and for the shear zone ϕ_S=16° and E_S=8,000 kPa were selected. Although this combination of parameters resulted in a good fit to the field movements at the toe, the friction angle defined for the shear zone is higher than that for the colluvium. This is not a reasonable assumption because the majority of shear displacements has occurred across the shear zone, due to its lower shear resistance. Therefore, the analyses were extended to have meaningful values for the friction angle of these materials while maintaining good agreement with the field movements.

In a third series of analyses (Figure 5.14) friction angles of both materials were changed, but results did not lead to a better simulation. Further trials were carried out keeping fixed properties for the shear zone at ϕ_S=13° , E_S=1,000 kPa and changing the properties of colluvium (Figure 5.15). Trial 21, with ϕ_C=13°, E_C=45,000 kPa, ϕ_S=13° and E_S=1,000 kPa, gave a reasonable fit to the field measurements among all the tested combinations.

Since the field observations indicate that a majority of the slip passes through the weathered marl (referred to as the shear zone in the discussion), a higher mobilized friction could be expected for the colluvium. Therefore, further trials were carried out by decreasing the friction of the shear zone and increasing the friction of the colluvium (Figure 5.16 and 5.17). Figure 5.17 shows the effect of a change in friction for both colluvium and the shear zone material. The T21-14 with material properties ϕ_C=15°, E_C=50,000 kPa, ϕ_S=11° and E_S=1,000 kPa, would be considered as the best approximation for the parametric combinations so far achieved. The selected values for the friction angles for the shear zone and the colluvium agree well with the laboratory values (Table 5.1).

Interpretation of pressuremeter data and cone test data for the colluvium indicate a Young's modulus in the range of 36,000 - 40,000 kPa. Therefore, the value used in the parametric analysis T21-14 is too high compared to the field data. Further trials were carried out using a reasonable value of Ec = 45,000 kPa (an average of parametric analysis value and field value) and changing the friction angles of both colluvium and shear zone. The use of ϕ_C=16°, E_C=45,000 kPa, ϕ_S=13° and E_S=1,000 kPa gave a better fit with the field movements (Figure 5.18). According to the laboratory values and interpreted values from field tests, this set of parameters is found within the acceptable range.

Based on the results of the numerical analysis of the Salledes test embankment B, it can be concluded that the use of elasto-plastic models (both rate-dependent and rate-independent) for the deforming body, i.e., shear zone, and overlying colluvium alone is not adequate to reproduce the field movement mechanism. In general, the calculations do not result in an unstable mechanism, whereas field movements show instability when the fifth layer is placed. Another observation is that when there is no construction taking place the calculations show a small movement, whereas the field movements in these intervals are significant.

The use of a hyperbolic stress strain relationship for the colluvium, which could result in a less stiff material above the shear zone as the loading increases, will be considered as an alternative.

To improve the results of the finite element analysis, non-linear elastic (hyperbolic) model (Duncan and Chang, 1970) was used for the colluvium. The combination of material parameters is shown in Table 5.3. It is observed from the results (Figure 5.19) that during construction the estimate of the movements is improved. Therefore, Figure 5.19 shows the results of the analysis carried out using the strain rate-dependent model to the shear zone and the hyperbolic model to the colluvium.

The results obtained using the strain rate-dependent model to the shear zone and the hyperbolic model to the colluvium, are compared with those of the analysis carried out with a rate-independent elasto-plastic model using upper and lower limit values for the friction in the shear zone. It seems that the use of the rate-dependent model resulted in a better approximation to the field movements. The calculated displacement pattern is shown in Figure 5.20. The horizontal and maximum shear strain contours are plotted in the Figures 5.21 and 5.22. They show that the strains are concentrated in the disturbed marl (shear zone).

Analyses were extended to the period after construction, but the very large slips observed in the field were difficult to compute using the small deformation finite element analysis. It is noted that movements of about 10 cm were recorded in some locations within a fairly rapid period (Figure 5.10). Further improvements to the model were not considered.

5.8 Conclusions

1 The use of elasto-plastic models, both rate-dependent and rate-independent, for the shear zone and the colluvium is shown not to be adequate to simulate the construction movements.

2 When the colluvium is modeled by a nonlinear elastic hyperbolic model the results are improved.

3 The material properties selected based on the previous analyses are as follow:

Shear zone:	Young's Modulus	= 1000 kPa
	Poisson's ratio	= 0.46
	Residual friction angle	= 13°
	Rate hardening parameter	= 0.018
	Reference plastic strain rate	= 0.001 /day
Colluvium:	Young's Modulus	= 45000 kPa
	Poisson's ratio	= 0.35
	Residual friction angle	= 16°

4 Although the inclusion of rate effects on residual strength has improved the calculated behavior, there is not a great advantage for using it for this field case.

Table 5.1 Material properties

	w (%)	LL (%)	IP (%)	γ (kN/m^3)	E (kPa)	q_c (kPa)	c' (kPa)	ϕ' (°)	C_u (kPa)
Colluvium	40	50-55	70-80	17.5	500	2000	0	15-24	50-80
Weathered marl	40	50	60-70	16	900	2000-5000	0	9	0-50
Marl	40	40	80	18	6000	>8000	-	-	100
Fill				22.5					

Table 5.2 Material properties used in the parametric analyses

Analysis number	Material	E (kPa)	v	γ (kN/m³)	c' (kPa)	φ' (°)	b	$\dot{\varepsilon}_o^p$ (/day)
	Marl	1200000	.46	18	-	-	-	-
	Fill	10000	.46	22.5	-	-	-	-
	Colluvium	10000	.46	17.5	5	15	-	-
T6	Weathered marl	80000	.46	16	0	9	0.0185	.001
T7		10000				15		
T9		9000				16		
T10		8000				16		
	Weathered marl	8000	.46	16	0	16	0.0185	.001
T10	Colluvium	10000	.46	17.5	5	15	-	-
T11		20000				15		
T12		30000				15		
T13	Weathered marl	3000	.46	16	0	16	0.0185	.001
	Colluvium	50000	.46	17.5	5	15	-	-
T14	Weathered marl	1000	.46	16	0	14	0.0185	.001
	Colluvium	50000	.46	17.5	5	14	-	-
T15	Weathered marl	1000	.46	16	0	13	0.0185	.001
	Colluvium	50000	.46	17.5	5	13	-	-
T16	Weathered marl	1000	.46	16	0	12	0.0185	.001
	Colluvium	50000	.46	17.5	5	12	-	-
	Weathered marl	1000	.46	16	0	13	0.0185	.001
T17	Colluvium	50000	.46	17.5	5	13	-	-
T18		40000				13		
T19		40000				15		
T20		45000				15		
T21		45000				13		
T22		50000				11		

Table 5.2 (Contd.) Material properties used in the parametric analyses

Analysis number	Material	E (kPa)	v	γ (kN/m^3)	c' (kPa)	ϕ' (^{o})	b	$\dot{\varepsilon}_o^p$ (/day)
	Colluvium	45000	.46	17.5	5	13	-	-
T21-2	Weathered marl	1000	.46	16	0	9	0.0185	.001
T21-3		1000				10		
T21-4		1000				11		
T21-5		1000				12		
T21-6		1000				13		
T21-13	Weathered marl	1000	.46	16	0	12	0.0185	.001
	Colluvium	50000	.46	17.5	5	14	-	-
T21-14	Weathered marl	1000	.46	16	0	11	0.0185	.001
	Colluvium	50000	.46	17.5	5	15	-	-
T21-15	Weathered marl	1000	.46	16	0	10	0.0185	.001
	Colluvium	50000	.46	17.5	5	16	-	-
T21-16	Weathered marl	1000	.46	16	0	10	0.0185	.001
	Colluvium	55000	.46	17.5	5	16	-	-
T210-2	Weathered marl	1000	.46	16	0	13	0.0185	.001
	Colluvium	45000	.46	17.5	5	16	-	-

Table 5.3 Material parameter chosen for the deformation analysis

Material	E (kPa)	n	R_f	k	v	γ (kN/m^3)	c' (kPa)	ϕ' (^{o})	b	$\dot{\varepsilon}_o^p$ (/day)
Marl	1200000				.46	18.0	-	-	-	-
Fill	10000				.46	22.5	-	-	-	-
Colluvium 1	45000				.3	17.5	-	-	-	-
Colluvium 2	-	.35	.9	750	-	17.5	5	16		
Weathered marl	1000				.46	16.0	0	13	0.0185	.001

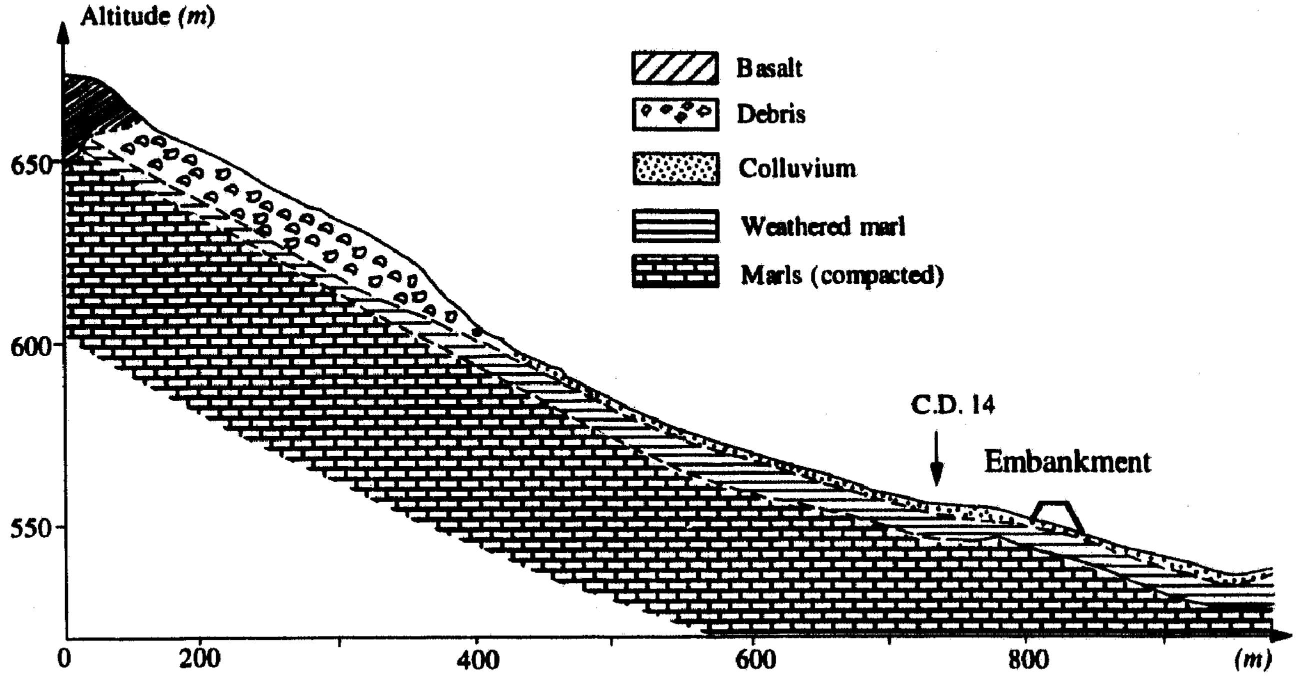

Figure 5.1 Geology of the site (after Cartier and Pouget, 1988)

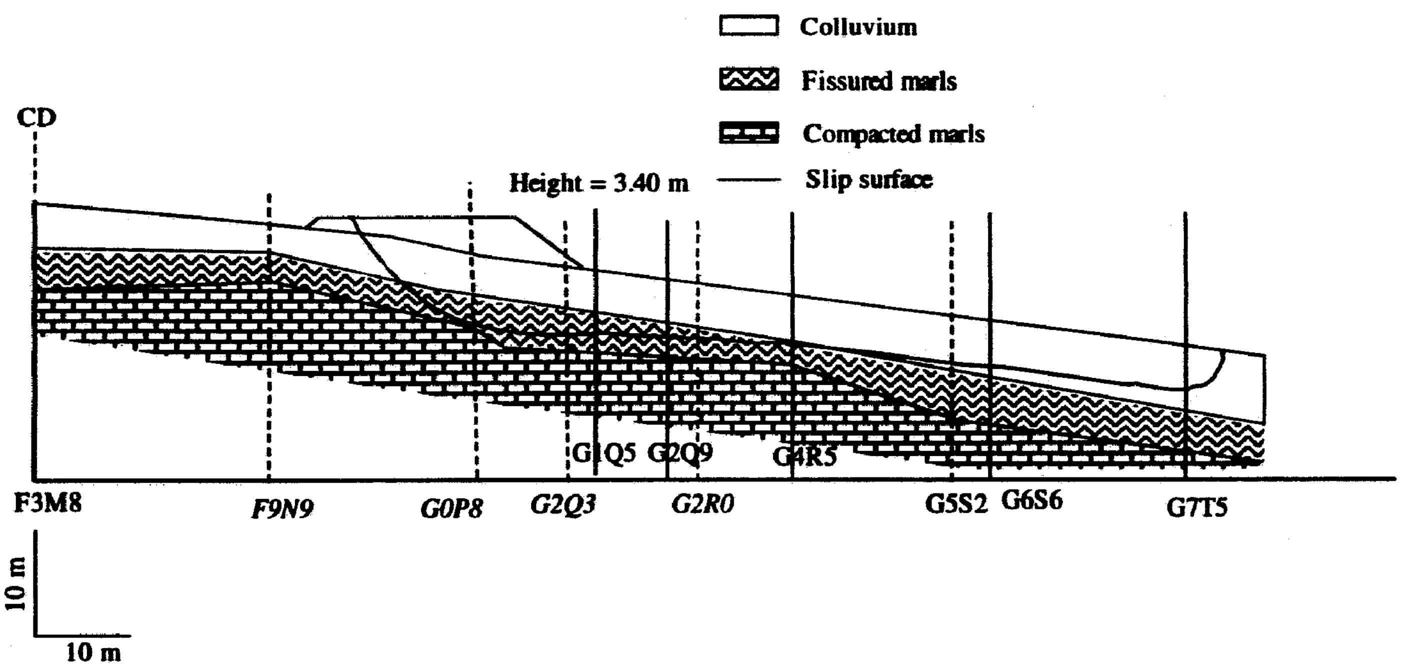

Figure 5.2 Cross section through centre of test embankment

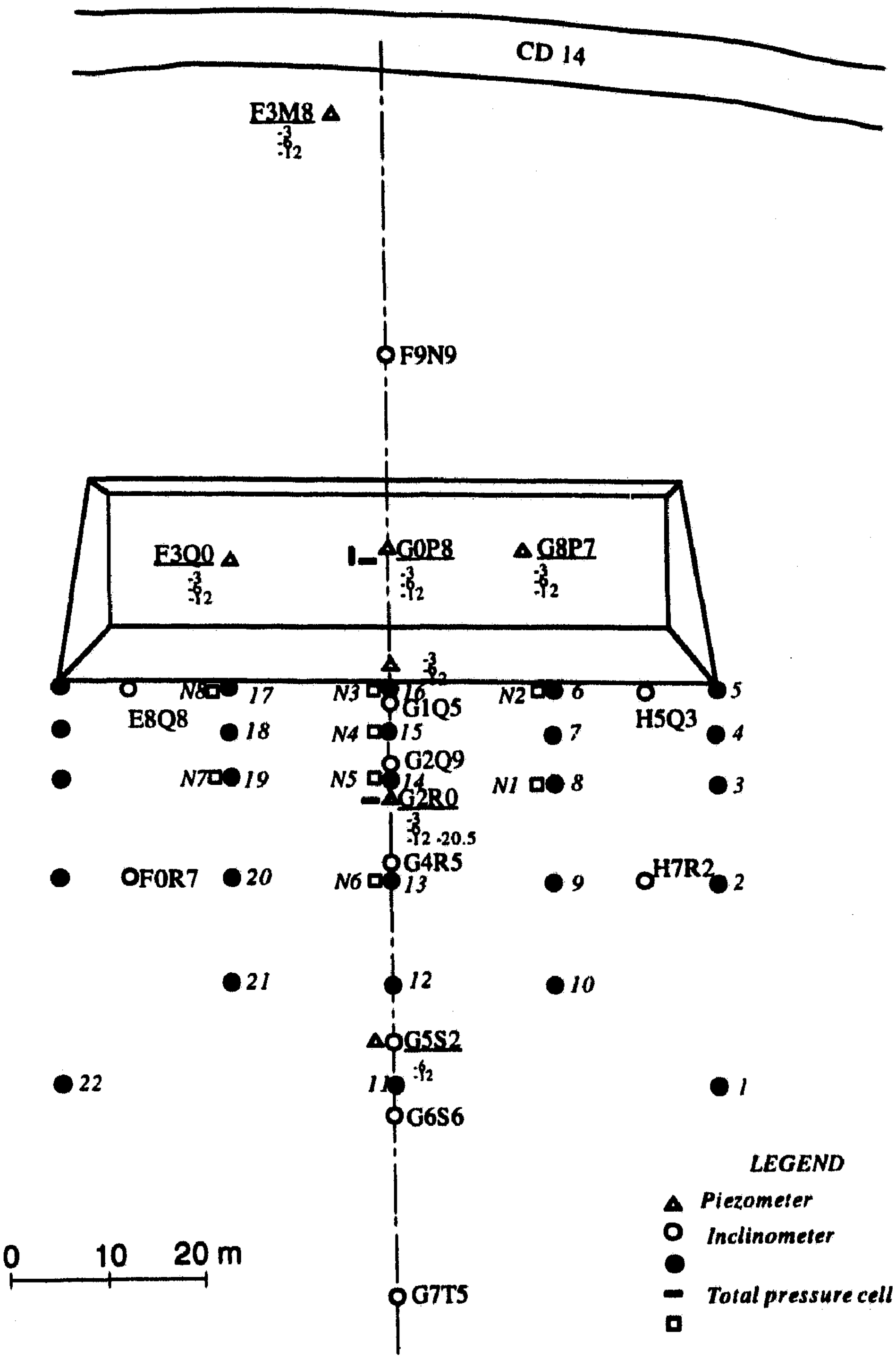

Figure 5.3 Plan of Instrumentation (after Cartier and Pouget, 1988)

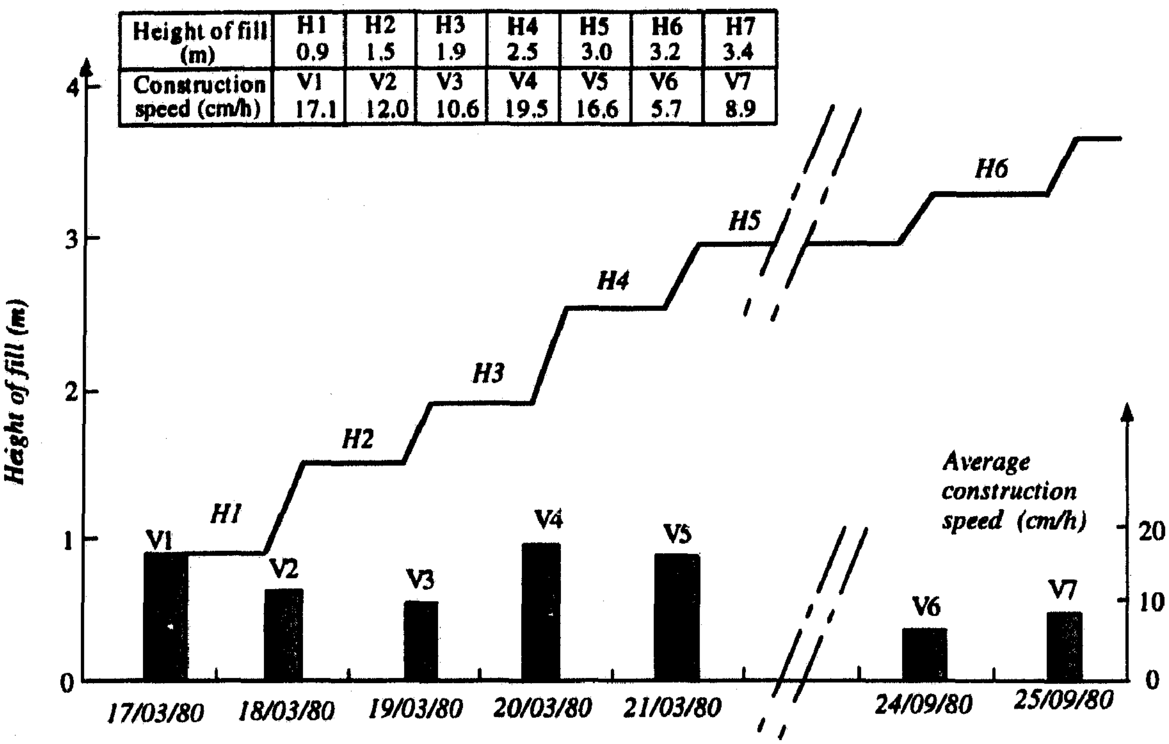

Height of fill (m)	H1 0.9	H2 1.5	H3 1.9	H4 2.5	H5 3.0	H6 3.2	H7 3.4
Construction speed (cm/h)	V1 17.1	V2 12.0	V3 10.6	V4 19.5	V5 16.6	V6 5.7	V7 8.9

Figure 5.4 Construction details of test embankment B

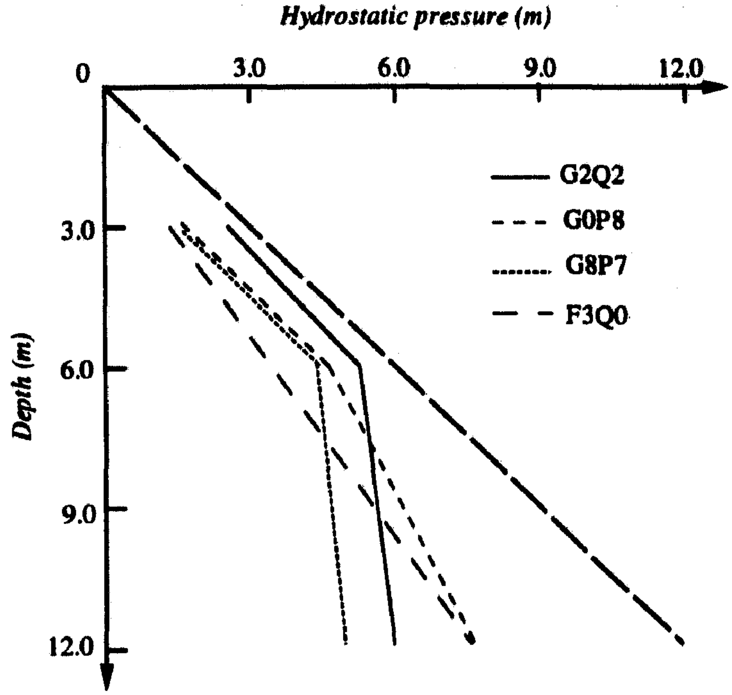

Figure 5.5 Piezometric data before construction(after Cartier and Pouget, 1988)

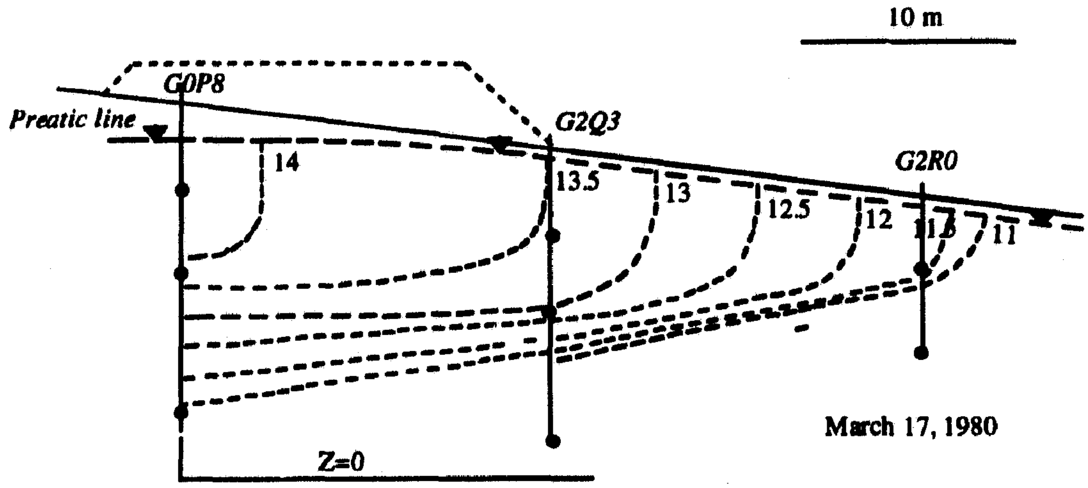

Figure 5.6 Distribution of equipotential lines beneath the embankment B
(after Cartier and Pouget, 1988)

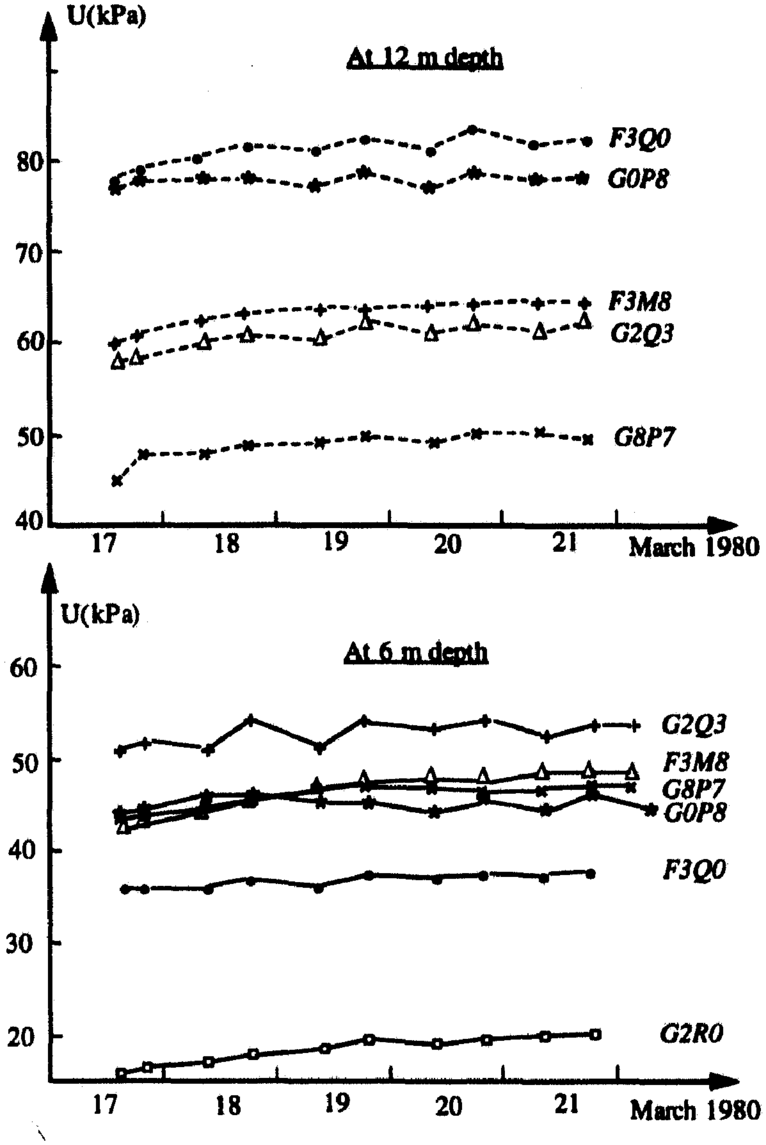

Figure 5.7 Distribution of pore pressure beneath embankment B during construction

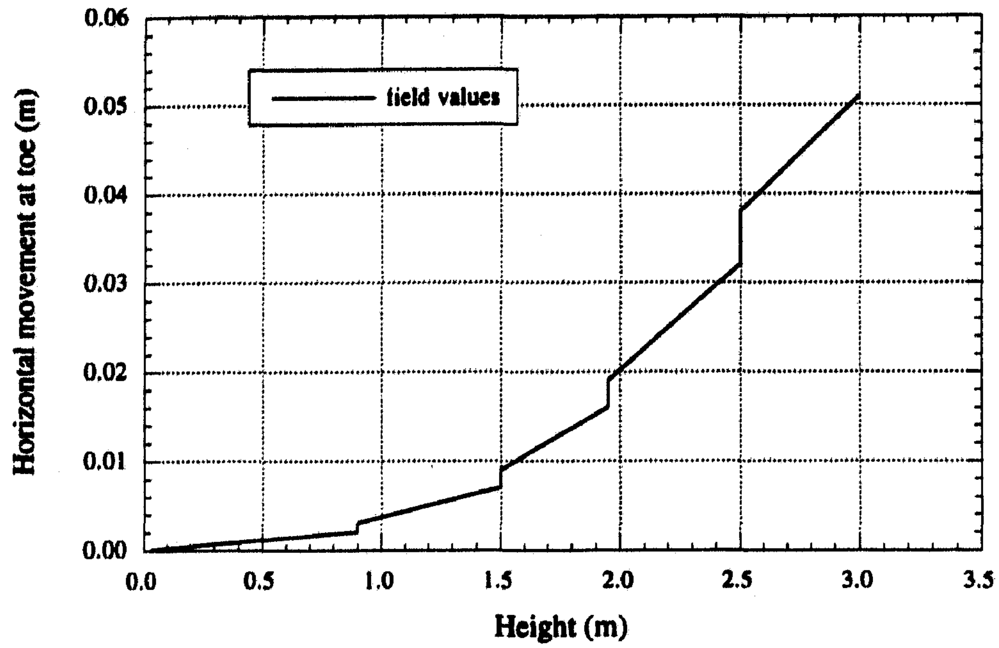

Figure 5.8 Movements at the toe during construction

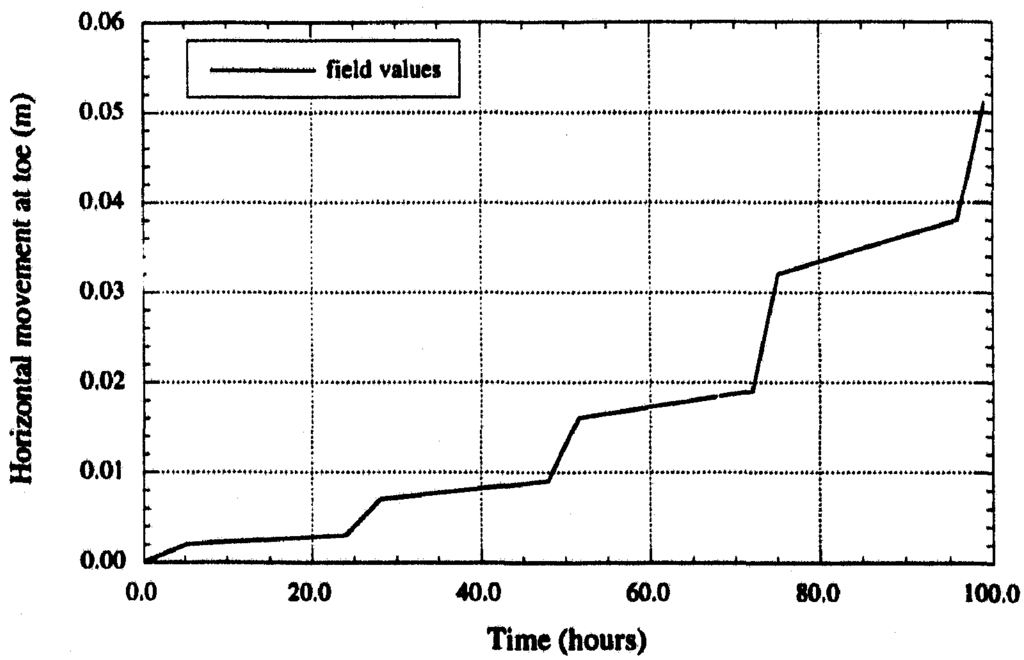

Figure 5.9 Movements at the toe during construction

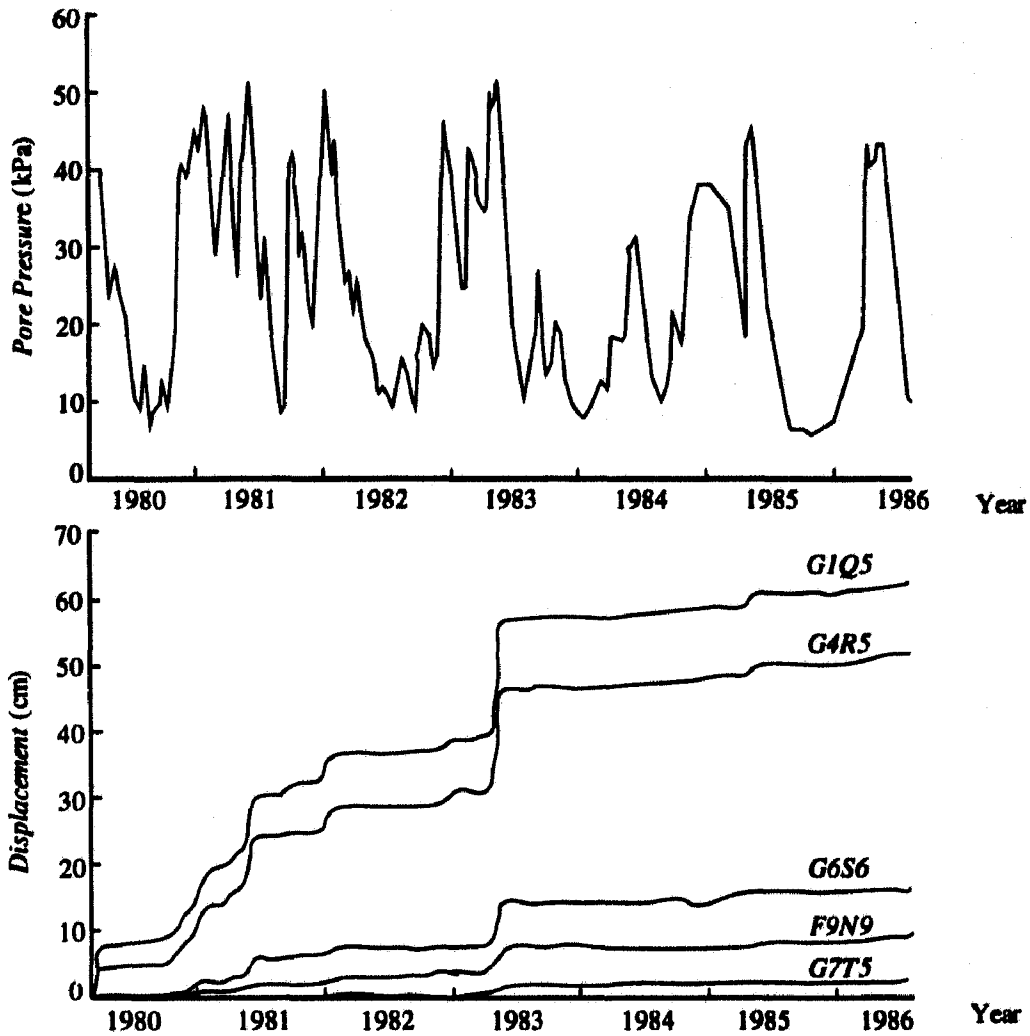

Figure 5.10 Comparison of Pore pressure with the Horizontal movement on the surface (after Cartier and Pouget, 1988)

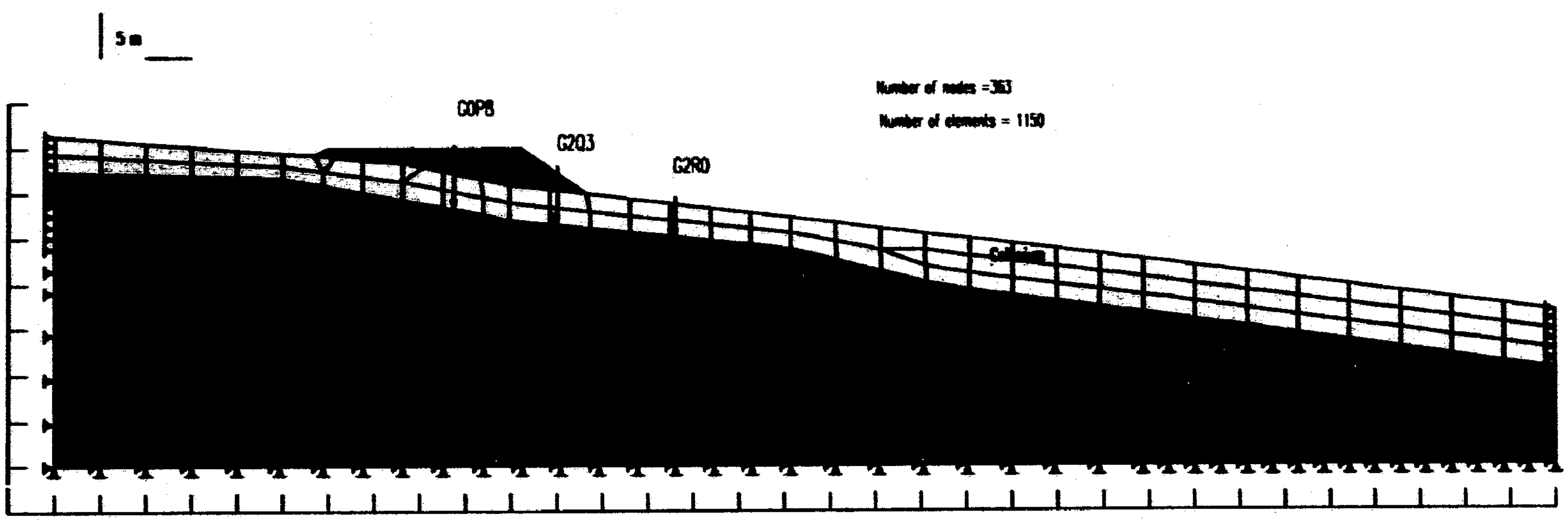

Figure 5.11 Finite element mesh for Salledes Test Embankment B

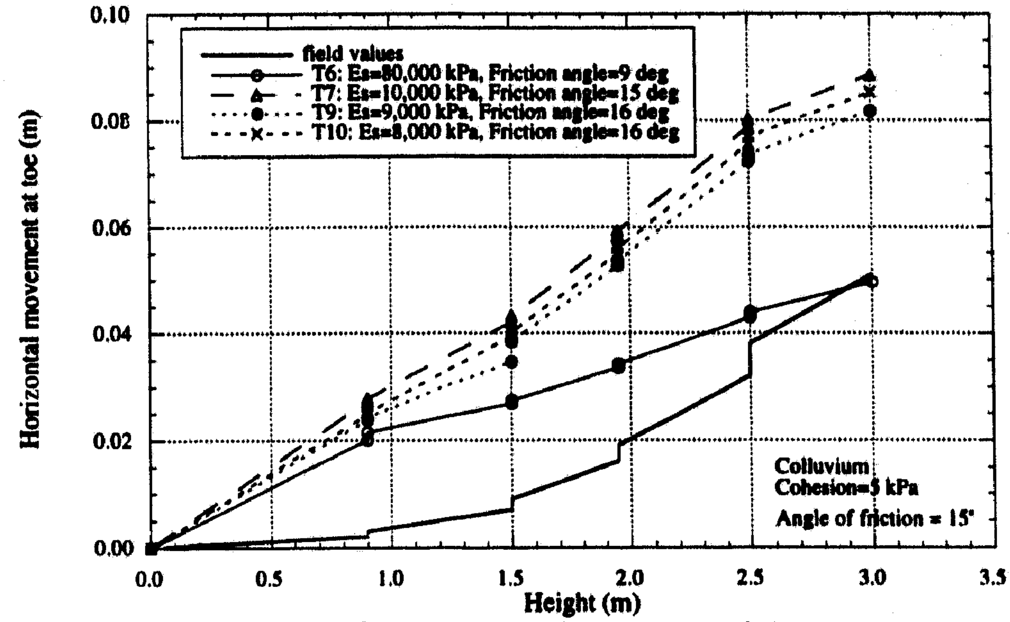

Figure 5.12 Effect of parametric variations of shear zone

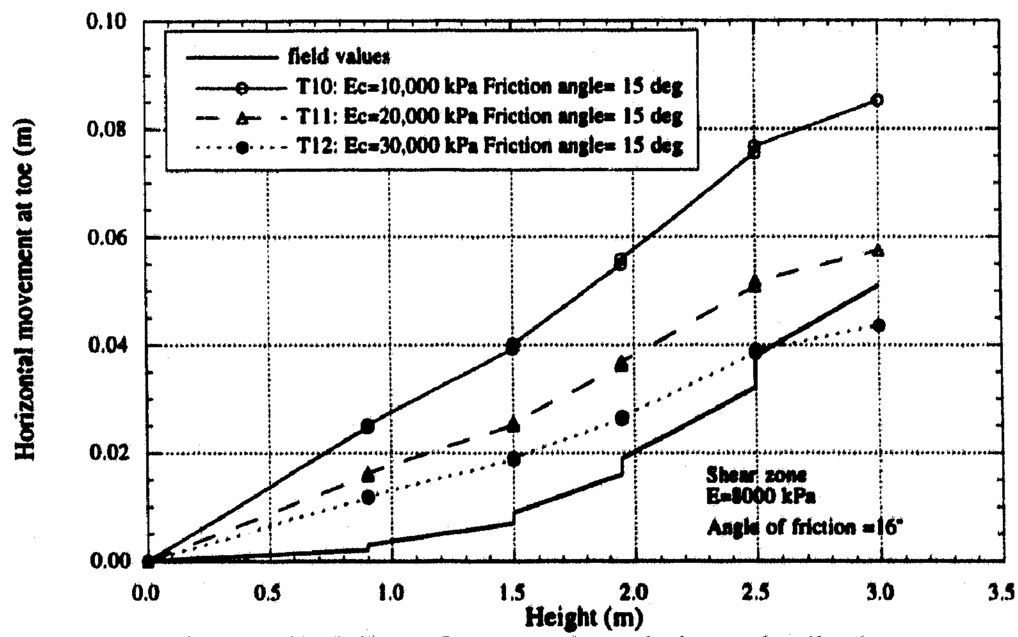

Figure 5.13 Effect of parametric variations of colluvium

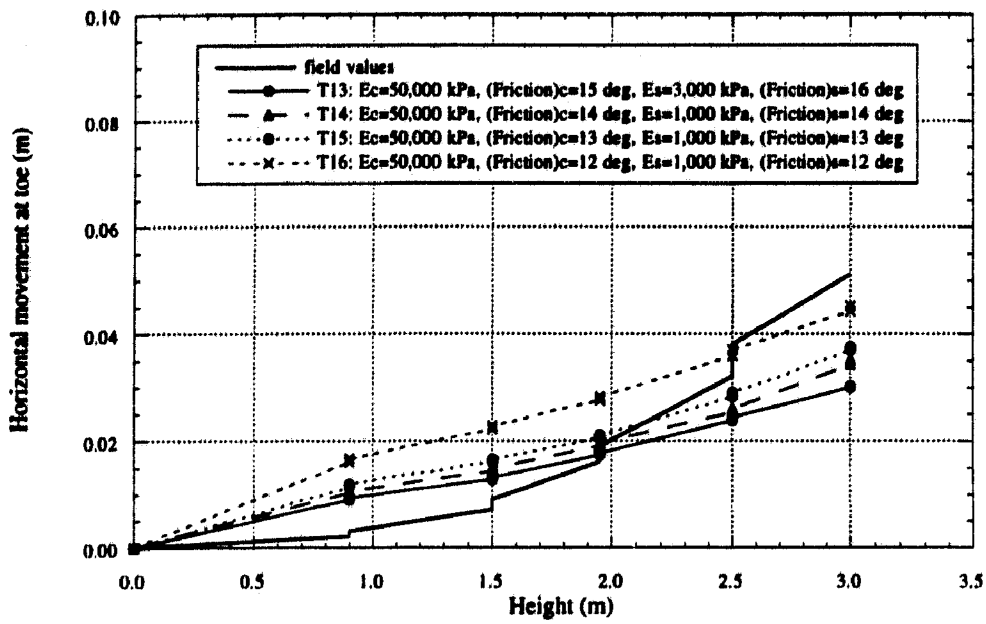

Figure 5.14 Effect of parametric variations of colluvium and shear zone

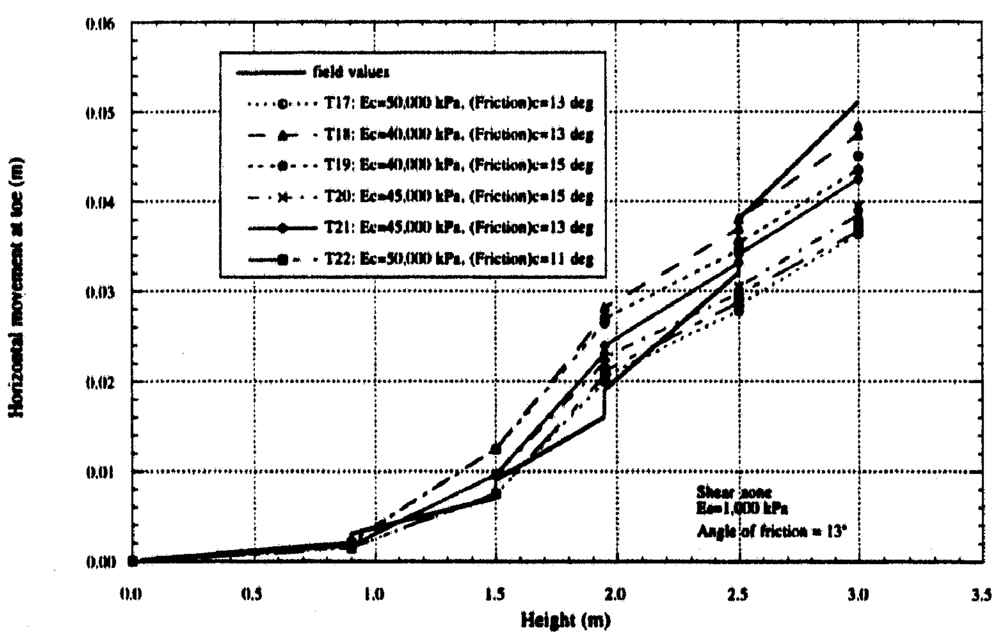

Figure 5.15 Effect of parametric variations of colluvium and shear zone

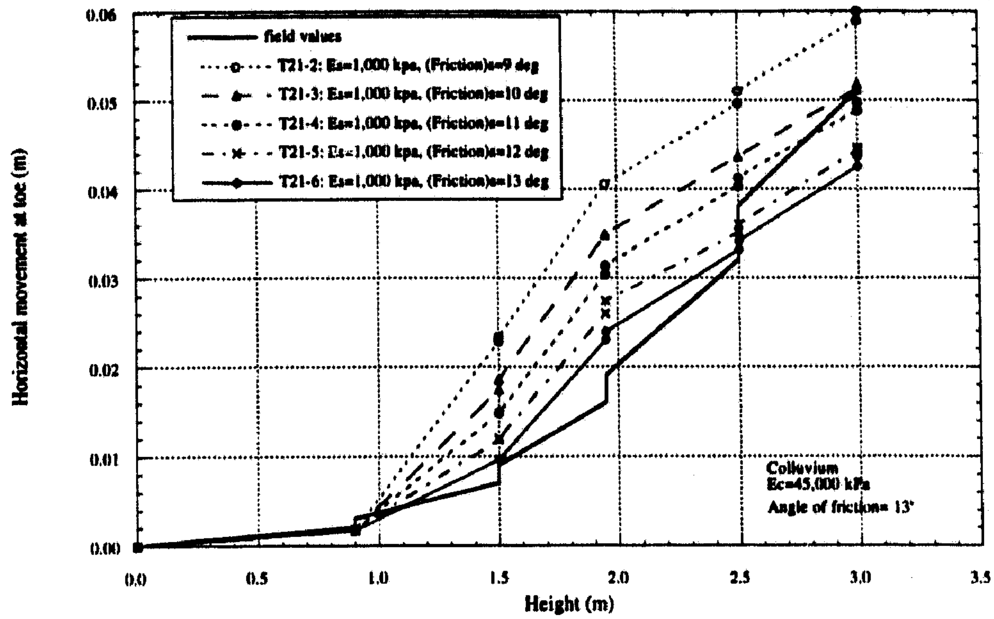

Figure 5.16 Effect of friction in shear zone

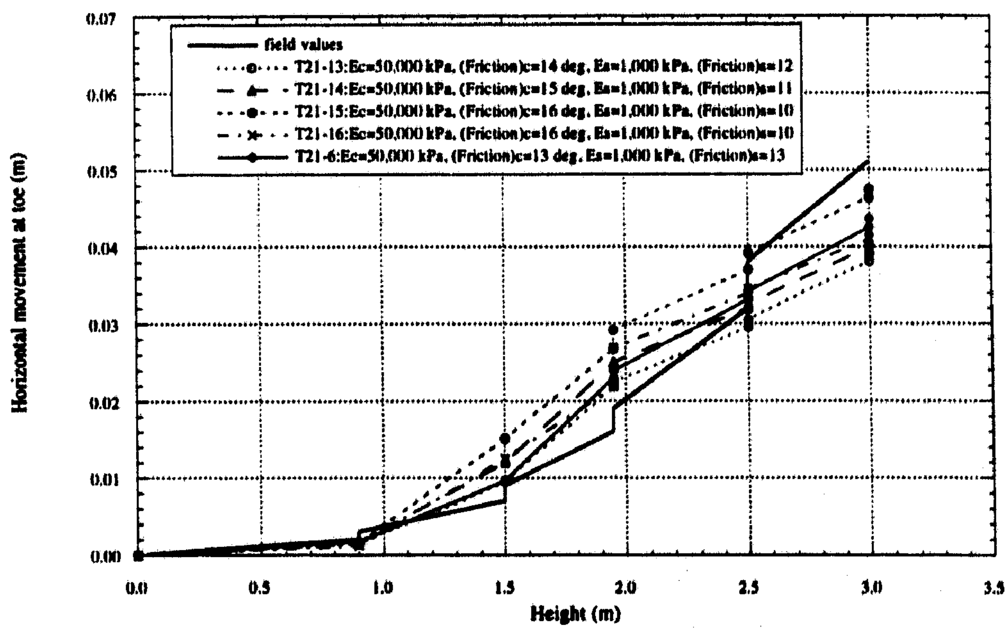

Figure 5.17 Effect of changes in friction in both shear zone and colluvium

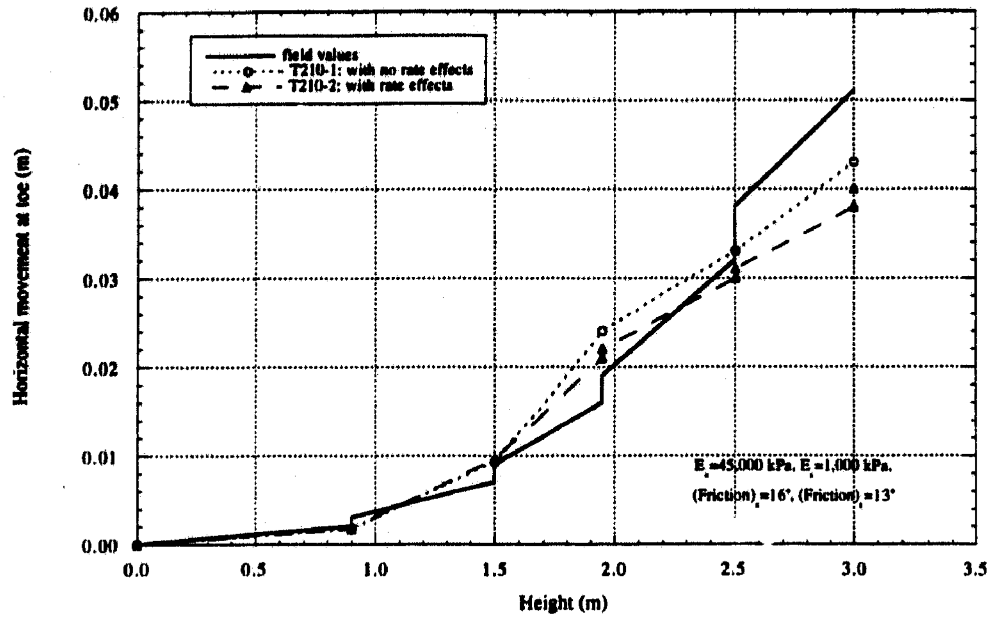

Figure 5.18 Effective Stress Analysis

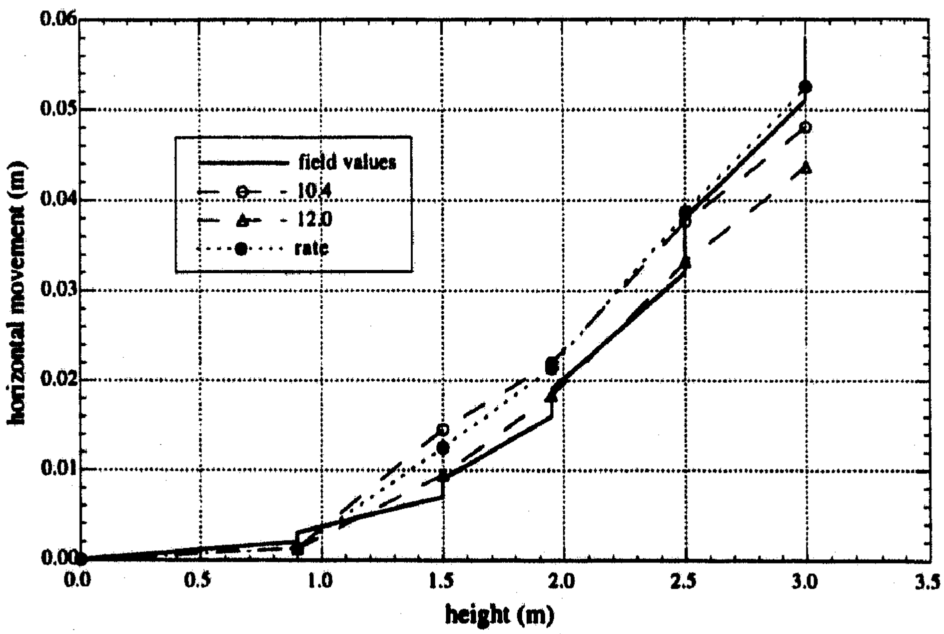

Figure 5.19 Use of Hyperbolic model to Colluvium

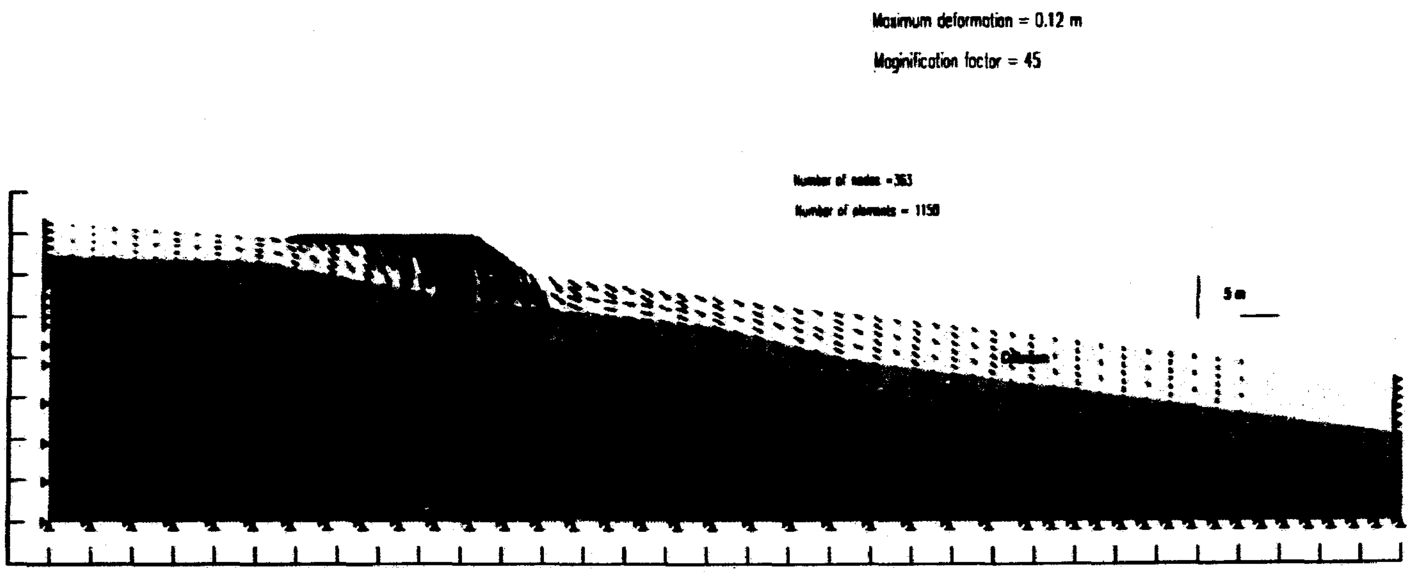

Figure 5.20 Displacement pattern at the end of construction

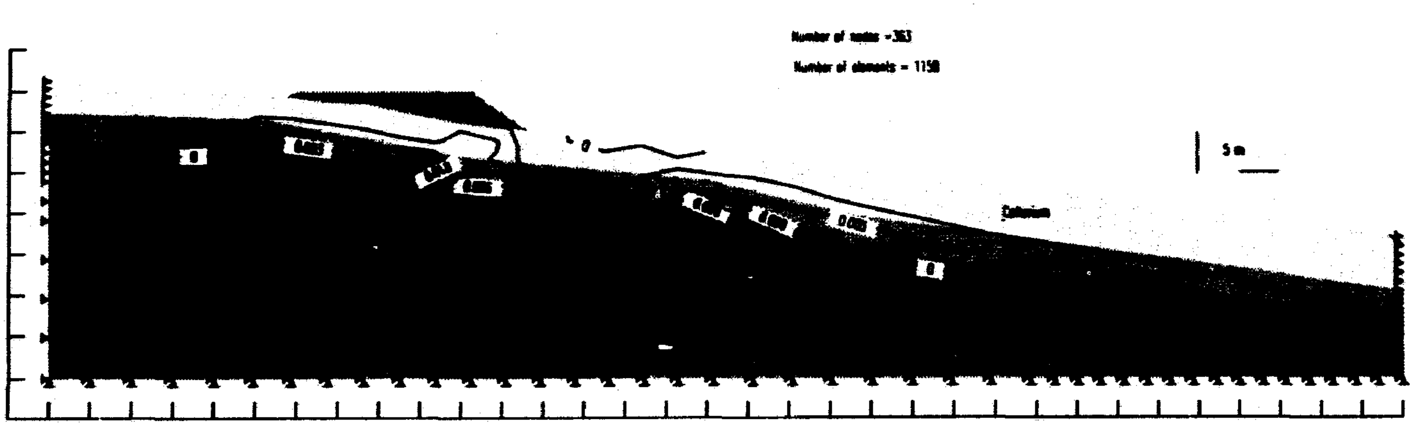

Figure 5.21 Horizontal strain contours

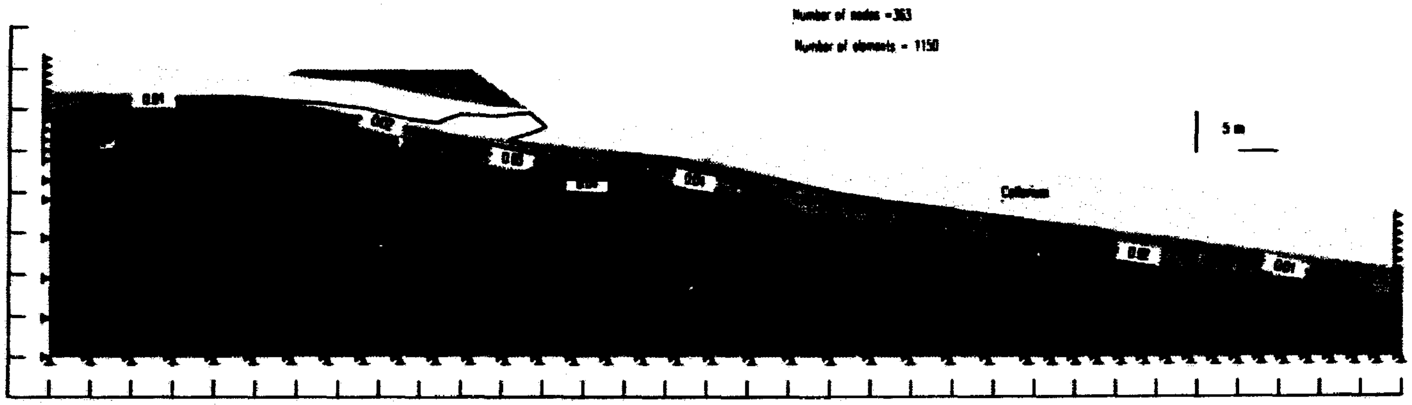

Figure 5.22 Maximum shear strain contours

CHAPTER 6

FOUNDATION MOVEMENTS AT SYNCRUDE TAILINGS DYKE

6.1 Introduction

Syncrude Canada Ltd. operates an oil sand mine about 40 km north of Fort McMurray in northern Alberta (Figure 6.1). The mine production over the planned 25-year life of the mine is in the order of 250,000 tonnes of oil sand per day. Approximately 475 million cubic meters of sand, 400 million cubic meters of fine tails and 50 million cubic meters of free water requires permanent storage within the Syncrude Tailings pond. To accommodate these volumes, approximately 18 km of dyke ranging from 32 to 90 m in final height has been constructed. The tailings pond has a surface area of 17 square kilometers.

The general layout of the tailings pond and perimeter dyke is shown in Figure 6.2. For planning purposes, the dyke perimeter has been divided into 700 m long segments, which are referred to as cells. The cell locations with respect to the dyke perimeter and numbering sequence are also shown in Figure 6.2. Figure 6.3 illustrates a typical design section for the tailings dyke. The compacted cell is constructed by using hydraulic construction techniques. This construction procedure involves sluicing of the tailings stream into construction cells oriented parallel to the dyke center line. The tailings sand placed in the construction cells is spread and compacted by wide pad dozers during the sluicing operation. During the winter months when cell construction is not feasible, the tailings stream is discharged upstream of the compacted shell. The coarse sand fraction settles out to form a beach with a 2 -3 % slope. The water and sludge fractions of the tailings stream flow into the pond.

Construction of the tailings dyke created various difficulties as a result of the existence of weak foundation materials. In some parts of the dyke, initial design sections have been altered to accommodate observed behavior. Intensive monitoring throughout the construction period by Syncrude provided valuable information to carry out analytical studies for researchers. Considering the mechanical behavior of stiff presheared clay under sustained loading and using a finite element approach, an attempt has been made in this study to simulate the field movement pattern at a selected cross section of the tailings dyke.

6.2 Geology of the site

The oil sands occur within the Cretaceous McMurray Formation. The McMurray Formation was deposited in a tidal environment and the sediments originate from successive deposition in fluvial, estuarine tidal deposition where tidal flats developed without strong wave energy (Fair and Handford, 1986).

In general, the foundation soils underlying the tailings disposal area consists of Pleistocene and Cretaceous units which overlie the McMurray formation (km) (Figure 6.4). The former Beaver Creek channel defines an approximate boundary between two distinct foundation geology conditions (illustrated in Figure 6.2). The portion of the channel to the west of the creek is underlain by glacial till and Clearwater Formation (kc). The area to the east of the former creek channel is primarily underlain by Pleistocene fluvial sand and gravel (pf) as well as glacial till (pg). The Clearwater

Formation has been eroded in the eastern area with the exception of localized remnants of its basal units (kcw and kca).

It is noted, as shown in Figure 6.5 that much of the foundation involves glacial till over Clearwater Formation. The Clearwater Formation contains some weak, highly plastic units (kca) which create circumstances that are conducive to weakening by glacio-tectonic deformation.

Features arising from glacio-tectonic deformation or glacial drag are widespread and have been recognized in the prairies of Western Canada and the USA, and in both Eastern and Western Europe (Morgenstern, 1987). When the bedrock is weak, extensive shearing results, with remnants containing slip surfaces at residual strength. This geological detail can exercise a dominant control on stability. Glacially-thrust features dominate the problem areas encountered in the foundation of Syncrude Tailings Dyke (Morgenstern, 1987).

6.3 The stratigraphy of foundation soils.

The stratigraphic sequence for the specific section (Cell 23) analyzed in this study is shown in Figure 6.5. It consists of a top layer of fluvial dense sand (pf) with an average thickness of 4m underlain by a layer of stiff sandy silt till (pgs) with the thickness increasing from 3m close to the center of the dyke to 10m close to the toe. Underneath the pgs material in the region near the center line of the dam, there exists an 8m thick layer of stiff clayey till (pgc) which disappears at approximately halfway between the center line and the toe.

Below the pg material, the basal units of Clearwater Formation are found (kca and kcw). The top unit, which is kca, consists of a 5m thick thinly laminated dark slickensided gray clay-silt. The gray colored fissured clay shale (kcw) layer of 2m thick is found underneath kca, along which the major horizontal movements have been observed. The bottom layer is the McMurray formation (km) or tar sand which is the strata of interest for the mining operation. It is found to be a very stiff material where no significant movement has been observed due to dyke construction.

6.4 Material properties based on laboratory tests

Handford (1985) presented the results of a testing program conducted by Syncrude on kca material. The direct shear tests performed on intact and slickensided samples obtained by the use of Pitcher barrel samplers from various locations in Cell 23 indicate, for intact samples average peak and residual strength parameters of $\phi_p' = 23^\circ$, $\phi_r' = 7.5^\circ$ and $C_p' = C_r' = 0$. Results for slickensided samples are: $\phi_p' = 12.5^\circ$, $\phi_r' = 7.3^\circ$ and $C_p' = C_r' = 0$.

Results of direct shear tests on tailings sand reported by Handford (1985) indicate strength parameters of $\phi_p' = 38^\circ$, $\phi_r' = 30^\circ$, $C_p' = 33$ kPa.

A series of undrained and drained triaxial extension tests on pgs material and undrained compression tests on pgc material were performed by Sego and Morgenstern (1986) on samples obtained using a Pitcher barrel sampler. The results indicated that the strength parameters could be represented by C'=20-30 kPa and $\phi' = 30-37^\circ$ for pgs material and C'=11 kPa and $\phi' = 32^\circ$ for pgc material.

A series of direct shear and ring shear tests were performed during this study on kca samples obtained using block samples from a test pit near borehole PNA-18G9219 in Cell 18 (Figure 6.6). The aim and details of these tests were reported in Chapter 2. The results indicate that there is an increase in residual friction angle of kca material in the order of 3.0-3.4% per logarithmic increase in plastic strain rate. The extrapolated residual friction angle at a strain rate of 0.001/day is found to be 6.6° from the ring shear test and 7.5° from the direct shear test.

6.5 Monitoring program

The dyke construction began in 1979, and the sequence is schematically shown in Figure 6.7. The lift thickness and the corresponding crest elevation in each year are tabulated in Table 6.2. There was no cell construction during 1982, 1987 and 1988 in Cell 23. The dyke was originally designed and constructed at 4:1 slopes. In 1983, the dyke slope was changed to 8.5:1 for all post 1983 construction. This had the effect of reducing the ultimate overall dyke slope to 6.8:1. A summary of the field instrumentation installed has been presented by Fair and Handford (1986). The slope inclinometer locations and the piezometer locations at Section 53+00E are shown in Figure 6.8 and Figure 6.9. By the end of 1984 a total displacement of 15.5cm was registered at the elevation close to the kca/kcw interface at location SI842332 (at berm 319). At the toe a total of 3.8cm was observed. By the end of 1985, at the same elevation, the displacement measured at SI842332 is 22.0cm and at the toe 7.0cm was recorded. By the end of 1986, these values had increased approximately to 25.0cm at berm 319 and 8.0cm at the toe. At the end of 1992, when the dyke construction was completed, the movement recorded at the same locations was 31.2cm and 11.6cm respectively. Figure 6.10 shows the measured horizontal movements along the shear zone from 1981 to 1991. It can be deduced from Figure 6.10 that the horizontal movements in the foundation are maximum at a location near berm 319 and diminish at about 100m distance from either side. These movements are confined to the portion where there are both *kca* and *kcw* materials. Typical time versus displacement plots for the inclinometers at the dyke toe and the berm 319 of Section 53+00E are given in Figure 6.11. They illustrate both the characteristic response to dyke construction and a gradual reduction in the rate of movement to a nominal low rate between lifts. Table 6.3 summarizes the maximum slope inclinometer readings recorded during the years of 1987 to 1991 and Table 6.4 summarizes the maximum compressive strain recorded by the sliding micrometer TSMA5. Table 6.5 gives the trend of movements at crest, berm and dyke toe in Cell 23.

Tables 6.6 and 6.7 show the pore pressure measurements at each piezometer locations. There is a substantial increase in pore pressure in the region close to the kca/kcw interface De Alencar (1988).

6.6 Deformation analyses

Previous analyses carried out by De Alencar (1988) were able to successfully capture the deformation pattern due to construction at Cell 23. Input of piezometric data as known quantities at each loading step made the numerical simulation less complicated. However, the conventional soil models used in his study were not able to compute continuing movements after the application of external loads (between construction lifts), whereas the field movements continue after the placement of construction layers. In other words, the time-dependent response of the material in the shear zone has to be considered in the deformation analyses. Since the materials in the shear zone are of low permeability and the observed pore pressures in the shear zone hardly show dissipation during the rest periods, the use of a consolidation analysis could not be expected to simulate the actual behavior after the placement of each layer. Therefore, it can be assumed that the continuation of movement after the application of external loads is due to a rate-dependent behavior of the material in the shear zone. Another possibility is the time dependent (creep) behavior of the till overlying the shear zone. It is important to know if the compressive strain in the till overlying the *kca* approaches the strain to failure measured in the laboratory tests. The insitu strain in the till is measured using the sliding micrometers. The maximum monitored strain in the till is 0.5 percent which is about 25% of the strain to failure in the laboratory. In addition, there is no evidence of any development of a passive shear zone and very little distortion is observed in the till. Hence, the effect of creep movements in the till are likely less important than the movements due to rate effects in the shear zone.

In this study, by incorporating deformation rate-dependent residual strength parameters for the material in the shear zone, a numerical simulation of field movements during and after construction is performed. The selection of basic material properties for the present analysis was based mainly on De Alencar's study. Also the piezometric measurements have been used as input to the deformation analysis.

The finite element mesh, shown in Figure 6.12, consisting of 522 six-noded-triangular and eight-noded-quadrilateral isoparametric elements with total number of 1637 nodes has been used to model the dyke and the foundation at Cell 23. The reduced level at original ground surface at the toe is 308m. For the purposes of analysis, a coordinate system is selected with the origin at 108m below the original ground level through the center line. The foundation materials, McMurray Formation, at the level of the origin were assumed to be unaffected by the construction of the dyke. That is, the bottom fixed boundary of the finite element mesh is defined at 108m below ground level. The vertical boundaries of the mesh are defined at the center line and at 1000m from the dyke center line.

Due to the stress path dependence of the material behavior, a realistic loading sequence is a fundamental requirement for obtaining the correct results. In this analysis, the loading sequence is composed of an initial linear elastic switch-on-gravity step in order to generate a pre-existing stress field with respect to the dyke construction, and subsequent layer by layer construction. The construction of dyke layers is simulated by adding elements in a three to four month period for each year. In the rest of the year, no external loading was applied to the model. The pore pressure value at each integration point is considered to be constant throughout each year, according to the average measured values at the piezometric locations.

The primary selection of material models is based on previous studies by De Alencar (1988), which includes linear elastic, non linear elastic (hyperbolic) and elastic perfectly plastic models. The material parameters are summarized in Table 6.1. In order to accommodate continuing movements after the construction, the deformation rate-dependent plastic model discussed in Chapter 3, was selected for the shear zone material (kcw). There is not enough evidence to specify a minimum strain rate below which the rate effects are negligible, mainly because of the time consumption in carrying out tests at very slow rates. Strain rates in the field are relatively low and yet the behavior is time dependent. Therefore, a reference effective plastic strain rate is taken as $1.0*E^{-7}$ /day below which the rate effects on the residual strength are considered negligible.

6.6.1 Pore pressure input

Pore pressure measurements in the field are available at specific locations where the piezometers are located. For the numerical analysis it is necessary to define or estimate pore pressure values at each integration point in the domain. For this purpose an interpolation was performed using the scheme presented by De Alencar (1988).

This scheme requires an initial guess about the pore pressure distribution and is then corrected as a function of the measured pore pressure values. The initial assumption for each year, in this case stated here, was chosen based on the phreatic line and considered as hydrostatic. Based on this initial distribution, the pore pressure at the piezometric locations are calculated using a weighting scheme. Then the errors between the calculated and the observed pore pressure at the piezometric locations are determined and compared with a specified tolerance. If errors at the piezometric locations are larger than the specified tolerance, a correction is applied to the pore pressure distribution. In this way, a pore pressure distribution is calculated until the errors at the piezometric locations are sufficiently small. The initially assumed distribution and corrected values are compared to the field measurements along the piezometers PN842319 and PN852304 in Figures 6.13 and 6.14 respectively. The results are considered very good. Since this interpolation technique was previously tested in De Alencar et al. (1992), further illustrations of its accuracy are not made.

6.6.2 Sensitivity of the movements to the rate hardening parameter 'b'

The residual friction angle of the kcw can be expressed as:

$$\tan\phi = \tan\phi_\circ\left(1 + b\ln\frac{\dot{\varepsilon}^p}{\dot{\varepsilon}^p_\circ}\right) \qquad (2.12)$$

In which, $\phi_\circ = 6.6°$ at $\dot{\varepsilon}^p_\circ = 0.001$ /day and b = 0.0185 for the Clearwater clay-shale (Chapter 2). The sensitivity of the 'b' parameter of the kcw layer was studied by keeping the other material parameters constant at the values given in the Table 6.1 and varying the b parameter within a reasonable range. Figures 6.15 and 6.16 show the movement versus time plots at kca-kcw interface at the berm 319 and the toe. As with the field movements, these plots, show similar progress of movement with time. Taking a larger value for 'b' means having a larger gradient in the residual friction angle vs. effective strain rate plot. In these analyses, a residual friction angle of 8.5° was defined at a strain rate of 0.001/day. Since most of the time, along the shear zone, the strain rate lies below this reference value, a lower value for the residual friction angle will be mobilized. Rate hardening parameters, b, of 0.015, 0.0175 and 0.020 were used in three sets of analyses. The sensitivity of b at the berm 319 is an increase of about 2cm/year horizontal movement when b increases from 0.015 to 0.020. A similar effect has been calculated at the dyke toe. When using a value of 0.0175 for the rate hardening parameter, the calculated movements show a better agreement with the field movements than 0.015 and 0.020. It is also noted that the rate hardening parameter as obtained from the laboratory tests is closer to 0.0175 (Equation 2.12 and 2.13). Because of these two reasons, b equal to 0.0175 was chosen for further analyses.

6.6.3 Sensitivity of movements to the thickness of kcw material

Although the borehole data indicate that the thickness of the kcw layer is about 1 to 2m, the shear zone is found only in a zone of 0.5 to 0.6m. Therefore, in numerical modeling if one defines the low residual friction angle throughout the kcw layer, the movements calculated could be overestimated. To model the deformation behavior with a reasonable accuracy, the residual state should be considered only for the material in the shear zone. In other words, if the actual thickness of kcw is used as the thickness of shear zone, an equivalent high value for the residual friction angle should be used.

In the first analysis the actual thickness of kcw (1 m) was considered as the thickness of the shear zone. To match the field behavior to a reasonable accuracy, an equivalent residual friction angle of 8.5° was used for the kcw. In the second analysis the thickness of kcw was reduced by 50% (0.5 m), which is close to the actual thickness of the shear band. The movements (Figures 6.17 and 6.18) were reduced significantly. In the third analysis the residual friction angle of 6.5° was used for the 0.5m-thick shear zone which resulted in a movement similar to the first analysis and to those in the field. In fact, the value of 6.5° was obtained from the results of ring shear tests. When the thickness of the shear zone was reduced to 0.5 m and the residual friction angle was reduced to 6.5°, the movements showed a significant increase and became close to the field movements. This exercise illustrates the importance of the selection of the thickness of shear band in analyzing field situations which involve shearing in confined zones. Firstly, in combination with the laboratory residual friction angle assigned to the shear band the magnitude of movements can be calculated to reasonable accuracy. Secondly, although it is not evident from the displayed results, the calculated movement profiles (variation of movements with depth) will be similar to the field profile.

6.6.4 Sensitivity of the movements to stiffness of till

In the previous analyses, the material parameters were selected based on the studies by Alencar (1988). Changing the stiffness of the till as shown in Table 6.8 resulted in the movement pattern at the berm and toe as shown in Figures 6.19 and 6.20. Both of the selected sets (Set no. 2 and 3) of material parameters underestimate the movements at the kca-kcw interface and overestimate the movements at the ground surface near the toe (Figures 6.21 and 6.22). If the stiffness of the till is further increased in order to match the movements at the ground surface, a further reduction of the movements will result at the shear zone. Therefore material properties set number 1 is considered for further analyses.

6.6.5 Calculated displacements

The selected material parameters used in the following analysis are summarized in Table 6.9. To illustrate the appropriateness of the selected model, the calculated and field values of displacements are compared in the following section. Figure 6.23 shows measured and calculated values of horizontal movement with time at the kca/kcw interface near berm 319 and the dyke toe. It also indicates the calculated movement pattern if the shear zone is modeled with a conventional elasto-plastic model. In this type of analysis there is no time-dependent response and therefore, the continuing movements between lifts are not computable. Figures 6.24 and 6.25 show the comparisons of field and calculated movements separately for berm and toe respectively. It is observed that in both locations calculated values display the same trend as the field data. At the berm, a slight underestimation of the movements in 1984 is found. In the case of the toe, the difference between calculated and measured displacements is smaller than that at the berm, for the period in which the history matching is performed. However, there is a slight difference in years after 1989.

The horizontal movement profiles at locations berm and toe (for 1985 and 1986) are plotted in Figures 6.26 and 6.27 respectively. At berm 319, a good agreement is seen between measured and calculated displacement versus elevation curve shapes. At the toe close to the ground surface, the calculated displacements are somewhat higher than the field values. This can be avoided if more care is taken in modeling the pgs material under passive stress conditions. These changes were not tried since the quality of the results were already adequate to validate the effective stress analysis, using a rate-dependent constitutive relationship for the residual strength in the shear zone. The results are more realistic than those of time-independent analyses.

6.6.6 Displacements, velocity, stresses, strain rates, and residual friction angle in shear zone

The calculated and measured displacements along the shear zone, compared for the years of 1984, 1985, 1986, 1989, 1990 and 1991, are shown in Figures 6.28 and 6.29. It can be seen that both calculated and field displacements show the same shape of distribution along the shear plane. These figures show, in accordance with what has been observed in the field, that the higher displacements occur at the berm 319 region, rapidly decreasing towards the toe and the center line of the dyke. It is noted that the observed movements at 285m from the center line are somewhat higher than the calculated movements. As Figure 6.10 shows, the field movements at this location are measured about 2m above the kca/kcw interface. Therefore, a direct comparison of field value and the calculated value can not be made.

The velocity along the top of kcw material layer is shown Figure 6.30. Here the velocity was obtained by dividing the difference in displacements by the corresponding time increment. Hence, the figure shows the average velocity during a cell construction period. The maximum average velocity of 0.85 mm/day is calculated for the year of 1984, when an incremental displacement of 7.6m occurred at the berm 319 in Cell 23 (Figure 6.23).

Field velocity data as shown by Table 6.5 indicate a maximum velocity of 3.5 mm/day. This velocity may have been reached in one instant or several instants during the year. But the calculated velocity is an average value during the construction process. If we were to calculate the velocities in each day, the solution time would have been increased. Therefore, a direct comparison cannot be made with the measured maximum velocity and the calculated average velocity.

However, one month after construction, the measured displacement at the berm 319 is 4.7 cm. This almost results in an average velocity, during the construction month, of 0.78 mm/day. This agrees well with the calculated average velocity in the construction period of 1984, which is 0.85 mm/day. Similarly the measured average velocity at the same location during the construction month 1985 is 0.35 mm/day. The calculated value as shown by Figure 6.30 is 0.32 mm/day and it is in complete agreement as well. The field value and the calculated value of the same quantity for the year 1986 are 0.23 mm/day and 0.18 mm/day respectively. Therefore, the field and calculated behavior resulted in similar velocities during the three years considered, and the maximum average velocities have been observed in the same location (berm 319).

When undertaking construction on moving ground, particularly movements themselves induced by construction operation, it is some times useful to define an allowable velocity as a construction control. However, if conventional plastic soil models had been used to analyze such a field problem, it would not be possible to calculate the anticipated velocities. Therefore, by using a rate-dependent numerical model, an understanding of anticipated velocities and how they deteriorate with time can be achieved.

The shear stress distributions calculated within the *kcw* material for the years of 1984 and 1985 are shown in Figure 6.31. The stresses just after the completion of construction in 1984 are shown by dark circles. After this moment , no external loads were applied to the foundation until the placement of the next layer in 1985. However, there is a noticeable amount of stress redistribution from the zone of higher velocity to the adjacent zone, causing further movements. This stress redistribution within the shear zone explains how the rate effects on residual strength produce a damping effect as an increment of load is applied, and how the moving mass converges on equilibrium with time. The stress redistribution and calculated movements after the loading in each year are entirely due to the rate effects.

The effective plastic strain rates along the top of the kcw material layer are shown in Figure 6.32 for years of 1984 and 1985. For the years earlier than 1983 the strain rates everywhere lie below the reference rate. In the year of 1984 the highest strain rates are observed close to the berm 319 and they decrease toward the reference rate as the distance from the berm increases. Another observation is that the material remains elastic far away from the berm (Figures 6.34 and 6.35). The occurrence of higher strain rates resulted in higher residual friction values during the construction stages (Figure

6.33) and during the rest periods, the movements continue with the rates and the residual friction values decreasing to the minimum values.

Of course the calculated response depends on the selected rate-dependent material parameters of $\dot{\varepsilon}_o^p$ and b. The value of b is selected based on the laboratory tests. Therefore, the only parameter with uncertainty is the reference plastic strain rate, below which the rate effects are negligible. Even without enough evidence, the selected value for $\dot{\varepsilon}_o^p = 1*10^{-7}$ /day seems to be appropriate, because of the closeness of the time-dependent response of the calculated movements to the field behavior.

6.6.7 Contours of strains, stress ratios and yield conditions

To illustrate stress, strain and yield conditions in the foundation, two construction years were selected. The year with the highest observed movements is 1984; therefore, it is selected. Year 1991 is selected because by this time the dyke construction was reaching the end. Contours of maximum shear strains are shown in Figures 6.36 and 6.37 for the years of 1984 and 1991. It is noted that the zone of higher distortion values are concentrated to a limited region which encloses the berm and the toe at the kca/kcw interface level. Very little distortion is observed in pgs material, which is in agreement with the movement pattern shown by the slope inclinometers in the field.

The contours of horizontal strains are plotted for the same years (Figures 6.38 and 6.39). They show a high strain gradient across the kcw and kca material. The field measurements of compressive strains, at sliding micrometer (TSMA5), are available since 1989. The micrometer, TSMA5, has been installed with approximately 12° to the horizontal. Therefore, the measured values are close to the horizontal strains at this location. The maximum measured compressive strain, with reference to the first reading in 1985, during each period is tabulated in Table 6.5. The calculated horizontal compressive strain at this location in the year of 1984 is less than 0.05%. The contours in the 1991 show 0.5% of horizontal compressive strain in pgs material, which is in complete agreement with the measured value in the year of 1991. Horizontal strain values, of course, are concentrated in the kcw layer (Figure 6.39).

The yield zones (Figure 6.34 and 6.35) migrate towards the center line of the dyke with time. The zone of maximum shear stress moves in this direction as well (Figure 6.40 and 6.41).

The failure ratio is defined as the ratio of the shear stress to the shear stress at which the Mohr circle of stresses touches the failure envelope. Thus, in terms of principal stresses:

$$\text{The failure ratio} = \frac{\sigma_1 - \sigma_3}{(\sigma_1 - \sigma_3)_f}$$

where,

$$(\sigma_1 - \sigma_3)_f = \frac{2C\cos\phi + 2\sigma_3 \sin\phi}{1 - \sin\phi}$$

The failure ratios in till are plotted and they show that the stress conditions in the till in 1991 are 20% of the shear stress at the failure (Figures 6.42 and 6.43). This indicates that this soil is within the elastic range and, therefore, creep of the till is not considerable.

6.7 Summary and Conclusions

1. Deformation analyses have been performed to simulate the time dependent response of the foundation soils at Cell 23, Section 53+00E of the Syncrude Tailings Dyke. Finite element effective stress analyses have been carried out with pore pressure at each integration point, as input to the analyses using the interpolation technique proposed by De Alencar (1988).

2. Sliding micrometer data and calculated strain distributions confirm that the strains within the pgs material overlying the Clearwater Formation are within the elastic region.

3. The yield zone beneath the dyke is confined to the Clearwater Formation. The maximum shear stress calculated in the pgs material is about 25% of the available strength.

4. Observations presented in 2 and 3 explain that the time dependent response of foundation soils are not due to the creep effects on the pgs material in the passive zone.

5. Since the materials in the shear zone are of low permeability and the observed pore pressures show little dissipation during the period between lifts, a consolidation analysis would not account for time-dependent movements.

6 The deformation rate-dependent model developed in Chapter 3 was used to model the material in the shear zone (kcw), which enables one to compute time-dependent movements of the foundation soil to a satisfactory level.

7 Hence confidence can be gained to use the developed model for similar field cases where the movement process is dominated by a previously sheared material.

8 If conventional plastic soil models had been used to analyze this field problem, it would not be possible to calculate the anticipated velocities. Therefore, by using a rate-dependent numerical model, an understanding of anticipated velocities and how they deteriorate with time can be achieved.

Table 6.1 Summary of material parameters used in the primary non-linear effective stress analyses

Material No	1	2	3	4	5	6	7	8
Parameter	km	kcw	kca	pgc	pgs	pf	ts1	ts2
E	$2*10^6$	10000	45000	-	-	-	5000	-
μ	0.35	0.45	0.40	0.40	0.43	0.30	0.30	0.30
b	-	0.015	-	-	-	-	-	-
$\dot{\varepsilon}^p_o$	-	$.1*10^{-6}$	-	-	-	-	-	-
ϕ	-	8.5	14	38	37	35	-	35
c	-	0	0	32	0	38	-	38
k	-	-	-	750	400	280	-	750
n	-	-	-	0.24	0.24	0.65	-	0.24
R_f	-	-	-	0.8	0.9	0.93	-	0.87
γ	21.5	20.0	20.0	21.5	21.5	20.0	20.0	20.0

Where:

E	- Elastic modulus (kPa)
μ	- Poisson's ratio
b	- Rate hardening parameter for residual strength
$\dot{\varepsilon}^p_o$	- Referance plastic strain rate (/day)
ϕ	- Angle of internal friction (°)
c	- Cohesion (kPa)
k	- Modulus number in hyperbolic elastic model
n	- Exponent in hyperbolic elastic model
R_f	- R_f factor in hyperbolic elastic model
γ	- Unit weight (kN/m^3)
TS1	- Tailings sand when layer is added; linear elastic model
TS2	- Tailing sand; hyperbolic elastic model

Table 6.2 Cell construction lift thickness

Year	1981	1982	1983	1984	1985	1986	1987	1988	1989	1990	1991	1992
lift (m)	6.0	0.0	3.0	3.0	3.0	3.0	0.0	0.0	3.0	6.0	3.0	3.0
crest ele m	325	325	328	331	334	337	337	337	340	346	349	352

Table 6.3 Maximum S.I. displacement in cell 23

Year	S.I no and location	Instal. date	Maximum Incremental displacement (cm)			Elevation of movement (m)	Soil unit
			record to date	during any const. season	during the year		
1987	238604	5/81	27.00	7.60	1.00	319.14 (289.88)	kcw/kca
1988	238823	12/80	31.20	7.60	0.60	319.5 (290.23-290.84)	kcw/kca
1989	228823		31.8	7.60	1.20		kcw/kca
1990	239013		33.0	7.60	3.50		kcw/kca
1991	239013		36.5	7.60	2.00		kcw/kca
1992	239013		38.5	7.60			

Table 6.4 Silding micrometer data (TSMA5)

period	maximum recorded compressive strain[1] (%)
92/7 - 94/10	.55
91/5 - 93/3	.54
90/12 - 92/7	.52
89/9 - 90/12	.45

[1] Relative to the first reading in 1985

Table 6.5 Trend data - cell 23

Location	year	Max. rate (mm/day)	1 month after construction (cm)	6 months after construction (cm)	1 year after construction (cm)	Year end disp. rate (cm/year)	Elevation of movement (m)
Crest	1985	0.05	0.05	0.20	0.30	0.10	
	1986	0.15	0.40	1.15	1.30	0.30	287.22
	1987	-	-	-	-	0.30	
	1988	-	-	-	-	0.10	
Berm 319	1981	0.30	0.80	3.80	4.60	1.50	
	1982	-	-	-	-	0.10	
	1983	0.70	1.60	5.80	7.40	3.90	
	1984	3.50	4.70	7.20	11.50	3.00	290.23-
	1985	1.30	2.10	4.70	7.30	2.60	290.84
	1986	1.10	1.40	2.30	3.20	1.80	
	1987	-	-	-	-	1.00	
	1988	-	-	-	-	0.60	
Dyke toe	1982	-	-	-	-	0.30	
	1983	0.25	0.70	2.40	2.90	2.70	
	1984	0.40	1.30	2.10	3.80	0.70	288.30-
	1985	0.40	0.65	1.70	1.80	0.80	288.91
	1986	0.30	0.50	1.30	1.60	0.45	
	1987	-	-	-	-	0.10	
	1988	-	-	-	-	0.65	

Table 6.6 Phreatic line elevation (in meters) during construction years

Year	at centre line	at toe
1979	304.0	302.0
1980	307.5	306.0
1981	311.0	308.0
1982	312.0	308.0
1983	314.0	308.0
1984	317.0	308.0
1985	319.0	308.0
1986	321.0	308.0
1987	319.2	308.0
1988	319.5	308.0
1989	320.0	308.0
1990	322.0	308.0
1991	323.4	308.0
1992	324.0	308.0

Table 6.7 Piezometer tip elevation and pore pressure untill 1986

Piezometer	Tip location (m)		Pore pressure (kPa)						
	X	Y	1980	1981	1982	1983	1984	1985	1986
PN802303	160.00	291.44	106.54	103.4	115.10	116.50	137.70	142.90	141.80
PN802304		300.56	79.30	77.50	88.70	85.50	106.90	110.80	110.3
PN802305		293.00	158.40	158.70	270.00	253.50	250.10	239.20	158.14
		302.42	106.50	235.80	157.90	165.60	165.40	165.50	164.60
PN802310	285.31	291.00	106.10	184.00	213.90	210.60	220.00	209.10	212.90
		292.65	101.30	161.10	191.00	190.00	210.13	193.50	194.7
		301.79	66.30	55.04	54.50	57.00	61.30	60.00	59.94
PN832305		290.91					3.80	3.40	3.83
PN842302		292.60					103.20	106.00	104.9
PN842318		291.35					60.30	61.30	61.30
		293.33					99.80	97.32	97.20
		298.06					64.20	63.20	63.20
		300.34					44.70	42.80	42.80
		304.31					16.90	15.60	15.60
PN842319		290.53					518.30	575.30	598.10
		294.19					245.40	246.30	256.10
		297.54					153.04	143.83	141.80
		299.68					126.70	128.70	128.70
		303.64					86.00	88.00	87.80
		107.60					59.00	62.00	59.80
PN852304	158.13	285.89						227.00	218.80
		288.08						386.00	388.60
		291.43						578.00	640.20
		294.12						319.42	252.90
PN852305		289.20						296.20	300.10
		291.49						532.50	672.00
		296.82						217.30	214.60
		300.63						181.40	181.60

Table 6.7 (contd.) Piezometer tip elevation and pore pressure untill 1986

Piezometer	Tip location (m)		Pore pressure (kPa)						
	X	Y	1980	1981	1982	1983	1984	1985	1986
PN852306	83.125	287.67						436.20	457.70
		289.65						527.20	686.20
		291.63						531.20	677.50
		296.20						184.20	184.40
		302.91						146.10	144.10
PN852307	217.19	288.3						184.40	180.50
		290.3						272.10	267.80
		291.4						403.00	477030
		292.9						417.20	491.70
		294.4						333.70	366.80
		296.6						180.50	175.70
		304.6						63.80	63.70
		109.7						17.70	16.60
PN852311	270.63	290.2						189.00	186.30
		291.0						267.50	288.40
		292.5						231.00	253.09
		294.8						206.20	260.90
		297.8						115.00	110.80
		306.8						19.62	18.60
		310.6						2.40	3.90
PN852312	324.06	288.5						168.00	176.50
		289.5						158.24	165.70
		290.8						141.30	154.01
		295.25						105.00	104.70
PN852316		290.74						144.70	144.70
		295.31						100.00	100.00
		301.4						40.22	40.20
		304.45						10.30	10.30

Table 6.7 (contd.) Piezometer tip elevation and pore pressure from 1987 to 1993

Piezo-meter	Soil unit	Tip location x	Tip location y	Pore pressure (kPa) 87	88	89	90	91	92	93
802303	pgc	160.0	291.44	131.2	136.79	141.5	150.23	155.03	149.64	148.76
802304	pgs		300.56	109.24	110.22	110.81	118.36	122.97	102.18	115.02
802305	pgs		302.42	159.35	154.84	156.01	156.31	159.54	162.29	156.99
	kca		293	230.15	225.34	220.34	219.95	216.71	216.81	214.16
802310	kca	285.31	291.12	211.61	211.91	210.04	208.18	202	204.75	205.73
	kca		292.65	196.41	192.39	182.2	188.67	189.94	191.02	188.96
	pgs		301.79	58.15	56.09	46.186	64.818	71.29	64.033	65.994
832305	kca		290.91	5.9817	36.969					
842302	kca		292.6	102.18	106.2	102.96	113.75	116.99	121.99	125.71
842318	kca		291.35	64.425	69.132	61.974	60.405	59.032	60.013	60.699
	kca		293.33	97.177	102.18	97.962	96.981	85.018	92.961	93.941
	pgs		298.06	62.17	67.171	58.64	60.013	57.953	57.953	59.032
	pgs		300.34	46.088	45.892	40.989	41.97	39.322	36.969	39.028
	pf		304.31	16.082	25.005	13.042	14.023	11.963	9.0215	11.963
842319	pgc		290.53	146.99	570.22	547.96	560.9	551.88	538.94	537.96
	pgc		294.19	232.5	231.72	219.16	238.97	230.93	232.01	238.97
	pgs		299.68	126.3	130.32	126.01	137.97	145.03	146.99	156.99
	pf		303.64	86.195	90.117	87.96	102.96	106	113.95	120.03
	ts		307.6	57.169	62.17	57.953	74.035	81.978	85.018	95.02
852304	km	158.13	285.89	209.46	215.73	212.01	219.46	222.01	220.73	221.52
	kcw		288.08	371.94	361.55	352.13	354.58	348.51	344.39	344.48
	pgc		291.43	657.3	643.76	645.33	651.61	646.71	647.98	647
	pgc		294.12	252.8	245.05	252.8	254.96	252.01	249.76	260.25
852305	kcw		289.2	297.71	298.59	291.92	217.01			
	ts		300.63	182.1	189.94	189.55	209.55	223.28	227.99	
852307	km	217.19	288.3	174.35	178.37	182	188.96	181.02	189.94	174.94
	kcw		290.3	250.54	247.5	239.95	238.97	245.93	242.01	238.87
	kca		291.4	477.06	467.06	463.33	467.94	462.06	465.79	461.86

Table 6.7 (contd.) Piezometer tip elevation and pore pressure from 1987 to 1993

Piezo-	Soil	Tip location		Pore pressure (kPa)						
meter	unit	x	y	87	88	89	90	91	92	93
			292.9	498.64	489.03	491.97	494.91	492.75	489.91	491.97
			294.4	354.78	346.74	335.27	329.48	327.52	335.76	326.44
	pgs		296.6	164.35	160.33	157.97	163.96	172.98	171.02	177
	pf		304.6	64.131	67.171	66.975	75.997	80.017	87.96	87.96
	ts		309.7	17.062	19.024	16.964	27.947	34.027	40.989	40.008
852311	kcw	270.63	290.2	178.37	188.37	181.02	189.94	191.02	189.84	222.01
	kca		291.4	274.57	270.16	272.61	285.94	293.98	293.98	293.49
	kca		292.95	256.43	254.56	257.02	255.94	258.39	253.98	230.15
	kca		294.8	270.65	273.1	268.98	268	267.02	267.21	265.94
	pgs		297.8	110.22	112.28	106.98	110.02	111	111	111.98
	pf		306.8	20.004	25.103	15.984	19.024	18.533	19.024	19.808
	ts		310.6	5.0011	12.748	0.9806				
852312	kcw	324.06	288.5	182.39	185.43	179.94	182.98	187	183.96	187.98
	kca		289.5	170.33	162.39	156.41	156.99	152.97	152.97	154.35
	kca		290.8	160.33	157.39	155.03	155.03	152.97	151.99	152.97
	pgs		295.2	110.22	111.2	102.96	103.94	101	102.18	102.96
852316	pgs		290.74	148.36	150.33	143.95	147.97	143.95	146.01	145.52
	pgs		295.31	103.26	110.32	101	106.98	101.98	98.943	99.139
	pgs		301.4	50.109	56.188	46.971	51.972	51.776	45.01	42.95
	pf		304.45	13.042	20.004	10.983	11.277	10.002	5.9817	8.0409
862309	kcw	75.0	287.67	311.63	307.71	305.95	333.99	354	350.96	366.94
	pgc		289.65	255.54	263.59					
	pgc		291.63	234.46	244.56	244.95	263.98	274.96	286.92	283.98
	pgs		296.4	198.38	206.51	204.06	227.99	236.03	247.01	243.97
	ts		302.91	132.28	139.34	141.01	163.96	171.02	183.96	192
862313	pgc		291	538.35	591.3	588.36	633.47	656.02	657.88	661.91
862316	pgc		290.85	621.7	638.76	679.26	729.37	780.56	714.17	806.25
	kcw		286.48		250.54	234.95	237.01	239.95	237.01	235.93

Table 6.7 (contd.) Piezometer tip elevation and pore pressure from 1987 to 1993

Piezo-	Soil	Tip location		Pore pressure (kPa)						
meter	unit	x	y	87	88	89	90	91	92	93
882319	kca	400.0	292.31		136.5	128.95	122.97	113.95	115.02	116
892309	kcw	324.0	287.84			187.98	191.02	192	191.02	192.98
	kca		290.89			138.95	176.02	174.06	177	173.96
	pgc		296.38			85.999	90.019	85.999	84.037	86.979
922305	pgc	0	290.2						664.94	707.5
922306	pgc	0	291.1						935.69	

Table 6.8 Material properties used in the sensitivity analyses

Property	Analysis number		
	1	2	3
kca:			
Elastic Modulus (kPa)	45,000	65,000	65,000
Pgc:			
Elastic Modulus (kPa)	45,000	65,000	85,000
Modulus number for Hyperbolic Model	750	750	950
Pgs:			
Elastic Modulus (kPa)	45,000	65,000	85,000
Modulus number for Hyperbolic Model	410	410	610

Table 6.9 Summary of material parameters used in the final non-linear effective stress analyses

Material No	1	2	3	4	5	6	7	8
Parameter	km	kcw	kca	pgc	pgs	pf	ts1	ts2
E	$2*10^6$	10000	45000	-	-	-	5000	-
μ	0.35	0.45	0.40	0.40	0.43	0.30	0.30	0.30
b	-	0.0175	-	-	-	-	-	-
$\overset{o}{\varepsilon}{}^{p}_{o}$	-	$.1*10^{-6}$	-	-	-	-	-	-
ϕ	-	6.5	14	38	37	35	-	35
C	-	0	0	32	0	38	-	38
k	-	-	-	750	400	280	-	750
n	-	-	-	0.24	0.24	0.65	-	0.24
R_f	-	-	-	0.8	0.9	0.93	-	0.87
γ	21.5	20.0	20.0	21.5	21.5	20.0	20.0	20.0

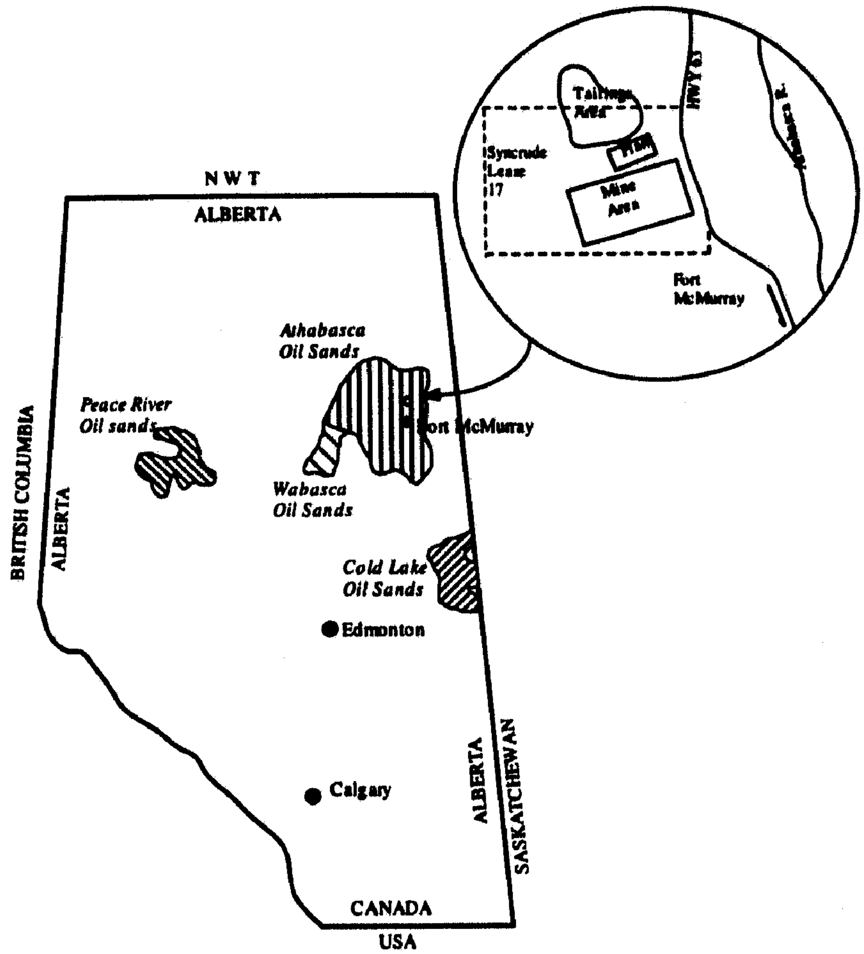

Figure 6.1 Location of Syncrude Canada Ltd. Mine site and Tailings area.

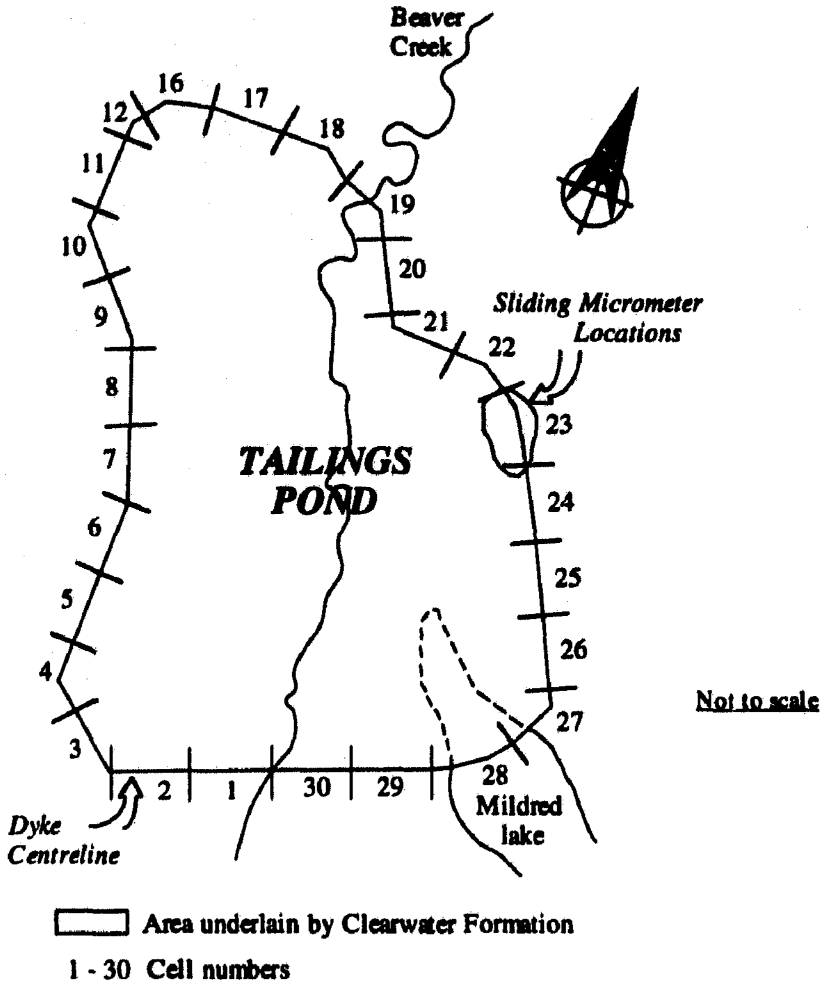

Figure 6.2 Layout of Syncrude Canada Ltd. Tailings Disposal Area

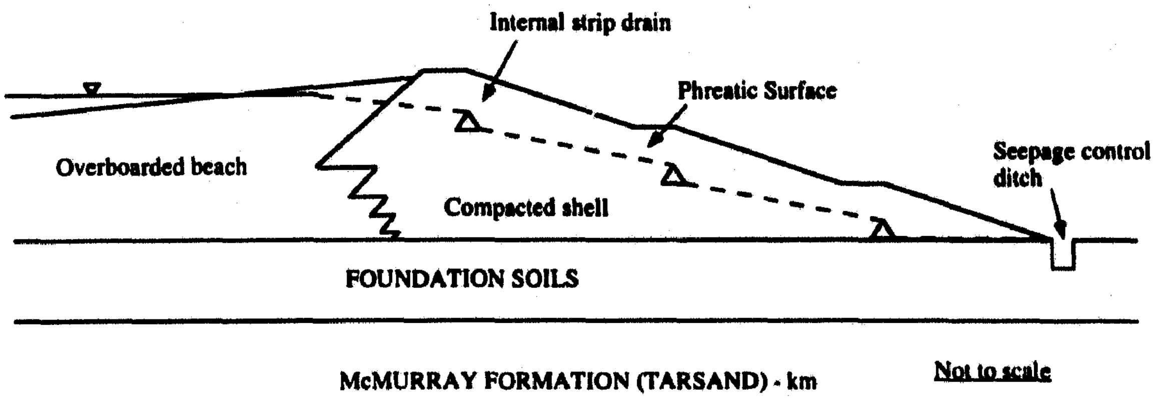

Figure 6.3 Typical cross-section of Tailings Dyke (After Fair and Handford, 1986)

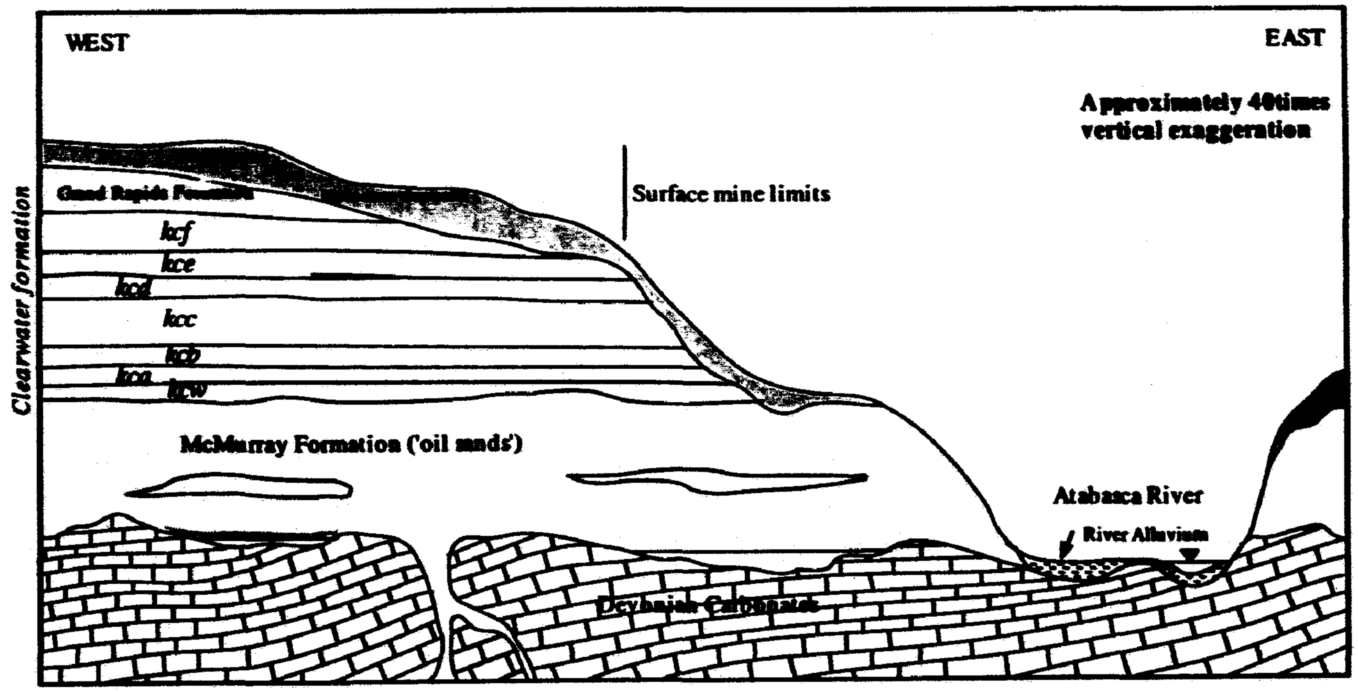

Figure 6.4 Schematic Cross-section of Syncrude Canada Ltd. Leases (after Isaac et al., 1982)

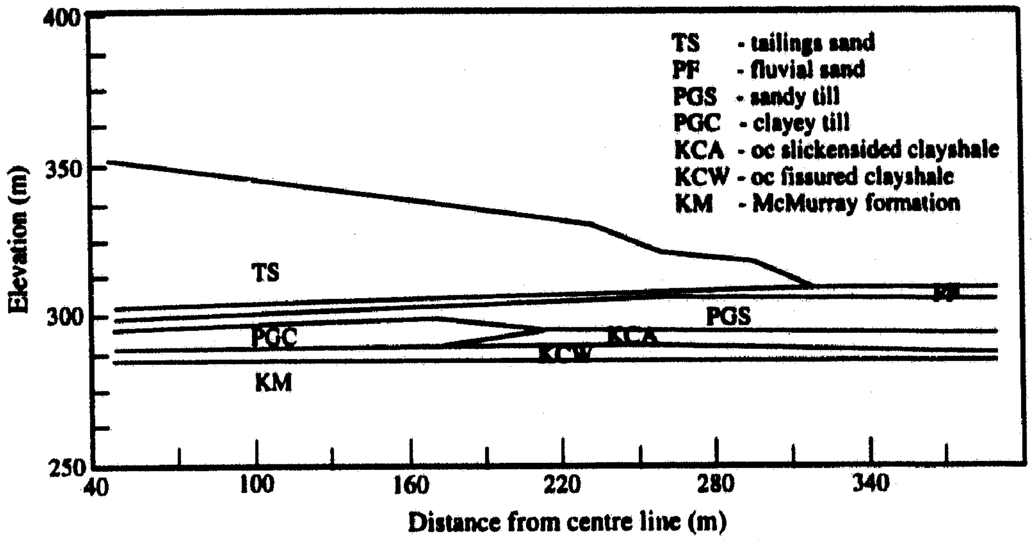

Figure 6.5 Stratigraphy of Cell 23, Section 53+00E

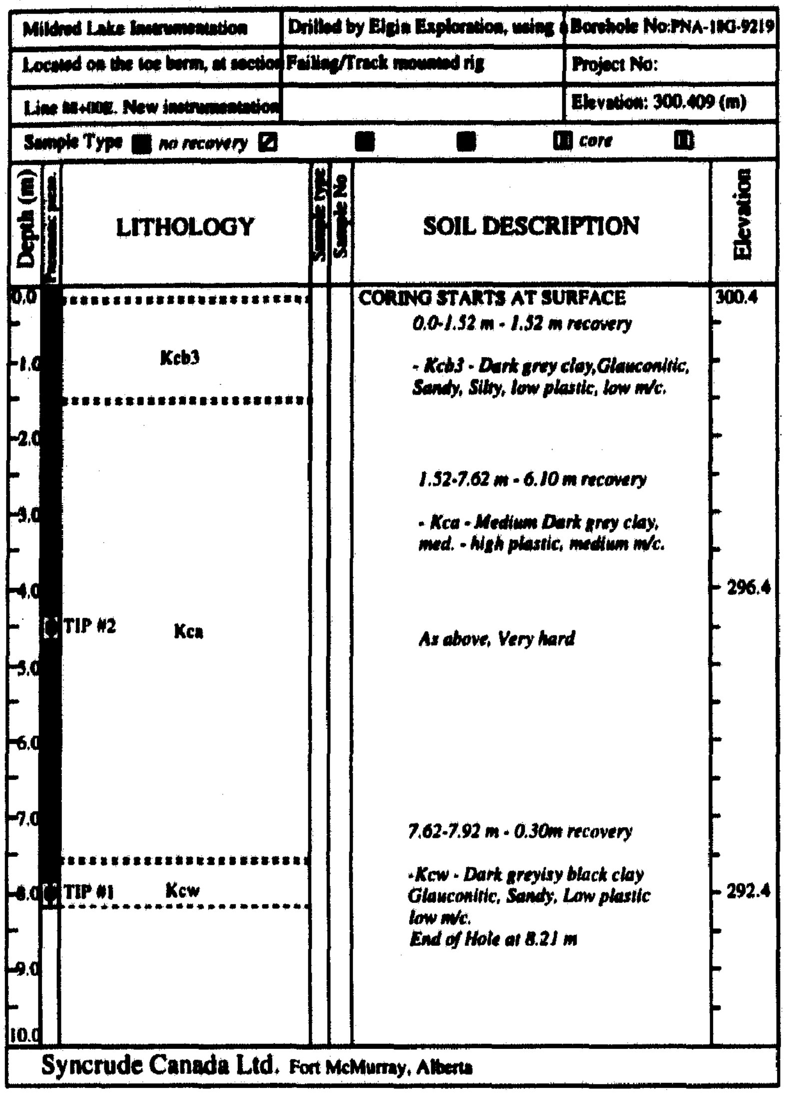

Figure 6.6 Borehole log at sampling location

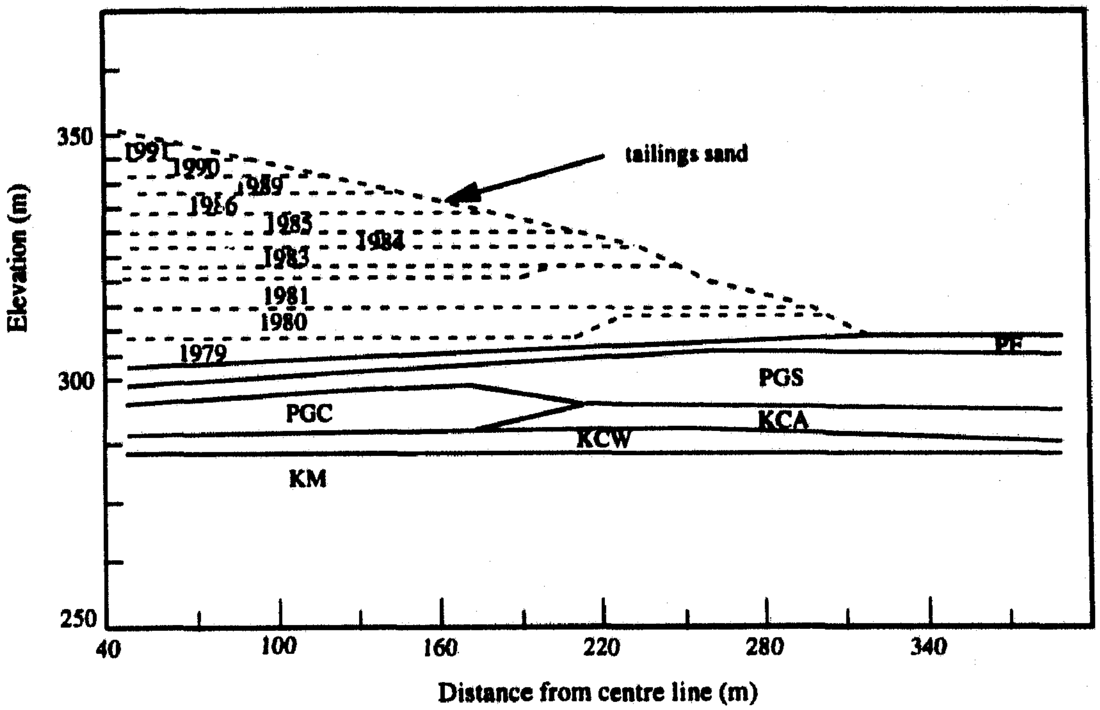

Figure 6.7 Construction stages from 1979 to 1992

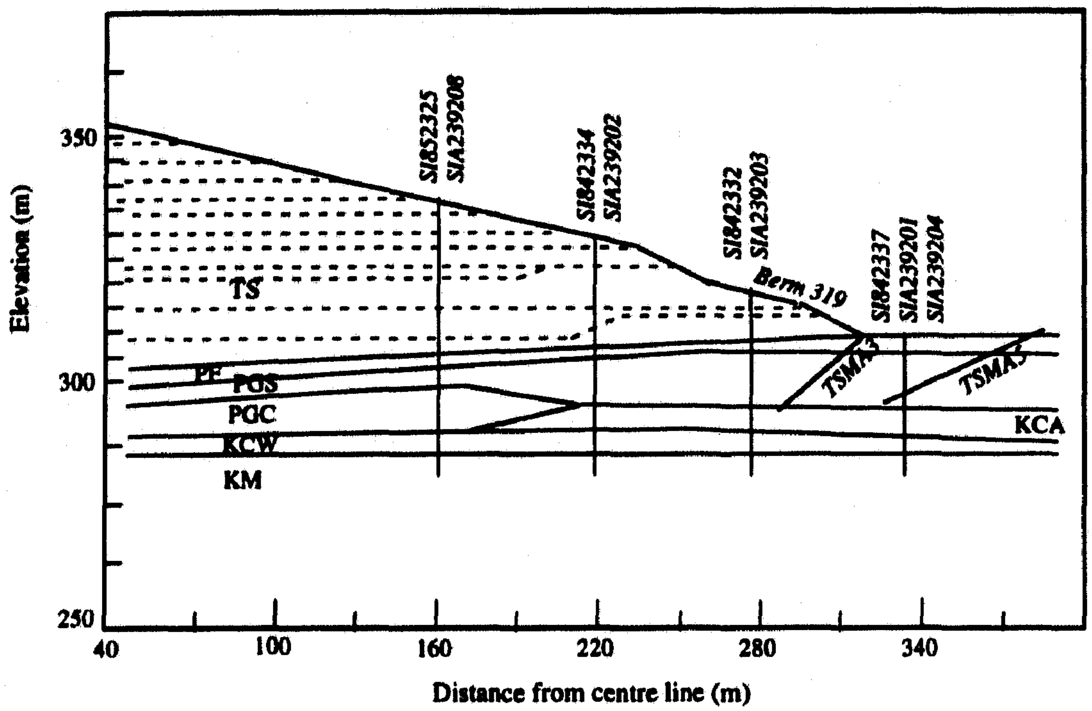

Figure 6.8 Locations of Slope inclinometers at cell 23, Section 53+00E

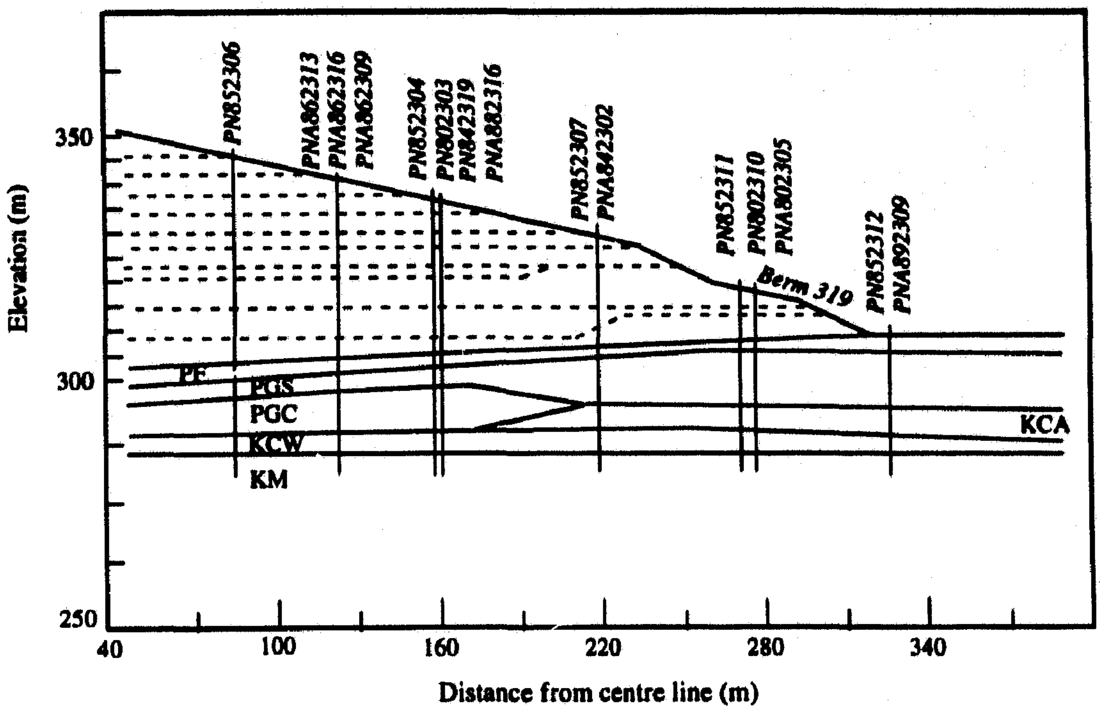

Figure 6.9 Positions of piezometers at cell 23, Section 53+00E

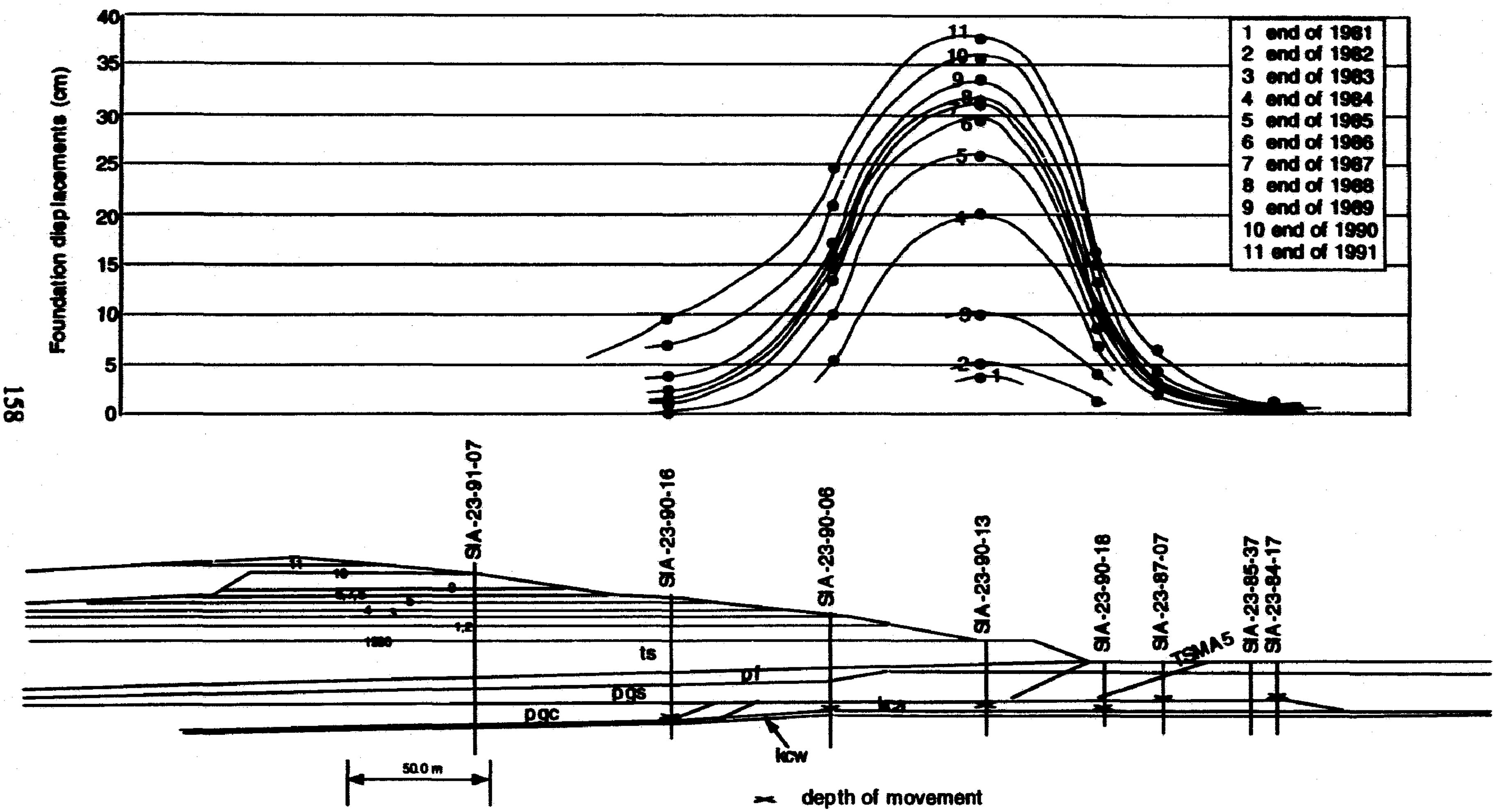

Figure 6.10 Slope inclinometer displacement at Section 53+00E, Cell 23

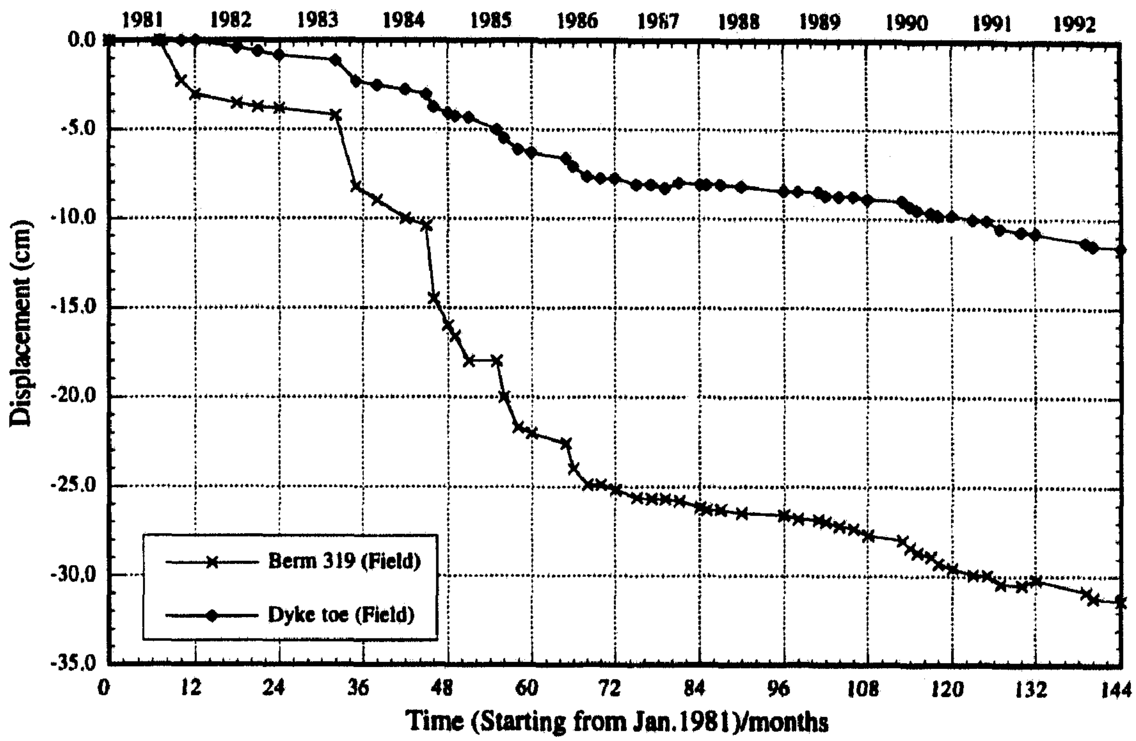

Figure 6.11 Field movements at dyke toe and berm (Cell 23, Section 53) at kcw/kca interface

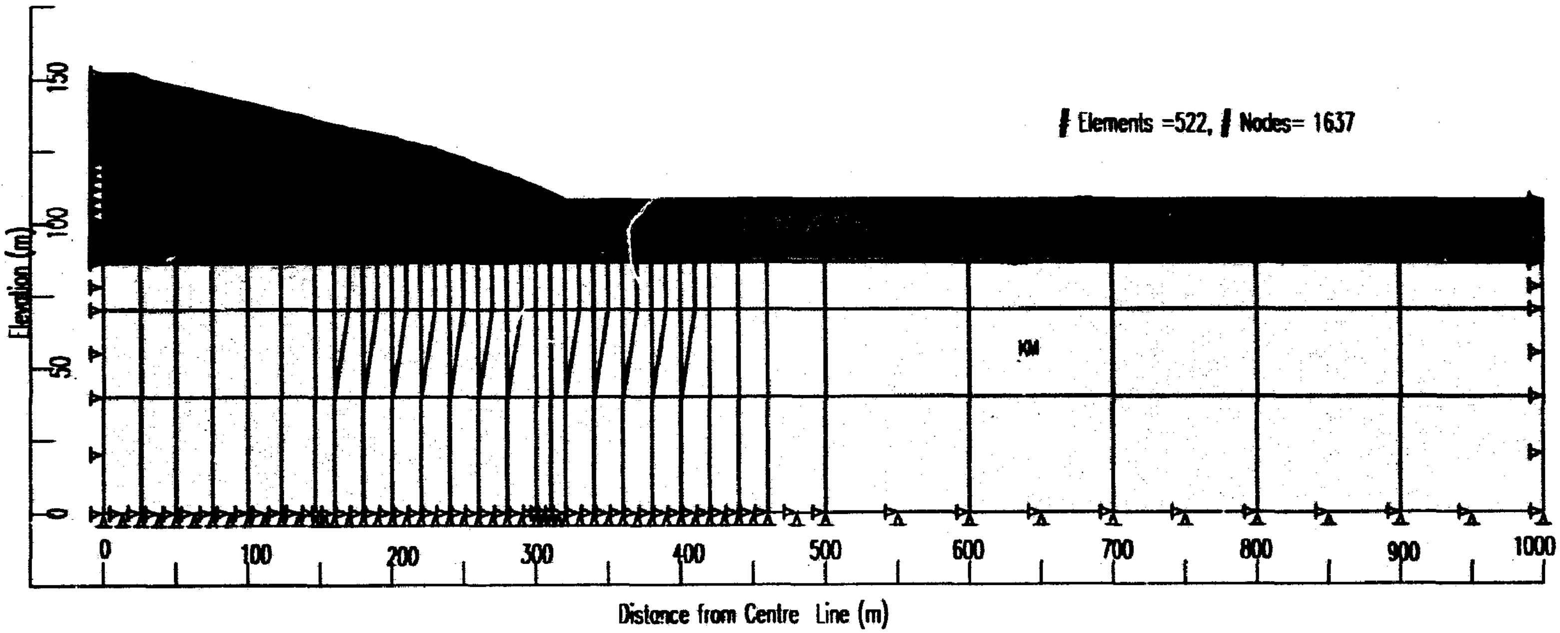

Figure 6.12 Finite element idealization of the SyncrudeTailings Dyke and the foundation

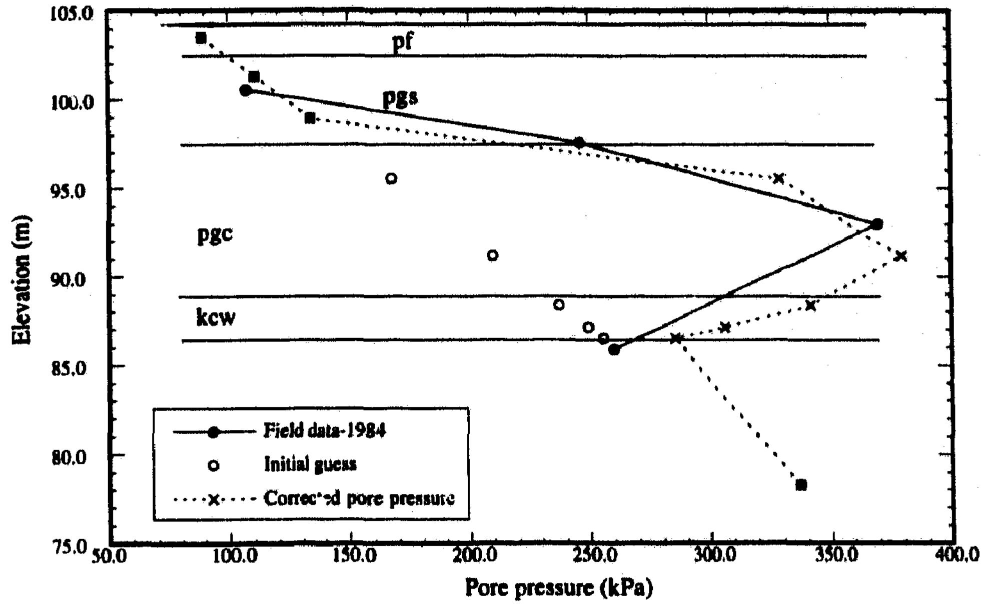

Figure 6.13 Comparison between measured and interpolated pore pressure at PN842319 position

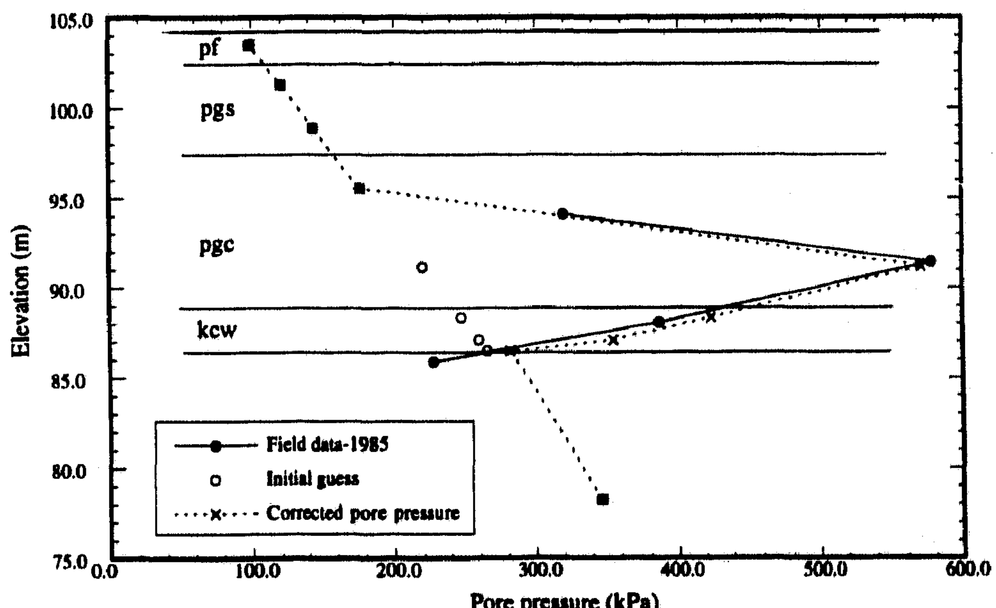

Figure 6.14 Comparison between measured and interpolated pore pressure at PN852304 position

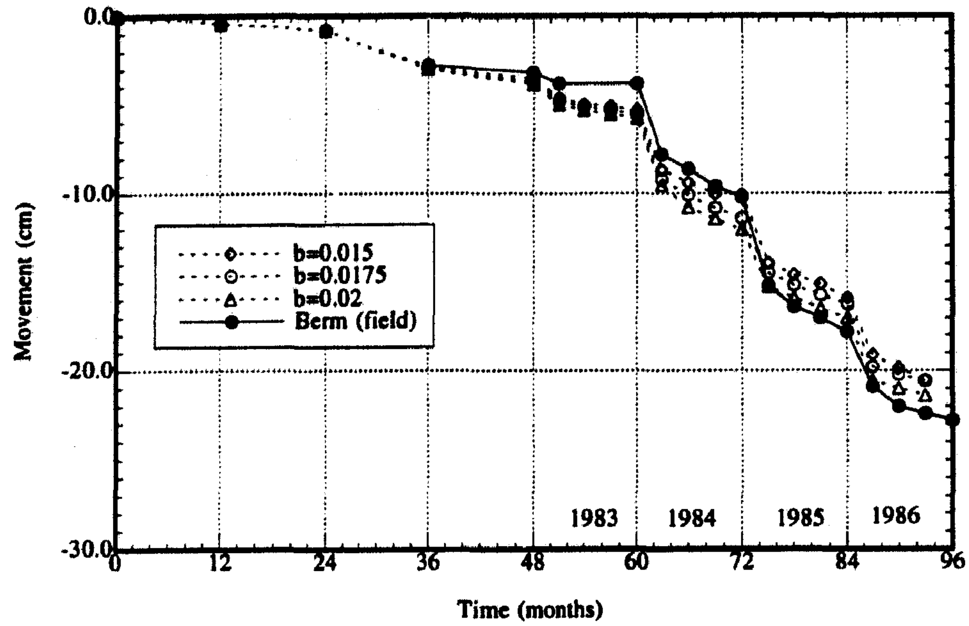

Figure 6.15 Sensitivity of calculated movements to 'b' at berm 319

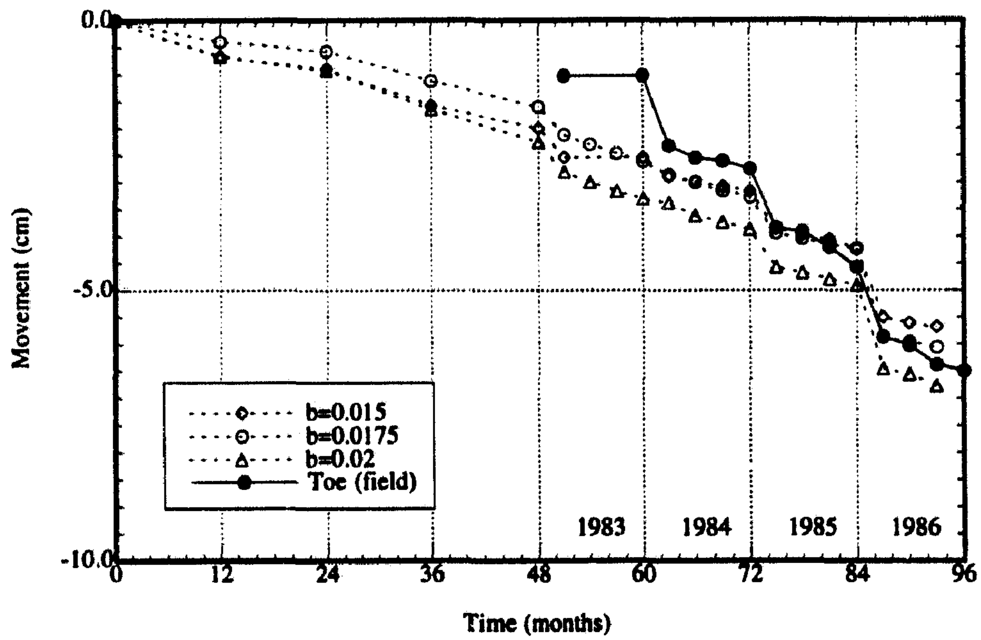

Figure 6.16 Sensitivity of calculated movements to 'b' at dyke toe

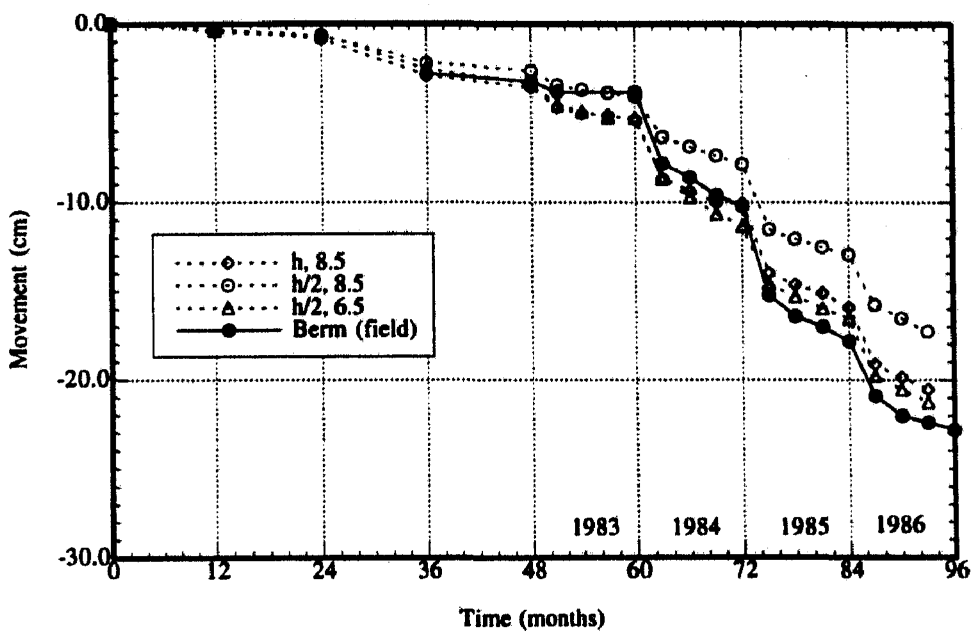

Figure 6.17 Sensitivity to 'thickness of kcw' at berm 319

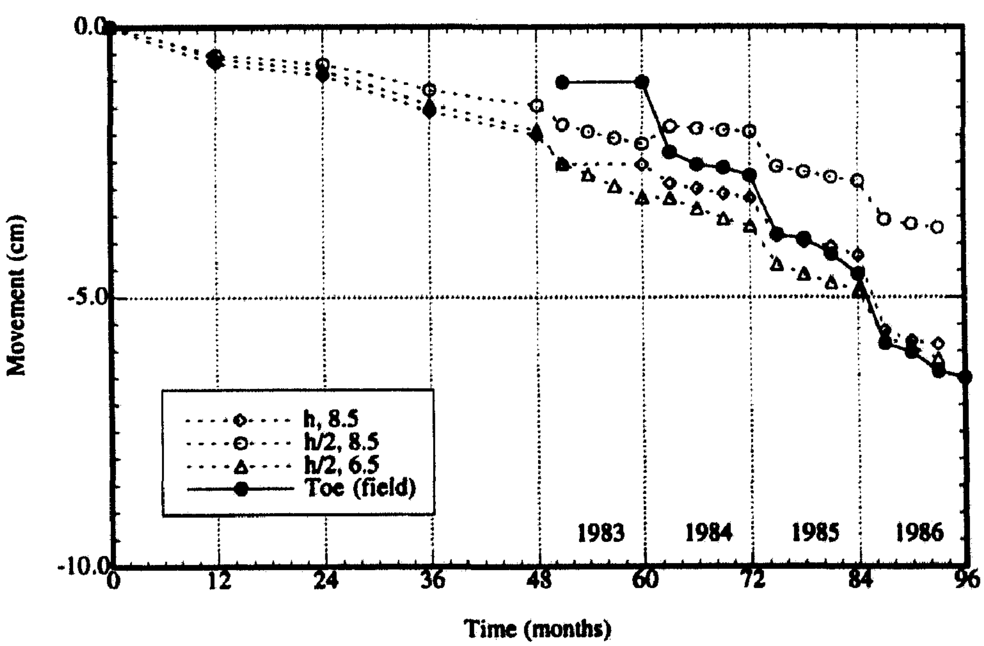

Figure 6.18 Sensitivity to 'thickness of kcw' at dyke toe

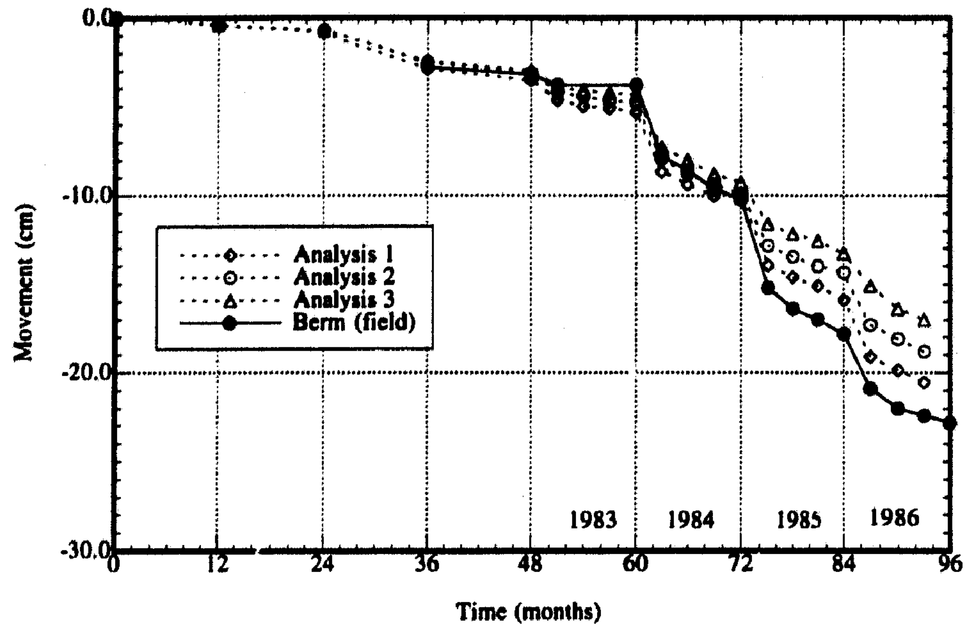

Figure 6.19 Sensitivity of movements at berm to 'stiffness of till'

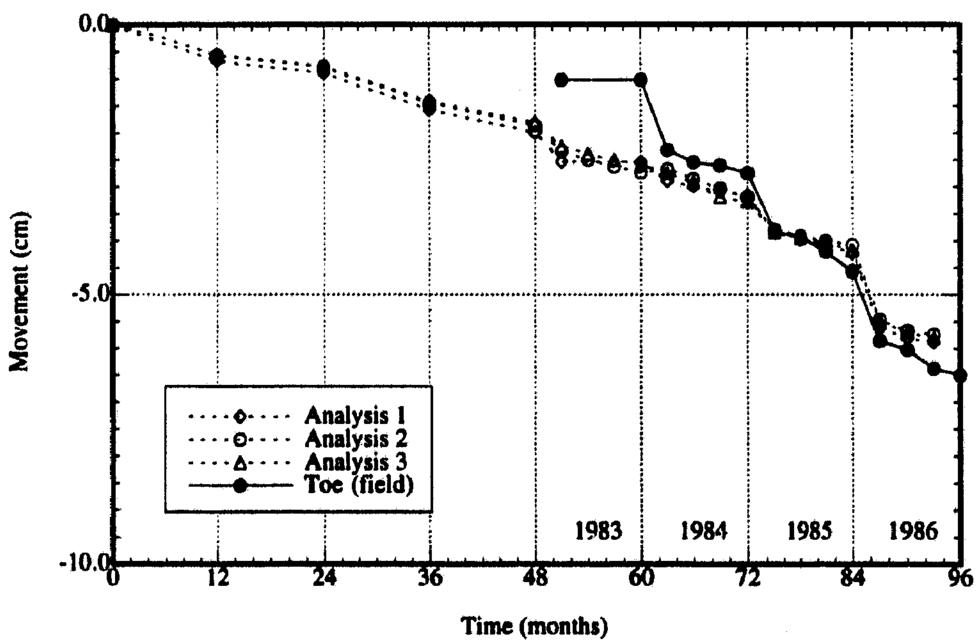

Figure 6.20 Sensitivity of movements at toe to 'stiffness of till'

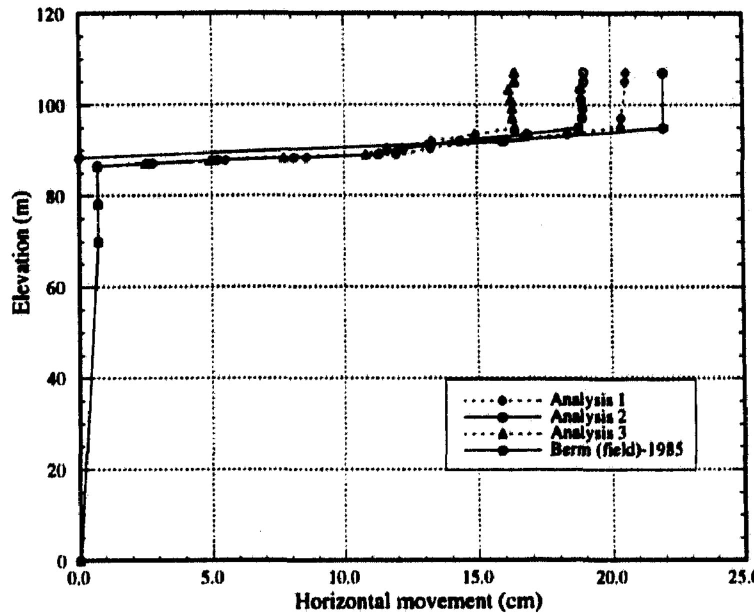

Figure 6.21 Sensitivity of Horizontal displacements to the stiffness of till at SI842332 (Berm 319) position

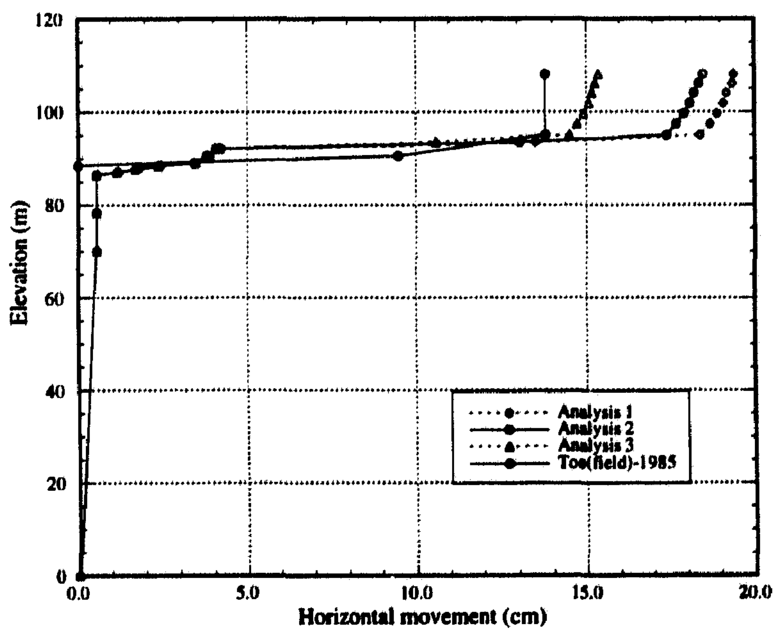

Figure 6.22 Sensitivity of Horizontal displacements to the stiffness of till at SI842337 (toe) position

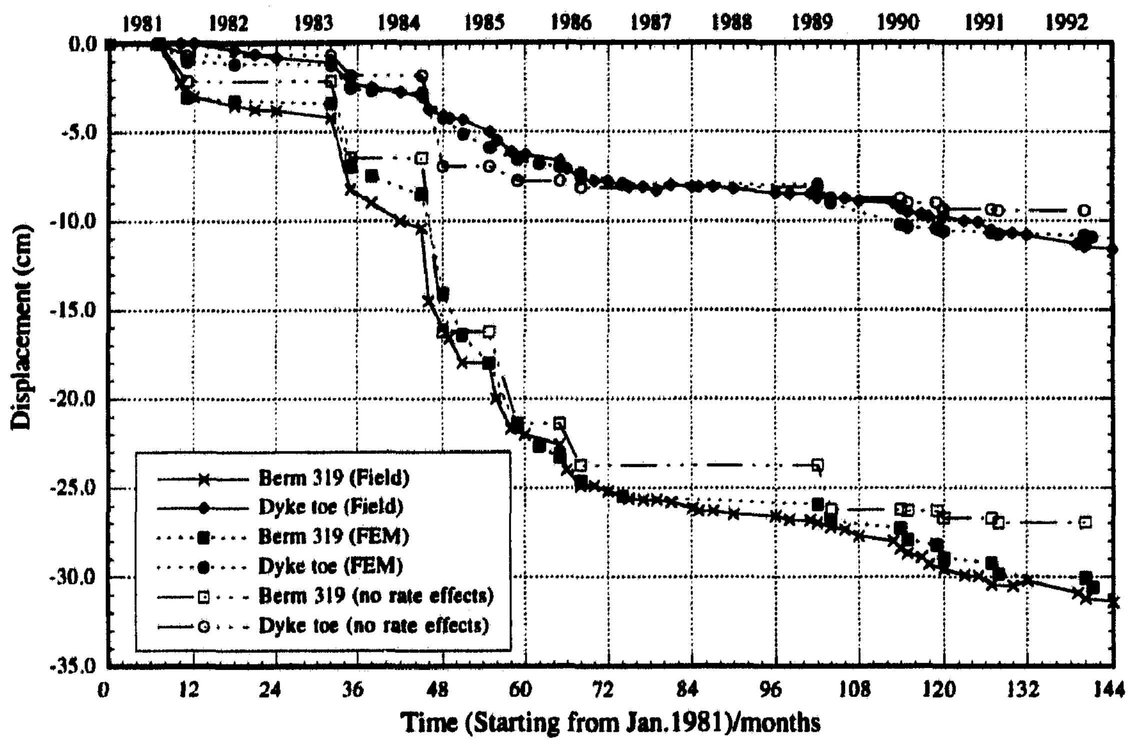

Figure 6.23 Horizontal movements at dyke toe and berm (Cell 23, Section 53) at kcw/kca interface

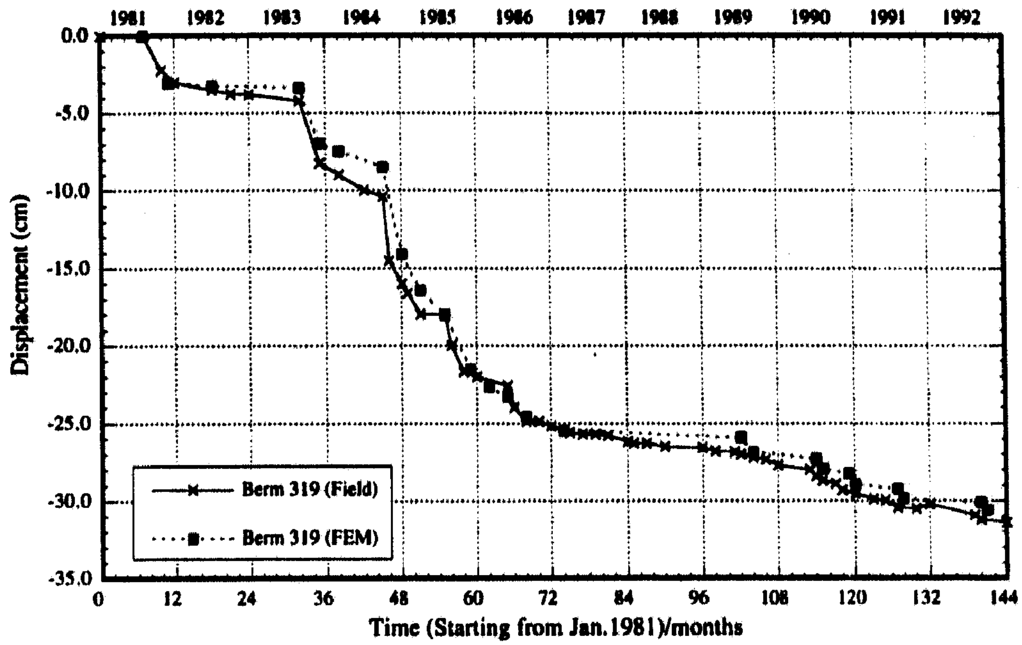

Figure 6.24 Movements at berm 319 (Cell 23, Section 53) at elevation 290.16 m SI 23-80-12 (kcw/kca interface)

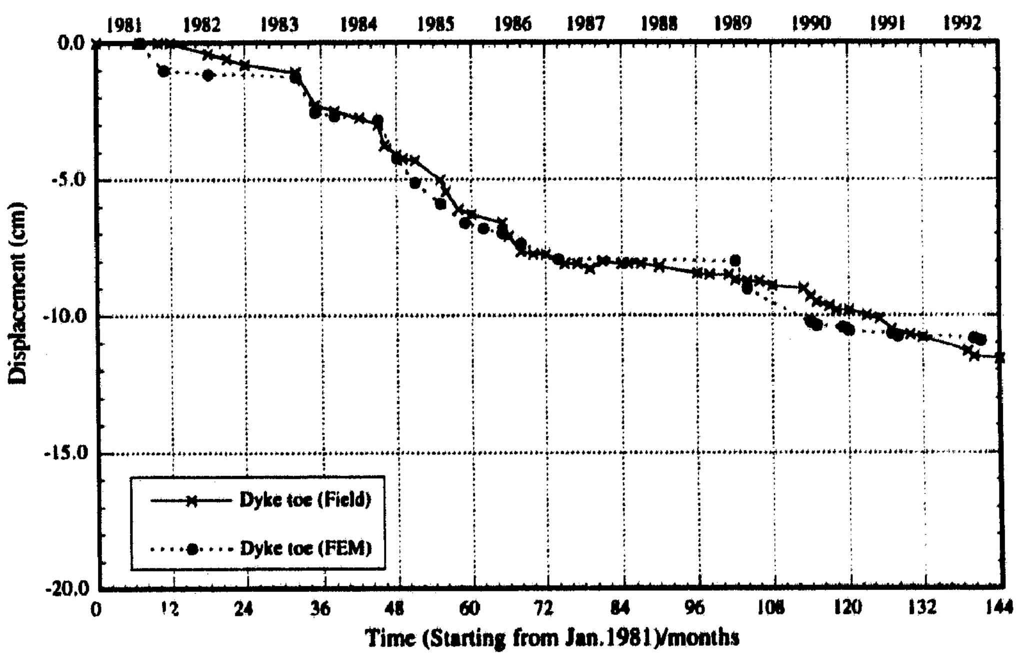

Figure 6.25 Movements at dyke toe (Cell 23, Section 53) at elevation 288.2m SI 23-81-03 (kcw/kca interface)

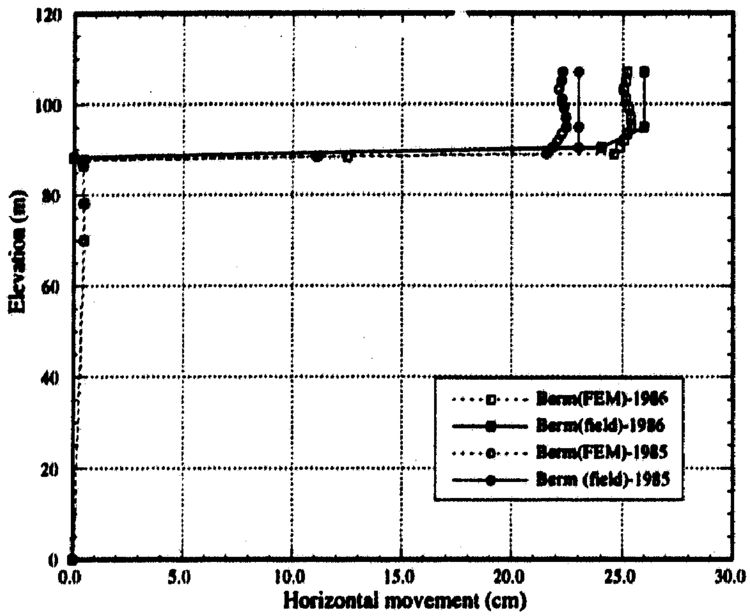

Figure 6.26 Comparison between measured and calculated Horizontal displacements at SI842332 (Berm 319) position

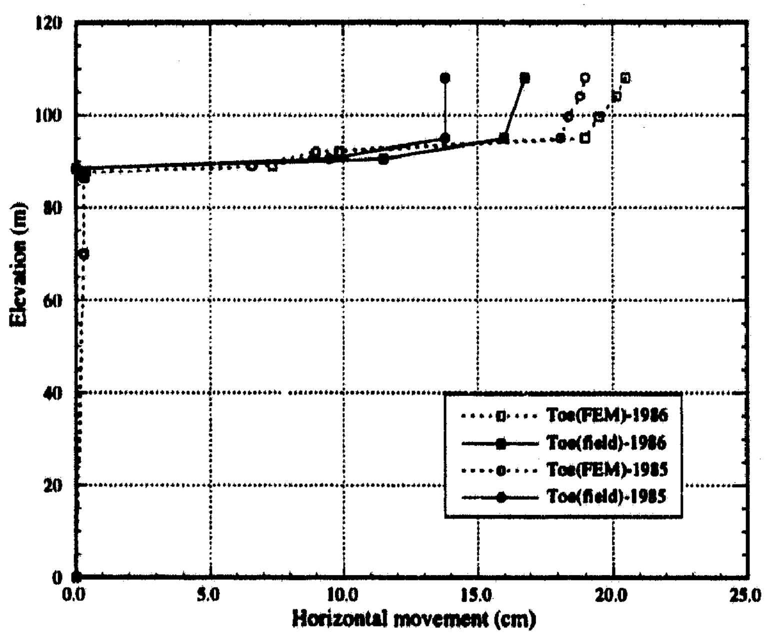

Figure 6.27 Comparison between measured and calculated Horizontal displacements at SI842337 (Toe) position

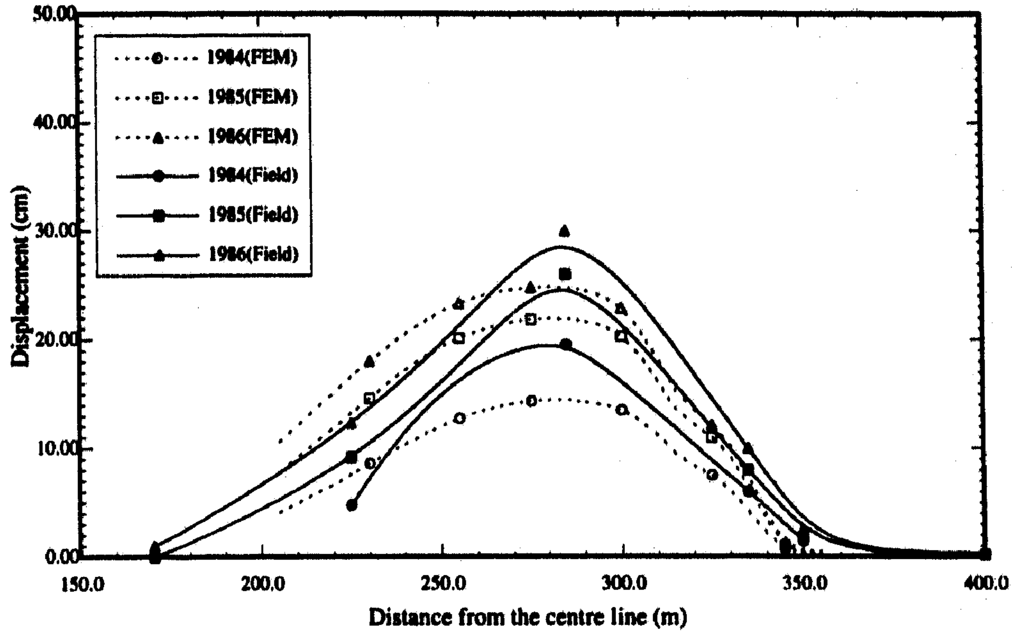

Figure 6.28 Displacement along the shear zone

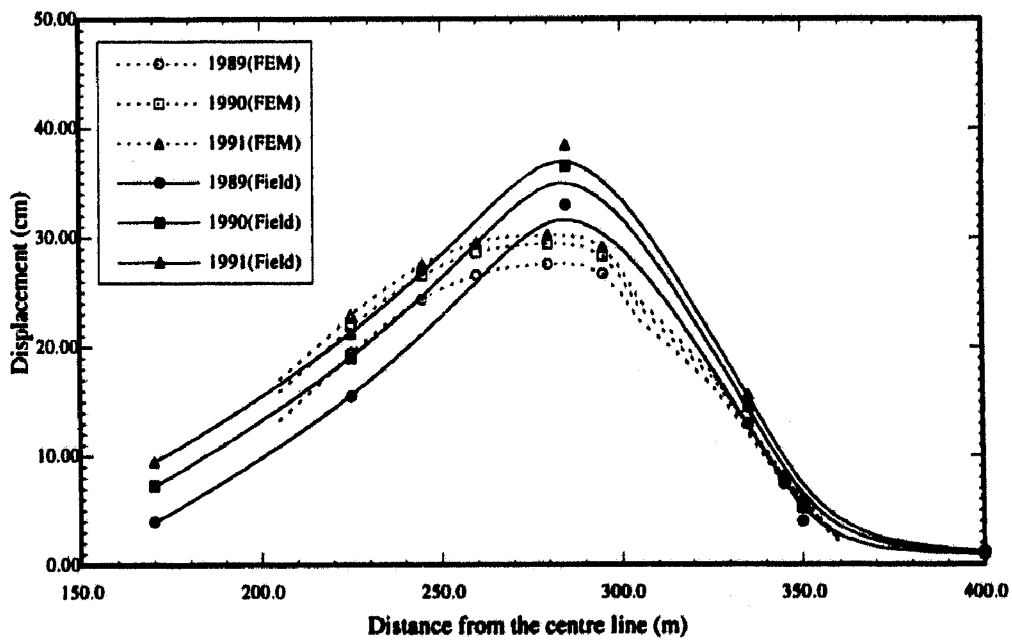

Figure 6.29 Displacement along the shear zone

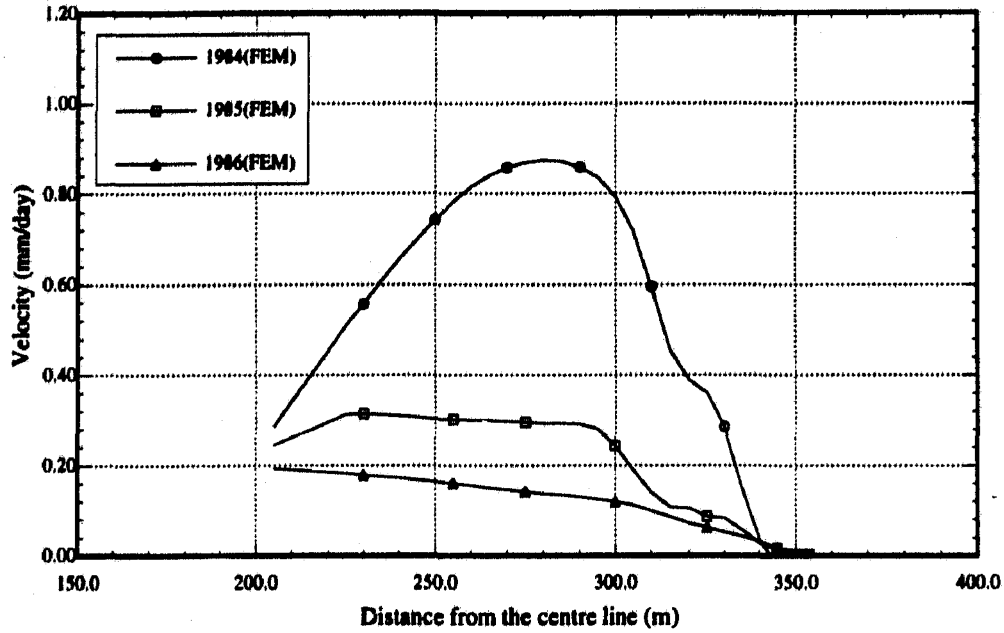

Figure 6.30 Velocity along the shear zone

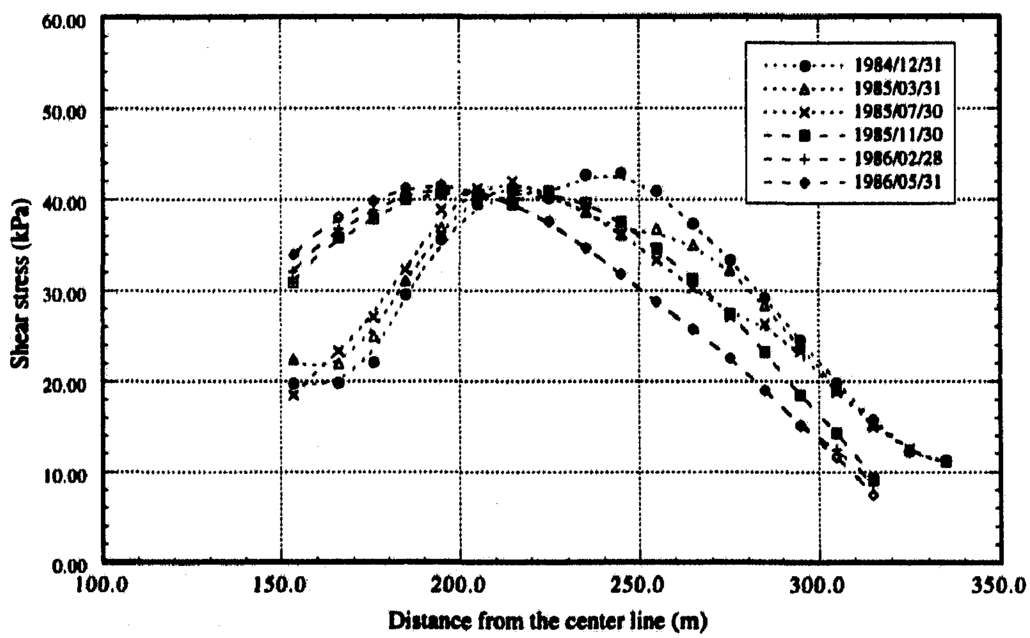

Figure 6.31 Calculated stress redistribution along shear surface during construction years 1984 & 1985

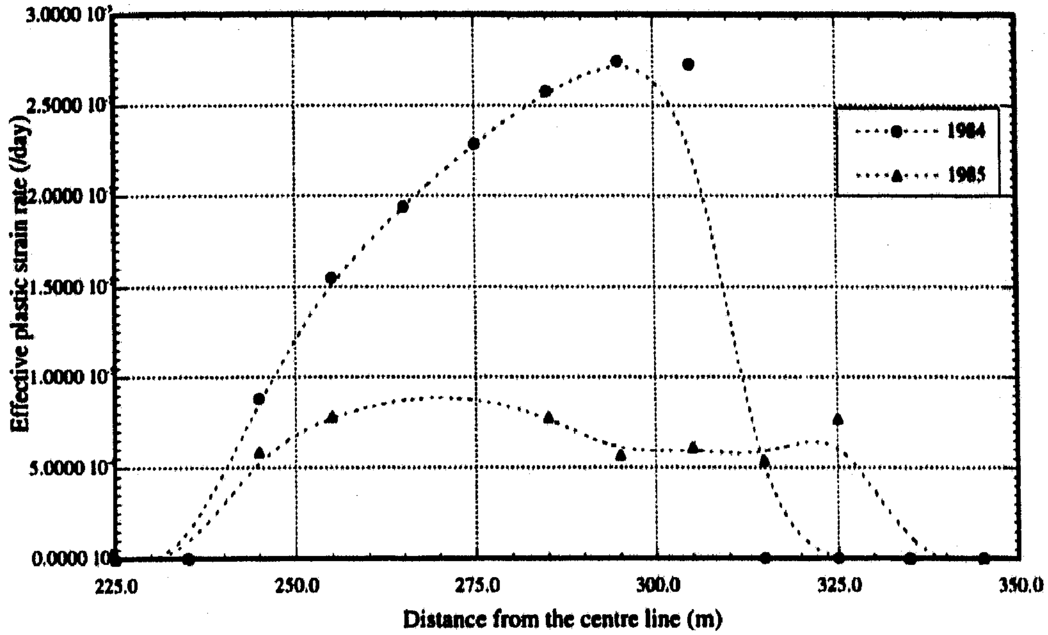

Figure 6.32 Effective plastic strain rate in shear zone

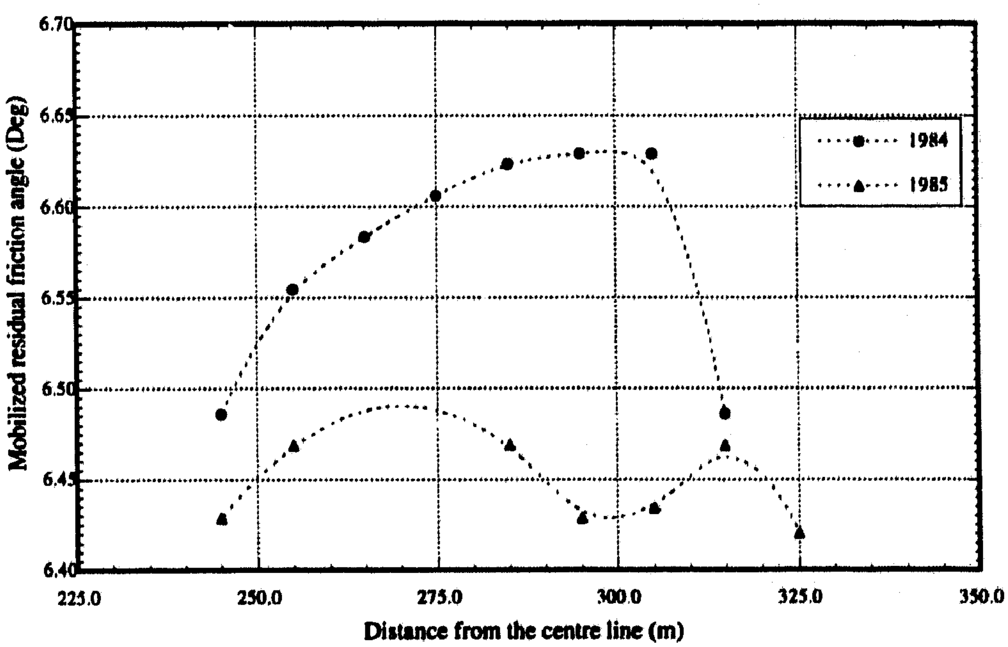

Figure 6.33 Mobilized residual friction angle in shear zone

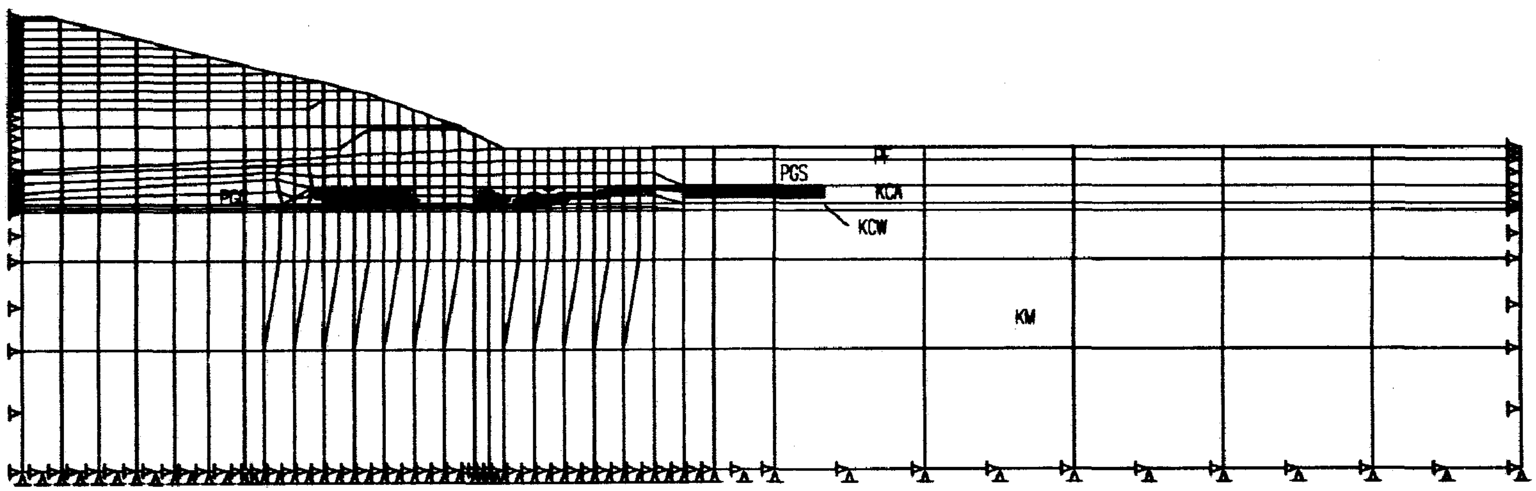

Figure 6.34 Yield zone at the end of construction year 1984

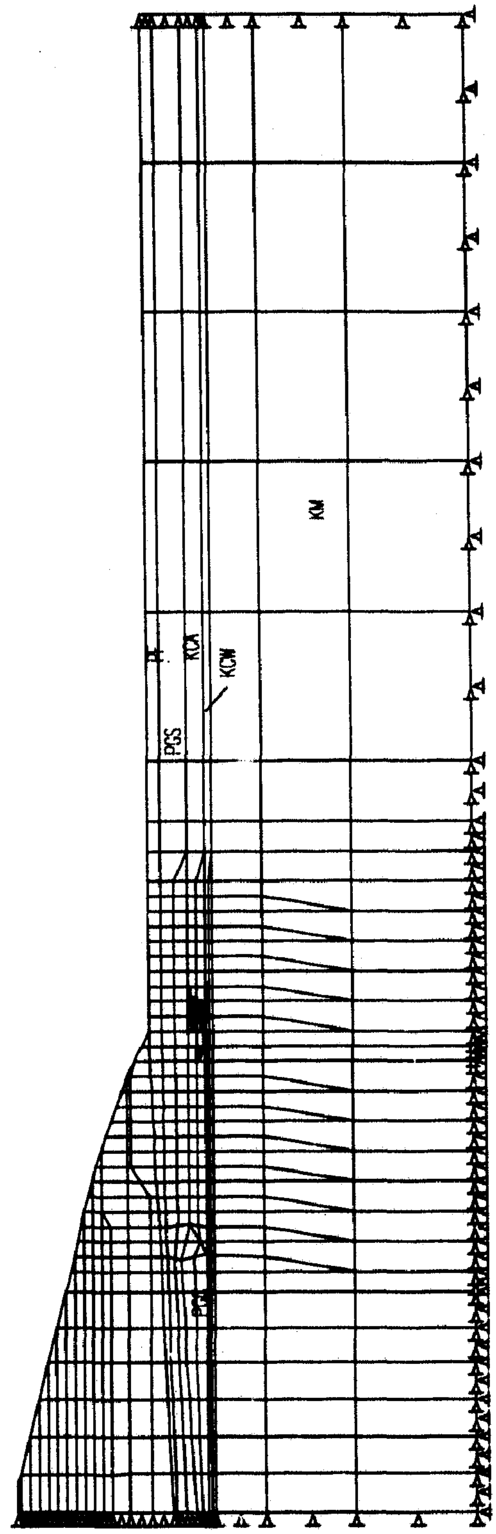

Figure 6.35 Yield zone at the end of construction year 1991

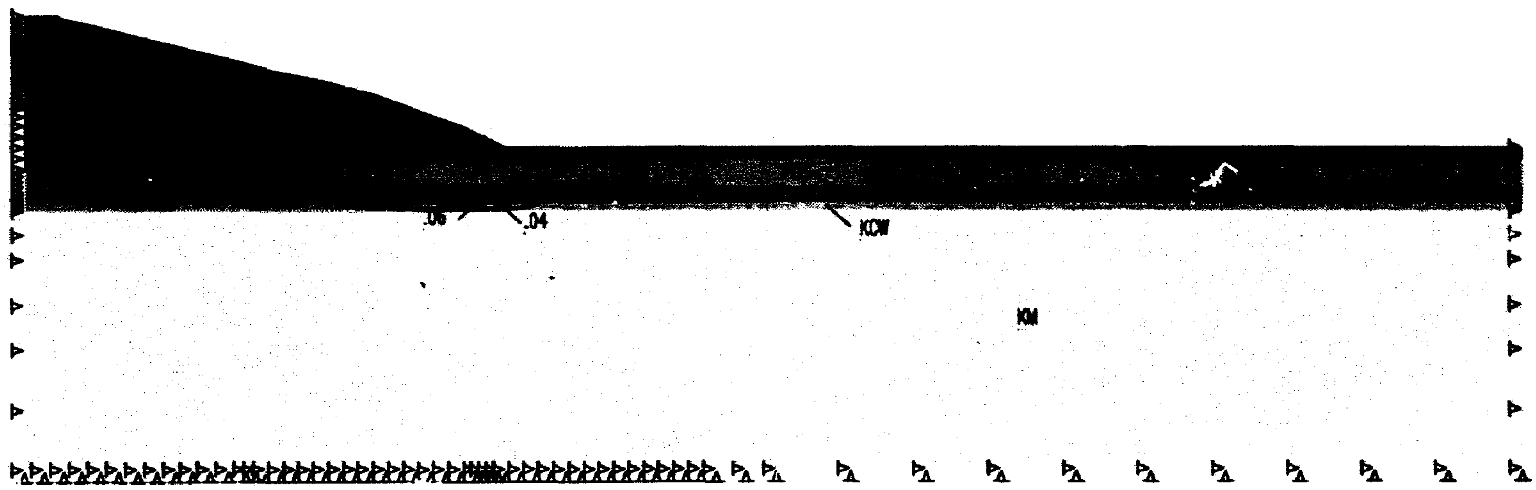

Figure 6.36 Maximum shear strain contours at the end of construction year 1984

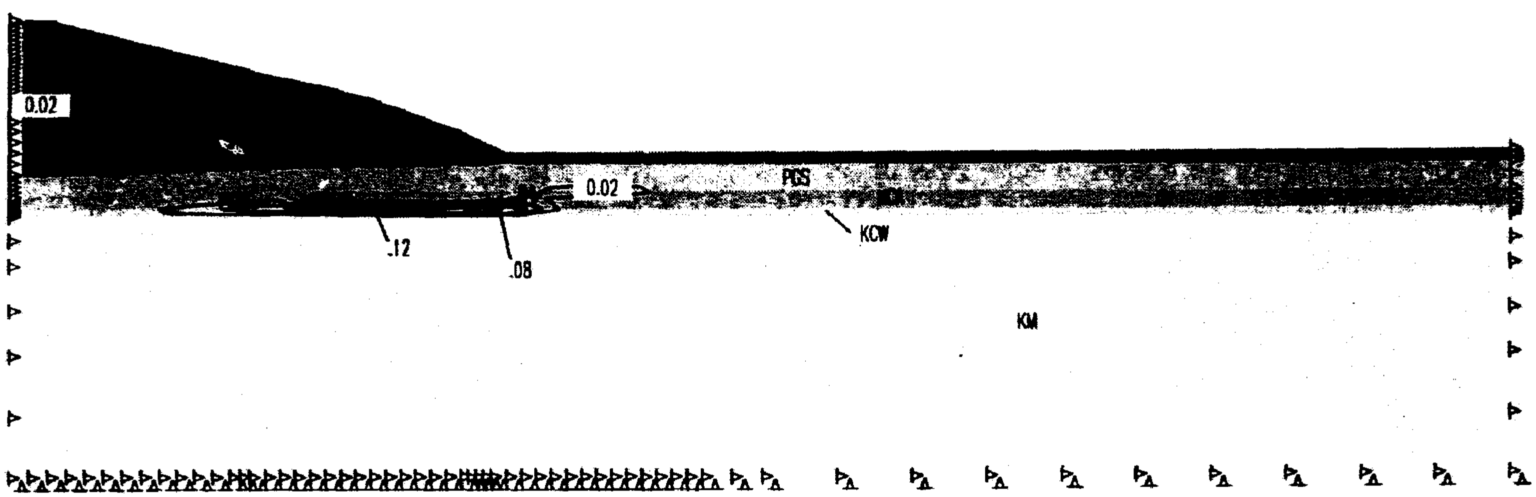

Figure 6.37 Maximum shear strain contours at the end of construction year 1991

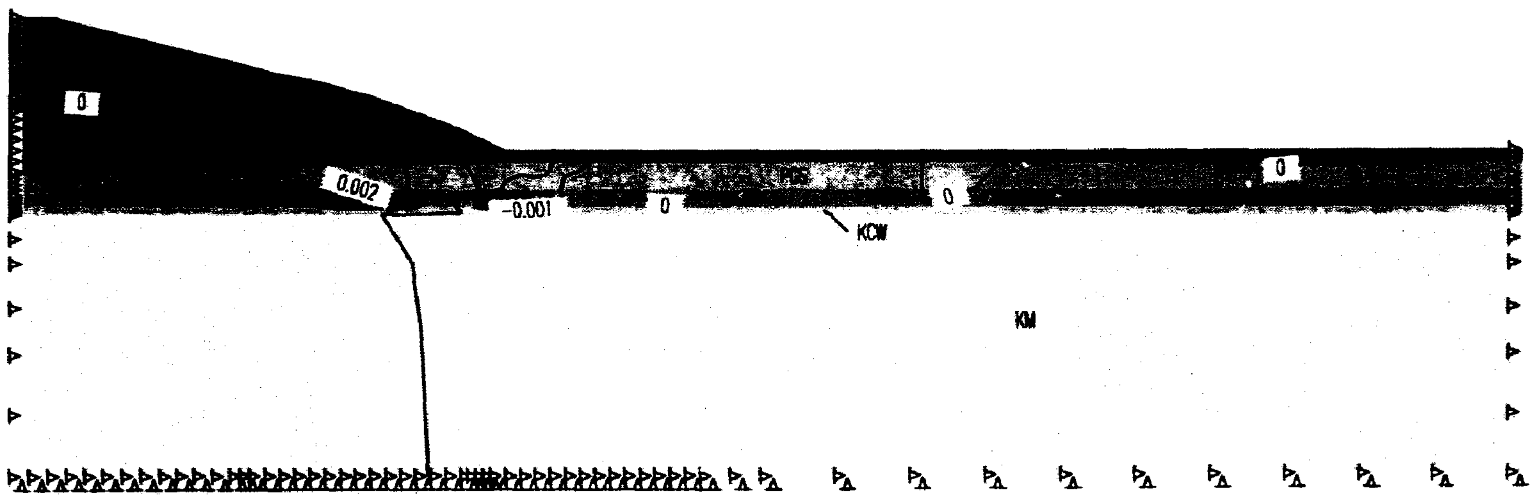

Figure 6.38 Horizontal strain contours at the end of construction year 1984

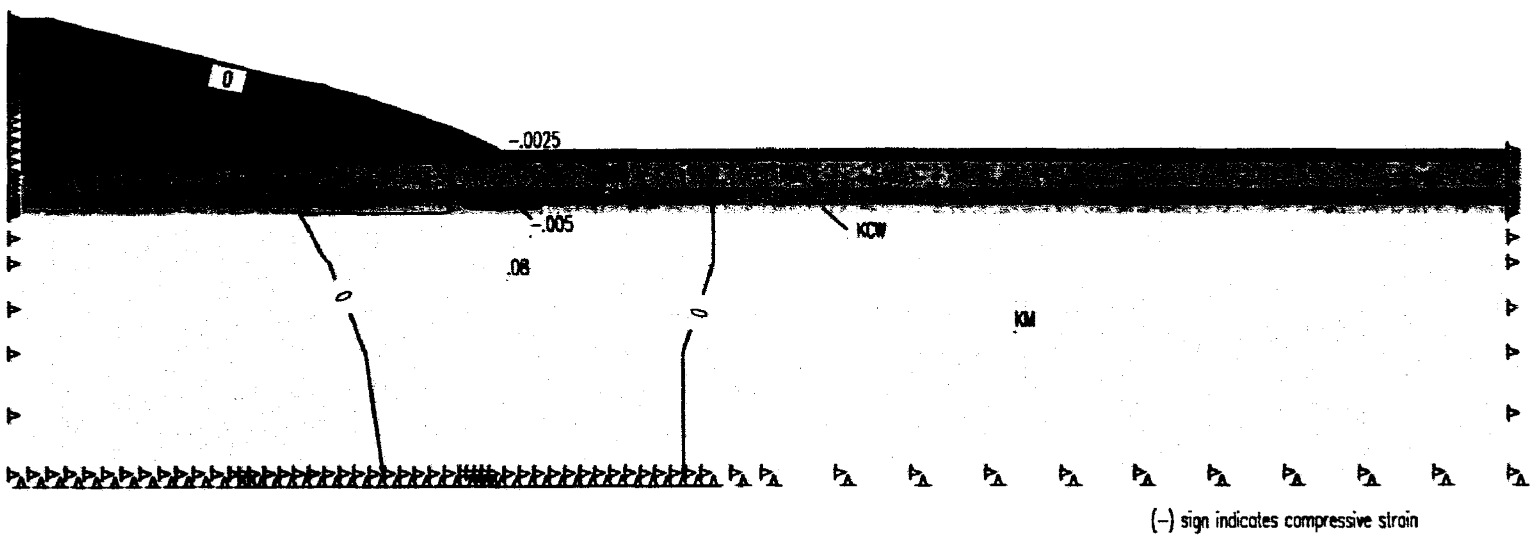

Figure 6.39 Horizontal strain contours at the end of construction year 1991

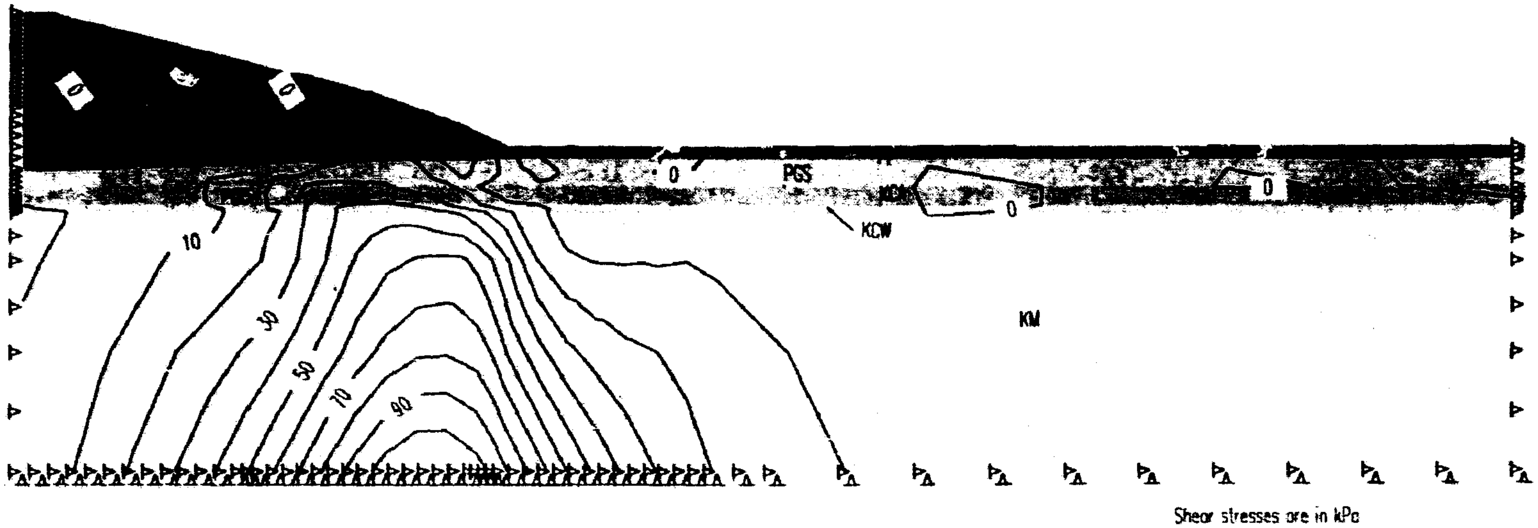

Figure 6.40 X-Y Shear stress contours at the end of construction year 1984

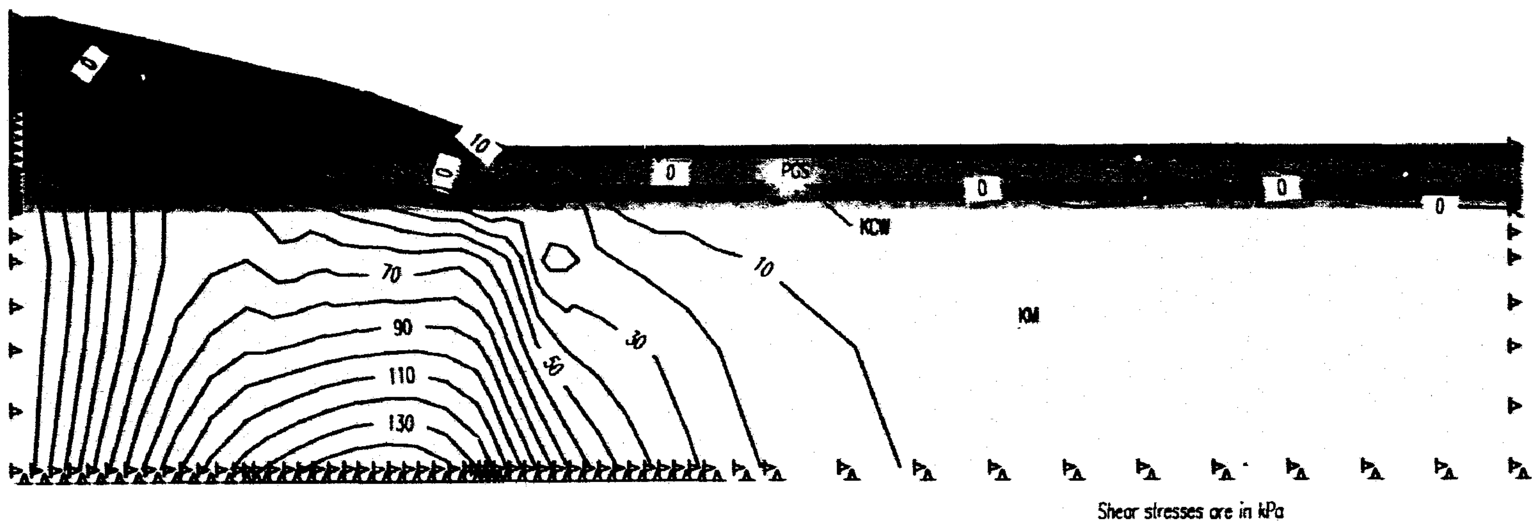

Figure 6.41 X-Y Shear stress contours at the end of construction year 1991

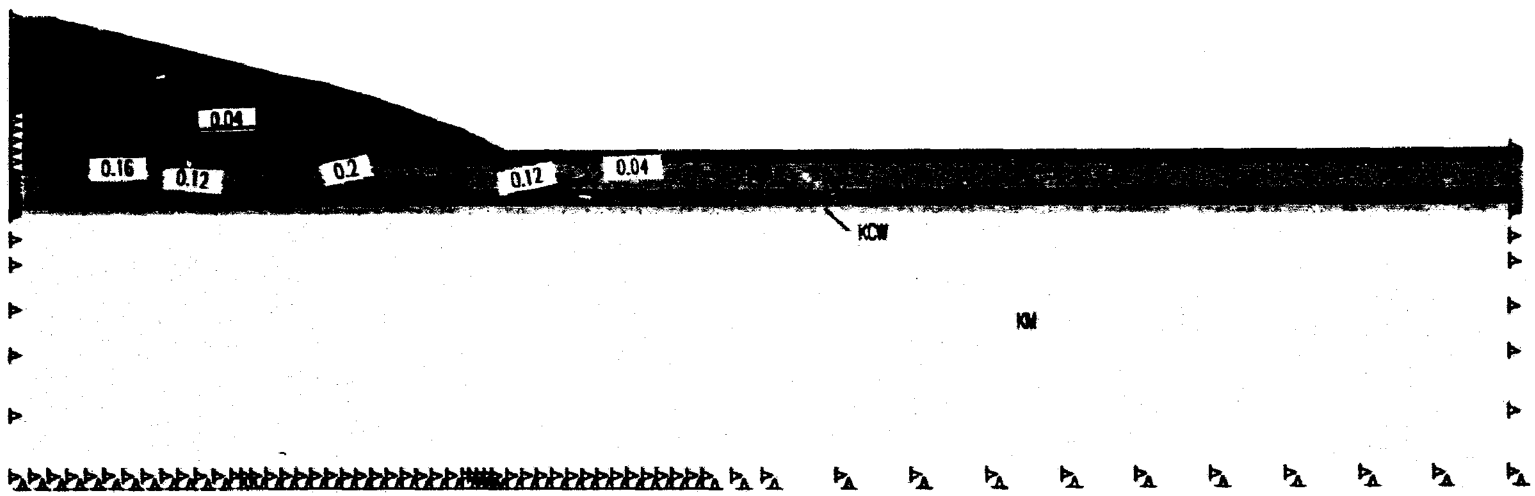

Figure 6.42 Failure ratio in the till at the end of construction year 1984

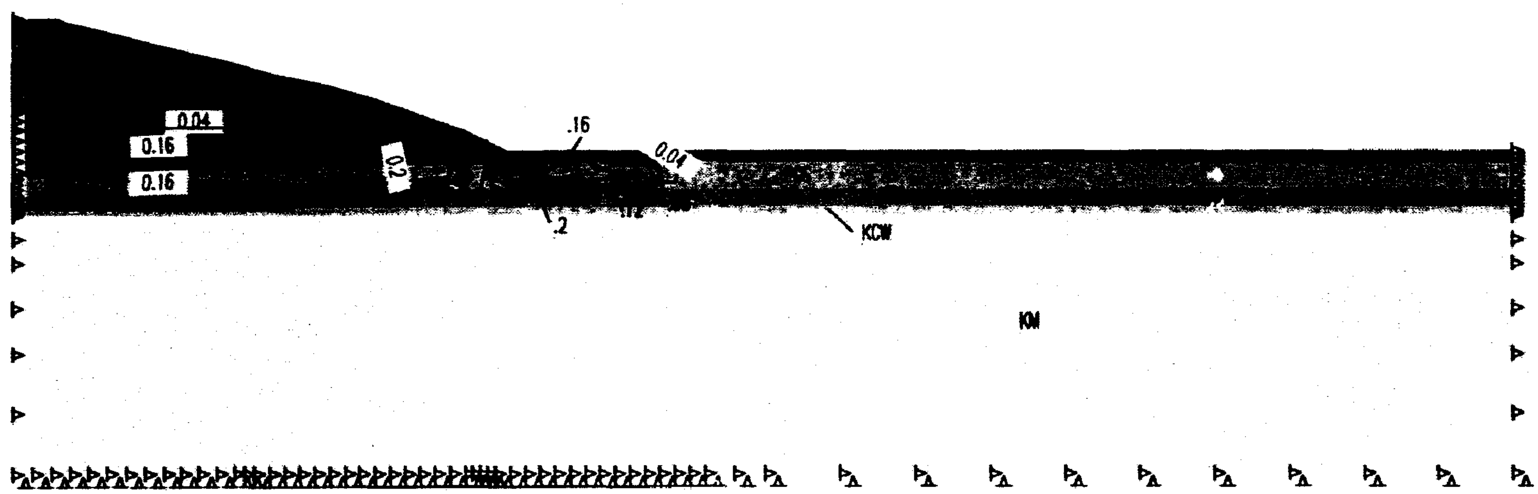

Figure 6.43 Failure ratio in the till at the end of construction year 1991

CHAPTER VII

7.1 Conclusions

1 The Clearwater clay shale at Syncrude tailings dyke site is found to have a deformation rate-dependent residual strength.

The high plastic clay of natural water content ~23%, clay content of ~49%, Liquid Limit of ~135% and Plastic Limit of ~28% shows relatively low residual friction angle under normal laboratory test rates. There is an increase of 3.4 to 3.5% of the residual shear strength when the rate is increased by ten times. On the ring shear test the soil shows a residual friction angle of 6.6° at a strain rate of 0.001/day, whereas this value for the direct shear test is 7.5°.

In general, rate effects observed here are relatively higher than those observed for London clay and Edale Shale (Petley, 1966). However, similar rate effects have been reported for a varved clay by Nieuwenhuis (1991) and Salt (1988). From the available test data, a broad correlation is found between plasticity and rate effects. Rate effects show a nearly linear increase with the plasticity of the clay.

2. Modeling the rate effects on residual strength in a deformation analysis can be done by an extension of the plasticity theory. The concept of dynamic yield surface, which is a function of the strain rate, can be used to calculate the behavior under plastic yielding. The main advantage in this type of formulation is that the model can be added into existing finite element programs with little difficulty.

3. Application to the Mam Tor landslide reveals that during a year with average rainfall over the area, a change of residual friction angle of 0.2° above the reference angle of 14° causes a control in the order of 10% of movements computed using a conventional elasto-plastic model. The observed horizontal movement at a road within the slide is ~0.1 m a year. The use of a rate-dependent soil model for the shear zone resulted in a similar magnitudes of movement.

4. The use of the rate-dependent model in the shear zone in combination with a non-linear elastic hyperbolic model for the overlying material at the Salledes test embankment (Cartier and Pouget, 1988) was able to simulate the construction movements of the foundation soils. However, using such a rate-dependent model does not produce any remarkable advantage for the case considered here. The finite element model used in this study was not able to simulate the large movements which occurred after construction.

5. The movements at Syncrude tailings dyke increase with time after each year's construction of the dyke layers. These movements occur under nearly constant effective stress conditions. Field monitoring reveals that the majority of movements occur within a relatively thin layer of *kcw* in the foundation of the dyke.

Modeling the *kcw* according to a deformation rate dependent model is performed here. Evolution of field movements with time is compared with computed movements for two selected locations at Cell 23, Section 53+00E of the dyke. The continuing movements after construction were found to be modeled to a reasonable accuracy using the concept of rate-dependence of residual strength of shear zone material.

Of all cases studied in this work, the case of foundation movements at the Syncrude tailings dyke can be chosen as a proper field case to show the applicability of the model developed during the same study.

7.1 Recommendations for further research

1. The existing literature on rate effects on the residual strength of clays is limited. Further residual strength tests on wide variety of clays, at different rates, would be useful to enhance the data base. The correlation found between rate effects and soil plasticity needs to be expanded for a large number of clays.

2. The strain rate-dependent model developed in this study can be extended, and applied to other materials such as, sand, frozen soils.

3. A study on the relationship between thickness of field shear zone and laboratory shear zone, and therefore, the relationship between laboratory and field strains will be useful.

4. Numerical models, which can handle the strain incompatibility, and large slips across the shear zone would improve the results of deformation analyses.

BIBLIOGRAPHY

Anderson, W.F. and Hammoud, F. 1988. Effect of testing procedures in ring shear tests. Geotechnical Testing Journal, **11**.3: 204-207.

Bertini, T., Cugusi, F., D'elia, B., Lango, G. and Rossi-Doria, M. 1992. Slow movement investigation in clay slopes. Proceedings, 6th International Symposium on Landslides, Christchurch, New Zealand, Vol.1. pp. 329-334.

Bishop, A.W., Green, G.E., Garga, V.K., Anderson. A., and Brown, J.D. 1971. A new ring shear apparatus and its application to the measurement of residual strength. Geotechnique, **21**.4: 273-328.

Blondeau, F. and Perrot, A. 1976. Le versant experimental de Ville-au-val (Meurthe et Moselle). Bull. liaison Labo. P.et Ch., No. special II, pp. 107-117.

Borja, R.I., Hsieh, H.S. and Kavazanjian, E. Jr. 1990. Double-yield-surface model II: Implementation and verification. ASCE, Journal of Geotechnical. Engineering Division, **9**: 1402-1421.

Borowicka, H. 1965. The influence of colloidal content on the shear strength of clay. Proceedings, 6th International Conference on Soil Mechanics and Foundation Engineering, Montreal, Vol. 1. pp.175-178.

Bracegirdle, A., Vaughan, P.R. and Hight, D.W. 1992. Displacement predictions using rate effects on residual shear strength. Proceedings, 6th International

Symposium on Landslides, Christchurch, New Zealand, Vol. 1. pp. 343-348.

Bromhead, E.N. 1979. A simple ring shear apparatus. Ground Engineering, **12**.5: 40-44.

Casagrande, A. and Wilson, D. 1951. Effect of rate of loading on the strength of clays and shales at constant water content. Geotechnique, **2**: 251-263.

Cartier, G. and Pouget, T.P. 1988. Etude du comportement d'un remblai construit sur un versant instable le remblai de Salledes (Puy - de - Dome). Report de recherche LPC No 153, Laboratoire Central des Ponts et Chaussees, Paris.

Chan D. H. and Morgenstern, N. R. 1992. PISA, Program for Incremental Stress Analysis, Users Manual. University of Alberta, Canada.

Chattopadhyay, P.K. 1972. Residual shear strength of some pure clay minerals. Ph.D. Thesis, University of Alberta, Canada.

Clauss, F.J. 1972. Solid lubricants and self-lubricating solids. Chapter 3, Academic press, New York.

Davis, R.O., Smith, N.R. and Salt, G.A. 1990. Pore fluid frictional heating and stability of creeping landslides. International Journal of Numerical and Analytical Methods in Geomechanics, **14**: 427-443.

Davis, R.O., Desai, C.S. and Smith, N.R. 1993. Stability of motions of translational landslides. ASCE Journal of Geotechnical Engineering, **119**: 251-263.

De Aencar, J.A. 1988. Deformations of dams on sheared foundations. Ph.D. Thesis, University of Alberta, Canada.

De Aencar, J.A., Chan, D.H. and Morgenstern, N.R. 1992. Incorporation of measured pore pressure in finite element analysis. Proceedings, 45th Canadian Geotechnical Conference, Toronto, Ontario, Vol. 62. pp. 1-10.

Drysdale, W. H. 1984. An extension of the theory of plasticity for rate effects, Mechanical properties at high rates of strains. Proceedings, Third Conference on Mechanical Properties of Materials at High Rates of Strains, Oxford, pp. 143-150.

Drysdale, W. H. 1987. The inclusion of rate and temperature dependent behavior within plastic theory. U S Army Ballistic Research Laboratory, Aberdeen Proving Ground, MD, pp. 691-697.

Duncan, J. M. and Chang, C. Y. 1970. Nonlinear analysis of stress and strains in soils. ASCE, Journal of the Soil Mechanics and Foundations Division, **96**. SM 5: 1629-1653.

Fair, A.E. and Handford, G.T. 1986. Overview of the tailings dyke instrumentation program at Syncrude Canada Ltd. *In* Geotechnical Stability in Surface Mining. *Edited by* R.K. Singhal, A. A. Balkema, Rotterdam, pp. 245-254.

Fukuzono, T. 1990. Recent studies on time prediction of slope failure. Landslide

News, **4**: 1-23.

Gibson, R. E. and Henkel, D. J. 1954. Influence of duration of tests at constant rate of strain on measured 'drained' strength. Geotechnique, **4**: 6-15.

Haggman A. J. 1971. Prediction of stress and strain under drained loading conditions. Ph.D. Thesis, MIT, USA.

Handford, G.T. 1985. Review of Cell 23 slope design, Syncrude Canada Ltd. Internal Report.

Hvorslev, M.J. 1960. Physical components of shear strength of saturated clays. ASCE Research Conference on Shear Strength of Saturated clays, University of Colorado, pp. 169-273.

Isaac, B.A., Dusseault, M.P., Lobb, G.D. and Root, J.D. 1982. Characterization of the lower Cretaceous overburden for oil sands surface mining within Syncrude Canada Ltd. Leases, Northeast Alberta, Canada. Proceedings, 4th International Association of Engineering Geology, India, pp. 381-384.

Kenney, T.C. 1967. The influence of mineral composition on the residual strength of natural soils. Proceedings, Geotechnical Conference, Oslo, NGI, Vol. 1. pp. 123-129.

Kocks U. F. 1975. *In* Constitutive equations in plasticity. *Edited by* A. S. Argon, MIT press, Cambridge, MA, pp. 81-113.

Kulhawy, F.H. and Mayne, P.W. 1990. Manual on estimating soil properties for foundation design. Final Report, Project 1493-6, EL-6800, Electric Power Research Institute, Palo Alto, California.

La Gatta, D.P. 1970. Residual strength of clays and clay shales by rotation shear tests. Harvard Soil Mechanics Series, No. 86, Harvard University, Cambridge, MA.

Lemos, L.J.L. 1986. The effect of shear rate on residual strength of Soil. Ph.D. thesis, University of London, England.

List, B.R. 1991. Stability analysis techniques through the monitoring of Syncrude's open pit oil sand slopes, Proceedings, 6th International Symposium on Landslides, Christchurch, New Zealand, Vol.2. pp. 1299-1304.

Lupini, J.F., Skinner, A.E. and Vaughan, P.R. 1981. The drained residual strength of cohesive soils. Geotechnique, 31.2: 181-213.

Mitchell, J.K. 1992. Fundamentals of soil behavior. Second Edition, John Wiley and Sons. Inc.

Morgenstern, N.R. 1985. Geotechnical aspects of environmental control. Proceedings, 11th International Conference on Soil Mechanics and Foundation Engineering, San Francisco, Vol. 1. pp. 155-185.

Morgenstern, N.R. 1987. Geotechnical control of stability on large projects.

Proceedings, 8th Pan American Conference on Soil Mechanics and Foundation Engineering, Cartagena, Vol.1. pp. 293-316.

Morgenstern, N.R. 1991. The role of analysis in the evaluation of slope stability. Proceedings, 6th International Symposium on Landslides, Christchurch, New Zealand. Vol. 3.

Morsy, M.M., Morgenstern, N.R. and Chan, D.H. 1994. Simulation of creep deformation in the foundation of Tar Island Dyke. Submitted to Canadian Geotechnical Journal.

Nieuwenhuis, J.D. 1991 The life time of a landslide. A.A. Balkema, Rotterdam.

Oka, F., Adachi, T. and Mimura, M. 1988. Elasto-Viscoplastic constitutive models for clays. International Conference on Rheology and Soil Mechanics, pp. 12-28.

Perzyna, P. 1963. The constitutive equations for work hardening and rate sensitive plastic materials. Proceedings, Vibration Problems, Warsaw, Vol.3. No.4. pp. 281-290.

Perzyna, P. 1963. The constitutive equations for rate sensitive plastic materials. Quarterly Journal of Applied Mathematics, 20.4: 321-332.

Saito, M. 1965. Forecasting the time of occurrence of slope failure. Proceedings, 6th International Conference on Soil Mechanics and Foundation Engineering, Montreal, Vol. 2. pp. 537-541.

Salt, G. 1988. Landslide mobility and remedial measures. Proceedings, 5th International Symposium on Landslides, Lausanne, Vol. 1. pp. 757-762.

Savage, R.H. and Schaefer, D.L. 1956. Vapor lubrication of graphite sliding contacts. Journal of Applied Physics, **27**: 136-138.

Sego, D.C. and Morgenstern, N.R. 1986. Strength behavior of foundation material - Syncrude Tailings Dyke. A report submitted to Syncrude Canada Ltd.

Singh, A. and Mitchell, J.K. 1968. Generalized stress-strain-time function for soil. ASCE Journal of Soil Mechanics and Foundation Engineering, **94**. SM1: 21-46.

Skempton, A.W. 1964. Long term stability of clay slopes. Geotechnique, **14**. 2: 77-102.

Skempton, A.W. 1985. Residual strength of clay landslides, folded strata and the laboratory. Geotechnique, **35**. 1: 3-18.

Skempton, A.W. and Petley, D.J. 1967. The strength along structural discontinuities in stiff clays. Proceedings, Geotechnical Conference, Oslo, NGI, Vol. 2. pp. 29-43.

Skempton, A.W., Leadbeath, A.B. and Chandler, R.J. 1989. The Mam Tor landslide, North Derbyshire. Phil. Trans., Royal Society of London, Vol. 329. pp. 503-547.

Stark, T.D. and Eid, H.T. 1994. Drained residual strength of cohesive soils. ASCE Journal of Geotechnical Engineering, **120**. GT5: 856-869.

Stevenson, I. P. 1972. Geological Sheet SK18SW (6 inches to a mile). British Geological Survey.

Suklje and Vidmar, S. 1961. A landslide due to long-term creep. Proceedings, 5th International Conference in Soil Mechanics and Foundation Engineering, Paris, Vol. 2. pp. 727-736.

Tan, S. 1991. Mildred Lake Dyke performance summary. GRB presentation report, Nov. 1991, Syncrude Canada Ltd.

Van Genuchten, P.M.B. 1988. Intermittent sliding of a landslide in varved clays. Proceedings, 5th International Symposium on Landslides, Lausanne, Vol.1. pp. 471-476.

Van Genuchten, P.M.B. 1990. On the viscous resistance in the movement mechanism of landslides in the French Alps. Proceedings, 6th International Congress IAEG, Amsterdam, Vol. 3. pp. 1739-1745.

Van Genuchten, P.M.B. and Nieuwenhuis, J.D. 1990. On the stability of seasonally sliding soil masses in the French Alps. Engineering Geology, **28**: 41-69.

Vulliet, L. and Hutter, K. 1988. Viscous type sliding laws for landslides. Canadian Geotechnical Journal, **25**: 467-473.

Vulliet, L. and Hutter, K. 1988. Continuum model for natural slopes in slow movement. Geotechnique, **38**. 2: 199-217.

Zak A. R. 1984. Finite element model for non axisymmetric structure with rate-dependent yield conditions. Contract report ARBRL CR 00524, Dept. of Aeronautical & Astronautical Engineering, University of Illinois, Urbana.

APPENDIX 2

Table A2.1 Physical Properties and Index values

Unit weight (kN/m^2)	18.6
Natural Water Content (%)	23
Specific Gravity	2.63
Liquid Limit (%)	135
Plasticity Limit (%)	28
Plasticity Index (%)	107
Liquidity Index (%)	-5
Clay Fraction (%) *	49

* Grain size distribution is shown in Figure A2.10.

Table A2.2 Engineering Properties

Coefficient of consolidation (m^2/year)	1.5 - 3.3
Overconsolidation ratio	~ 3
Coefficient of volume compressibility (m^2/kN.)	0.9 -3.0
Hydraulic conductivity (m/year)	0.17 - 0.11

Table A2.3 Summary of test results

Displacement rate		0.185 mm/day or 0.7 mm/day	1.0 mm/day	7.0 mm/day
RS 500	S (kPa)	59.88	61.96	63.69
	ϕ (deg.)	6.8	7.1	7.3
DS 500	S (kPa)	68.91	69.37	71.25
	ϕ (deg.)	7.8	7.9	8.1
DS 100	S (kPa)	13.71	14.07	14.31
	ϕ (deg.)	7.9	8.1	8.3
RS 500 (Sheared)	S (kPa)	59.34	61.66	63.41
	ϕ (deg.)	6.8	7.1	7.3
DS 500 (Sheared)	S (kPa)	68.50	69.50	70.80
	ϕ (deg.)	7.9	8.0	8.2
DS 100 (Sheared)	S (kPa)	14.20	14.34	14.69
	ϕ (deg.)	8.1	8.2	8.4
RS100	S (kPa)	12.20	12.56	12.98
	ϕ (deg.)	7.0	7.2	7.4
DS 100 (new)	S (kPa)	14.15	14.20	14.50
	ϕ (deg.)	8.2	8.1	8.3
DS500 (new)	S (kPa)	64.70	66.27	68.25
	ϕ (deg.)	7.5	7.5	7.8

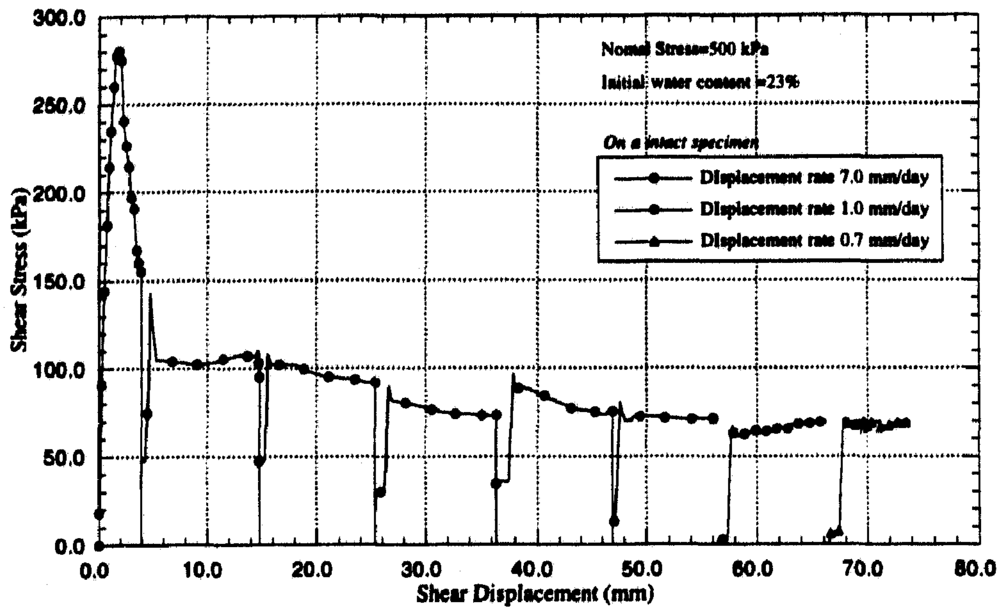

Figure A2-1 Direct shear test series 1 for kca at Syncrude site

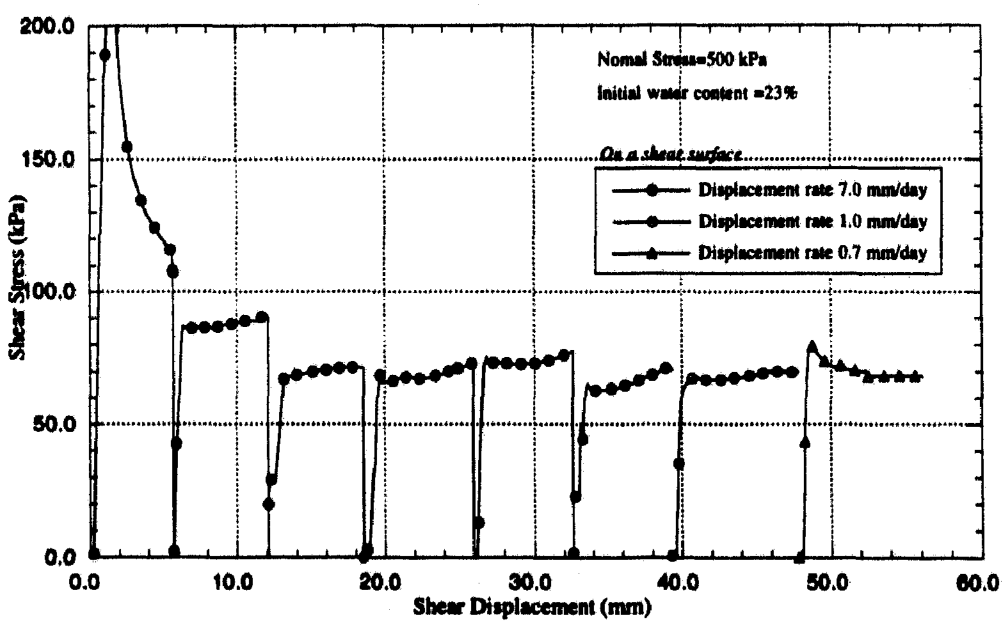

Figure A2-2 Direct shear test series 2 for kca at Syncrude site

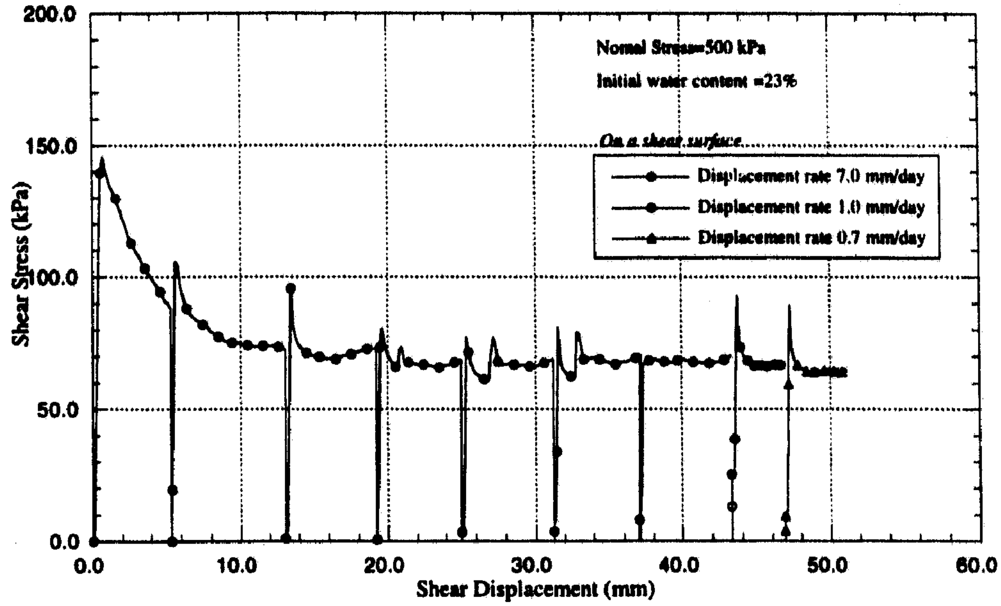

Figure A2-3 Direct shear test series 3 for kca at Syncrude site

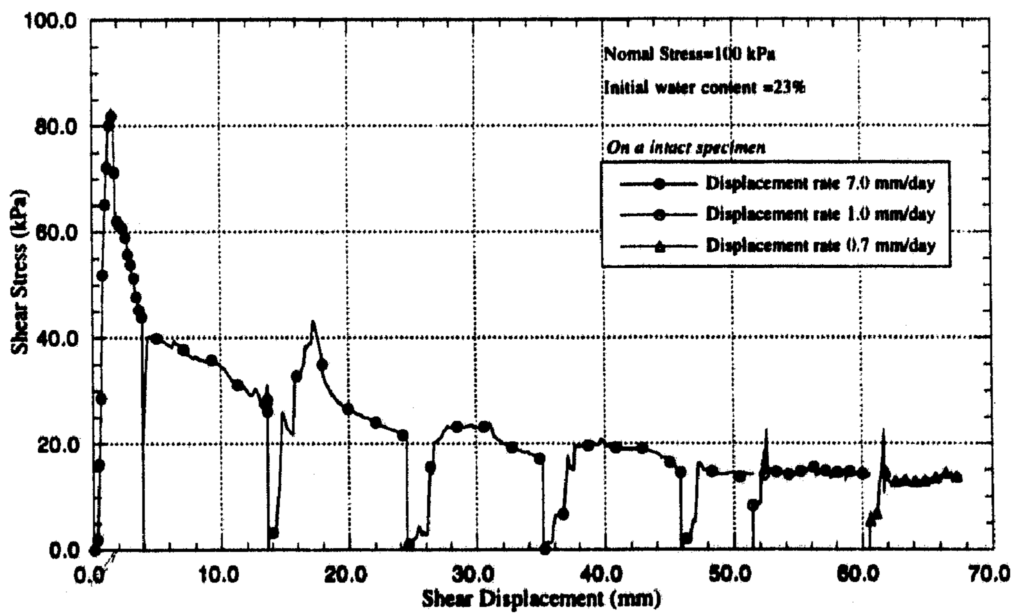

Figure A2-4 Direct shear test series 4 for kca at Syncrude Site

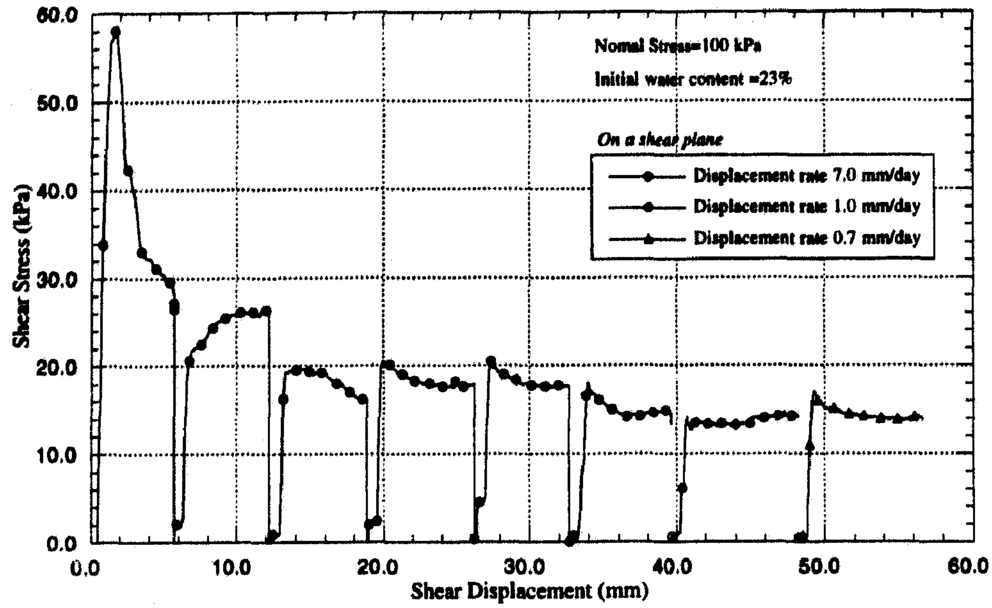

Figure A2-5 Direct shear test series 5 for kca at Syncrude site

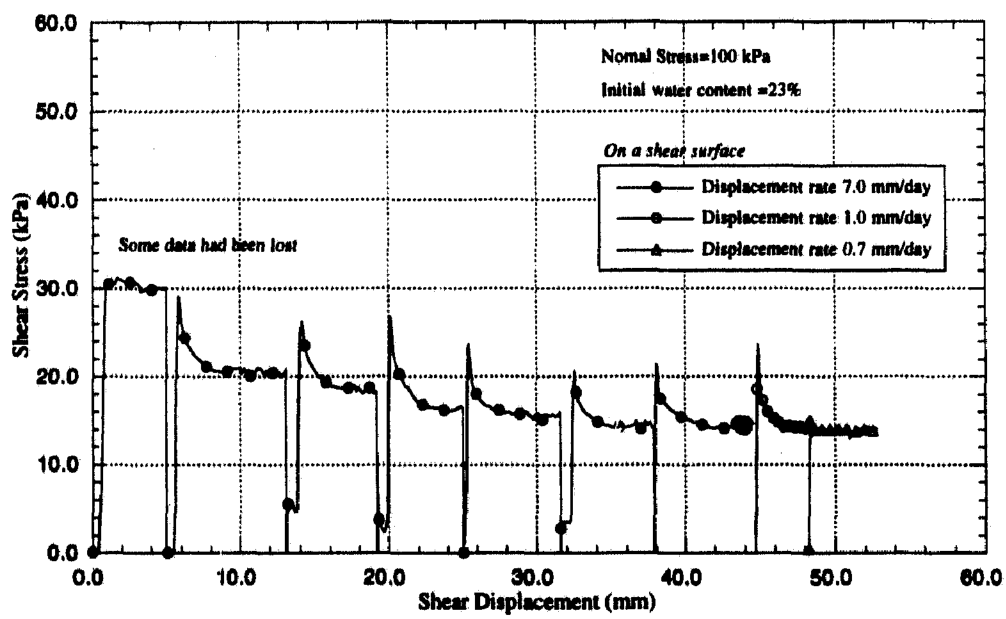

Figure A2-6 Direct shear test series 6 for kca at Syncrude site

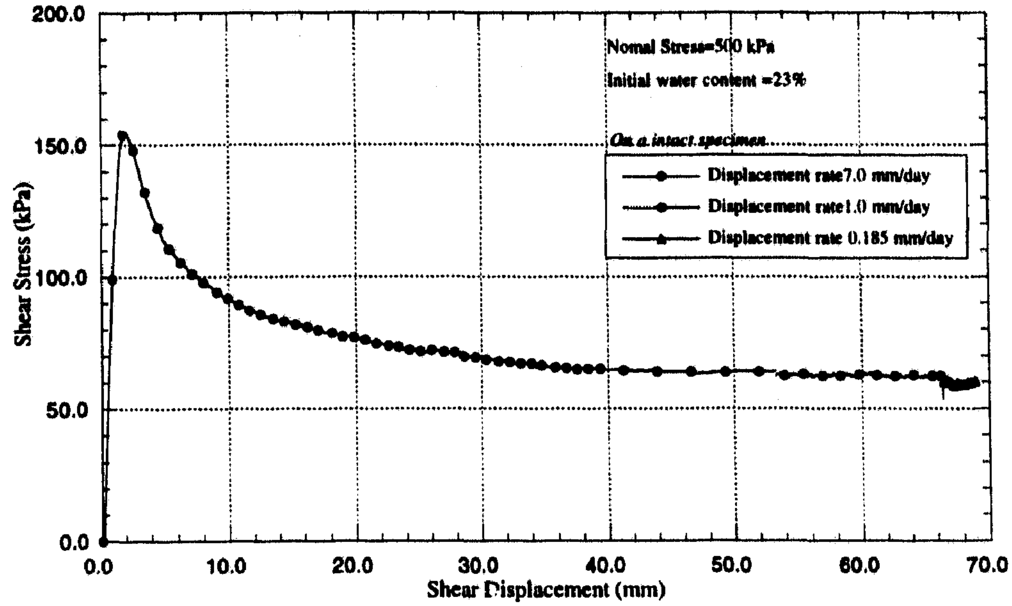

Figure A2-7 Ring shear test series 1 for kca at Syncrude site

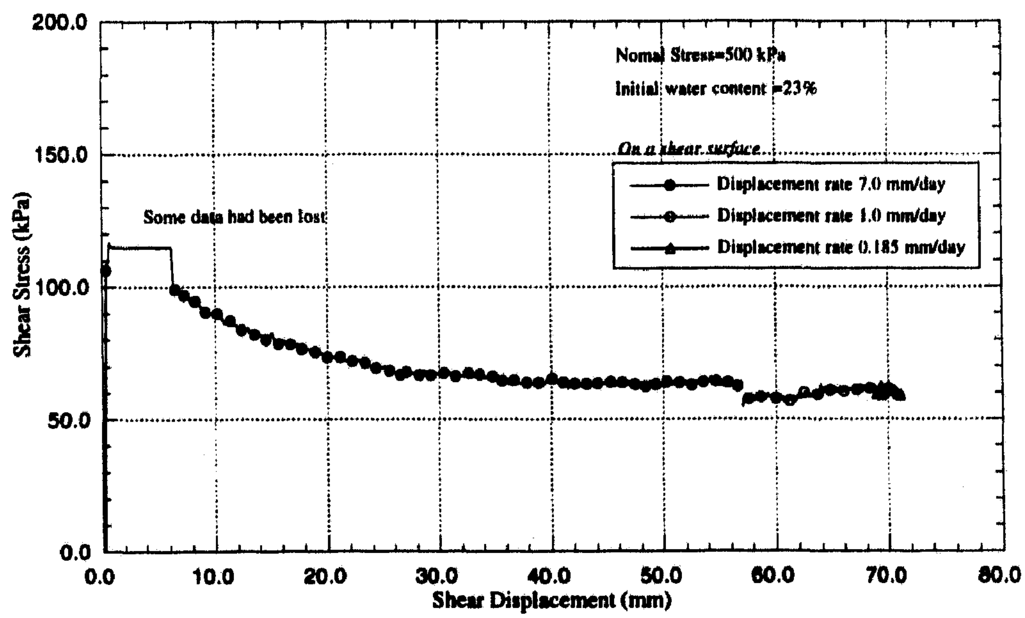

Figure A2-8 Ring shear test series 2 for kca at Syncrude site

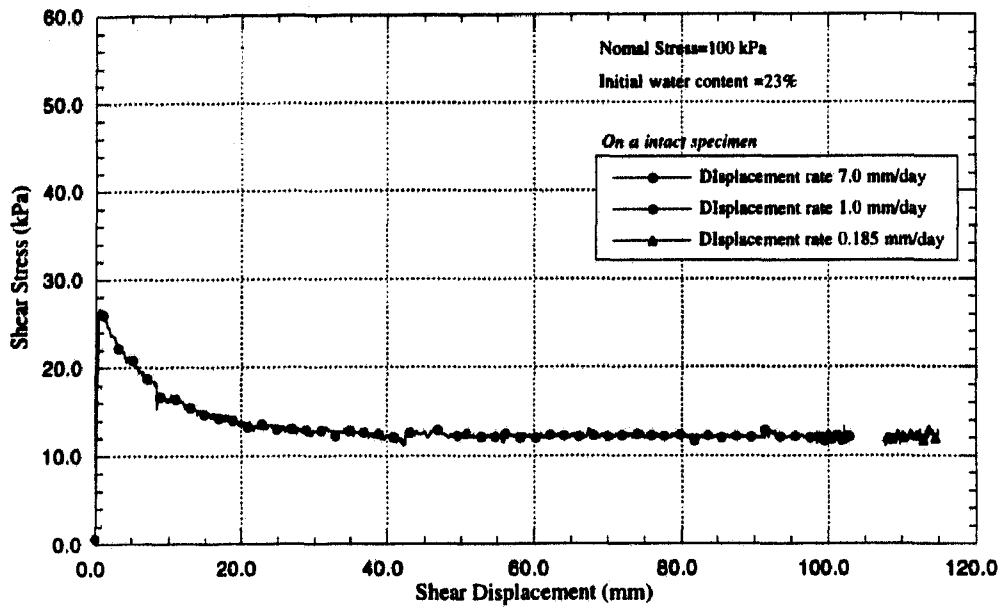

Figure A2-9 Ring Shear test series 3 for kca at Syncrude site

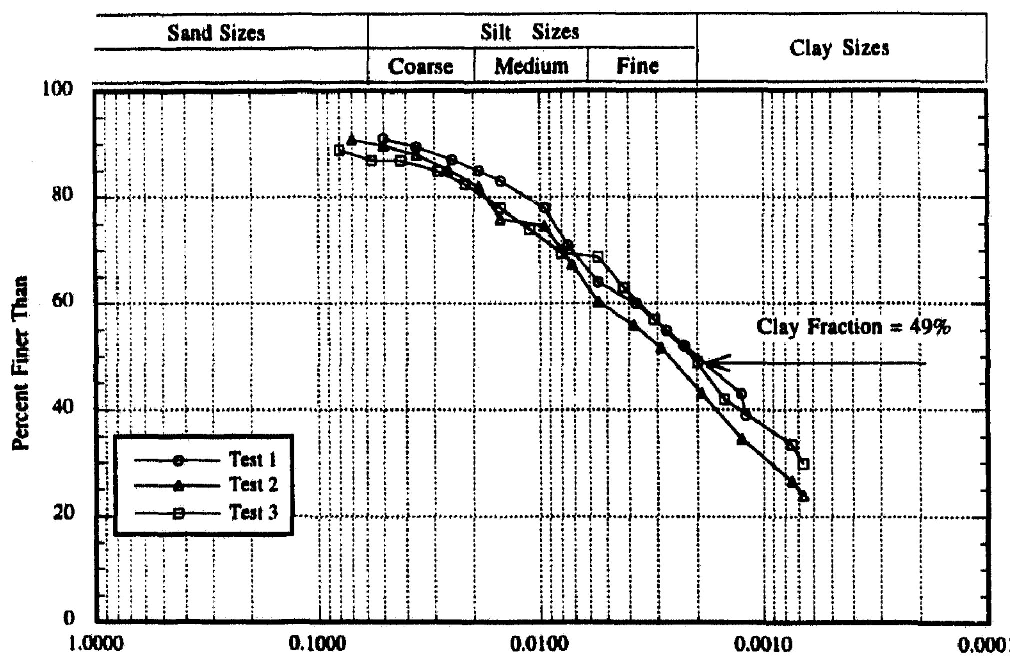

Figure A2-10 Particle size distribution

APPENDIX 3

APPENDIX 3-1

Derivation of Constitutive Equations for a Material with Strain hardening/softening and Strain rate dependency.

Yield function F can be expressed as:

$$F\left(\sigma_{ij}, \varepsilon_{ij}^{p}, \overset{\circ}{\varepsilon}{}^{p}\right) = 0$$

$$\frac{\partial F}{\partial \sigma_{ij}} \overset{\circ}{\sigma}_{ij} + \frac{\partial F}{\partial \varepsilon_{ij}^{p}} \overset{\circ}{\varepsilon}{}_{ij}^{p} + \frac{\partial F}{\partial \overset{\circ}{\varepsilon}{}^{p}} \overset{\circ\circ}{\varepsilon}{}^{p} = 0 \qquad \text{(A3-1)}$$

Rewriting Equation (A3-1) ,

$$\frac{\partial F}{\partial \sigma_{ij}} \overset{\circ}{\sigma}_{ij} + \frac{\partial F}{\partial \varepsilon_{ij}^{p}} \overset{\circ}{\varepsilon}{}_{ij}^{p} - \left[-\frac{\partial F}{\partial \overset{\circ}{\varepsilon}{}^{p}} \right] \overset{\circ\circ}{\varepsilon}{}^{p} = 0 \qquad \text{(A3-2)}$$

But,

$$\overset{\circ}{\sigma}_{ij} = C_{ijkl}^{e} (\overset{\circ}{\varepsilon}_{kl} - \overset{\circ}{\varepsilon}{}_{kl}^{p}) \qquad \text{(A3-3)}$$

from flow rule of plasticity,

$$\overset{\circ}{\varepsilon}{}_{kl}^{p} = \lambda \frac{\partial g}{\partial \sigma_{kl}} \qquad \text{(A3-4)}$$

The plastic potential function, g , is defined such that during plastic deformation there is no volume change and it passes through the same point in stress space as F .

Defining effective plastic strain rate as

$$\overset{\circ}{\varepsilon}^p = \sqrt{\frac{1}{2}\overset{\circ}{\varepsilon}{}^p_{ij}\overset{\circ}{\varepsilon}{}^p_{ij}} \tag{A3-5}$$

from (A3-4) and (A3-5)

$$\overset{\circ}{\varepsilon}^p = \sqrt{\frac{1}{2}\left(\lambda\frac{\partial g}{\partial \sigma_{ij}}\right)\left(\lambda\frac{\partial g}{\partial \sigma_{ij}}\right)} \tag{A3-6}$$

Therefore,

$$\lambda = \overset{\circ}{\varepsilon}^p \Big/ \sqrt{\frac{1}{2}\left(\frac{\partial g}{\partial \sigma_{kl}}\right)\left(\frac{\partial g}{\partial \sigma_{kl}}\right)} \tag{A3-7}$$

combining (A3-4) and (A3-7)

$$\overset{\circ}{\varepsilon}{}^p_{kl} = \frac{\overset{\circ}{\varepsilon}^p}{\sqrt{\frac{1}{2}\left(\frac{\partial g}{\partial \sigma_{mn}}\right)\left(\frac{\partial g}{\partial \sigma_{mn}}\right)}}\frac{\partial g}{\partial \sigma_{kl}} \tag{A3-8}$$

from (A3-2), (A3-3) and (A3-8),

$$\frac{\partial F}{\partial \sigma_{ij}} C^e_{ijkl}\left[\overset{\circ}{\varepsilon}_{kl} - \frac{\overset{\circ}{\varepsilon}^p}{\sqrt{\frac{1}{2}\left(\frac{\partial g}{\partial \sigma_{mn}}\right)\left(\frac{\partial g}{\partial \sigma_{mn}}\right)}}\frac{\partial g}{\partial \sigma_{kl}}\right] + \frac{\partial F}{\partial \varepsilon^p_{ij}}\overset{\circ}{\varepsilon}{}^p_{ij} - \left[-\frac{\partial F}{\partial \overset{\circ}{\varepsilon}^p}\right]\overset{\circ\circ}{\varepsilon}^p = 0$$

$$-\left[-\frac{\partial F}{\partial \overset{\circ}{\varepsilon}^p}\right]\overset{\circ\circ}{\varepsilon}^p + \frac{\frac{\partial F}{\partial \varepsilon^p_{ij}}\frac{\partial g}{\partial \sigma_{ij}}}{\sqrt{\frac{1}{2}\left(\frac{\partial g}{\partial \sigma_{mn}}\right)\left(\frac{\partial g}{\partial \sigma_{mn}}\right)}}\overset{\circ}{\varepsilon}^p - \frac{\frac{\partial F}{\partial \sigma_{ij}} C^e_{ijkl}\frac{\partial g}{\partial \sigma_{kl}}}{\sqrt{\frac{1}{2}\left(\frac{\partial g}{\partial \sigma_{mn}}\right)\left(\frac{\partial g}{\partial \sigma_{mn}}\right)}}\overset{\circ}{\varepsilon}^p + \frac{\partial F}{\partial \sigma_{ij}} C^e_{ijkl}\overset{\circ}{\varepsilon}_{kl} = 0 \tag{A3-9}$$

Rearranging above equation,

$$\overset{\circ\circ}{\varepsilon}^{p} + \left(\frac{\frac{\partial F}{\partial\sigma_{ij}} C^{e}_{ijkl} \frac{\partial g}{\partial\sigma_{kl}} - \frac{\partial F}{\partial \varepsilon^{p}_{ij}}\frac{\partial g}{\partial\sigma_{ij}}}{\frac{\partial K}{\partial\overset{\circ}{\varepsilon}^{p}}\sqrt{\frac{1}{2}\left(\frac{\partial g}{\partial\sigma_{mn}}\right)\left(\frac{\partial g}{\partial\sigma_{mn}}\right)}} \right)\overset{\circ}{\varepsilon}^{p} = \frac{\frac{\partial F}{\partial\sigma_{ij}}C^{e}_{ijkl}\overset{\circ}{\varepsilon}_{kl}}{\left[-\frac{\partial F}{\partial\overset{\circ}{\varepsilon}^{p}}\right]} \qquad \text{(A3-10)}$$

Equation (A3-10) is a first order nonlinear differential equation of $\overset{\circ}{\varepsilon}^{p}$

Initial condition in small time interval is, at t=0, $\overset{\circ}{\varepsilon}^{p} = \overset{\circ}{\varepsilon}^{p}_{I}$. where, $\overset{\circ}{\varepsilon}^{p}_{I}$ is the effective plastic strain rate at the end of i^{th} interval.

Thus, the effective plastic strain rate is continuous even after an abrupt change in stress. In order to generate a specific plastic constitutive equation, the exact dependence of f over the variables has to be known.

Solution to the Equation (A3-10)

$$d\sigma_{ij} = \left(C^{e}_{ijmn} - \frac{C^{e}_{ijkl}\frac{\partial g}{\partial\sigma_{kl}}\frac{\partial F}{\partial\sigma_{\alpha\beta}}C^{e}_{\alpha\beta mn}}{\frac{\partial F}{\partial\sigma_{\alpha\beta}}C^{e}_{\alpha\beta mn}\frac{\partial g}{\partial\sigma_{mn}} - \frac{\partial F}{\partial\varepsilon^{p}_{kl}}\frac{\partial g}{\partial\sigma_{kl}}} \left(1 - e^{-\frac{\frac{\partial F}{\partial\sigma_{\alpha\beta}}C^{e}_{\alpha\beta mn}\frac{\partial g}{\partial\sigma_{mn}} - \frac{\partial F}{\partial\varepsilon^{p}_{kl}}\frac{\partial g}{\partial\sigma_{kl}}}{\sqrt{\frac{1}{2}\left(\frac{\partial g}{\partial\sigma_{mn}}\right)\left(\frac{\partial g}{\partial\sigma_{mn}}\right)}\left[-\frac{\partial F}{\partial\overset{\circ}{\varepsilon}^{p}}\right]}\Delta t} \right) \right) d\varepsilon_{mn}$$

$$-C^{e}_{ijkl}\frac{\partial g}{\partial\sigma_{kl}}\left(\frac{\overset{\circ}{\varepsilon}^{p}_{I}\Delta t}{\sqrt{\frac{1}{2}\left(\frac{\partial g}{\partial\sigma_{mn}}\right)\left(\frac{\partial g}{\partial\sigma_{mn}}\right)}} \right) e^{-\frac{\frac{\partial F}{\partial\sigma_{\alpha\beta}}C^{e}_{\alpha\beta mn}\frac{\partial g}{\partial\sigma_{mn}} - \frac{\partial F}{\partial\varepsilon^{p}_{kl}}\frac{\partial g}{\partial\sigma_{kl}}}{\sqrt{\frac{1}{2}\left(\frac{\partial g}{\partial\sigma_{mn}}\right)\left(\frac{\partial g}{\partial\sigma_{mn}}\right)}\left[-\frac{\partial F}{\partial\overset{\circ}{\varepsilon}^{p}}\right]}\Delta t}$$

(A3-11)

Equation (A3-11) is now a suitable incremental relation over a time step Δt, which gives the change in stress in terms of change in total strain and in terms of parameters which can be calculated from the previous time step. The second term on the right hand side of equation (A 3-11) represents the initial rate effects.

APPENDIX 3-2

Solution of Equation 3.17

$$\frac{\partial K}{\partial \overset{\circ}{\varepsilon}^{p}} \overset{\circ\circ}{\varepsilon}^{p} + \frac{\partial F}{\partial \sigma_{ij}} C^{e}_{ijkl} \frac{\partial g}{\partial \sigma_{kl}} \frac{\overset{\circ}{\varepsilon}^{p}}{\sqrt{\frac{1}{2}\left(\frac{\partial g}{\partial \sigma_{mn}}\right)\left(\frac{\partial g}{\partial \sigma_{mn}}\right)}} = \frac{\partial F}{\partial \sigma_{ij}} C^{e}_{ijkl} \overset{\circ}{\varepsilon}_{kl}$$

(A3-12)

let, $$U = \exp\left\{ \frac{\frac{\partial F}{\partial \sigma_{ij}} C^{e}_{ijkl} \frac{\partial g}{\partial \sigma_{kl}}}{\sqrt{\frac{1}{2}\left(\frac{\partial g}{\partial \sigma_{mn}}\right)\left(\frac{\partial g}{\partial \sigma_{mn}}\right)}\left[-\frac{\partial F}{\partial \overset{\circ}{\varepsilon}^{p}}\right]} \right\} t$$

multiplying both side of the equation (A3-12) by U

$$U \overset{\circ}{\varepsilon}^{p} = \int e^{\left\{ \frac{\frac{\partial F}{\partial \sigma_{ij}} C^{e}_{ijkl} \frac{\partial g}{\partial \sigma_{kl}}}{\sqrt{\frac{1}{2}\left(\frac{\partial g}{\partial \sigma_{mn}}\right)\left(\frac{\partial g}{\partial \sigma_{mn}}\right)}\left[-\frac{\partial F}{\partial \overset{\circ}{\varepsilon}^{p}}\right]} t \right\}} \frac{\frac{\partial F}{\partial \sigma_{ij}} C^{e}_{ijkl} \overset{\circ}{\varepsilon}_{kl}}{\left[-\frac{\partial F}{\partial \overset{\circ}{\varepsilon}^{p}}\right]} dt + c \qquad \text{(A3-13)}$$

Where c is an integration constant. For a small time increment, $\overset{\circ}{\sigma}_{ij}$ can be assumed as constant. Therefore, $\overset{\circ}{\varepsilon}_{ij}$ and $\frac{\partial F}{\partial \overset{\circ}{\varepsilon}^{p}}$ will be constant.

$$U\overset{\circ}{\varepsilon}{}^{p} = e^{\left\{ \frac{\frac{\partial F}{\partial \sigma_{ij}} C^{e}_{ijkl} \frac{\partial g}{\partial \sigma_{kl}}}{\sqrt{\frac{1}{2}\left(\frac{\partial g}{\partial \sigma_{mn}}\right)\left(\frac{\partial g}{\partial \sigma_{mn}}\right)}\left[-\frac{\partial F}{\partial \overset{\circ}{\varepsilon}{}^{p}}\right]} t \right\}} \frac{\frac{\partial F}{\partial \sigma_{ij}} C^{e}_{ijkl} \overset{\circ}{\varepsilon}_{kl} \sqrt{\frac{1}{2}\left(\frac{\partial g}{\partial \sigma_{mn}}\right)\left(\frac{\partial g}{\partial \sigma_{mn}}\right)}}{\frac{\partial F}{\partial \sigma_{ij}} C^{e}_{ijkl} \frac{\partial g}{\partial \sigma_{kl}}} + c \quad \text{(A3-14)}$$

Initial condition in small time interval is, at t=0, $\overset{\circ}{\varepsilon}{}^{p} = \overset{\circ}{\varepsilon}{}^{p}_{i}$. Where, $\overset{\circ}{\varepsilon}{}^{p}_{i}$ is the effective plastic strain rate at the end of i^{th} interval.

Thus, the effective plastic strain rate is continuous even after an abrupt change in stress. In order to generate specific plastic constitutive equation the exact dependence of f over the variables have to be known.

$$\overset{\circ}{\varepsilon}{}^{p} = \frac{\frac{\partial F}{\partial \sigma_{ij}} C^{e}_{ijkl} \overset{\circ}{\varepsilon}_{kl} \sqrt{\frac{1}{2}\left(\frac{\partial g}{\partial \sigma_{mn}}\right)\left(\frac{\partial g}{\partial \sigma_{mn}}\right)}}{\frac{\partial F}{\partial \sigma_{ij}} C^{e}_{ijkl} \frac{\partial g}{\partial \sigma_{kl}}} + c e^{\left\{ -\frac{\frac{\partial F}{\partial \sigma_{ij}} C^{e}_{ijkl} \frac{\partial g}{\partial \sigma_{kl}}}{\sqrt{\frac{1}{2}\left(\frac{\partial g}{\partial \sigma_{mn}}\right)\left(\frac{\partial g}{\partial \sigma_{mn}}\right)}\left[-\frac{\partial F}{\partial \overset{\circ}{\varepsilon}{}^{p}}\right]} t \right\}} \quad \text{(A3-15)}$$

Let,

$$A = \frac{\frac{\partial F}{\partial \sigma_{ij}} C^{e}_{ijkl} \overset{\circ}{\varepsilon}_{kl} \sqrt{\frac{1}{2}\left(\frac{\partial g}{\partial \sigma_{mn}}\right)\left(\frac{\partial g}{\partial \sigma_{mn}}\right)}}{\frac{\partial F}{\partial \sigma_{ij}} C^{e}_{ijkl} \frac{\partial g}{\partial \sigma_{kl}}} \quad \text{(A3-16a)}$$

$$B = -\frac{\frac{\partial F}{\partial \sigma_{ij}} C^e_{ijkl} \frac{\partial g}{\partial \sigma_{kl}}}{\sqrt{\frac{1}{2}\left(\frac{\partial g}{\partial \sigma_{mn}}\right)\left(\frac{\partial g}{\partial \sigma_{mn}}\right)}\left[-\frac{\partial F}{\partial \mathring{\varepsilon}^p}\right]} \tag{A3-16b}$$

Then,

$$\mathring{\varepsilon}^p = A + ce^{Bt}$$

$$\mathring{\varepsilon}^p = A - (A - \mathring{\varepsilon}^p_I)e^{Bt} \tag{A3-17}$$

At time t, effective plastic strain rate,

using Equation (3.15) and rearranging subscripts in A & B and simplifying,

$$\mathring{\varepsilon}^p_{ij} = \frac{A - (A - \mathring{\varepsilon}^p_I)e^{Bt}}{\sqrt{\frac{1}{2}\left(\frac{\partial g}{\partial \sigma_{mn}}\right)\left(\frac{\partial g}{\partial \sigma_{mn}}\right)}} \frac{\partial g}{\partial \sigma_{ij}} \tag{A3-18}$$

where,

$$A = \frac{\frac{\partial F}{\partial \sigma_{\alpha\beta}} C^e_{\alpha\beta mn} \mathring{\varepsilon}_{mn}}{\frac{\partial F}{\partial \sigma_{\alpha\beta}} C^e_{\alpha\beta mn} \frac{\partial g}{\partial \sigma_{mn}}} \tag{A3-18b}$$

$$B = -\frac{\frac{\partial F}{\partial \sigma_{\alpha\beta}} C^e_{\alpha\beta mn} \frac{\partial g}{\partial \sigma_{mn}}}{\sqrt{\frac{1}{2}\left(\frac{\partial g}{\partial \sigma_{mn}}\right)\left(\frac{\partial g}{\partial \sigma_{mn}}\right)}\left[-\frac{\partial F}{\partial \mathring{\varepsilon}^p}\right]} \tag{A3-18c}$$